

Smart Wearables in Healthcare: Signal Processing, Device Development, and Clinical Applications

Lead Guest Editor: Chengyu Liu

Guest Editors: Feng Liu, Li Zhang, Yi Su, and Alan Murray





**Smart Wearables in Healthcare:
Signal Processing, Device Development,
and Clinical Applications**

Journal of Healthcare Engineering

**Smart Wearables in Healthcare:
Signal Processing, Device Development,
and Clinical Applications**

Lead Guest Editor: Chengyu Liu

Guest Editors: Feng Liu, Li Zhang, Yi Su, and Alan Murray



Copyright © 2018 Hindawi. All rights reserved.

This is a special issue published in “Journal of Healthcare Engineering.” All articles are open access articles distributed under the Creative Commons Attribution License, which permits unrestricted use, distribution, and reproduction in any medium, provided the original work is properly cited.

Editorial Board

Saverio Affatato, Italy
Francesca Apollonio, Italy
Hasan Ayaz, USA
William Bertucci, France
Patrick Boissy, Canada
Hongwei Chen, USA
Daniel H.K. Chow, Hong Kong
Gianluca Ciardelli, Italy
Elena De Momi, Italy
Costantino Del Gaudio, Italy
Tiago H. Falk, Canada
Mostafa Fatemi, USA
Jesus Favela, Mexico
David Dagan Feng, Australia
Joseph Finkelstein, USA
Jesus Fontecha, Spain
Jean-Luc Gennisson, France
Shahram M. Ghanaati, Germany
Luca Giancardo, USA
Antonio Gloria, Italy
Kheng-Lim Goh, Singapore
Pedro Gomes, Portugal
Carlos Gómez, Spain
Philippe Gorce, France
Sophia Z. Gu, Australia
Vincenzo Guarino, Italy
Valentina Hartwig, Italy

David Hewson, UK
Andreas H. Hielscher, USA
Ernesto Iadanza, Italy
Norio Iriguchi, Japan
Jingfeng Jiang, USA
Zhongwei Jiang, Japan
Rashed Karim, UK
Pasi A. Karjalainen, Finland
Chandan Karmakar, Australia
John S. Katsanis, Greece
Terry K.K. Koo, USA
Panagiotis Kosmas, UK
Michel Labrosse, Canada
Jui-Yang Lai, Taiwan
Xiang Li, USA
Feng-Huei Lin, Taiwan
Yuan-Pin Lin, Taiwan
Maria Lindén, Sweden
Dongfei Liu, Finland
Francisco Lopez-Valdes, Spain
Zufu Lu, Australia
Ilias Maglogiannis, Greece
Andreas Maier, Germany
Mehran Moazen, UK
Rafael Morales, Spain
David Moratal, Spain
Angkoon Phinyomark, Canada

Vincenzo Positano, Italy
Alessandro Ramalli, Italy
Alessandro Reali, Italy
Lei Ren, UK
Jose Joaquin Rieta, Spain
Emanuele Rizzuto, Italy
Sébastien Roth, France
Simo Saarakkala, Finland
Hélder A. Santos, Finland
Emiliano Schena, Italy
Maurizio Schmid, Italy
Jiann-Shing Shieh, Taiwan
Tiago H. Silva, Portugal
Redha Taiar, France
Jinshan Tang, USA
Vinoy Thomas, USA
Ioannis G. Tollis, Greece
Kazunori Uemura, Japan
Uche Wejinya, USA
Damon W.K. Wong, Singapore
Ying Yang, UK
Haihong Zhang, Singapore
Hongbo Zhang, Finland
Ping Zhou, USA
Loredana Zollo, Italy

Contents

Smart Wearables in Healthcare: Signal Processing, Device Development, and Clinical Applications

Chengyu Liu , Feng Liu , Li Zhang, Yi Su, and Alan Murray
Editorial (2 pages), Article ID 1696924, Volume 2018 (2018)

Multichannel Surface EMG Decomposition Based on Measurement Correlation and LMMSE

Yong Ning , Yuming Zhao, Akbarjon Juraboev, Ping Tan, Jin Ding, and Jinbao He
Research Article (12 pages), Article ID 2347589, Volume 2018 (2018)

Atrial Fibrillation Beat Identification Using the Combination of Modified Frequency Slice Wavelet Transform and Convolutional Neural Networks

Xiaoyan Xu, Shoushui Wei , Caiyun Ma, Kan Luo , Li Zhang, and Chengyu Liu 
Research Article (8 pages), Article ID 2102918, Volume 2018 (2018)

Performance Analysis of Ten Common QRS Detectors on Different ECG Application Cases

Feifei Liu, Chengyu Liu , Xinge Jiang, Zhimin Zhang, Yatao Zhang , Jianqing Li , and Shoushui Wei 
Research Article (8 pages), Article ID 9050812, Volume 2018 (2018)

A Study of the Effects of Daily Physical Activity on Memory and Attention Capacities in College Students

Dinh-Van Phan , Chien-Lung Chan , Ren-Hao Pan, Nan-Ping Yang , Hsiu-Chen Hsu, Hsien-Wei Ting, and K. Robert Lai 
Research Article (9 pages), Article ID 2942930, Volume 2018 (2018)

A Novel Neural Network Model for Blood Pressure Estimation Using Photoplethysmography without Electrocardiogram

Ludi Wang , Wei Zhou, Ying Xing , and Xiaoguang Zhou 
Research Article (9 pages), Article ID 7804243, Volume 2018 (2018)

Earable RCC: Development of an Earphone-Type Reliable Chewing-Count Measurement Device

Kazuhiro Taniguchi , Hisashi Kondo, Toshiya Tanaka, and Atsushi Nishikawa 
Research Article (8 pages), Article ID 6161525, Volume 2018 (2018)

Noninvasive Estimation of Joint Moments with Inertial Sensor System for Analysis of STS Rehabilitation Training

Kun Liu , Jianchao Yan , Yong Liu , and Ming Ye 
Research Article (15 pages), Article ID 6570617, Volume 2018 (2018)

A Digital Compressed Sensing-Based Energy-Efficient Single-Spot Bluetooth ECG Node

Kan Luo , Zhipeng Cai, Keqin Du , Fumin Zou, Xiangyu Zhang, and Jianqing Li 
Research Article (11 pages), Article ID 2687389, Volume 2018 (2018)

A Novel Sleep Respiratory Rate Detection Method for Obstructive Sleep Apnea Based on Characteristic Moment Waveform

Yu Fang , Zhongwei Jiang , and Haibin Wang 
Research Article (10 pages), Article ID 1902176, Volume 2018 (2018)

A Remote Health Monitoring System for the Elderly Based on Smart Home Gateway

Kai Guan, Minggang Shao, and Shuicai Wu
Research Article (9 pages), Article ID 5843504, Volume 2017 (2018)

Editorial

Smart Wearables in Healthcare: Signal Processing, Device Development, and Clinical Applications

Chengyu Liu ¹, Feng Liu ², Li Zhang,³ Yi Su,⁴ and Alan Murray⁵

¹State Key Laboratory of Bioelectronics, Jiangsu Key Laboratory of Remote Measurement and Control, School of Instrument Science and Engineering, Southeast University, Nanjing 210096, China

²University of Queensland, Brisbane, Australia

³University of Northumbria, Newcastle upon Tyne, UK

⁴Institute of High Performance Computing, A*STAR, Singapore

⁵Newcastle University, Newcastle upon Tyne, UK

Correspondence should be addressed to Chengyu Liu; chengyu@seu.edu.cn

Received 26 August 2018; Accepted 27 August 2018; Published 9 October 2018

Copyright © 2018 Chengyu Liu et al. This is an open access article distributed under the Creative Commons Attribution License, which permits unrestricted use, distribution, and reproduction in any medium, provided the original work is properly cited.

Recently, smart wearables, typically as wearable electrocardiogram (ECG), electroencephalography (EEG), electromyography (EMG), blood pressure (BP), photoplethysmography (PPG), heart sound, respiration, sleep, and motion monitoring, have been gaining a significant role in the field of healthcare and are looking to be a big and promising market in the technology industry. They are scientifically and clinically useful for better monitoring of real-time, long-term, and dynamic physiological and pathological processes, thus providing opportunities for the development of new diagnostic and therapeutic techniques. These could be expedient for the management of chronic illnesses, such as cardiovascular disease (CVD), sleep disorders, emotional problems, cognitive impairment, and functional decline, as well as for healthcare applications for special populations, such as for the aged, pregnant women, athletes, and astronauts. The mainstream in smart wearables research is moving towards more sophisticated methodologies based on clinical “big data,” artificial intelligence (AI), advanced signal processing, service robots, and networks, as well as more robust signal acquisition approaches.

In this context, many researchers have addressed recent technology advances in signal processing and device development for smart wearables, as well as the implementation of these technologies for clinical applications. The processing and analysis of wearable physiological signals (ECG, EEG, EMG, BP, PPG, etc.) is a key issue for smart wearable devices. The preliminary work mainly includes

dynamic signal quality assessment, signal transformation and decomposition, feature extraction and selection, and the following machine learning-based methods.

Y. Ning and colleagues decomposed multichannel surface electromyography (sEMG) signals into their constituent motor unit action potential (MUAP) trains. A combination method of measurement correlation (MC) and linear minimum mean square error (LMMSE) was proposed, named as MC-LMMSE, which was validated on both simulated and experimental electrode array sEMG signals. This study showed that the MC-LMMSE method can extract a relatively large number of MUs with strong robustness to noise.

As PPG technology has been widely applied to wearable sensors, L. Wang et al. developed a method for automatically estimating systolic blood pressure (SBP) and diastolic blood pressure (DBP) based only on a PPG signal. In this study, a multitaper method (MTM) was used for feature extraction and an artificial neural network (ANN) method was used for SBP and DBP estimation, obtaining a relatively high accuracy of BP estimation with an absolute error of 4.02 ± 2.79 mmHg for SBP and 2.27 ± 1.82 mmHg for DBP.

QRS complex location is important and even essential for ECG signal processing. F. Liu et al. performed a systematic evaluation work on ten widely used and high-efficient QRS detection algorithms, aiming at verifying their performances and usefulness in different application situations, especially in the dynamic noisy ECG environment. Four experiments were

carried out on six internationally recognized databases. For the clean clinical ECG signals, the majority of the QRS detectors reported high-level detection accuracies, whereas the accuracy of all algorithms significantly decreased for poor signal quality ECG signals. Thus, some special preprocessing and postprocessing procedures are needed. In addition, the QRS detector needs to be carefully selected in special situations, such as paced rhythm ECGs. This study offers a reference for selecting from the existing algorithms.

Clinical applications for chronic illnesses detection, including cardiac arrhythmia, hypertension, heart failure, sleep disorder, emotional problem, cognitive impairment, and functional decline, are the main target. The automatic detection and diagnosis algorithms for special diseases are the soul of clinical application. Typical works included in this special issue are summarized as follows:

X. Xu et al. proposed a new framework for automatic atrial fibrillation (AF) beat identification, which combines modified frequency slice wavelet transform (MFSWT) and convolutional neural networks (CNNs). This work achieved a relatively high accuracy of 84.9%. The study indicated that it was possible to accurately identify AF or non-AF ECGs from a short-term signal episode.

Obstructive sleep apnea (OSA) is a major breathing-related sleep disorder. Y. Fang et al. proposed a novel sleep respiratory rate detection based on the characteristic moment waveform (CMW) method. This method could detect sleep respiratory rate accurately. In addition, the apnea sections can be detected by the sleep respiratory rate curve with a given threshold, and the time duration of the segmentation of the breath can be calculated for detailed evaluation of the OSA state.

D. V. Phan and team evaluated the relationship between daily physical activity (DPA) and memory capacity, as well as the association between daily activity and attention capacity, using spatial span test (SST) and trail making test (TMT). The study showed that the short-term effects of very active time duration (VATD) and calories burnt on the day are significantly and negatively associated with memory and attention capacities of college students.

Intelligent health monitoring systems combining wearable technologies for health monitoring and disease diagnosis also aroused widespread concern among researchers.

K. Guan et al. designed a remote health monitoring system for the elderly. This proposed system consisted of three parts: smart clothing, a smart home gateway, and a health care server. The system could monitor the ECG signals and motion signals of the elderly, and has the potential to provide long-term and continuous home health-care monitoring services.

For gastrectomy patients requiring dietary support, K. Taniguchi et al. developed a chewing-count measurement device, named wearable reliable chewing-count (RCC), using an earphone-type sensor to display the information on a tablet terminal in real time. This earphone-type RCC measurement device could experimentally distinguish chewing from other actions. It can catch chewing actions and accurately count the number of chews with high probability.

Based on a piecewise three-segment sit-to-stand (STS) biomechanical model and a double-sensor difference algorithm, K. Liu and his group proposed an original approach for noninvasive estimation of lower limb joint moments for analysis of STS rehabilitation training with only inertial measurement units. This work presented joint kinematic and kinetic analysis using a customized wearable sensor system composed of accelerometers and gyroscopes. Compared with a referenced camera system, the proposed system was evaluated on five healthy subjects and five patients in rehabilitation. The results showed that the newly developed system was available for spatiotemporal analysis of STS task with fewer sensors and a high degree of accuracy, and can be used as a reference for rehabilitation training or feedback for the control of a powered exoskeleton system.

Low power- and energy-efficient hardware is still the obstacle for long-term real-time wearable devices. K. Luo et al. developed a digital compressed sensing- (CS-) based single-spot Bluetooth ECG node to deal with this challenge. Each node consisted of an ultra-low-power analog front-end, a microcontroller, and a Bluetooth 4.0 communication module. A periodic sleep/wake-up scheme and a CS-based compression algorithm were implemented in each node. This scheme can reduce the airtime over energy-hungry wireless links. The energy consumption of the proposed node is 6.53 mJ, and the energy consumption of the radio has a decrease of 77.4%.

Overall, the development of smart medical wearables still has far to go, from hardware devices (electrode and sensor design) to data processing and analysis. There is much meticulous work still to be done, including wearing comfort, energy consumption, database annotation, signal quality, building standards, and more. Even for ECG it would be an interesting study to see specifically how a multielectrode system responded to very specific situations, such as movement (always a current problem, although different electrode positions are likely to respond differently), body position, and heart rate. It is important to get beyond overall accuracy. Anyway, the gradual improvement of smart medical wearable devices will contribute a tremendous amount of power to human healthcare.

Conflicts of Interest

The editors declare that they have no conflicts of interest regarding the publication of this special issue.

*Chengyu Liu
Feng Liu
Li Zhang
Yi Su
Alan Murray*

Research Article

Multichannel Surface EMG Decomposition Based on Measurement Correlation and LMMSE

Yong Ning ^{1,2}, Yuming Zhao,³ Akbarjon Juraboev,¹ Ping Tan,¹ Jin Ding,¹ and Jinbao He⁴

¹School of Automation and Electrical Engineering, Zhejiang University of Science and Technology, Hangzhou 310023, China

²School of Computing, University of Portsmouth, Portsmouth PO1 3HE, UK

³China Coal Research Institute, Beijing 100013, China

⁴Ningbo University of Technology, Ningbo 315211, China

Correspondence should be addressed to Yong Ning; ningyong0816@126.com

Received 19 January 2018; Revised 9 April 2018; Accepted 14 May 2018; Published 28 June 2018

Academic Editor: Chengyu Liu

Copyright © 2018 Yong Ning et al. This is an open access article distributed under the Creative Commons Attribution License, which permits unrestricted use, distribution, and reproduction in any medium, provided the original work is properly cited.

A method based on measurement correlation (MC) and linear minimum mean square error (LMMSE) for multichannel surface electromyography (sEMG) signal decomposition was developed in this study. This MC-LMMSE method gradually and iteratively increases the correlation between an optimized vector and a reconstructed matrix that is correlated with the measurement matrix. The performance of the proposed MC-LMMSE method was evaluated with both simulated and experimental sEMG signals. Simulation results show that the MC-LMMSE method can successfully reconstruct up to 53 innervation pulse trains with a true positive rate greater than 95%. The performance of the MC-LMMSE method was also evaluated using experimental sEMG signals collected with a 64-channel electrode array from the first dorsal interosseous muscles of three subjects at different contraction levels. A maximum of 16 motor units were successfully extracted from these multichannel experimental sEMG signals. The performance of the MC-LMMSE method was further evaluated with multichannel experimental sEMG data by using the “two sources” method. The large population of common MUs extracted from the two independent subgroups of sEMG signals demonstrates the reliability of the MC-LMMSE method in multichannel sEMG decomposition.

1. Introduction

Electromyographic (EMG) signals are comprised of action potentials produced by the muscle fibers contained in different motor units (MUs) [1]. It is of great importance for physiological investigation and clinical diagnosis to decompose EMG signals into their constituent motor unit action potential (MUAP) trains. EMG signal decomposing will lead to a better understanding of the properties of MU control and reveal the MUAP changes due to muscle fiber denervation/reinnervation [2]. It will also aid in the examination of neuromuscular diseases (e.g., amyotrophic lateral sclerosis) and the process of evaluating the degree of dysfunction found in upper motoneuron diseases such as Parkinson's disease [3], cerebral palsy [4], hemiparetic stroke [5], and other disorders [6, 7]. Furthermore, EMG decomposition can facilitate the study of the interpulse interval (IPI) variability [8], recruitment strategies [9],

myoelectrical manifestations of fatigue [10], and short-term MU synchronization [11].

EMG signals can be detected by introducing a fine wire or needle sensor into the muscle tissue or by placing sensors on the surface of the skin. In the course of studying these EMG signals, it has been found that the surface detection of EMG provides several advantages over wire or needle detection. For example, surface electrodes can be used quickly and easily, without causing discomfort for the subject or requiring medical supervision [12], and measurements can be performed with a high degree of repeatability. More importantly, surface EMG (sEMG) is also able to obtain global information about muscle activities and consequently records a vast amount of information [12]. This makes it more convenient for studying neuromuscular control mechanisms than the invasive methods, which offer less information about global muscle activities and are more difficult to utilize.

Over the past few decades, great strides have been made in decomposing indwelling EMG signals [13–15]. However surface EMG decomposition remains a difficult task. There is routinely a high level of action potential overlapping and cancellation within sEMG signals. The volume conduction effect for propagating action potentials is also enhanced in surface recordings due to the relatively large distance between electrodes and sources [12]. In addition, there exists the spatial integrating effect caused by surface electrodes. Hence, the differences in surface action potential shapes from different MUs are not as distinguishable as with intramuscular recordings [12]. Together, all of these factors make sEMG decomposition an extremely difficult task, especially at high force levels.

Various approaches for sEMG decomposition have been proposed over the past years in both sEMG recording and processing [16–21]. In particular, the design of surface electrode arrays comprised of a number of tiny electrode probes with a small interelectrode distance promises to increase the motor unit discrimination capacity by reducing MUAP superimposition while providing spatial information across the muscle. The extraction of a single MU from sEMG has also become a feasible task at very low force levels with appropriate signal processing methods such as two-dimensional template matching [20]. Recent developments in sEMG decomposition have further allowed for the extraction of a number of simultaneously firing MUs at relatively high force levels. Nawab et al. [17] developed a remarkable sEMG decomposition technique using a specially designed 5-pin Laplace electrode array in conjunction with a knowledge-based artificial intelligence framework. Holobar and Zazula proposed the convolution kernel compensation (CKC) method [18] and the gradient CKC approach (GCKC) [19] to decompose multichannel sEMG signals recorded with high density electrode arrays. It has been demonstrated that the GCKC method holds the promise of high efficiency and a strong antinoise performance in sEMG decomposition [19], but it has a strict requirement for the length of the EMG signals for its iterative process to converge. It has become easier to a certain extent for decomposing multichannel SEMG signals which are originally difficult to process since the CKC method was introduced into the field of SEMG decomposition. Other multichannel signal processing methods have also been tested with high density sEMG decomposition, including traditional template matching, independent component analysis, higher order cumulants, and correlation measurement, but most of these methods have been limited to relatively low muscle contraction levels.

In view of the existing facts, it is hard to decompose complex superposition sEMG signals. Moreover, the decomposing procedure is also a bit cumbersome. For example, it usually needs multiple steps to build a correlation vector between the IPT and the measurements in the past. While in this article, it only needs an iterative procedure to form the correlation vector. A method based on measurement correlation and linear minimum mean square error (MC-LMMSE) was developed in this study to decompose multichannel sEMG signals. The MC-LMMSE

method is firstly used to reconstruct a matrix correlated with the measurement matrix. Then, it gradually and iteratively increases the correlation between an optimized vector and a reconstructed matrix until a satisfactory innervation pulse train (IPT) is obtained. The performance of the MC-LMMSE method was assessed with both simulated and experimental sEMG signals. The results demonstrated that the MC-LMMSE method can successfully extract more MUs and reconstruct IPTs with a higher true positive rate (TPR) than the GCKC method, even from complex superposition signals.

2. Materials and Methods

2.1. Data Model. Multichannel sEMG signals can be modelled as a linear-time-invariant multi-input-multi-output system [22] if the muscle contraction is maintained at a constant force level. This system can be represented by the matrix form as follows [18]:

$$X(n) = G\bar{s}(n) + W(n), \quad (1)$$

where $X(n) = [x_1(n), \dots, x_M(n)]^T$ is the M measurements, $x_j(n)$ is the n th sample of the j th measurement, $W(n) = [w_1(n), \dots, w_M(n)]^T$ stands for a vector of zero-mean white noise, G denotes a mixing matrix which consists of all of the channel responses $g_{ij} = [g_{ij}(0), \dots, g_{ij}(Q-1)]$ (the j th source in sEMG signals appearing in the i th measurement) of Q samples, and $\bar{s}(n)$ is an extended form of the N sources $s(n) = [s_1(n), \dots, s_N(n)]^T$ can be described as $\bar{s}(n) = [s_1(n), s_1(n-1), \dots, s_1(N-Q+1), \dots, s_N(n), s_N(n-1), \dots, s_N(n-Q+1)]^T$.

2.2. Method of LMMSE. Given a vector form $\mathbf{X} = [x(0), x(1), \dots, x(N-1)]$ whose probability density function (PDF) is unknown, the linear estimator of a variable θ related to the \mathbf{X} statistics can be written as follows:

$$\hat{\theta} = \sum_{n=0}^{N-1} a_n x(n) + a_N. \quad (2)$$

Choose the weighting coefficients a_n 's to minimize the Bayesian mean square error (MSE):

$$\text{Bmse}(\hat{\theta}) = E_{X\theta} \{ (\theta - \hat{\theta})^2 \}, \quad (3)$$

where the resultant estimator $\text{Bmse}(\hat{\theta})$ is termed the linear minimum mean square error (LMMSE) estimator [23]. Substituting (2) in (3), then it becomes

$$\text{Bmse}(\hat{\theta}) = E \left\{ \left[\theta - \sum_{n=0}^{N-1} a_n x(n) - a_N \right]^2 \right\}. \quad (4)$$

Differentiating and setting this equal to zero,

$$\frac{\partial \text{Bmse}(\hat{\theta})}{\partial a_N} = -2E \left\{ \left[\theta - \sum_{n=0}^{N-1} a_n x(n) - a_N \right] \right\} = 0. \quad (5)$$

Then, it produces

$$a_N = E(\theta) - \sum_{n=0}^{N-1} a_n E[x(n)]. \quad (6)$$

Substituting (6) in (4), then it becomes

$$\text{Bmse}(\hat{\theta}) = E \left\{ \left[\sum_{n=0}^{N-1} a_n [x(n) - E(x(n))] - (\theta - E(\theta)) \right]^2 \right\}. \quad (7)$$

Let $\mathbf{a} = [a_0, a_1, \dots, a_{N-1}]$, and it has

$$\begin{aligned} \text{Bmse}(\hat{\theta}) &= E \left\{ \left[\mathbf{a}^T (X - E(X)) - (\theta - E(\theta)) \right]^2 \right\} \\ &= E \left\{ \mathbf{a}^T (X - E(X)) (X - E(X))^T \mathbf{a} \right. \\ &\quad \left. - E \left\{ \mathbf{a}^T (X - E(X)) (\theta - E(\theta)) \right\} \right. \\ &\quad \left. - E \left\{ (\theta - E(\theta)) (X - E(X))^T \mathbf{a} \right\} + E \left\{ (\theta - E(\theta))^2 \right\} \right\} \\ &= \mathbf{a}^T C_{XX} \mathbf{a} - \mathbf{a}^T C_{X\theta} - C_{\theta X} \mathbf{a} + C_{\theta\theta}. \end{aligned} \quad (8)$$

Because $C_{\theta X} = C_{X\theta}^T$, it has

$$\text{Bmse}(\hat{\theta}) = \mathbf{a}^T C_{XX} \mathbf{a} - 2\mathbf{a}^T C_{X\theta} + C_{\theta\theta}. \quad (9)$$

Equation (9) can be maximized by taking the gradient:

$$\frac{\partial \text{Bmse}(\hat{\theta})}{\partial \mathbf{a}} = 2C_{XX} \mathbf{a} - 2C_{X\theta}, \quad (10)$$

and setting it to zero, which results in

$$\mathbf{a} = \mathbf{C}_{XX}^{-1} C_{X\theta}. \quad (11)$$

Substituting (6) and (11) into (2) produces

$$\hat{\theta} = E(\theta) + C_{X\theta} C_{XX}^{-1} (X - E(X)). \quad (12)$$

If the means of θ and X are zero, then

$$\hat{\theta} = C_{X\theta} C_{XX}^{-1} X. \quad (13)$$

For multichannel sEMG signals, $\hat{\theta}$ is the innervation pulse train (IPT) that needs to be estimated, X is the measured multichannel sEMG signal, and $C_{X\theta}$ is a parameter that needs to be calculated. It has been pointed out in [18] that all firing times of MU need to be known in advance to calculate $C_{X\theta}$, which can be written as

$$C_{X\theta} = \frac{1}{\text{card}(\psi_j)} \sum \bar{X}(\psi_j), \quad (14)$$

where set ψ_j contains all firing times of the same MU and \bar{X} is the extended form of the measured signal X . The LMMSE estimator can be obtained after substituting (14) in (13). In fact, it is very hard to know MU firing times beforehand. In view of this, a method that is able to identify complete or most of firing time of MU was proposed; therefore, we can achieve the results or approach results of LMMSE.

2.3. Measurement Matrix Autocorrelation. Multiplied by a $1 \times M$ vector ν from both sides, (1) becomes

$$\nu X(n) = \nu G \bar{s}(n) + \nu W(n). \quad (15)$$

The i th IPT in $\bar{s}(n)$ can be calculated with (16) if $\nu G = [0, 0, \dots, 1, 0, \dots, 0]_{1 \times N_Q}$ (suppose the value of the $(i-1)Q + r + 1$ th element is 1, and all other values are 0), and the noise term $W(n)$ is negligible.

$$s_i(n-r) \approx \nu X(n), \quad 0 \leq r \leq Q-1. \quad (16)$$

In practice, it is difficult and even impossible to find such a vector ν if the mixing matrix G is unknown, but $s_i(n-r)$ can still be satisfactorily reconstructed as long as one of the elements in ν is far greater than others.

The similarity S_{AB} between vectors A and B can be evaluated as follows [24]:

$$S_{AB} = \frac{\text{Inner}[A, B]}{\|A\| \cdot \|B\|}, \quad (17)$$

where $\text{Inner}[\cdot]$ denotes the inner product and $\|\cdot\|$ denotes the norm. The shapes of the MUAPs generated by the same MU should have a certain degree of similarity when the isometric muscle contraction is held at a constant force. Therefore, the inner product of two vectors which are associated with different time instants fired by the same MU, should be relatively large. This property provides the possibility to estimate the IPTs of MUs with the following equation:

$$P_j(n_i) = \nu X(n_i) = \text{Inner}[\nu, X(n_i)], \quad n_i = 1, 2, \dots, N_s, \quad (18)$$

where $P_j(n_i)$ is the value of the estimated innervation pulse train $P_j(n)$ at the sample time n_i , N_s denotes the number of sample times in each channel, and ν is a $1 \times M$ vector. If ν has a strong correlation with the measurement vectors associated with the time instants fired by a particular MU, the firing pattern of this MU will be easily observed in $P_j(n)$. The vector ν , then, increases the values in $P_j(n)$ at time instants when this MU is firing and decreases other values at time instants when it is not. The following average form [18] can be used as ν to achieve such a purpose:

$$\nu = \frac{1}{N_\nu} \sum X(\varphi_{n_\nu}), \quad (19)$$

where $\varphi_{n_\nu} = \{n_{\nu 1}, n_{\nu 2}, \dots, n_{\nu m}\}$ denotes the time instants fired by the particular MU, $X(\varphi_{n_\nu})$ is the series of measurement vectors associated with φ_{n_ν} , and N_ν is the number of elements in φ_{n_ν} . An ideal ν will have a stronger correlation with all the measurement vectors contained in $X(\varphi_{n_\nu})$ and, in this case, due to the average result, $P_j(\varphi_{n_\nu})$ should be larger than other values in $P_j(n)$ and can be easily observed. It is difficult, however, to find a satisfactory vector ν , as the firing pattern of any MU is unknown in practice. As a result, it is necessary to develop an advanced approach to better estimate ν in order to successfully reconstruct the IPTs.

2.4. Measurement Correlation Based on LMMSE (MC-LMMSE). An iterative algorithm based on LMMSE is developed in the proposed MC-LMMSE method to gradually

optimize the vector f in order to achieve a better IPT reconstruction. Assuming $Y(n)_{M \times N_s}$ is a matrix which has a certain column correlation with $X(n)$, then the IPT estimation equation can be rewritten as

$$s_i(n-r) \approx f_{1 \times M} Y(n)_{M \times N_s}, \quad 0 \leq r \leq Q-1, \quad (20)$$

where the vector f plays the same role as the aforementioned vector v . Replace $X(n)$ with $Y(n)$ in (19) and the vector f can be rewritten as

$$f = \frac{1}{N_v} \sum [Y(\varphi_{nv})]. \quad (21)$$

In this article, the matrix $Y(n)$ in the MC-LMMSE method is reconstructed from unitary matrices obtained from the singular value decomposition (SVD) of the measurement matrix $X(n)$ (see Step 1 below). Other matrices can also be selected. The high column correlation of the matrix $Y(n)$ helps the MC-LMMSE increase the values of $s_i(n-r)$ in (20) at the time instants fired by the same MU. Hence, the influence of noise on its IPT estimation results is significantly suppressed.

An initial vector f will first be formed from any time instants fired by an MU. The MC-LMMSE method will then be implemented by following the steps listed below to make f approximate the ideal vector in (21) and to reconstruct future IPTs with high accuracy. The schematic outline of the MC-LMMSE is shown in Figure 1.

- (1) Decompose the matrix $X^T(n)$ into $X^T(n) = UDV^T$ using SVD, where T denotes the transpose, and estimate the matrix $Y(n)_{M \times N_s} = [U_{N_s \times M} V_{M \times M}^T]^T$.
- (2) Randomly select sEMG signals from a few channels and denote each channel signal by $X_j(n)$; calculate the Teager energy operator [25] of $X_j(n)$, $\xi_{nj} = X_j(n)^2 - X_j(n-1)X_j(n+1)$, and set a threshold (thre); identify all the time instants in ϕ_{nj} which satisfy $\xi_{nj} > \text{thre}$ to form $\varphi_{nj} = \{n_{j1}, n_{j2}, \dots, n_{jx}\}$.
- (3) Choose $f_0 = Y(n_{jx})^T$, $n_{jx} \in \varphi_{nj}$, and then estimate an IPT $P_{jx}(n) = f_0 Y(n) = Y_{(n_{jx})}^T Y(n)$ from each time instant in φ_{nj} according to (20).
- (4) Identify d_k (the subscript k denotes the k th iteration) time instants, $\varphi_{nx} = \{n_{x1}, n_{x2}, \dots, n_{xd_k}\}$ corresponding to the highest peaks for each initial IPT $P_{jx}(n)$, where $d_k = A \cdot B^k + C \cdot k$ (A and C are constants greater than or equal to zero, where in most instances $1 \leq B \leq 3$), and then replace f_0 with $f = (1/N_x) \sum Y(\varphi_{nx})$. A new IPT $P_{jx}(n)$ will be obtained by substituting f into (20). The vector f will be gradually improved by repeating this iterative process until $d_k > N_p$ (N_p is a rough estimate number of firing times in each IPT) at which point the final IPT will be obtained.
- (5) Classify all the IPTs into groups for each specific MU.

Note that after substituting $Y(n)$ in Step (1) into (20), it is similar to CKC method [18]. Both of them are correlation method in essence. However, it is helpful for simplifying the decomposition expression by using (20) and understanding the distinguishing feature of these correlation methods to decompose sEMG.

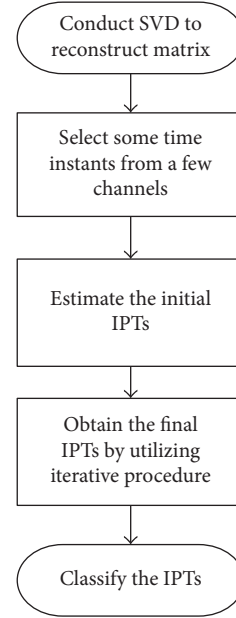


FIGURE 1: Schematic outline of the proposed MC-LMMSE algorithm.

The MC-LMMSE and classic CKC have some similarities, which include that (1) they directly estimate IPTs from measurement matrix without involving calculation of unknown mixing matrix G , (2) they all need to select some vectors of measurement corresponding to discharged time instants. However, there are also differences between them that lead to different results (see the following section of results). In MC-LMMSE method, a new way to reconstruct matrix correlated with the measurement matrix was proposed (20). Then, sEMG signals can be decomposed by using the reconstructed matrix. In this article, the SVD method was used to reconstruct the correlation matrix. The measurement matrix itself can also be directly used as the correlation matrix (see the previous section of measurement matrix autocorrelation). In addition, other effective ones such as the measurement matrix transformed by FastICA [26] can also be used as the correlation matrix. Hence, it may further obtain better results if the correlation matrix is properly selected in future. Another difference comparing with CKC is the utilization of iterative technique in Step (4) which can achieve more precise IPTs, and more number of MU firing time is an improved iteration method of CKC. Because it can find more number of time instants φ_{nv} discharged by one MU in the process of gradually and iteratively calculating vector f in (21) in terms of the characteristics of sEMG and the algorithm. Therefore, the quality of f can be improved a lot when comparing with classic CKC and GCKC methods.

2.5. Simulated Signals

2.5.1. Simulated Signals Generated by Random Mixing Matrices.

Ten sources were assumed and the IPTs $s_i(n) = \sum_{k=1}^{200} \delta(n - 100 \cdot k + S_i(k))$ were randomly generated in the simulation with a mean IPI of 100 samples. The lengths

of the IPTs were set to 20,000 samples where $S_i(k)$, $k = 1, 2, \dots, 200$, was uniformly distributed over the interval $[-10, 10]$. The zero-mean mixing matrix G was also randomly generated with a length g_{ij} of 10 samples. The number of measurements was set to 25 and the number of delayed repetitions of each original measurement was set to 9. Therefore, the number of extended IPTs was increased to 190 with 250 measurements. Gaussian zero-mean noises were added to each signal with different signal-to-noise ratios (SNRs) of -10 dB, -5 dB, 0 dB, 5 dB, and 10 dB. The measurement matrix autocorrelation method did not need to reconstruct the matrix $Y(n)$ in Step 1, while $Y(n_{jx})$ in Step 3 and $Y(\varphi_{nx})$ in Step 4 were replaced by $X(n_{jx})$ and $X(\varphi_{nx})$, respectively. The number of channels and threshold value in Step 1 were set to 10 and $0.45 MA_{nj}$ (MA_{nj} denotes the maximum absolute value of ξ_{nj} in the Step 2), respectively, when the MC-LMMSE method was implemented. The number of iterations to estimate $\hat{c}t_{jx}$ [19] and the number of main decomposition loops were set to 40 and 500, respectively, when the method of GCKC was implemented. The scalar function $f(t) = (1/3)t^3$ was taken in (9) from [19]. An IPT was selected as real when its TPR was greater than 75%.

2.5.2. Simulated Signals Generated by Gaussian Function [27]. The extracellular single fiber action potential (SFAP) was depicted by the sum of three basic Gaussian functions [28].

$$\phi(t) = \sum_{i=1}^3 U_i e^{-((t-C_i)/(V_i))^2}, \quad (22)$$

where t is time, U_i is the amplitude factor, V_i is the bandwidth, and C_i is the position of the center of the peak. With this equation, one may approximate a particular triphasic action potential waveform with considerable accuracy by adjusting U_i and V_i . Each fiber is assumed to be parallel to the skin surface, so the shape of the SFAP detected by the electrodes is considered to be a function of the physiological parameters, such as the fiber location within a 3-dimensional Cartesian coordinate system, and the muscle fiber conduction velocity. U_i and V_i in (22) were depicted as

$$U_i = f_1(x, y, z, cv), \quad (23)$$

$$V_i = f_2(x, y, z, cv), \quad (24)$$

where y stands for the vertical fiber depth below the surface of the skin, z represents the center position along the fiber in the z - x plane, x is the fiber center position in the z - x plane perpendicular to the z direction, and cv is the conduction velocity of muscle fiber. The MUAP shapes detected by different electrodes were depicted as the summation of the SFAP shapes contained in the MUs. The MUAP trains were then generated by the convolution of the MUAP shapes with their corresponding firing times. Finally, the composite sEMG signals were modelled as linear summations of the MUAP trains. The characteristics of the MUAP, such as the amplitude distribution, shape, and duration, were determined by the morphological properties of the active muscle fibers contained within corresponding MUs. The sEMG signals can be simulated with considerable similarity

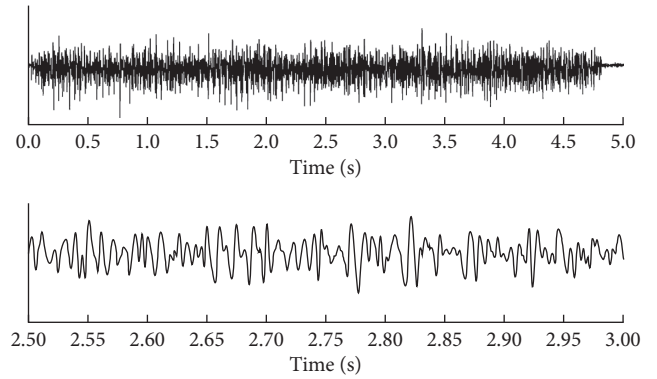


FIGURE 2: Simulated signals generated by a Gaussian function. The top trace represents one channel of the simulated synthetic signal generated by a Gaussian function with SNR = 20 dB, while the second is an expanded segment (0.5 s) of the raw signal. The average firing rate of all MUs was 20 ± 5 Hz for the 60 MUs that were activated.

by adjusting the parameters of Gaussian functions according to the characteristics of real sEMG signals. In this article, the sEMG signals are just roughly simulated. However, it can still demonstrate the basic characteristics of sEMG.

The depths of the centers for all measured MUs were uniformly distributed from 1 mm to 6 mm. A random number of fibers (uniformly distributed between 30 mm and 70 mm) were assumed in active MUs. All semifiber lengths were set to 50 mm, and the tendon and endplate positions of the fibers were uniformly distributed in the range of ± 5 mm. The conduction velocities of active MUs were set to 4.0 m/s, the firing rates of the MUs were normally distributed with the mean, and standard deviation of 20 ± 5 Hz and 60 active MUs were assumed in total. The starting times of MUs were chosen from 10 ms to 200 ms. A 16×16 electrode-array grid with a 3 mm interelectrode distance in both directions was employed for recording the sEMG signals. This grid center was placed at the center of the muscle and the signals were sampled with frequency of 2,000 Hz. The numbers of fibers, position of the active MUs, and discharging patterns were all randomly generated. The signals were also corrupted by additive Gaussian zero-mean noise with SNR of 20 dB as shown in Figure 2. The number of delayed repetitions of each original measurement was set to 9 [18, 19].

2.6. Experimental Signals. The experimental sEMG signals were collected from the first dorsal interosseous (FDI) muscles of three adult subjects. The procedures were approved by the Institutional Review Board of Northwestern University (Chicago, USA), and all three subjects gave their written consent before the experiment. Subjects were seated upright in a mobile Biodex chair (Biodex, Shirley, NY). A standard 6 degrees-of-freedom load cell (ATI Inc, Apex, NC) setup was used along with standard procedures for minimizing spurious force contributions from unrecorded muscles as described in [29] to accurately record the isometric contraction force of the FDI muscle during index finger abduction. sEMG signals were recorded from the FDI

TABLE 1: The number of reconstructed IPTs (Nr) (mean \pm std. dev.), true positive rate (TPR) (mean \pm std. dev.), and misplaced rate (MR) (mean \pm std. dev.) for different decomposition methods.

Methods	Parameters	SNR (dB)				
		-10	-5	0	5	10
Measurement matrix autocorrelation	Nr	8.2 \pm 1.5	9.6 \pm 0.6	9.6 \pm 0.6	9.8 \pm 0.5	9.8 \pm 0.5
	TPR (%)	85.7 \pm 1.9	97.6 \pm 0.9	99.1 \pm 0.3	99.4 \pm 0.2	99.4 \pm 0.5
	MR(%)	3.98 \pm 1.06	2.16 \pm 0.67	1.02 \pm 0.23	0.98 \pm 0.13	0.91 \pm 0.06
GCKC	Nr	5.0 \pm 0.7	9.0 \pm 1.2	10 \pm 0	10 \pm 0	10 \pm 0
	TPR (%)	85.9 \pm 4.0	99.5 \pm 0.2	99.9 \pm 0.1	99.6 \pm 0.4	99.9 \pm 0.0
	MR(%)	3.59 \pm 1.12	1.05 \pm 0.33	0.69 \pm 0.26	0.66 \pm 0.35	0.58 \pm 0.17
MC-LMMSE	Nr	10 \pm 0				
	TPR (%)	92.8 \pm 1.0	99.7 \pm 0.0	100 \pm 0	100 \pm 0	100 \pm 0
	MR(%)	2.81 \pm 0.85	1.02 \pm 0.13	0 \pm 0	0 \pm 0	0 \pm 0

muscle using a flexible 2-dimensional 64-channel surface electrode array (8 \times 8 array with the electrode probe diameter of 1.2 mm, and the center-to-center probe distance of 4 mm) (TMS International BV, The Netherlands) [30]. The skin of the tested muscle was carefully prepared and the electrode array was attached to the FDI muscle with a double adhesive sticker and further secured with medical tapes [29]. The maximum voluntary contraction (MVC) was first measured. Each subject was then asked to generate an isometric contraction force of the FDI muscle at the different contraction levels of 2 N, 4 N, 6 N, and 8 N. Multiple trials were performed with one force level being recorded for each trial. The subject was asked to maintain the force as stable as possible for up to 15 s. A Refa amplifier (TMS International BV, The Netherlands) was used to record sEMG signals. The signals were sampled at 2 kHz with a bandpass filter set at 10–500 Hz. The number of delayed repetitions of each original measurement was set to 9 [18].

2.7. Validation. For simulated signals, the parameter TPR and MR defined in (25) and (26) are used to further validate the accuracy of sEMG signal decomposition algorithm, and defined in (26):

$$\text{TPR} = \frac{\text{TP}}{\text{TP} + \text{FN}}, \quad (25)$$

$$\text{MR} = \frac{\text{TP}}{\text{TP} + \text{FN}}, \quad (26)$$

where TP is the number of correctly identified firing times of pulses in the reconstructed IPT, FP is the number of misplaced discharges, and FN stands for the number of unidentified firing times of pulses in the IPT. For the simulated signals generated by the Gaussian function, the firing time tolerance was set to ± 1 sample. Therefore, each identified firing time was considered as true if it was detected within ± 0.5 ms (sampling frequency of 2,000 samples/s) from its actual position along the signal. The value defined in (25) was averaged over 10 trials for all identified IPTs. For simulated signals generated by random mixing matrices, the time tolerance was set to 0. The value defined in (25) in this case was also averaged over 10 trials for all identified IPTs.

For experimental signals, to validate the accuracy of MC-LMMSE algorithm, the “two-source” technique, in which all

64 channels of the electrode array were divided into two independent groups with equal number of channels, was used as an alternative to using intramuscular EMG together with surface EMG [16, 17]. The coincident rate of the firing times of the MUs, which are decomposed from both channel groups using the MC-LMMSE algorithm, were calculated, and a high coincident rate was taken to suggest a favourable performance of the algorithm.

3. Results and Discussion

3.1. Simulated Signals

3.1.1. Tests on Signals Generated by Random Mixing Matrices. Ten trials were conducted to test the performance of the proposed MC-LMMSE method in decomposing the sEMG signals simulated by random mixing matrices and the results were averaged over the 10 trials. The number of reconstructed IPTs, corresponding TPR and MR achieved by the measurement matrix autocorrelation, GCKC and the MC-LMMSE method at different SNRs are presented in Table 1. Results show that the measurement matrix autocorrelation method could not completely reconstruct the IPTs even with a high SNR of 10 dB. The GCKC method only reconstructed an average of 5 IPTs when SNR was set to -10 dB. The MC-LMMSE method reconstructed all the 10 IPTs successfully with the high TPRs at all tested SNR levels (-10 dB to 10 dB) and the TPR maintained over 92% even in severely noisy environments (SNR = -10 dB). Results demonstrate that the MC-LMMSE method offers superior performance to the measurement matrix autocorrelation and GCKC methods of sEMG decomposition. In addition, a parameter called pulse-to-noise-ratio (PNR) [31] was also utilized to evaluate the performance of MC-LMMSE method. The average PNR was 12.37 dB and infinite, respectively, when SNR was set at -10 dB and greater than 0 dB.

3.1.2. Tests on Signals Generated by Gaussian Function. The GCKC and MC-LMMSE methods were employed to decompose the sEMG signals generated by a Gaussian function. On average, 26 IPTs were reconstructed by the GCKC method with a TPR of 92.67% and MR of 4.26%; while 53 IPTs were reconstructed by the MC-LMMSE method with a TPR of 97.89% and MR of 1.93% (Figures 3 and 4).

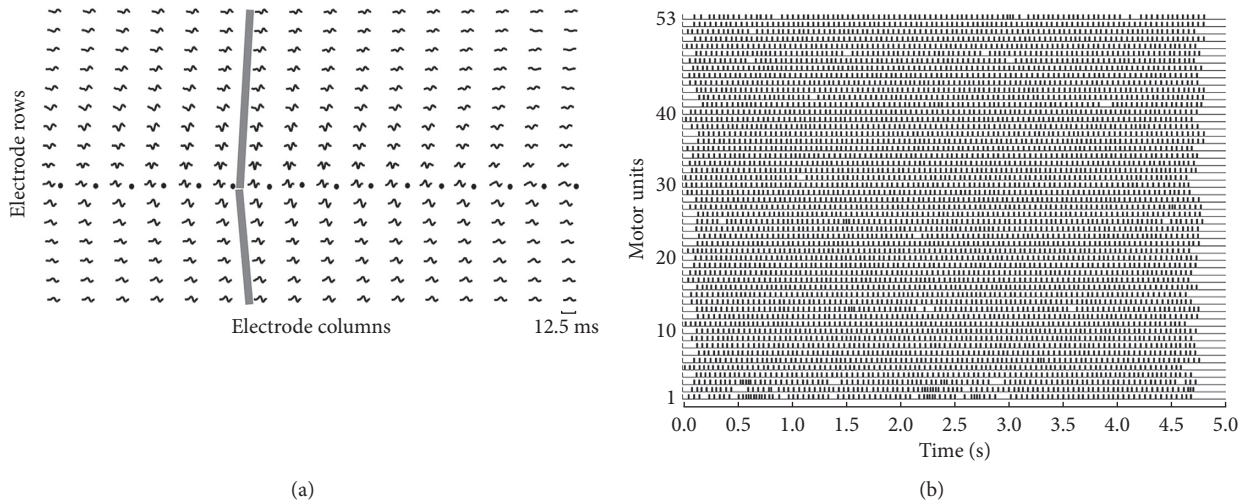


FIGURE 3: MUAP templates and MU discharge patterns from simulated signals generated by Gaussian functions. (a) Multichannel MUAP templates estimated by the spike-triggered averaging of the simulated sEMG. The locations of the innervation zones (black circles) and the propagation of MUAPs (grey lines) are indicated. (b) MU discharge patterns are identified from the multichannel simulated sEMG signals.

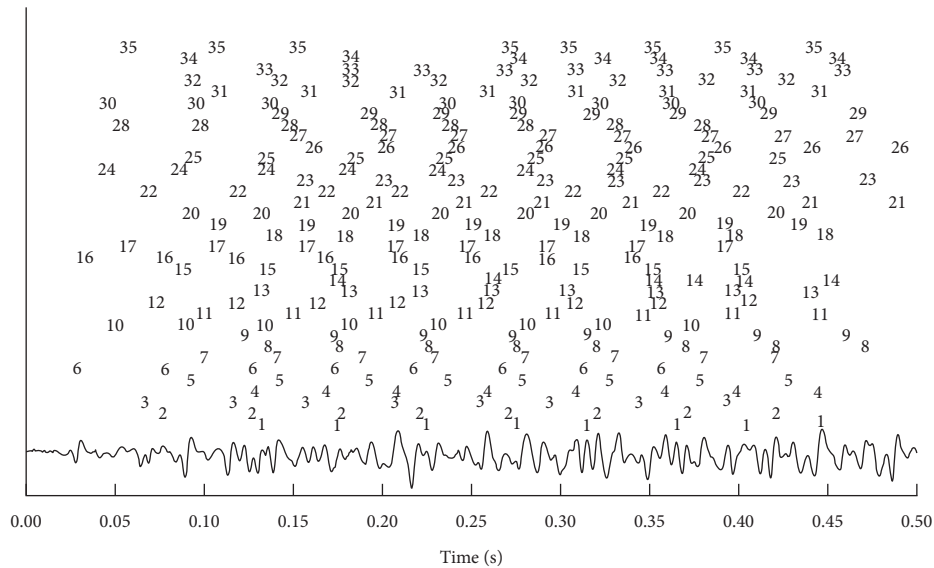


FIGURE 4: A decomposition example of simulated signals generated by Gaussian functions from one channel. The firing times of each extracted MU are indicated by an assigned label at top of the signal.

The average PNR of MC-LMMSE was 27.39 dB. Figure 3(a) shows the MUAP shapes of one MU, detected by the 16 × 16 electrode array, which were estimated using the spike-triggered averaging method [32]. The innervation zone of the MU and the propagation of MUAPs can also be clearly observed.

Figure 3(b) shows the 53 IPTs reconstructed from the signals. The firing times of each extracted MU are indicated by an assigned label at top of the signal in Figure 4. Thirty-five MUs can be correctly identified from this channel and the challenge caused by overlapped action potentials appears to be solved by the proposed MC-LMMSE method. The parameters used in the MC-LMMSE and GKC methods for this test are the same as those used in Test 1, except that the number of main decomposition loops in the GKC method was set to 5,000.

3.2. Tests on Experimental Signals. Figure 5(a) shows the force profile and the 16 IPTs identified from the sEMG signals of the FDI muscles by using the MC-LMMSE method. These sEMG recordings were taken during an isometric constant force contraction at 10% of the maximum voluntary contraction (MVC).

It can be seen that the firing rate of MUs changes with the fluctuation of the contraction force; Figure 5(b) compares the summation of the identified MUAP trains and their residuals respective to the original sEMG signals, where the signal-to-interference ratio (SIR) [33] between the sum of identified MUAP trains and raw sEMG signal was 59.73%. Figure 6 shows the mean and standard deviation of discharge rates of the extracted 16 MUs from FDI muscles. It can be seen from the figure that the average discharge rates of these

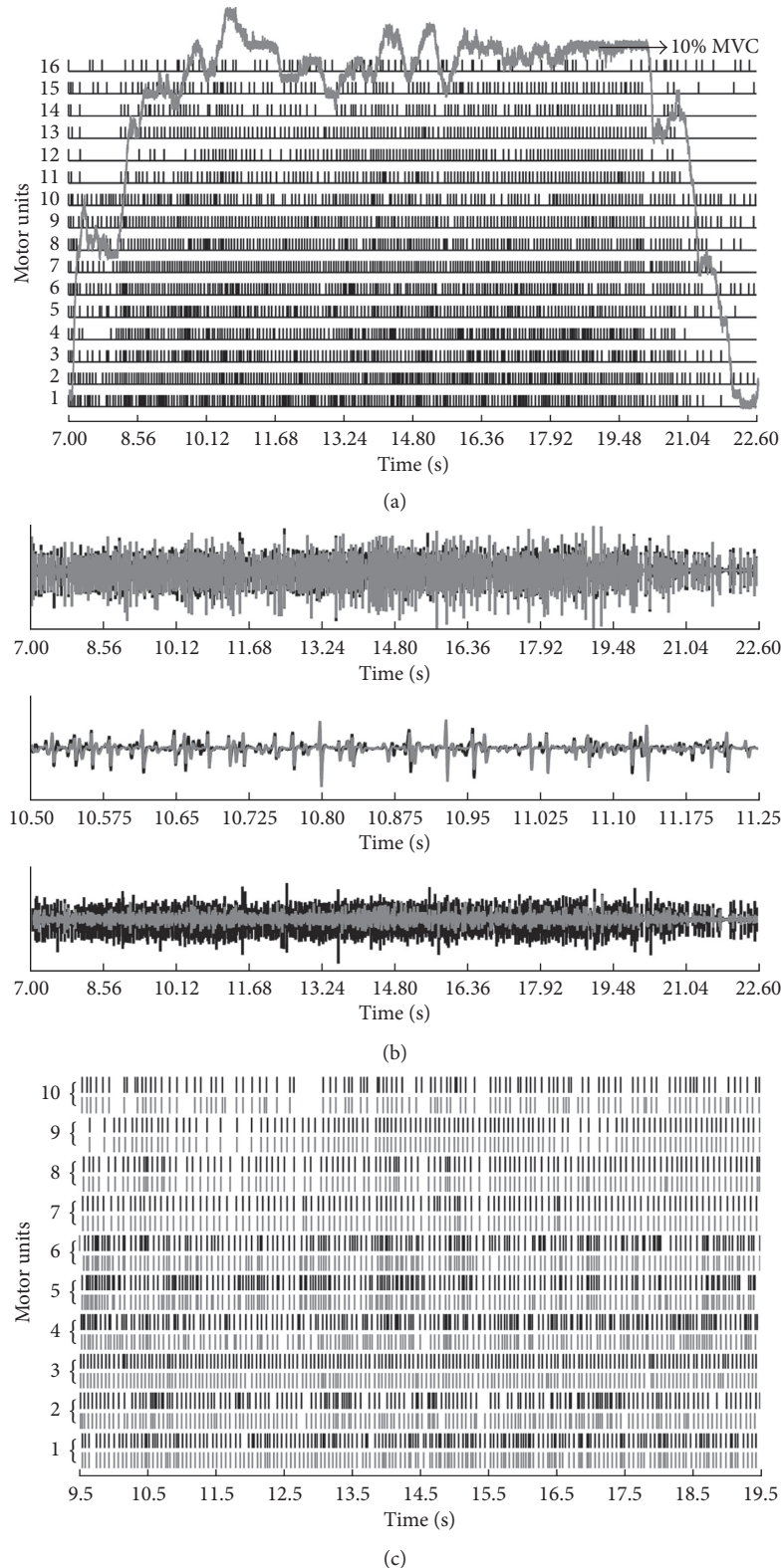


FIGURE 5: Results obtained from first dorsal interosseous (FDI) muscle. (a) MU discharge patterns with the force profile identified from the FDI muscle during an isometric constant force contraction at 10% MVC (2 N (Subject A)). Each vertical line indicates a MU discharge at a given time instant. ((b) Top panel) the sum of identified MUAP trains (grey lines) compared to the raw sEMG signal (black lines) in one selected channel from the first dorsal interosseous (FDI) muscles during an isometric constant force contraction at 10% MVC (Subject A). ((b) Middle panel) an expanded view of the top panel. ((b) Bottom panel) the residual (grey lines) compared to the raw sEMG (black lines) after the subtraction of the reconstructed MUAP trains. (c) MU firing patterns identified from Group 1 (black lines) and Group 2 (grey lines). All 64 channel signals were divided into 2 independent groups, with the even numbered columns selected as one group and the odd numbered columns as the other group.

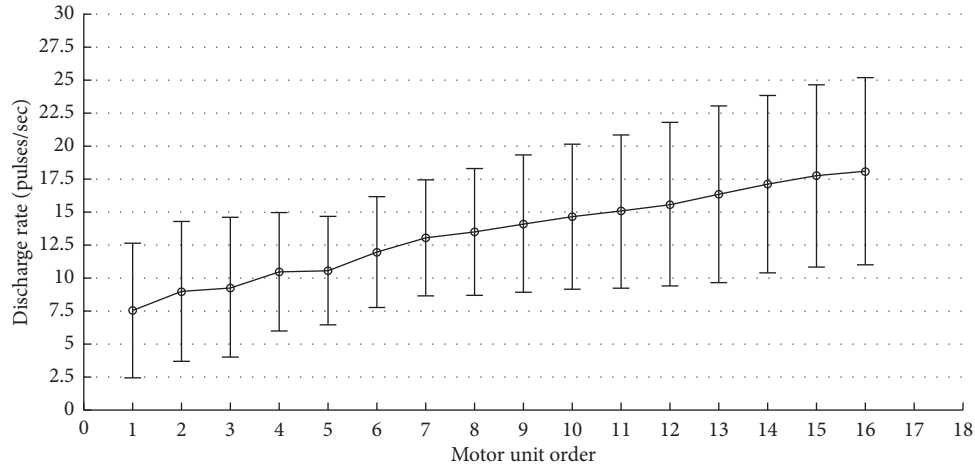


FIGURE 6: The mean and standard deviation of discharge rates of the extracted 16 MUs from first dorsal interosseous (FDI) muscle during an isometric constant force contraction at 10% MVC (2 N).

TABLE 2: Parameters (mean \pm std. dev.) obtained from all channels and two independent channel groups.

Methods	Contraction force (N)	2	4	6	8
GCKC	Number of MUs extracted from all channels	5.7 \pm 2.5	8.0 \pm 0.0	5.7 \pm 4.0	6.7 \pm 2.3
	Number of MUs extracted from all channels	11.7 \pm 4.5	13 \pm 1.7	11 \pm 3.5	13 \pm 1.5
MC-LMMSE	Number of MUs extracted from channels in Group 1	9.3 \pm 4.5	9.0 \pm 0.0	7.7 \pm 3.5	7.3 \pm 1.5
	Number of MUs extracted from channels in Group 2	8.7 \pm 3.5	9.0 \pm 1.0	7.7 \pm 2.1	8.0 \pm 1.7
	Number of common MUs extracted from both groups	7.7 \pm 4.0	8.7 \pm 0.6	6.7 \pm 2.5	7.3 \pm 1.5
	Percentage of common pulses in common MUs (%)	90 \pm 6	92 \pm 5	94 \pm 4	95 \pm 5

extracted 16 MUs range from 7.55 ± 5.1 to 18.1 ± 7.1 pulses/second. Different MUs correspond to different average discharge rate patterns, which are monotonically increasing. Considering the individual differences of the physiological characteristics [34], these values may differ slightly from the previous reported results; however, overall they are similar [34, 35].

The results achieved by the GCKC and MC-LMMSE methods are shown in Table 2. It can be seen that the MC-LMMSE method extracted more MUs than the GCKC method, especially in the cases of high force contraction. The parameters used in the MC-LMMSE and GCKC methods in this test are the same as in Test 1. The performance of the MC-LMMSE method with the experimental electrode array sEMG was further investigated by using the “two sources” method. All of the 64 channel signals recorded at different contraction force levels were divided into 2 independent groups, each with 32 channels. sEMG signals recorded from channels with even column numbers were selected to form Group 1, while signals recorded from channels with odd column numbers were selected to form Group 2. The proposed MC-LMMSE method was applied to each of the groups for sEMG decomposition, and the numbers of MUs extracted from all the channel signals, signals in Group 1 and signals in Group 2, were compared (Table 2 and Figure 5(c)). It can be seen that, overall, the number of extracted MUs decreases as the number of EMG channels decreases. This trend becomes more remarkable in cases where a higher force of contraction was applied. It can also be seen that

results achieved from the two independent groups share over 84% of the commonly extracted MUs and show over 90% of the same firing times for the common MUs.

4. Discussion

One important concept to decompose high density array signals like sEMG is proposed in this article. There are two important steps for decomposing signals which lead to its superior performance compared to other decomposition methods. One is the appropriate selection of the matrix which is correlated to the measurement matrix; the other one is the estimation of the reconstructed IPTs with the iterative optimization process presented in Step 4. Both steps are critical in achieving favourable decomposition results. In fact, $\bar{X}^T(n)C_{\bar{X}\bar{X}}^{-1}$ in [18] can also be considered as a matrix correlated with the measurement matrix. In addition to the mentioned correlated matrix in this article, other matrices have also been found that can decompose sEMG signals. The decomposition results are likely to improve in near future. However, like other decomposition methods, the MC-LMMSE method also has some limitations. For example, there ought to be at least thousands of samples in sEMG signals, otherwise if the length of signals is too short, it will be difficult to obtain satisfactory results. It can be seen from the results of the simulation data that this MC-LMMSE method requires a larger number of detected electrodes to get better results. But only 64 electrodes were used to record the real sEMG signals in this article. Hence, if hundreds of electrodes could be employed to

record the real signals, there is hope that a larger number of MUs could be extracted, and the allowable force of muscle contraction could also become larger.

The matrix $Y(n)$ in the MC-LMMSE method is constructed with a high level of column correlation from the unitary matrices obtained using the SVD of the measurement matrix. This high column correlation is able to help the MC-LMMSE suppress the influence of noise, as the correlation between vector f and the other vectors from $Y(n)$ associated with the firing times of the same MU is further enhanced by the iterative optimization procedure in Step 4. (In fact, the results obtained by MC-LMMSE can better approach the LMMSE estimator when compared with CKC which is derived from LMMSE estimator. Please refer to [18] for further understanding why MC-LMMSE method can get such results.) Therefore, both the employment of a SVD of the measurement matrix and the iterative optimization procedure in the MC-LMMSE contribute to the improvement of the decomposition performance when compared to the other methods tested in this paper (Figure 3, Tables 1 and 2). The time instants in each iteration step corresponding to the highest peaks in $p_{jx}(n)$ are usually the firing times of a particular MU, making it possible to employ such an optimizing approach to improve the vector f . Both the decomposition method presented in this study and CKC method are based on high density surface EMG recordings; however, the MC-LMMSE method employs a different approach for IPT estimation. It differs from CKC that (21) was adopted in the proposed MC-LMMSE algorithm to gradually optimize the vector f and give it a stronger correlation with the different vectors from matrix $Y(n)$ associated with the firing time instants of a particular MU. Instead, Equation (20) is utilized in the MC-LMMSE method to estimate the IPTs, where $Y(n)$ is reconstructed by the unitary matrices obtained through the SVD of $X(n)$, and the vector f is obtained by an iterative optimization procedure. The final IPTs can then be obtained by substituting f into (20). CKC and GCKC are the two typical sEMG signal decomposition methods. Moreover, GCKC can get better results compared with CKC [19], hence we chose GCKC method as a comparison here. The following relevant published articles have little improvement in performance and many of them are related applications for decomposition. It should be noted that although the results obtained by MC-LMMSE seem to be superior to CKC, it had better be further confirmed by an independent research team.

IPTs can be relatively easily reconstructed from sEMG signals with a low degree of MUAP superposition as long as d_k in Step 4 is similar to N_p (Table 1). However, it will be difficult to satisfactorily reconstruct the IPTs from sEMG signals with a high degree of MUAP superposition in cases where d_k is small. For these scenarios, more iteration steps will be needed to optimize the vector f to adequately reconstruct the IPTs (Figures 3(b) and 4).

In order to evaluate the performance of the proposed MC-LMMSE method in experimental sEMG decomposition, the 64 sEMG channels were divided into two independent groups with equal numbers of channels in each. The “two sources” method was employed to compare MUs which were independently decomposed from the two groups of the sEMG

signals. Comparison results in Table 2 confirm the high stability, efficiency, and accuracy of the MC-LMMSE method in experimental sEMG decomposition. As a correlation method, the MC-LMMSE method requires a relatively large number of electrodes to achieve good decomposition results; a reduction in the number of electrodes leads to a reduction in the amount of correlation information, which will affect the number of reconstructed IPTs in decomposition results. Consequently, it is necessary to increase the number of recording electrodes under the premise that the amount of information in the sEMG is fully provided if a large number of extracted MUs are desired, particularly in cases of relatively high muscle contraction levels (Table 2).

The major challenges in sEMG decomposition can be summarized as follows [17]: (1) the occurrence of large amounts of superposition between the action potentials from different MUs; (2) the changes in shapes of the different action potentials contained in every MUAP train; (3) high degree of similarity in action potential shapes between different MUAP trains. Those challenges can be overcome to some extent by using the proposed MC-LMMSE method. IPTs can still be reconstructed with high accuracy even if they have a high degree of MUAP superposition (Figures 3(b) and 4). The shapes of the action potentials in MUAP trains may change during the isometric muscle contractions as a result of the changes in conduction velocity (e.g., caused by muscle fatigue) or movement of the electrode, making the decomposition task more challenging. However, even if a large degree of change in MUAP shape occurs quickly, the MC-LMMSE method can still be used to reconstruct the IPTs efficiently and accurately by increasing the iterations in Step 4 or by dividing the signal recordings into short epochs, which could then be considered stationary in the absence of shape changes. It is unlikely that the shapes of the action potentials contained in different MUAP trains are similar across all observed channels and, as a result, the correlation between the measurements vectors associated with different MUs can be neglected. Note that both MC-LMMSE and CKC build on the low probability of different MUs to share the exact firing time [18]. MU synchronization does affect the decomposition performance. How much it affects in detail depends on the level of the synchronization and the complexity of the sEMG signal, such as the degree of MUAP waveform superposition, the amount of noise, and so on. In fact, it is extremely difficult to encounter a very high synchronization rate when decomposing real sEMG signals. The formula of probability of synchronization rate was given in (12) of [18]. It can also be seen from the formula that the probability of synchronization is very low. The literature [36] also shows that in the case of very high synchronization rate, it can still be decomposed well by GCKC method. CKC, GCKC, and MC-LMMSE are all based on LMMSE and correlation methods. If GCKC and CKC can do that, the method in this study can also do that.

5. Conclusions

In summary, a new MC-LMMSE method was developed for multichannel sEMG decomposition based on the principle that the measurement vectors associated with the firing

times of a single MU have a certain degree of similarity. The MC-LMMSE method gradually and iteratively increases the correlation between the optimized vectors and the reconstructed matrix to better decompose complex sEMG signals. The superior performance of the MC-LMMSE method was demonstrated with both simulated and experimental electrode array sEMG signals. The results show that, in each case, the MC-LMMSE method can extract a relatively large number of MUs with strong robustness to noise and excellent accuracy.

Data Availability

The data used to support the findings of this study are available from the corresponding author upon request.

Conflicts of Interest

The authors declare that there are no conflicts of interest regarding the publication of this paper.

Acknowledgments

The authors would like to thank Mr. Thomas Potter from the University of Houston for editing the manuscript. This work was supported by National Natural Science Foundation of China (51677171), Zhejiang Provincial Natural Science Foundation of China (LY17C100001), Department of Education of Zhejiang Province (Y201533132), China Scholarship Council, and Ningbo Natural Science Foundation of China (2017A610218).

References

- [1] R. Merletti and P. A. Parker, *Electromyography: Physiology, Engineering, and Non-Invasive Applications*, John Wiley & Sons, Hoboken, NJ, USA, 2004.
- [2] C. J. De Luca, P. J. Foley, and Z. Erim, "Motor unit control properties in constant-force isometric contractions," *Journal of Neurophysiology*, vol. 76, no. 3, pp. 1503–1516, 1996.
- [3] V. Ruonala, E. Pekkonen, O. Airaksinen, M. Kankaanpää, P. A. Karjalainen, and S. M. Rissanen, "Levodopa induced changes in electromyographic patterns in patients with advanced Parkinson's disease," *Frontiers in Neurology*, vol. 9, no. 35, 2018.
- [4] J. W. Yoo, D. R. Lee, Y. J. Cha, and S. H. You, "Augmented effects of EMG biofeedback interfaced with virtual reality on neuromuscular control and movement coordination during reaching in children with cerebral palsy," *Neurorehabilitation*, vol. 40, no. 2, pp. 175–185, 2017.
- [5] T. A. Caires, L. F. R. M. Fernandes, L. J. Patrizzi et al., "Immediate effect of mental practice with and without mirror therapy on muscle activation in hemiparetic stroke patients," *Journal of Bodywork and Movement Therapies*, vol. 21, no. 4, pp. 1024–1027, 2017.
- [6] B. Barth, K. Mayer, U. Strehl, A. J. Fallgatter, and A.-C. Ehlis, "EMG biofeedback training in adult attention deficit/hyperactivity disorder: an active (control) training?," *Behavioural Brain Research*, vol. 329, pp. 58–66, 2017.
- [7] M. J. Zwarts and D. F. Stegeman, "Multichannel surface EMG: basic aspects and clinical utility," *Muscle & Nerve*, vol. 28, no. 1, pp. 1–17, 2003.
- [8] E. A. Clancy and N. Hogan, "Probability density of the surface electromyogram and its relation to amplitude detectors," *IEEE Transactions on Biomedical Engineering*, vol. 46, no. 6, pp. 730–739, 1999.
- [9] N. Fallentin, K. Jorgensen, and E. B. Simonsen, "Motor unit recruitment during prolonged isometric contractions," *European Journal of Applied Physiology and Occupational Physiology*, vol. 67, no. 4, pp. 335–341, 1993.
- [10] R. Merletti, M. Knaflitz, and C. J. De Luca, "Myoelectric manifestations of fatigue in voluntary and electrically elicited contractions," *Journal of Applied Physiology*, vol. 69, no. 5, pp. 1810–1820, 1990.
- [11] J. L.F. Weytjens and D. Vansteenbergh, "The effects of motor unit synchronization on the power spectrum of the electromyogram," *Biological Cybernetics*, vol. 51, no. 2, pp. 71–77, 1984.
- [12] P. Zhou and W. Z. Rymer, "MUAP number estimates in surface EMG: Template-matching methods and their performance boundaries," *Annals of Biomedical Engineering*, vol. 32, no. 7, pp. 1007–1015, 2004.
- [13] S. Karimimehr, H. R. Marateb, S. Muceli, M. Mansourian, M. A. Mañanas, and D. Farina, "A real-time method for decoding the neural drive to muscles using single-channel intra-muscular EMG recordings," *International Journal of Neural Systems*, vol. 27, no. 6, article 1750025, 2017.
- [14] J. Roussel, P. Ravier, M. Haritopoulos, D. Farina, and O. Buttelli, "Decomposition of multi-channel intramuscular EMG signals by cyclostationary-based blind source separation," *IEEE Transactions on Neural Systems and Rehabilitation Engineering*, vol. 25, no. 11, pp. 2035–2045, 2017.
- [15] X. Ren, C. Zhang, X. Li, G. Yang, T. Potter, and Y. Zhang, "Intramuscular EMG decomposition basing on MUAPs detection and superposition resolution," *Frontiers in Neurology*, vol. 9, no. 2, 2018.
- [16] M. Chen, X. Zhang, X. Chen, and P. Zhou, "Automatic implementation of progressive FastICA peel-off for high density surface EMG decomposition," *IEEE Transactions on Neural Systems and Rehabilitation Engineering*, vol. 26, no. 1, pp. 144–152, 2018.
- [17] S. H. Nawab, S. S. Chang, and C. J. De Luca, "High-yield decomposition of surface EMG signals," *Clinical Neurophysiology*, vol. 121, no. 10, pp. 1602–1615, 2010.
- [18] A. Holobar and D. Zazula, "Multichannel blind source separation using convolution kernel compensation," *IEEE Transactions on Signal Processing*, vol. 55, no. 9, pp. 4487–4496, 2007.
- [19] A. Holobar and D. Zazula, "Gradient convolution kernel compensation applied to surface electromyograms," in *Proceedings of the Independent Component Analysis and Signal Separation*, vol. 4666, pp. 617–624, London, UK, September 2007.
- [20] M. Chen and P. Zhou, "A novel framework based on FastICA for high density surface EMG decomposition," *IEEE Transactions on Neural Systems and Rehabilitation Engineering*, vol. 24, no. 1, pp. 117–127, 2016.
- [21] I. Gligorijevic, J. P. Van Dijk, B. Mijovic, S. Van Huffel, J. H. Blok, and M. De Vos, "A new and fast approach towards sEMG decomposition," *Medical & Biological Engineering & Computing*, vol. 51, no. 5, pp. 593–605, 2013.
- [22] D. Zazula and A. Holobar, "An approach to surface EMG decomposition based on higher-order cumulants," *Computer Methods and Programs in Biomedicine*, vol. 80, pp. S51–S60, 2005.
- [23] S. M. Key, *Fundamentals of Statistical Signal Processing: Estimation Theory*, Prentice-Hall Int., Englewood Cliffs, NJ, USA, 1993.

- [24] Y. Ma, S. H. Lao, E. Takikawa, and M. Kawade, "Discriminant analysis in correlation similarity measure space," in *Proceedings of the 24th International Conference on Machine Learning*, pp. 577–584, Corvallis, OR, USA, June 2007.
- [25] H. Teager and S. Teager, *Evidence for Nonlinear Sound Production Mechanisms in the Vocal Tract: Speech Production and Speech Modelling*, Springer, Berlin, Germany, 1990.
- [26] Y. Ning, J. Li, and S. Zhu, "Research on decomposition of surface EMG signals based on FastICA and channel correlation," *Space Medicine & Medical Engineering*, vol. 30, no. 3, pp. 191–197, 2017, in Chinese.
- [27] Y. Ning and Y. Zhang, "A new approach for multi-channel surface EMG signal simulation," *Biomedical Engineering Letters*, vol. 7, no. 1, pp. 45–53, 2017.
- [28] J. Clark and R. Plonsey, "A mathematical evaluation of the core conductor model," *Biophysical Journal*, vol. 6, no. 1, pp. 95–112, 1966.
- [29] X. Li, A. Suresh, P. Zhou, and W. Z. Rymer, "Alterations in the peak amplitude distribution of the surface electromyogram poststroke," *IEEE Transactions on Biomedical Engineering*, vol. 60, no. 3, pp. 845–852, 2013.
- [30] P. Zhou, N. L. Suresh, and W. Z. Rymer, "Surface electromyogram analysis of the direction of isometric torque generation by the first dorsal interosseous muscle," *Journal of Neural Engineering*, vol. 8, no. 3, article 036028, 2011.
- [31] A. Holobar, M. A. Minetto, and D. Farina, "Accurate identification of motor unit discharge patterns from high-density surface EMG and validation with a novel signal-based performance metric," *Journal of Neural Engineering*, vol. 11, no. 1, p. 016008, 2014.
- [32] K. G. Keenan, D. Farina, R. Merletti, and R. M. Enoka, "Amplitude cancellation reduces the size of motor unit potentials averaged from the surface EMG," *Journal of Applied Physiology*, vol. 100, no. 6, pp. 1928–1937, 2006.
- [33] A. Holobar, M. A. Minetto, A. Botter, F. Negro, and D. Farina, "Experimental analysis of accuracy in the identification of motor unit spike trains from high-density surface EMG," *IEEE Transactions on Neural Systems and Rehabilitation Engineering*, vol. 18, no. 3, pp. 221–229, 2010.
- [34] P. Zhou and W. Z. Rymer, "Can standard surface EMG processing parameters be used to estimate motor unit global firing rate?," *Journal of Neural Engineering*, vol. 1, no. 2, pp. 99–110, 2004.
- [35] C. J. De Luca, R. S. LeFever, M. P. McCue, and A. P. Xenakis, "Behaviour of human motor units in different muscles during linearly varying contractions," *Journal of Physiology*, vol. 329, no. 1, pp. 113–128, 1982.
- [36] A. Holobar, V. Glaser, J. A. Gallego, J. L. Dideriksen, and J. Farina, "Non-invasive characterization of motor unit behaviour in pathological tremor," *Journal of Neural Engineering*, vol. 9, no. 5, article 056011, 2012.

Research Article

Atrial Fibrillation Beat Identification Using the Combination of Modified Frequency Slice Wavelet Transform and Convolutional Neural Networks

Xiaoyan Xu,¹ Shoushui Wei ,¹ Caiyun Ma,¹ Kan Luo ,² Li Zhang,³ and Chengyu Liu ⁴

¹School of Control Science and Engineering, Shandong University, Jinan 250061, China

²School of Information Science and Engineering, Fujian University of Technology, Fuzhou 350118, China

³Department of Computing Science and Digital Technologies, Faculty of Engineering and Environment, University of Northumbria, Newcastle NE1 8ST, UK

⁴The State Key Laboratory of Bioelectronics, Jiangsu Key Lab of Remote Measurement and Control, School of Instrument Science and Engineering, Southeast University, Nanjing 210096, China

Correspondence should be addressed to Shoushui Wei; sswei@sdu.edu.cn and Chengyu Liu; bestlcy@sdu.edu.cn

Received 18 January 2018; Revised 6 April 2018; Accepted 9 May 2018; Published 2 July 2018

Academic Editor: Maurizio Schmid

Copyright © 2018 Xiaoyan Xu et al. This is an open access article distributed under the Creative Commons Attribution License, which permits unrestricted use, distribution, and reproduction in any medium, provided the original work is properly cited.

Atrial fibrillation (AF) is a serious cardiovascular disease with the phenomenon of beating irregularly. It is the major cause of variety of heart diseases, such as myocardial infarction. Automatic AF beat detection is still a challenging task which needs further exploration. A new framework, which combines modified frequency slice wavelet transform (MFSWT) and convolutional neural networks (CNNs), was proposed for automatic AF beat identification. MFSWT was used to transform 1 s electrocardiogram (ECG) segments to time-frequency images, and then, the images were fed into a 12-layer CNN for feature extraction and AF/non-AF beat classification. The results on the MIT-BIH Atrial Fibrillation Database showed that a mean accuracy (Acc) of 81.07% from 5-fold cross validation is achieved for the test data. The corresponding sensitivity (Se), specificity (Sp), and the area under the ROC curve (AUC) results are 74.96%, 86.41%, and 0.88, respectively. When excluding an extremely poor signal quality ECG recording in the test data, a mean Acc of 84.85% is achieved, with the corresponding Se, Sp, and AUC values of 79.05%, 89.99%, and 0.92. This study indicates that it is possible to accurately identify AF or non-AF ECGs from a short-term signal episode.

1. Introduction

Atrial fibrillation (AF) is the most common type of arrhythmia in clinical disease and gradually becomes the world's rising healthcare burden [1]. According to Framingham heart study, lifetime risk of AF is about 25% [2]. The disease shows that the atrial activity is irregular, and the resulting complications such as stroke and myocardial infarction (MI) [3], endanger the health and lives of humans seriously [4]. Therefore, developing automatic AF detection algorithm is of great clinical and social significance [5, 6].

Generally, AF is significantly different from normal heart rhythm on electrocardiogram (ECG) signals [7]. During AF, RR interval is absolutely irregular and the P-wave is replaced by the continuous irregular F-wave, which is an important

feature of AF [8]. Many scholars proposed diverse methods based on RR interval feature, but the accuracy of AF is not sufficient due to the complication of the ECG signals [9], and the pattern recognition ability of the existing statistical and general method is not satisfactory owing to a variety of noise interference [10].

In recent years, AF detection algorithms based on the time domain characteristics have been developed rapidly. Chen et al. [11] developed a multiscale wavelet entropy-based method for paroxysmal atrial fibrillation (PAF) recognition. In their work, recognition and prediction used support vector machine- (SVM-) based method. Fifty recordings from the MIT-BIH PAF Prediction Database were chosen to test the proposed algorithm, with an average sensitivity of 86.16% and average specificity of 89.68%.

Maji et al. [12] used empirical mode decomposition (EMD) to extract P-wave mode components and corresponding parameters to determine the occurrence of AF. This proposed algorithm was tested with a total of 110 cycles of normal rhythm and 68 cycles of AF rhythm from the MIT-BIH AF Database. An average sensitivity of 92.89% and an average specificity of 90.48% were achieved. Ladavich and Ghoraani [13] constructed the Gaussian mixture model of the P-wave feature space. The model was then used to detect AF, with an average sensitivity of 88.87% and average specificity of 90.67%, while the positive predictive value was only 64.99%. Although relatively fine detection performances were achieved by the aforementioned methods, problems and questions exist. First, different methods used different signal length for AF identification. How will be the accuracy if performed on a very short-term (such as 1 s) ECG segment? This can show the ability for transient AF detection. In addition, ECG waveforms have various morphology and the abnormal waveforms are different when AF occurs, leading to poor generalization capability of the developed machine learning-based model. Thus, how to improve the model generalization capability is a key issue.

Convolutional neural networks (CNNs) [14] can extract features automatically without manual intervention and expert priori knowledge. Meanwhile, time-frequency (T-F) technology as a preprocess operation is to convert 1D ECG signals to 2D T-F features which can be used to transfer to a classifier. There are many common T-F methods at present, such as the short-time Fourier transform (STFT), the Wigner-Ville distribution (WVD), and the continuous wavelet transform (CWT) [15]. Luo et al. [16] presented a modified frequency slice wavelet transform (MFSWT) in 2017. MFSWT follows the rules of producing T-F representation and contains the information of ECG signals in both time and frequency domains, such as P-wave, QRS-wave, and T-wave. Additionally, MFSWT can locate the above characters accurately and avoid the complexity of setting parameters. The spectrogram of MFSWT can be expressed as images, while the combination of CNN and images is one of the most excellent choices. For example, Liu et al. [17] proposed the method to learn conditional random fields (CRFs) using structured SVM (SSVM) based on features learned from a pretrained deep CNN for image segmentation. Ravanbakhsh et al. [18] introduced a feature representation for videos that outperforms state-of-the-art methods on several datasets for action recognition. Lee and Kwon [19] built a fully connected CNN, which trained on relatively sparse training samples, and a newly introduced learning approach called residual learning for hyperspectral image (HSI) classification.

In this study, MFSWT was adopted to acquire T-F images for short-term AF and non-AF ECG segments from the MIT-BIH Atrial Fibrillation Database (MIT-BIH AFDB). A deep CNN with a total of 12 layers was developed to train an AF/non-AF classification model. Indices including accuracy, sensitivity, specificity, and the area under the curve were used for model evaluation based on a 5-fold cross validation method [20], to evaluate the stability and generalization ability of the proposed method in

comparison with the existing methods. The existing research has achieved very good performance, but there is no validation for large data. In this paper, we used all the data in the database to increase the generalization ability of the model.

2. Methods

2.1. Modified Frequency Slice Wavelet Transform. In our previous work, modified frequency slice wavelet transform (MFSWT) [16] was proposed for heartbeat time-frequency spectrum generation, with following the major principle of frequency slice wavelet transform (FSWT) [21]. The modified transform generates T-F representation from the frequency domain, and a bound signal-adaptive frequency slice function (FSF) was introduced to serve as a dynamic frequency filter. The window size of FSF smoothly changes with energy frequency distribution of signal in low-frequency area. The MFSWT has good performance for low-frequency ECG signals, and its advantages include signal-adaptive, accurate time-frequency component locating. The reconstruction is also independent of FSF, and it is readily accepted by clinicians.

Assume $\hat{f}(k)$ is the Fourier transform of $f(t)$. The MFSWT can be defined as follows:

$$W_f(t, \omega) = \frac{1}{2\pi} \int_{-\infty}^{+\infty} \hat{f}(k) \hat{p}^* \left(\frac{\mu - \omega}{q(f(k))} \right) e^{-ikt} dk, \quad (1)$$

where t and ω are observed time and frequency, respectively, “*” represents conjugation operator, and \hat{p} is the frequency slice function (FSF):

$$\hat{p}(x) = e^{-x^2/2}. \quad (2)$$

q is defined as a scale function of $\hat{f}(u)$,

$$q = \delta + \text{sign}(|\nabla \hat{f}(u)|). \quad (3)$$

It makes the transform to incorporate signal-adaptive property. In (3), δ corresponds to maximum $|\hat{f}(u)|$. $\nabla(\cdot)$ is a differential operator, and $\text{sign}(\cdot)$ means signum function, which returns 1 if the input is greater than zero, 0 if it is zero, or -1 if it is less than zero. In (2), $\hat{p}(0) = 1$, according to the claim in [21], then the original signal can be reconstructed as follows:

$$f(t) = \frac{1}{2\pi} \int_{-\infty}^{+\infty} \int_{-\infty}^{+\infty} W_f(t, \omega) e^{i\omega(t-\tau)} d\tau d\omega. \quad (4)$$

Figure 1 shows 4 s normal ECG, atrial fibrillation signals, and their corresponding MFSWT spectra, respectively, from 06426 recording. By the MFSWT, the time domain characteristics in ECG signal wave, such as P-wave, QRS-wave, and T-wave, have accurately been located in the signal spectrum. At the same time, each component of the spectrum of the T-F space distribution is corresponded well with the ECG signal frequency before.

In this study, the MFSWT is used as a tool to generate spectrograms of an ECG signal for CNN-based classification. The 1 s window, centered at the detected R-peaks (0.4 s before and 0.6 s after), was used to segment each

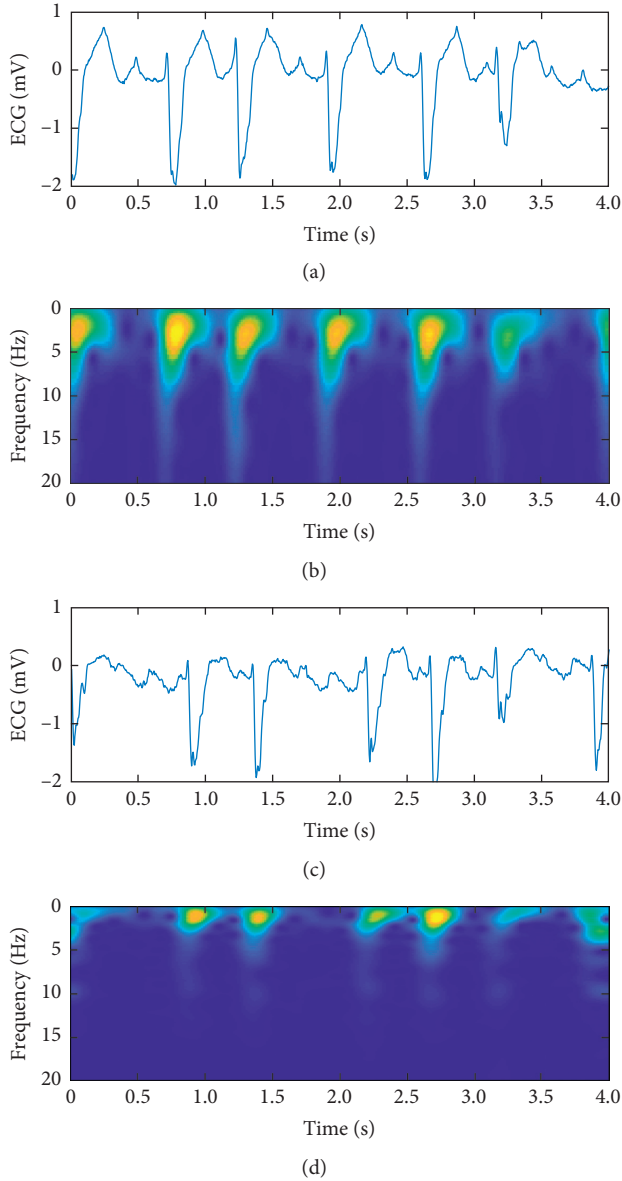


FIGURE 1: Examples from a 4 s normal ECG segment and a 4 s AF ECG segment, as well as their corresponding MFSWT spectra: (a) normal ECG signal; (b) MFSWT spectrum of the normal ECG signal; (c) AF ECG signal; (d) MFSWT spectrum of the AF ECG signal.

heartbeat. Subsequently, the T-F spectrograms with the size of 250×90 (corresponded 1 s time interval and 0–90 Hz frequency range) were produced by the proposed MFSWT. This is then followed by data reducing. An average 5×2 template operator reduces the size of spectrograms to 50×45 .

2.2. Convolutional Neural Networks (CNNs). Deep CNN was improved by Lecun et al. [22]. CNN had breakthrough performance over the last few decades for solving pattern recognition problems [23], especially in image classification [24]. It has become a popular method for feature extraction

and classification without requiring preprocessing and pretraining algorithm [25].

CNN is a composition of sequences of functions or layers that maps an input vector to an output vector. The input x_k^l is expressed as follows:

$$x_k^l = \sum_{i=1}^{N_{l-1}} \text{conv2D}(w_{ik}^{l-1}, s_i^{l-1}) + b_k^l. \quad (5)$$

Similarly, b_k^l and w_{ik}^{l-1} are the bias and kernel of the k th neuron at layer l , respectively. s_i^{l-1} is the output of the i th neuron at layer $l-1$, and $\text{conv2D}(\cdot, \cdot)$ means a regular 2D convolution without zero padding on the boundaries. So, the output y_k^l can be described as follows:

$$y_k^l = f\left(\sum_{i=1}^{N_{l-1}} \text{conv2D}(w_{ik}^{l-1}, s_i^{l-1}) + b_k^l\right). \quad (6)$$

Besides, CNN also involves back-propagation (BP), in order to adjust the delta error of the k th neuron at layer l . Assuming that the corresponding output vector of the input is $[y_1^l, y_2^l, \dots, y_{N_l}^l]$, and its ground truth class vector is $[t_1, t_2, \dots, t_{N_l}]$, we can write the mean absolute error (MSE) as follows:

$$E = E(y_1^l, y_2^l, \dots, y_{N_l}^l) = \sum_{i=1}^{N_l} (y_i^l - t_i)^2. \quad (7)$$

Thus, the delta error can be concluded as

$$\Delta_k^l = \frac{\partial E}{\partial x_k^l}. \quad (8)$$

The implementation of CNN [14] is as shown in Figure 2.

By the MFSWT, we have converted the signals to characteristic waves in a 2D space. Then, we use CNN to learn relevant information from the characteristic waves in a 2D space and achieve classification. The input to the CNN is characteristic waves in a 2D space computed from the exacted signals. The CNN was implemented using the Neural Network Toolbox in Matlab R2017a.

In this paper, we use CNN to automatically extract the features of the labeled image and calculate the scores to classify the predicted image. A 12-layer network structure is developed, which contains 3 convolution layers, 3 ReLU layers, a max pooling layer, and 3 full-connection layers besides the input and output layers. We tested the effect of number of filters in each layer and obtained these values by running a grid search approach. Figure 3 illustrates the architecture of the implemented network and its detailed components for each layer.

3. Experiment Design

3.1. Database. The database was from the MIT-BIH AFDB [26]. The MIT-BIH AFDB contains a large number of ECG data that have been annotated by a professional cardiologist, which is the authoritative ECG database in the classification of arrhythmia. This database may be useful for development and evaluation of atrial fibrillation/flutter detectors that rely

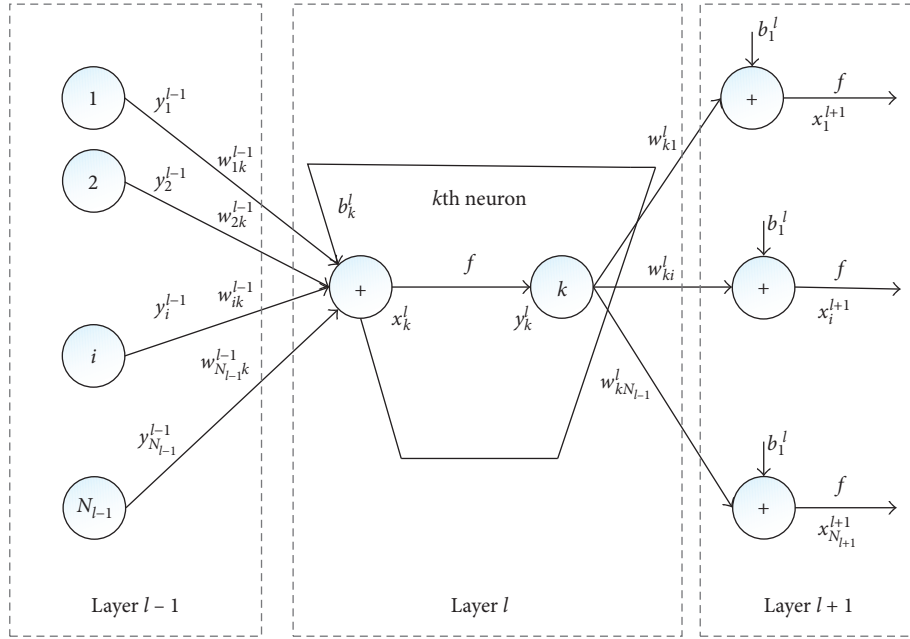


FIGURE 2: The implementation of CNNs.

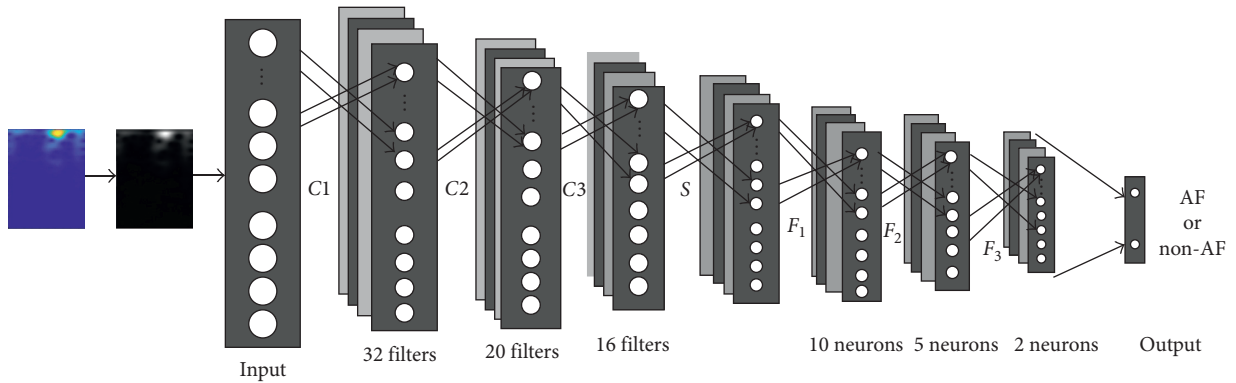


FIGURE 3: The architecture of the network.

on timing information only. It consists of 25 recordings (obtained from ambulatory ECG recordings of 25 subjects). The individual recordings are each 10 hours 15 min in duration and contain two ECG signals; each sampled at 250 samples per second with 12-bit resolution over a range of ± 10 millivolts. The reference manual annotation files contain rhythm change annotations (with the suffix.atr) [27] and the rhythm annotations of types: AF, AFL (atrial flutter), J (AV junctional rhythm), and N (used to indicate all other rhythms) [28]. In our experiment, AFL, J, and N are attributed to non-AF category. Figure 4 shows the ECG examples (each 4 s) of the four rhythm types (normal, AF, atrial flutter, and AV junction) from the “06426” recording.

3.2. Signal Preprocessing. There are a total of 25 recordings in AFDB, and two of them (numbers 00735 and 03665) have no relevant ECG data. Thus, 23 recordings are included in the experiment. In order to split the dataset equally, we divide

the 23 recordings into five groups, and the basis for grouping is to reduce the differences of number in the two classes. The recording numbers for 5 groups are 5, 4, 5, 5, 4, subsequently. This experiment uses 5-fold cross validation for evaluation. For example, when using the first group to test, it means that the whole data in 04015, 04126, 04936, 07879, and 08405 recordings are used to verify, and the remaining 17 records are all used to train the model. Detailed recordings of grouping conditions are shown in Table 1.

We employ a balanced image dataset to train the model. That is, we choose the same number of AF samples from the non-AF category for training, while all the samples in the remaining fold for test. For example, for testing the fold 1, there are 415,109 normal images and 294,136 AF images as training data from the folds 2–5. We use all the 294,136 AF images and then randomly select 294,136 normal images, resulting in 588,272 images as training CNN model. Then, we test the performance of the developed CNN model using all data in fold 1, that is, 123,083 normal images and 90,403

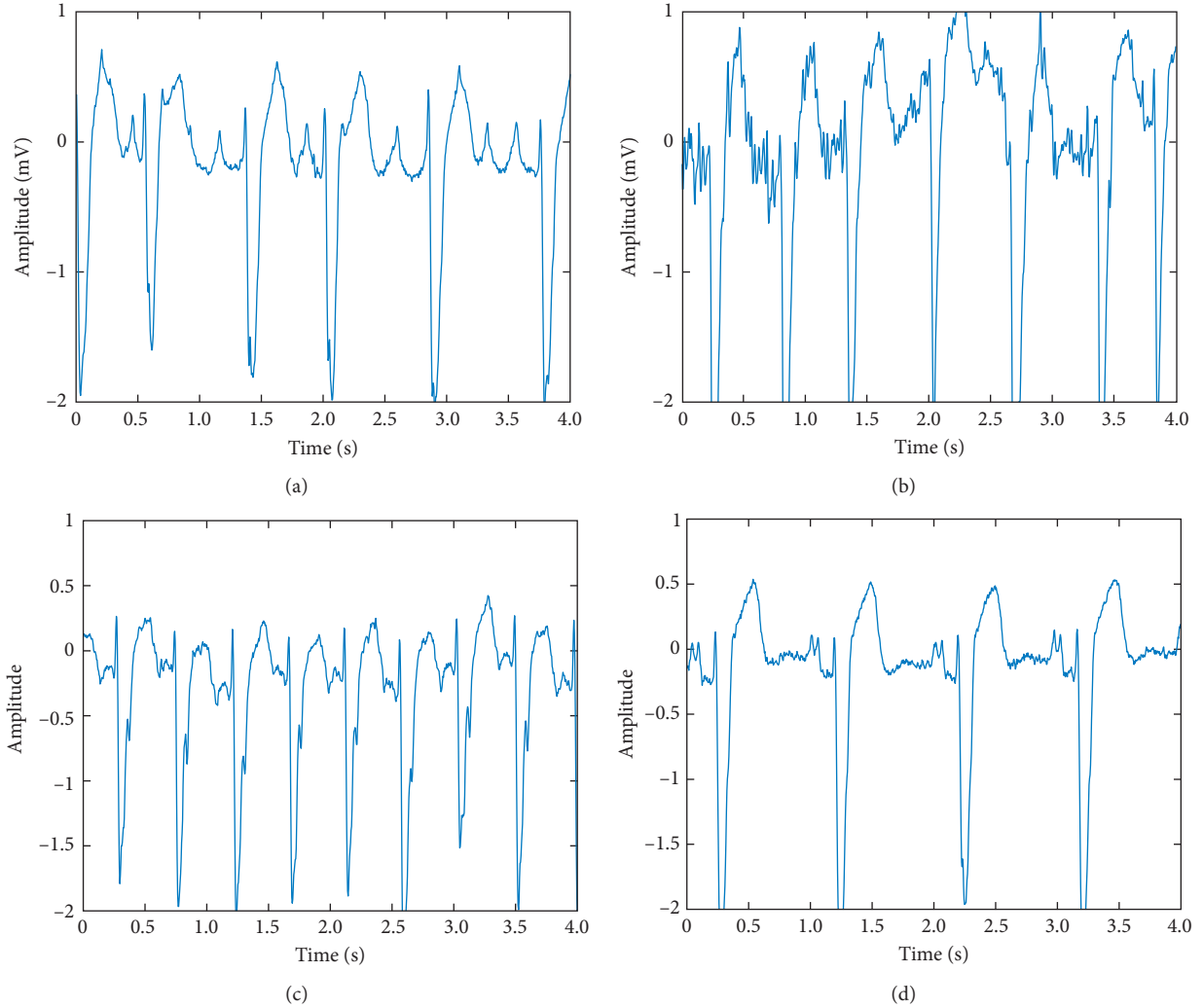


FIGURE 4: ECG examples of the four rhythm types: (a) normal, (b) atrial fibrillation, (c) atrial flutter, and (d) AV junction rhythm.

AF images. Table 2 presents the detailed numbers for each fold testing.

4. Results

4.1. Epoch Number of the CNN. The grid search method [29] is applied to select the optimal epoch number of the CNN. Figure 5 shows the AUC of the test set (AUC is defined as the area under the ROC curve, often used to evaluate the classifier with imbalance data) at varying epoch number, and Figure 6 shows training and test accuracies at varying epoch number. We can see from Figure 5 that the AUC of test set is at a high level while epoch number is 15, and the wave becomes stable in Figure 6. Therefore, we choose the number of epochs as 15.

According to the introduction of Section 2.2 on CNN architecture, the input layer (layer 0) is for images with the size of $50 \times 45 \times 1$ and is convolved with a kernel size of 10×9 to produce the layer 1. Layer 2 is the ReLU layer. The output of layer 2 is convolved with a kernel size of 8×7 to develop the layer 3 and layer 4. Similarly, a subsequent feature maps are convolved with a kernel size of 9 to acquire the layer 5 and

TABLE 1: Recordings of grouping conditions.

Fold	Recordings				
1	04015	04126	04936	07879	08405
2	04043	04048	07859	07910	
3	04746	05261	08215	08378	08455
4	04908	06426	07162	08219	08434
5	05091	05121	06453	06995	

layer 6. A max pool layer with the stride of 2 (layer 7) is applied to the generated characteristics. Then, the feature has been extracted. Finally, features are transported to layer 8 with 10 neurons and connected to 5 and 2 neurons in layer 9 and layer 10, respectively, to classify. In addition, we select the epoch number as 15, and the learning rate initial value is set to 0.001 while the number of minimal batches is 256. In addition, specific parameter is shown in Table 3.

4.2. Performance Metrics. This research uses the MIT-BIH AFDB to verify the proposed method to detect AF performance. Four widely used metrics, that is, sensitivity (Se),

TABLE 2: Numbers of the images for testing each fold.

Testing fold	Training		Balanced training		Test	
	Non-AF	AF	Non-AF	AF	Non-AF	AF
1	415,109	294,136	294,136	294,136	123,083	90,403
2	422,935	302,194	302,194	302,194	115,257	82,345
3	424,919	300,509	300,509	300,509	113,273	84,030
4	441,739	314,916	314,916	314,916	96,453	69,623
5	448,066	326,401	326,401	326,401	90,126	58,138

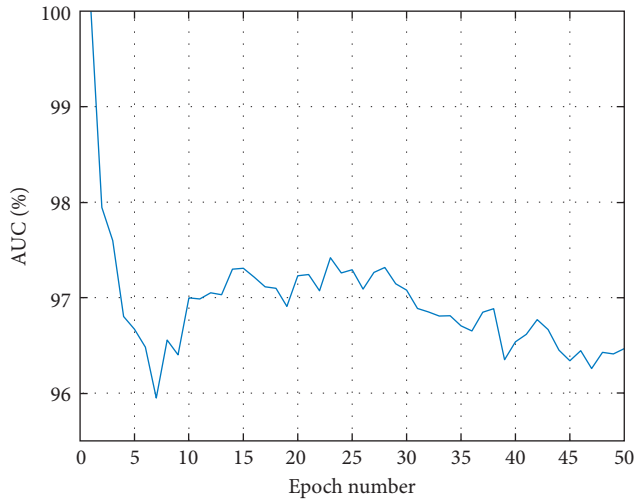


FIGURE 5: The AUC of test set at varying epoch number.

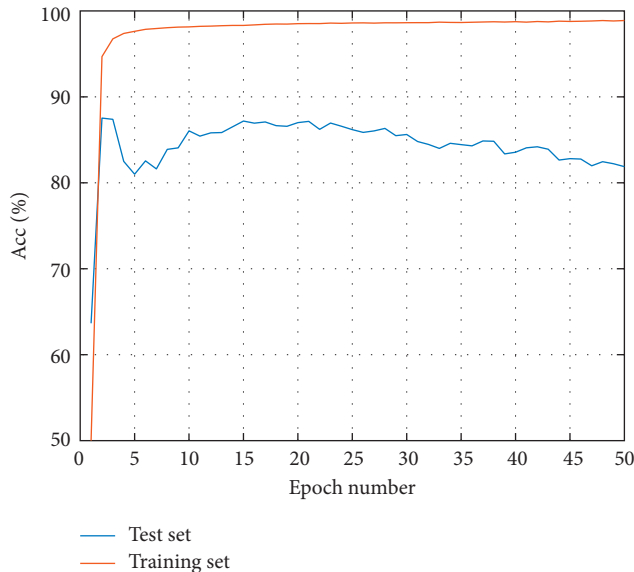


FIGURE 6: Test Acc and training Acc at varying epoch number.

specificity (Sp), accuracy (Acc), and the area under the curve (AUC), were used (and defined below) for assessment of classification performance. In addition, AUC and Acc refer to the overall system performance, while the remaining

TABLE 3: The optimal CNN specifications designed for the ECG classification problem.

Parameters	Values
Learning rate	0.001
First convolutional layer kernel size	10 * 9
Number of feature maps in the first convolutional and subsampling layer	32
Second convolutional layer kernel size	8 * 7
Number of feature maps in the second convolutional and subsampling layer	20
Third convolutional layer kernel size	9
Number of feature maps in the third convolutional and subsampling layer	16
Subsampling layer kernel size	2
Number of neurons in the first fully connected layer	10
Number of neurons in the second fully connected layer	5
Number of neurons in the third fully connected layer	2
Number of epochs	15
Number of minimal batches	256

indexes are specific to each class, and they measure the generalization ability of the classification algorithm to differentiate events.

Moreover, the Acc includes both test set accuracy and training set accuracy. According to the attribute of the label (positive or negative), the result can generate four basic indexes: true positive (TP), false positive (FP), true negative (TN), and false negative (FN), and in this case, Acc is the ratio of the number of correct predicted labels and total number of the labels, thus $Acc = (TP + TN) / (TP + TN + FP + FN)$. Se is the true positive rate and is the probability of incorrectly diagnosing into positive among all positive patients, so $Se = TP / (TP + FN)$. Sp is proportion of incorrectly diagnosing into negative among all negative patients, so $Sp = TN / (TN + FP)$. ROC curve is based on a series of different ways of binary classification (boundary value or decision threshold), with true positive rate (Se) as the ordinate, the false positive rate (1-Sp) as the abscissa, and AUC is defined as the area under the ROC curve, often used to evaluate the classifier with imbalance data. Each fold is tested by a specific classifier with the same parameters as shown in Section 4.1; besides, we also selected the average and standard deviation (SD) of the experimental results to be evaluated, and the results are summarized in Table 4.

From Table 4, a mean Acc of 81.07% from 5-fold cross validation is achieved for the test data. The corresponding Se, Sp, and AUC results are 74.96%, 86.41%, and 0.88. It is worth to note that the results from the fourth fold are low. This is because there is an extremely poor signal quality ECG recording in the fourth fold divided as shown in Table 1, which has significantly different time-frequency features compared to the clean ECG signals. So the results from the folds 1, 2, 3, and 5 are recalculated as shown in Table 4 to exclude the low-quality signal effect. Herein, a mean Acc of 84.85% is achieved for the test data, with the corresponding Se, Sp, and AUC values of 79.05%, 89.99%, and 0.92.

TABLE 4: The experimental results.

Fold	Test data				Training data			
	Acc (%)	Se (%)	Sp (%)	AUC	Acc (%)	Se (%)	Sp (%)	AUC
1	86.63	77.95	95.97	0.95	97.59	96.68	98.54	0.99
2	86.82	84.28	88.62	0.93	98.21	97.81	98.62	0.99
3	83.55	78.90	87.38	0.91	97.80	96.77	98.88	0.99
4	65.93	58.59	72.08	0.70	98.26	98.51	98.00	0.98
5	82.41	75.06	87.99	0.90	98.40	98.56	98.24	0.99
Mean	81.07	74.96	86.41	0.88	98.05	97.67	98.46	0.99
SD	8.68	9.74	8.73	0.10	0.34	0.91	0.34	0
Mean [#]	84.85	79.05	89.99	0.92	98.00	97.46	98.57	0.99
SD [#]	1.92	3.34	3.48	0.02	0.32	0.78	0.23	0

[#]The results only from the average of the folds 1, 2, 3, and 5.

TABLE 5: Comparison with reference studies.

Algorithm	Data	Acc (%)	Se (%)	Sp (%)	AUC
Chen et al. [11]	50 signals	—	89.68	86.16	—
Maji et al. [12]	178 cycles	—	90.48	92.89	—
Ladavich and Ghoraani [13]	14,600 beats	—	90.67	88.87	—
Proposed method	All recordings	81.07	74.96	86.41	0.88
Proposed method	All recordings but excluding one fold with extreme noisy recording	84.85	79.05	89.99	0.92

5. Discussion and Conclusion

An ECG is widely used in medicine to monitor small electrical changes on the skin of a patient's body arising from the activities of the human heart. Due to the variability and difficulty of AF, traditional detection algorithm cannot be extracted to distinguish obvious characteristics accurately.

In our work, we present a unique architecture of CNN to distinguish AF beats from all other types of ECG beats. MFSWT is adopted to acquire the T-F images of AF and non-AF, respectively, and then, we divide all the data in the MIT-BIH AFDB into training set and test set different from the existing models and build a deep CNN with a total of 12 layers to extract the characters of training set. Finally, the test set is evaluated by the trained model to obtain the performance indexes (including Acc, Se, Sp, and AUC).

Compared with other studies, the difference is that we use all ECG recordings in the MIT-BIH AFDB. However, other studies only selected a part of the recordings for training and testing, and Table 5 shows the comparison between our study and other studies. Obviously, the proposed method does not improve the Acc, Se, and Sp significantly, but this paper uses lots of data to train the model in order to improve the generalization ability of the model. Moreover, we use an important indicator called AUC to evaluate the unbalanced data model and obtained a good evaluation standard.

In short, we proposed a protocol for AF beat detection as follows. (1) Use all the recordings of MIT-BIH Atrial Fibrillation Database for algorithm development and validation. (2) Use 5-fold cross validation to examine the algorithm performance. The results have been registered for Acc, Se, Sp, and AUC. Group the folds by recordings rather

than heartbeats to prevent heartbeats of the same patient from appearing in both training and test sets. (3) Use a separate database, for instance AF Database, as an independent test to evaluate the generalization ability of the algorithm. We believe that accurate AF beat recognition can facilitate the detection of AF rhythm. As the first step, AF beat is particularly important. Only by improving the accuracy and generalization of AF beat detection can we more effectively implement AF surveillance.

In addition, more data could be used to evaluate the proposed method; for example, we only focus on one ECG lead, and the study can be extended to two ECG leads. We also can try to use more databases for verification. This algorithm can be used for monitoring and prevention of AF, which has great practical meaning.

Data Availability

The data used to support the findings of this study are available from the open-access MIT-BIH Atrial Fibrillation Database.

Conflicts of Interest

The authors declare that they have no conflicts of interest.

Acknowledgments

The project was partly supported by the National Natural Science Foundation of China (61571113 and 61671275), the Key Research and Development Programs of Jiangsu Province (BE2017735), the Natural Science Foundation of Shandong Province in China (2014ZRE2733), and the

Fundamental Research Funds for the Central Universities in Southeast University (2242018k1G010). The authors thank the support from the Southeast-Lenovo Wearable Intelligent Lab.

References

- [1] J. J. Rieta, F. Ravelli, and L. Sörnmo, "Advances in modeling and characterization of atrial arrhythmias," *Biomedical Signal Processing and Control*, vol. 8, no. 6, pp. 956–957, 2013.
- [2] D. M. Lloydjones, "Lifetime risk for development of atrial fibrillation: the Framingham Heart Study," *Circulation*, vol. 110, no. 9, pp. 1042–1046, 2004.
- [3] E. Z. Soliman, F. Lopez, W. T. O'Neal et al., "Atrial fibrillation and risk of ST-segment elevation versus non-ST segment elevation myocardial infarction: the atherosclerosis risk in communities (ARIC) study," *Circulation*, vol. 131, no. 21, pp. 1843–1850, 2015.
- [4] P. Langley, M. Dewhurst, L. Y. Di Marco et al., "Accuracy of algorithms for detection of atrial fibrillation from short duration beat interval recordings," *Medical Engineering and Physics*, vol. 34, no. 10, pp. 1441–1447, 2012.
- [5] C. Bruser, J. Diesel, M. D. H. Zink, S. Winter, P. Schauerte, and S. Leonhardt, "Automatic detection of atrial fibrillation in cardiac vibration signals," *IEEE Journal of Biomedical and Health Informatics*, vol. 17, no. 1, pp. 162–171, 2013.
- [6] G. Y. H. Lip, C. M. Brechin, and D. A. Lane, "The global burden of atrial fibrillation and stroke: a systematic review of the epidemiology of atrial fibrillation in regions outside North America and Europe," *Chest*, vol. 142, no. 6, pp. 1489–1498, 2012.
- [7] D. T. Linker, "Accurate, automated detection of atrial fibrillation in ambulatory recordings," *Cardiovascular Engineering and Technology*, vol. 7, no. 2, pp. 182–189, 2016.
- [8] Y. Li, X. Tang, A. Wang, and H. Tang, "Probability density distribution of delta RR intervals: a novel method for the detection of atrial fibrillation," *Australasian Physical and Engineering Sciences in Medicine*, vol. 40, no. 3, pp. 707–716, 2017.
- [9] A. Petrenas, L. Sörnmo, V. Marozas, and A. Lukosevicius, "A noise-adaptive method for detection of brief episodes of paroxysmal atrial fibrillation," in *Proceedings of Computing in Cardiology Conference*, pp. 739–742, Zaragoza, Spain, September 2013.
- [10] N. Larburu, T. Lopetegui, and I. Romero, "Comparative study of algorithms for atrial fibrillation detection," in *Proceedings of Computing in Cardiology Conference*, pp. 265–268, Hangzhou, China, September 2011.
- [11] Y. Chen, Z. Wang, and Q. Li, "Multi-scale wavelet entropy based method for paroxysmal atrial fibrillation recognition," *Space Medicine and Medical Engineering*, vol. 26, no. 5, pp. 352–355, 2013.
- [12] U. Maji, M. Mitra, and S. Pal, "Automatic detection of atrial fibrillation using empirical mode decomposition and statistical approach," *Procedia Technology*, vol. 10, no. 1, pp. 45–52, 2013.
- [13] S. Ladavich and B. Ghorani, "Rate-independent detection of atrial fibrillation by statistical modeling of atrial activity," *Biomedical Signal Processing and Control*, vol. 18, pp. 274–281, 2015.
- [14] S. Kiranyaz, T. Ince, and M. Gabbouj, "Real-time patient-specific ECG classification by 1-D convolutional neural networks," *IEEE Transactions on Biomedical Engineering*, vol. 63, no. 3, pp. 664–675, 2016.
- [15] Z. Yan, A. Miyamoto, Z. Jiang, and X. Liu, "An overall theoretical description of frequency slice wavelet transform," *Mechanical Systems and Signal Processing*, vol. 24, no. 2, pp. 491–507, 2010.
- [16] K. Luo, J. Li, Z. Wang, and A. Cuschieri, "Patient-specific deep architectural model for ECG classification," *Journal of Healthcare Engineering*, vol. 2017, Article ID 4108720, 13 pages, 2017.
- [17] F. Liu, G. Lin, and C. Shen, *CRF Learning with CNN Features for Image Segmentation*, Elsevier Science Inc., Amsterdam, Netherlands, 2015.
- [18] M. Ravanbakhsh, H. Mousavi, M. Rastegari, V. Murino, and L. S. Davis, "Action recognition with image based CNN features," <http://arxiv.org/abs/1512.03980>.
- [19] H. Lee and H. Kwon, "Going deeper with contextual CNN for hyperspectral image classification," *IEEE Transactions on Image Processing*, vol. 26, no. 10, pp. 4843–4855, 2017.
- [20] R. Kohavi, "A study of cross-validation and bootstrap for accuracy estimation and model selection," in *Proceedings of International Joint Conference on Artificial Intelligence*, pp. 1137–1143, Montreal, QC, Canada, August 1995.
- [21] Z. Yan, A. Miyamoto, and Z. Jiang, "Frequency slice algorithm for modal signal separation and damping identification," *Computers and Structures*, vol. 89, no. 1-2, pp. 14–26, 2011.
- [22] Y. Lecun, L. Bottou, Y. Bengio, and P. Haffner, "Gradient-based learning applied to document recognition," *Proceedings of the IEEE*, vol. 86, no. 11, pp. 2278–2324, 1998.
- [23] X. Jiang, Y. Pang, X. Li, and J. Pan, "Speed up deep neural network based pedestrian detection by sharing features across multi-scale models," *Neurocomputing*, vol. 185, pp. 163–170, 2016.
- [24] A. Krizhevsky, I. Sutskever, and G. E. Hinton, "ImageNet classification with deep convolutional neural networks," in *Proceedings of International Conference on Neural Information Processing Systems*, pp. 1097–1105, Lake Tahoe, NV, USA, December 2012.
- [25] S. Chaib, H. Yao, Y. Gu, and M. Amrani, "Deep feature extraction and combination for remote sensing image classification based on pre-trained CNN models," in *International Conference on Digital Image Processing*, p. 104203D, Prague, Czech, July 2017.
- [26] K. Jiang, C. Huang, S. Ye, and H. Chen, "High accuracy in automatic detection of atrial fibrillation for Holter monitoring," *Journal of Zhejiang University*, vol. 13, no. 9, pp. 751–756, 2012.
- [27] F. D. Murgatroyd, B. Xie, X. Copie, I. Blankoff, A. J. Camm, and M. Malik, "Identification of atrial fibrillation episodes in ambulatory electrocardiographic recordings: validation of a method for obtaining labeled R-R interval files," *Pacing and Clinical Electrophysiology Pace*, vol. 18, no. 6, p. 1315, 1995.
- [28] A. Petrenas, L. Sörnmo, A. Lukosevicius, and V. Marozas, "Detection of occult paroxysmal atrial fibrillation," *Medical and Biological Engineering and Computing*, vol. 53, no. 4, pp. 287–297, 2015.
- [29] J. A. A. Brito, F. E. Mcneill, C. E. Webber, and D. R. Chettle, "Grid search: an innovative method for the estimation of the rates of lead exchange between body compartments," *Journal of Environmental Monitoring*, vol. 7, no. 3, p. 241, 2005.

Research Article

Performance Analysis of Ten Common QRS Detectors on Different ECG Application Cases

Feifei Liu,^{1,2} Chengyu Liu ,¹ Xinge Jiang,³ Zhimin Zhang,³ Yatao Zhang ,³ Jianqing Li ,¹ and Shoushui Wei ³

¹The State Key Laboratory of Bioelectronics, Jiangsu Key Lab of Remote Measurement and Control, School of Instrument Science and Engineering, Southeast University, Nanjing, China

²Shandong Zhong Yang Software Limited Company, Jinan, China

³School of Control Science and Engineering, Shandong University, Jinan, China

Correspondence should be addressed to Chengyu Liu; bestlcy@sdu.edu.cn and Shoushui Wei; sswei@sdu.edu.cn

Received 16 January 2018; Revised 22 March 2018; Accepted 10 April 2018; Published 8 May 2018

Academic Editor: Norio Iriguchi

Copyright © 2018 Feifei Liu et al. This is an open access article distributed under the Creative Commons Attribution License, which permits unrestricted use, distribution, and reproduction in any medium, provided the original work is properly cited.

A systematical evaluation work was performed on ten widely used and high-efficient QRS detection algorithms in this study, aiming at verifying their performances and usefulness in different application situations. Four experiments were carried on six internationally recognized databases. Firstly, in the test of high-quality ECG database versus low-quality ECG database, for high signal quality database, all ten QRS detection algorithms had very high detection accuracy ($F1 >99\%$), whereas the $F1$ results decrease significantly for the poor signal-quality ECG signals (all $<80\%$). Secondly, in the test of normal ECG database versus arrhythmic ECG database, all ten QRS detection algorithms had good $F1$ results for these two databases (all $>95\%$ except RS slope algorithm with 94.24% on normal ECG database and 94.44% on arrhythmia database). Thirdly, for the paced rhythm ECG database, all ten algorithms were immune to the paced beats ($>94\%$) except the RS slope method, which only output a low $F1$ result of 78.99%. At last, the detection accuracies had obvious decreases when dealing with the dynamic telehealth ECG signals (all $<80\%$) except OKB algorithm with 80.43%. Furthermore, the time costs from analyzing a 10 s ECG segment were given as the quantitative index of the computational complexity. All ten algorithms had high numerical efficiency (all <4 ms) except RS slope (94.07 ms) and sixth power algorithms (8.25 ms). And OKB algorithm had the highest numerical efficiency (1.54 ms).

1. Introduction

Cardiovascular diseases (CVDs) are the most common cause of death globally. In 2012, CVDs were the cause of death for about 17.5 million people, which equated to about 31% of all global deaths [1]. An electrocardiogram (ECG) signal, the expression of the myocardium electrical activity on the body's surface, provides important information about the status of cardiac activity [2]. The accurate and real-time heart beat detection of the ECG signal plays a fundamental role in monitoring of CVDs [3].

The QRS complex is the most striking waveform within the ECG signal. It serves as the basis for the automated determination of the heart rate, as well as the benchmark point for classifying the cardiac cycle and identifying any

abnormality. Over the last few decades, the QRS complex detection has been extensively studied. In 1984, Pahlm and Sornmo discussed the QRS detection methods developed before 1984 in the aspects of digital preprocessing and detection rule, which is a very early paper for systematically analyzing the QRS detection methods [4]. In 2002, Köhler et al. reviewed and compared the great variety of QRS detection algorithms [5]. They grouped all the algorithms into four categories, respectively, based on signal derivatives, wavelet, neural network, and additional approaches. The algorithmic comparisons with respect to the computational load and detection accuracies were carried out to rate the algorithms. This literature was the most cited review paper about QRS detection algorithms. In 2014, Elgendi et al. investigated the existing QRS detection

methodologies to target a universal fast-robust detector for portable, wearable, battery-operated, and wireless ECG systems [6]. This study compared the different QRS enhancement and detection techniques based on three assessment criteria: (1) robustness to noise, (2) parameter choice, and (3) numerical efficiency.

However, the review [4] did not compare the performances of different QRS detectors. In the review [5], the computational load and detection accuracies of QRS detection algorithms were not based on a standard database, and the comparison results were not given quantitatively. In the review [6], the comparison results were only based on the MIT-BIH arrhythmia database, but these results were from different literatures. In these literatures, some investigators have excluded some records [7] from the MIT-BIH arrhythmia database or excluded some segments with ventricular flutter [8] for the sake of reducing noise in the processed ECG signals.

In 1990, the noise sensitivities from nine different QRS detection algorithms were evaluated on a normal, single-channel lead, synthesized ECG database corrupted with five different types of synthesized noise [9]. In 2006, three methods were quantitatively compared using a similar algorithm structure but applying different transforms to the differentiated ECG [10]. The three transformations used were the Hilbert transformer, the squaring function, and a second discrete derivative stage. In 2008, the traditional first-derivative based squaring function method [11] and the Hilbert transform-based method [12], as well as their modifications with improved detection thresholds, were analyzed in the literature [13]. In 2013, Álvarez et al. analyzed the performances of three algorithms [14], Pan and Tompkins algorithm [15], Hamilton and Tompkins algorithm [11], and a phasor transform-based algorithm [16]. However, some studies [9, 10, 13, 14] quantitatively compared different QRS detection algorithms based on the same database, that is, the MIT-BIH arrhythmia database. The MIT-BIH arrhythmia database was widely used to evaluate QRS detection algorithms as it includes different shapes of arrhythmic QRS complexes and noise. As shown in many literatures, majority of the QRS detection algorithms had high detection sensitivity and positive predictivity on the MIT-BIH arrhythmia database (>99%) [1, 6]. However, performances of multiple algorithms on multiple source ECG databases lack. For example, the evaluation on ECG signals monitored by portable devices has not been systematically studied, which also challenges the current signal processing algorithms. The ECG signals recorded from the dynamic and mobile equipment are inevitably noise corrupted, consisting of more uncontrollable aspects, such as physiology, pathology, and artificial effects [17]. Therefore, the performance comparison of the commonly used algorithms should be extended to multiple source ECG databases.

In this study, the performances of ten widely used and high-efficient QRS detection algorithms were systematically evaluated on six ECG databases, with a special focus on the comparison between two opposite types or special application situations: high-quality ECG database versus low-quality ECG database, normal ECG database versus arrhythmic ECG

database, paced rhythm ECG database, and dynamic telehealth ECG database. These ten algorithms were reported as high-efficient algorithms and suitable for mobile device situations [6, 17].

2. Methods

2.1. Databases

2.1.1. High and Poor Signal Quality ECG Databases. Two hundred ECG records from the 2014 PhysioNet/CinC Challenge [12, 13] were used in this study. These records were from two databases: 100 records (named 100~199, sampled at 250 Hz) from the training set and another 100 records (sampled at 360 Hz) from the augmented training set. Each record is 10 min long. The signal quality of ECG signals in the training set is always good, whereas the signal quality in the augmented training set is very poor. Thus, the training set was used as a high-quality ECG database and the augmented training set was used as a poor quality ECG database in this study.

2.1.2. Normal Sinus Rhythm and Arrhythmia ECG Databases. Eighteen long-term ECG records from the MIT-BIH normal sinus rhythm (NSR) database were used as the normal subjects' data. Each record has a time length of two hours. ECG signals were sampled at 128 Hz. Subjects included in this database were found to have no significant arrhythmias. Besides, 44 of the 48 records from the MIT-BIH arrhythmia (ARR) database were used as the patients' data. Four records were excluded as they are paced ECGs. Each of the remaining 44 records had a time length of half an hour. ECG signals were sampled at 360 Hz.

2.1.3. Pacemaker Rhythm ECG Database. Four records from the MIT-BIH arrhythmia database (records 102, 104, 107, and 217) including pacing signals were regarded as the pacemaker rhythm ECG database in this study.

2.1.4. Telehealth ECG Database. Two hundred fifty lead-I ECGs from the TELE database [3] were used as telehealth ECG database in this study. These ECG records were recorded using the TeleMedCare Health Monitor (TeleMedCare Pty., Ltd., Sydney, Australia) in a telehealth environment [18] and were sampled at 500 Hz.

All ECG records from the above six databases selected in this study had manually annotated QRS complex locations, and these locations were used as the references for the algorithm evaluations [14]. Table 1 describes all these databases in detail.

2.2. Preprocessing. A unified signal preprocessing session was performed before QRS detection for the fair comparisons among different QRS detection methods. This session included three steps: flat line detection, signal detrending, and band-pass filtering.

TABLE 1: The list of six databases.

Database	Description	Number of beats	Number of records	Record length (min)	Total time (min)	Sample frequency (Hz)	Source
A	High-quality ECGs	72,415	100	10	1000	250	2014 PhysioNet/CinC challenge training set (https://physionet.org/challenge/2014/)
	Low-quality ECGs	78,618	100	10	1000	360	2014 PhysioNet/CinC challenge augmented training set (https://physionet.org/challenge/2014/)
B	Normal subjects	1,806,792	18	120	2160	500	MIT-BIH NSR database (https://physionet.org/physiobank/database/nsrdb/)
	Arrhythmia patients	103,724	44	30	1320	360	MIT-BIH arrhythmia database (https://www.physionet.org/physiobank/database/mitdb/)
C	Paced rhythm ECGs	8923	4	30	120	360	MIT-BIH arrhythmia database (https://www.physionet.org/physiobank/database/mitdb/)
D	Telehealth environment ECGs	6708	250	0.5	125	500	Harvard dataverse TELE database (https://dataverse.harvard.edu/dataset.xhtml?persistentId=doi:10.7910/DVN/QTGOEP)
Total	—	2,077,180	516	—	5725	—	—

2.2.1. Flat Line Detection. ECG was detected as a flat line signal, if the portion of samples with constant amplitude was higher than 80% [19].

2.2.2. Signal Detrending. Firstly, the least-squares fit of the ECG signal data was computed. Then, the best fitted value was removed from the ECG signal. The Matlab function “detrend.m” was used to remove the linear trend in the ECG signal.

2.2.3. Band-Pass Filtering. The third-order Butterworth [20] band-pass filter was used to filter the ECG signal at a frequency range of 0.05–40 Hz. The Butterworth filter is a type of signal processing filter designed to have as flat a frequency response as possible in the passband. It is also referred to as a maximally flat magnitude filter.

2.3. QRS Detection Algorithms. As is known to all, QRS detection is a hot research topic for more than 40 years. A lot of QRS detectors have been proposed. It would be impractical to compare all of them. Three criteria for selecting the suitable algorithms were used in this study: algorithm efficiency, detection accuracy, and implementability. According to the three criteria, ten algorithms were selected from about 30 papers about QRS detection.

Any algorithm selected in this study should be widely used, with low computational complexity, and it could be executed in real-time circumstances on the mobile devices. As having limitations in terms of phone memory and processor capability, ECG monitoring using battery-operated, portable device is desirable for the efficient (fast and fewer calculations) QRS detection algorithms. Meanwhile, the QRS

detection algorithms should have high detection accuracy, which is an essential basis for the actual applications. As we know, researchers not always could write the right program according to the description of some papers. So, the implementability was also a key point for QRS detectors.

Table 2 shows the detailed information of these ten algorithms in four aspects. The first three methods were all Pan–Tompkins-based algorithms and based on the same principle, but there were many differences in the operating approach. For more information, see [21].

2.4. Evaluation Methods. The sensitivity (Se), positive predictivity (+P), and F1 measure [31] were used as the evaluation indexes, which are defined as follows:

$$Se = \frac{TP}{TP + FN} \times 100\%,$$

$$+P = \frac{TP}{TP + FP} \times 100\%, \quad (1)$$

$$F1 = \frac{2 \times TP}{(2 \times TP + FP + FN)} \times 100\%,$$

where TP is the number of QRS complexes truly detected, FP is the number of false positive (extra falsely detected QRS complexes), and FN is the number of false negative (missed detected QRS complexes).

Figure 1 shows an example of TP (marked as blue “o”), FN (green “+”), and FP (pink “o”) detections from the record 41,778 in the low-quality database. Red “+” signs indicated the reference QRS annotations (R-ref). A tolerance time window of 50 ms was used and denoted by the vertical grey

TABLE 2: Ten selected QRS detection algorithms.

Methods	Filtering	Extracting features	Setting threshold	Postprocessing
Pan-Tompkins algorithm [15]				
Hamilton-mean algorithm [11]	5–15 Hz band-pass filter	Derivative; square; integrate	Two sets of adaptive thresholds	Searching back; T wave judging
Hamilton-median algorithm [11]				
RS slope algorithm [21–23]	Median filter	Derivative; detecting negative slope	10 groups of duration empirical thresholds; one fixed amplitude threshold	200 ms refractory blanking technology
Sixth power algorithm [24]	Two-stage median filter	Sixth power	One adaptive threshold	Determining end point K
Finite state machine (FSM) algorithm [25]	/	Derivative; integrate; square	Three thresholding stages	/
U3 transform algorithm (U3) [26]	8–30 Hz band-pass filter	U3 transform	Two fixed thresholds	Searching back; 270 ms refractory blanking technology
Difference operation algorithm (DOM) [2, 27]	8–30 Hz band-pass filter	Derivative; detecting positive extreme points	Positive threshold; negative threshold	Optimizing; matching filtered signal
“jqrs” algorithm [28–30]	Sombrero hat-like low-pass filter	Integrate	One fixed threshold	Searching back; 200 ms refractory blanking technology
Optimized knowledge-based algorithm (OKB) [1]	8–20 Hz band-pass filter	Squaring; integration	Two dynamic thresholds	Determining the maxima of each block as R peak

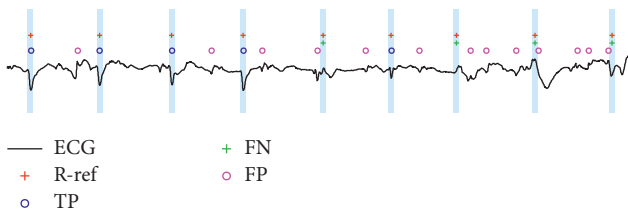


FIGURE 1: Example of TP (marked as blue “o”), FN (green “+”), and FP (pink “o”) detections from record 41,778 in the low-quality database. Reference QRS annotations (R-ref) are marked as red “+.” Vertical grey areas denote the tolerance time window of 50 ms.

areas to determine the TP detections. If the detected QRS location is within the current vertical grey area, it is considered as TP detection. If the detected QRS location is out of the current vertical grey area, it is considered as FP detection. If there is no detected QRS location within the current vertical grey area, it is considered to be FN detection. If more than one detected QRS locations exist within the current vertical grey area, one is considered to be TP detection and the others FP detection.

In this study, the ECG signal was firstly segmented into 10 s ECG episodes with a 50% overlap; that is, each episode had 5 s overlap with the previous one. Then the employed QRS detection algorithms were performed on each 10 s ECG episode. Then, the results of QRS locations from all 10 s episodes were integrated as the final algorithm output.

3. Results

Figure 2 illustrates the line graph for $F1$ results of the ten algorithms on these six ECG databases. All ten QRS detection algorithms had good $F1$ results for the high signal

quality ECG data (all >99%, black square line). However, the $F1$ results decrease significantly for the poor signal quality ECG signals (all <80%, red round line), where the OKB algorithm reported the highest $F1$ result at 75.35%, while the RS slope algorithm gave the lowest $F1$ result of 63.66%. The blue equilateral triangle line and magenta inverted triangle line represent the results of the NSR and ARR ECG database, that is, the normal subjects and arrhythmia patients, respectively. All ten QRS detection algorithms had high $F1$ results for these two databases (all >95% except RS slope algorithm with 94.24% on NSR database and 94.44% on ARR database). The OKB algorithm still reported the highest $F1$ result of 97.89% and 97.09% on both databases. For the Paced-rhythm ECG database, all ten algorithms were immune to the paced beats (>94%) except the RS slope method, which only output a low $F1$ result of 78.99% (green rhombus line). However, for the telehealth database, the detection accuracies had obvious decline when dealing with the dynamic telehealth ECG signals. All the other nine algorithms reported $F1$ result lower than 80% except the OKB algorithm with an $F1$ score of 80.43%. Sixth power algorithm gave the lowest $F1$ result of 74.08% (black triangle line).

In this study, all of the tests were implemented in MATLAB 2014a (The MathWorks, Inc., Natick, MA, USA) on Intel TM i5 CPU 3.30 GHz. Figure 2 also illustrates the histogram for the time costs. This time costs were from analyzing an ECG segment (i.e., 10 s ECG signals in this study) on the six ECG databases. All ten algorithms had high numerical efficiency (all <4 ms) except RS slope (mean: 94.07 ms, SD: 24.85 ms) and sixth power algorithms (mean: 8.25 ms, SD: 2.12 ms). OKB algorithm had the highest numerical efficiency (mean: 1.54 ms, SD: 0.15 ms).

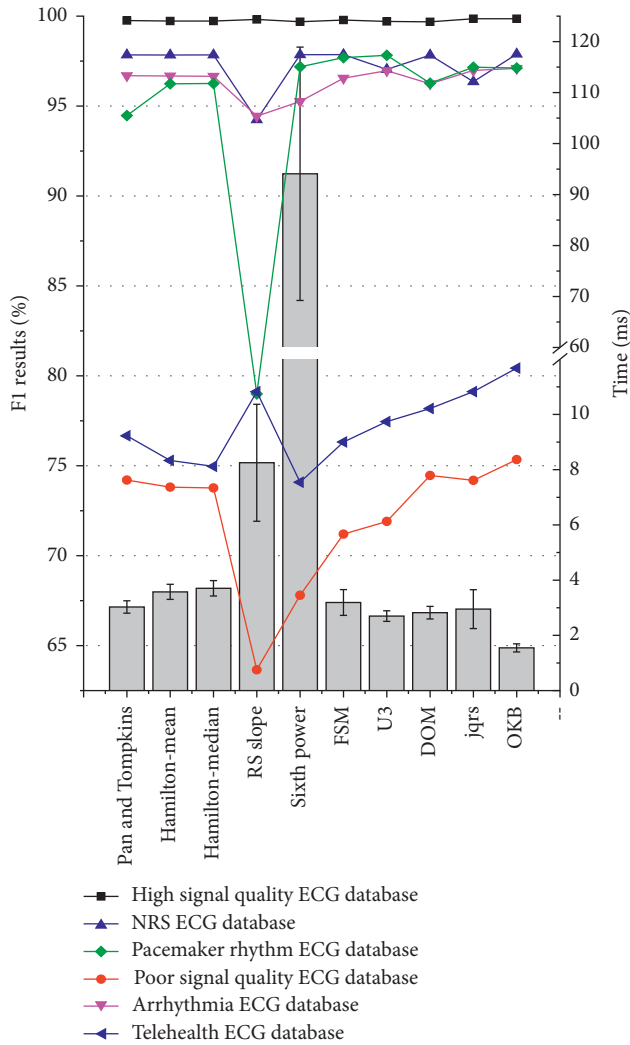


FIGURE 2: Line graph for $F1$ results and histogram for the average time costs.

4. Discussion

In this study, the performances of ten widely used QRS detection algorithms with low computational complexity were systematically evaluated on six ECG databases, with a special focus on the comparison between two opposite types or special application situations: high-quality ECG database versus low-quality ECG database, normal ECG database versus arrhythmic ECG database, paced rhythm ECG database, and dynamic telehealth ECG database. These ten widely used algorithms were reported as very efficient algorithms and suitable for mobile device situations.

QRS detection has been extensively studied for over 40 years. However, most QRS detectors focused on clean clinical ECG data which are collected using gelled adhesive electrodes applied in precise locations. To the authors' best knowledge, a few of these detectors have been tested by ECG data with poor signal quality. In the literature [9], Gary et al. analyzed the performances of nine different QRS detection algorithms on the ECG data corrupted with five different types of synthesized calibrated noise and reported that the

detection accuracies of these algorithms degraded with the noise level increasing. Xie et al. [32] and Khamis et al. [3] both reported that the performance of QRS detectors on the telehealth dynamic ECG database were poor if the detecting was carried without any preprocessing. The test results in this study also confirmed this case; that is, the detection accuracies of any detectors were not good for the ECG signal with poor signal quality and high noise level. How to settle this problem? In the literatures [3, 32], the artifact masking technology was used as a preprocessing step to avoid using noisy data in the calculation of means or thresholds during QRS detection. As reported, this technology highly improved the detection accuracies, but this did not remove the need for the QRS detector to be robust in the presence of some noise. In the PhysioNet/Computing in Cardiology Challenge 2014 [33], multimodal physiological signals were used to detect heart beats, which could improve the detection accuracy. In addition, the multilead ECG data fusion method [31, 34, 35] could be a promising method for QRS complex detection on the poor signal quality ECG database. In this paper, group A database included high and poor signal quality ECG databases. For the high signal quality ECG database, all ten QRS detection algorithms had high $F1$ (>99%), while the highest $F1$ result of poor signal quality database was only 75.35%.

ECG signals from different individuals show variability, and the variability is greater among healthy subjects and patients, especially for the patients with cardiac arrhythmia. Arrhythmia ECGs have different ECG patterns compared with the normal state. Different arrhythmia states, such as premature arrhythmias, ventricular arrhythmias, and conduction arrhythmias, present various ECG waveforms [37]. QRS detection is difficult because of the physiological variability of the QRS complexes. In addition, the irregular heart rate could increase the detection difficulty objectively [38]. However, the performances of ten algorithms tested in this paper did not decline significantly on the arrhythmias database. One possible reason was that the MIT-BIH arrhythmia database was widely used to evaluate QRS detection algorithms as it includes different shapes of arrhythmic QRS complexes and noise [3, 11, 15]. And some QRS detectors were optimized by this database [1]. In this study, all ten QRS detection algorithms had high $F1$ results for NSR and ARR databases (all >95% except RS slope algorithm with 94.24% on NSR database and 94.44% on ARR database). The OKB algorithm still reported the highest $F1$ result of 97.89% and 97.09% on both databases. In this algorithm, the optimized parameters were fixed through training on the MIT-BIH arrhythmia database using a rigorous brute-force search-based method.

The paced beat is another threat, especially for the algorithm based on slope and amplitude. However, in this study, only the performance of RS slope algorithm declined significantly unexpectedly. This algorithm distinguished the RS slope from other negative slopes based on the consistency of its amplitude and duration. In the paced ECG databases, there were many ventricular fusion beats including pacing irritation signal and QRS complex wave. The negative slope in the ventricular fusion beat was no longer prominent, as

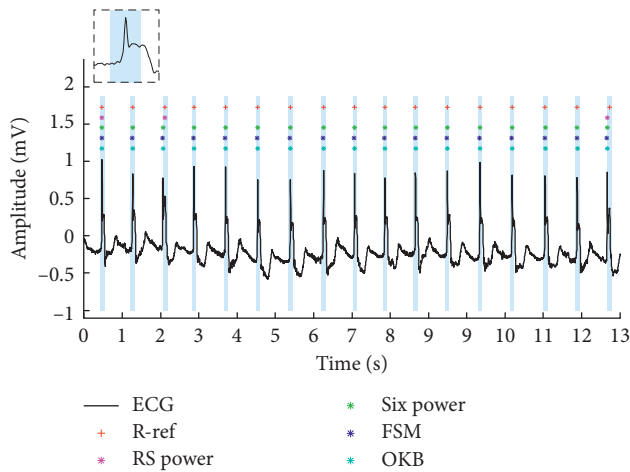


FIGURE 3: Example for the ventricular fusion beat.

shown in Figure 3. In the ventricular fusion beat, this consistency had been destroyed. Because of that the number of false negative of RS slope algorithm was extremely big (RS slope algorithm: 3045 and the second largest was only 773). Other nine algorithms were robust to the effect of paced beat. Seven of these methods (Pan and Tompkins-based three algorithms [11, 15], FSM [25], U3 [26], “jqrs” [28], and OKB [1] algorithms) regarded peak energy as the characteristic value by integration, square or six power operations. The discontinuous RS slope has little influence on the peak energy extract. U3 transform algorithm used a nonlinear transform in the time-domain based on the curve-length concept [39], which was not influenced by the RS slope deformation. In the DOM algorithm [2], positive and negative threshold detection could remove this fluctuation in the RS slope.

The current advances in battery-driven devices such as smartphones and tablet computers have made these technologies a necessary part of daily life, even in developing countries [40]. In this way, the telehealth dynamic ECG database was used as an application test in this study. This database was collected by dry electrodes using the TeleMedCare health monitor. In this database, average 25.67% (SD 22.78) of each recording was visually identified as artifact, which was typical of data recorded in an unsupervised setting [3]. The literature [3] reported the detection results of three QRS detectors. When no special treatment was applied, the overall Se of the Pan and Tompkins [15] and FSM [25] algorithms was less than 50% and +P was less than 66%, whereas the UNSW algorithm [3] has an overall Se of 97.88% and +P of 71.67%. In this paper, the UNSW algorithm was not selected because of its high complexity. For this database, all other nine algorithms in this paper reported *F1* result lower than 80% except that the OKB algorithm reported a *F1* score of 80.43%. And sixth power algorithm gave the lowest *F1* result of 74.08%.

With advances in computational power, the demand for numerical efficiency has decreased. However, this is still more the case when the ECG signals are collected and analyzed in hospitals, but not for the case of portable ECG

devices, which are battery-driven [41]. Currently, portable battery-operated systems such as mobile phones with wireless ECG sensors have the potential to be used in continuous cardiac function assessment that can be easily integrated into daily life. However, there is a significant trade-off as there will always be a power-consumption limitation in processing ECG signals on battery-operated devices [42]. Recently, researchers have put an increased effort into developing efficient ECG analysis algorithms to run with mobile phones. Elgendi et al. [6] and Sufi et al. [17] both reported that the derivative and threshold are an efficient combination for detecting QRS if developed properly. They categorized the QRS detectors as low, medium, or high in terms of its numerical efficiency, based on the number of iterations and the number of equations employed, but not analyzed quantitatively. This study reported the time costs of these ten efficient QRS detectors as the quantitative index of the computational complexity. Although all these ten algorithms were based on the combination of derivative and threshold, the time costs were variable. Sixth power algorithm (mean: 94.07 ms, SD: 24.85 ms) was most time consuming because of the K point determination by the minima of the standard deviation of enhanced data with a fixed size of 16 samples. RS slope algorithm (mean: 8.25 ms, SD: 2.12 ms) was the second time-consuming algorithm due to ten groups of duration parameters detection. OKB algorithm (mean: 1.54 ms, SD: 0.15 ms) was the most efficient algorithm. The time cost of the other seven algorithms was about 3 ms.

There are some limitations in this study. Firstly, it should be noted that there must be many other good QRS detectors with high algorithm efficiency, detection accuracy, and operability. Due to the limited time and our viewpoints, only ten QRS detectors were selected in this study. Secondly, because some algorithms were published in a theoretical way without online code [1, 25] and some literatures only include a few guidelines for real implementation and do not fully explain the necessary preprocessing operations [23, 26], some QRS algorithms were coded by ourselves. Therefore, the detection results in this study may be different from those in the other literatures, but these differences are slight. Thirdly, a unified signal filtering was performed before QRS detection for the fair comparisons among different QRS detection methods. Then the second filtering operation was performed based on the different filtering requirements of different algorithms. However, the effect of the double-filtering was unknown. At last, for ECG database with poor signal quality, the performances of all these ten QRS detectors in this study were not good. How to improve the detection results on these databases with much noise will be a research focus.

We have carefully checked and verified the databases and algorithms employed in this paper and ensured the results' reliability. We are responsible for all the risks.

5. Conclusion

In this study, a systematical evaluation work was performed on ten widely used QRS detection algorithms with low computational complexity in different application situations.

Four experiments were carried on six internationally recognized databases. For the clean clinical ECG signals including normal subjects and arrhythmia patients, most QRS detectors have higher detection accuracies, whereas all these algorithms are not suitable for the poor signal quality ECG signals with high noise level. Thus, some special treatment methods need to be done for such case. For some special situation, such as paced rhythm, the QRS detector needs to be selected carefully. Although the derivative and threshold are an efficient combination for detecting the QRS complex wave, the preprocessing and postprocessing also have an influence on the computing cost. Therefore, the QRS detection algorithms need to be developed properly for the mobile ECG and portable battery-operated systems.

In conclusion, we have systematically evaluated ten widely used QRS detection algorithms and verified their performances and usefulness in different application situations. These results could offer reference for reasonably employing these algorithms.

Data Availability

The data used to support the findings of this study are available from the corresponding author upon request.

Conflicts of Interest

The authors declare that there are no conflicts of interest to this work.

Authors' Contributions

Feifei Liu and Chengyu Liu drafted the manuscript. Feifei Liu, Chengyu Liu, Jianqing Li, and Shoushui Wei designed the study. All the authors contributed the data analysis and reviewed the manuscript.

Acknowledgments

This work was supported by the National Natural Science Foundation of China under Grant no. 61571113, the Key Research and Development Programs of Jiangsu Province under Grant no. BE2017735, and Shandong Provincial Natural Science Foundation in China under Grant no. ZR2014EEM003.

References

- [1] M. Elgendi, "Fast QRS detection with an optimized knowledge-based method: evaluation on 11 standard ECG databases," *PLoS One*, vol. 8, article e73557, 2013.
- [2] Y. C. Yeh and W. J. Wang, "QRS complexes detection for ECG signal: the difference operation method," *Computer Methods and Programs in Biomedicine*, vol. 91, no. 3, pp. 245–254, 2008.
- [3] H. Khamis, R. Weiss, Y. Xie, C. W. Chen, N. Lovell, and S. Redmond, "QRS detection algorithm for telehealth electrocardiogram recordings," *IEEE Transactions on Biomedical Engineering*, vol. 63, pp. 1377–1388, 2016.
- [4] O. Pahlm and L. Sörnmo, "Software QRS detection in ambulatory monitoring—a review," *Medical and Biological Engineering and Computing*, vol. 22, no. 4, pp. 289–297, 1984.
- [5] B. U. Kohler, C. Hennig, and R. Orglmeister, "The principles of software QRS detection," *IEEE Engineering in Medicine and Biology Magazine*, vol. 21, pp. 42–57, 2002.
- [6] M. Elgendi, B. Eskofier, S. Dokos, and D. Abbott, "Revisiting QRS detection methodologies for portable, wearable, battery-operated, and wireless ECG systems," *PLoS One*, vol. 9, article e84018, 2014.
- [7] G. B. Moody and R. G. Mark, "The impact of the MIT-BIH arrhythmia database," *IEEE Engineering in Medicine and Biology Magazine*, vol. 20, pp. 45–57, 2001.
- [8] J. P. Martinez, R. Almeida, S. Olmos, and A. P. Rocha, "A wavelet-based ECG delineator: evaluation on standard databases," *IEEE Transactions on Biomedical Engineering*, vol. 51, pp. 570–581, 2004.
- [9] G. M. Friesen, T. C. Jannett, M. A. Jadallah, S. L. Yates, S. R. Quint, and H. T. Nagle, "A comparison of the noise sensitivity of nine QRS detection algorithms," *IEEE Transactions on Biomedical Engineering*, vol. 37, pp. 85–98, 1990.
- [10] N. M. Arzeno, C. S. Poon, and Z. D. Deng, "Quantitative analysis of QRS detection algorithms based on the first derivative of the ECG," in *Proceedings of the 28th Annual International Conference of the IEEE Engineering in Medicine and Biology Society (EMBS'06)*, pp. 1788–1791, New York, NY, USA, August–September 2006.
- [11] P. S. Hamilton and W. J. Tompkins, "Quantitative investigation of QRS detection rules using the MIT/BIH arrhythmia database," *IEEE Transactions on Biomedical Engineering*, vol. 33, no. 12, pp. 1157–1165, 1986.
- [12] D. S. Benitez, P. A. Gaydecki, A. Zaidi, and A. P. Fitzpatrick, "A new QRS detection algorithm based on the Hilbert transform," in *Proceedings of the Computers in Cardiology 2000*, pp. 379–382, Cambridge, MA, USA, September 2000.
- [13] N. M. Arzeno, Z. D. Deng, and C. S. Poon, "Analysis of first-derivative based QRS detection algorithms," *IEEE Transactions on Biomedical Engineering*, vol. 55, pp. 478–484, 2008.
- [14] R. A. Álvarez, A. J. M. Penín, and X. A. V. Sobrino, "A comparison of three QRS detection algorithms over a public database," *Procedia Technology*, vol. 9, pp. 1159–1165, 2013.
- [15] J. Pan and W. J. Tompkins, "A real-time QRS detection algorithm," *IEEE Transactions on Biomedical Engineering*, vol. 32, no. 3, pp. 230–236, 1985.
- [16] A. Martínez, R. Alcaraz, and J. J. Rieta, "Application of the phasor transform for automatic delineation of single-lead ECG fiducial points," *Physiological Measurement*, vol. 31, pp. 1467–1485, 2010.
- [17] F. Sufi, Q. Fang, and I. Cosic, "ECG R-R peak detection on mobile phones," in *Proceedings of the 29th Annual International Conference of the IEEE Engineering in Medicine and Biology Society*, pp. 3697–3700, Lyon, France, August 2007.
- [18] S. J. Redmond, Y. Xie, D. Chang, J. Basilakis, and N. H. Lovell, "Electrocardiogram signal quality measures for unsupervised telehealth environments," *Physiological Measurement*, vol. 33, pp. 1517–1533, 2012.
- [19] D. Hayn, B. Jammerbund, and G. Schreier, "QRS detection based ECG quality assessment," *Physiological Measurement*, vol. 33, pp. 1449–1461, 2012.
- [20] G. Bianchi, *Electronic Filter Simulation and Design*, Amacom, New York, NY, USA, 2007.
- [21] P. Podziemski and J. Gieraltowski, "Fetal heart rate discovery: algorithm for detection of fetal heart rate from noisy,

- noninvasive fetal ECG recordings,” in *Proceedings of the Computing in Cardiology Conference (CinC 2013)*, pp. 333–336, Zaragoza, Spain, September 2013.
- [22] J. J. Gieraltowski, K. Ciuchcinski, I. Grzegorzczuk, and K. Kosna, “Heart rate variability discovery: algorithm for detection of heart rate from noisy, multimodal recordings,” in *Proceedings of the Computing in Cardiology 2014*, pp. 253–256, Cambridge, MA, USA, September 2014.
- [23] J. Gieraltowski, K. Ciuchcinski, I. Grzegorzczuk, K. Kosna, M. Solinski, and P. Podziemski, “RS slope detection algorithm for extraction of heart rate from noisy, multimodal recordings,” *Physiological Measurement*, vol. 36, no. 8, pp. 1743–1761, 2015.
- [24] A. K. Dohare, V. Kumar, and R. Kumar, “An efficient new method for the detection of QRS in electrocardiogram,” *Computers and Electrical Engineering*, vol. 40, no. 5, pp. 1717–1730, 2013.
- [25] R. Gutierrez-Rivas, J. Garcia, W. Marnane, and A. Hernandez, “Novel real-time low-complexity QRS complex detector based on adaptive thresholding,” *IEEE Sensors Journal*, vol. 15, no. 10, pp. 6036–6043, 2015.
- [26] M. Paoletti and C. Marchesi, “Discovering dangerous patterns in long-term ambulatory ECG recordings using a fast QRS detection algorithm and explorative data analysis,” *Computer Methods and Programs in Biomedicine*, vol. 82, no. 1, pp. 20–30, 2006.
- [27] T. D. Cooman, G. Goovaerts, C. Varon, D. Widjaja, T. Willemen, and S. V. Huffel, “Heart beat detection in multimodal data using automatic relevant signal detection,” *Physiological Measurement*, vol. 36, pp. 1691–1704, 2015.
- [28] J. Behar, J. Oster, and G. D. Clifford, “Non-invasive FECG extraction from a set of abdominal sensors,” in *Proceedings of the Computing in Cardiology Conference (CinC 2013)*, pp. 297–300, Zaragoza, Spain, September 2013.
- [29] J. Behar, J. Oster, and G. D. Clifford, “Combining and benchmarking methods of foetal ECG extraction without maternal or scalp electrode data,” *Physiological Measurement*, vol. 35, pp. 1569–1589, 2014.
- [30] A. E. Johnson, J. Behar, F. Andreotti, G. D. Clifford, and J. Oster, “Multimodal heart beat detection using signal quality indices,” *Physiological Measurement*, vol. 36, no. 8, pp. 1665–1667, 2015.
- [31] P. Laguna, R. Jan, and P. Caminal, “Automatic detection of wave boundaries in multilead ECG signals: validation with the CSE database,” *Computers and Biomedical Research*, vol. 27, no. 1, pp. 45–60, 1994.
- [32] Y. Xie, S. J. Redmond, J. Basilakis, and N. H. Lovell, “Effect of ECG quality measures on piecewise-linear trend detection for telehealth decision support systems,” in *Proceedings of the International Conference of the IEEE Engineering in Medicine and Biology*, pp. 2877–2880, Lyon, France, August 2010.
- [33] G. Moody, B. Moody, and I. Silva, “Robust detection of heart beats in multimodal data,” in *Proceedings of the PhysioNet/Computing in Cardiology Challenge 2014*, pp. 549–552, Cambridge, MA, USA, September 2014.
- [34] C. A. Ledezma, G. Perpiñan, E. Severeyn, and M. Altuve, “Data fusion for QRS complex detection in multi-lead electrocardiogram recordings,” in *Proceedings of the International Symposium on Medical Information Processing and Analysis*, Cuenca, Ecuador, November 2015.
- [35] S. Torbey, S. G. Akl, and D. P. Redfearn, “Multi-lead QRS detection using window pairs,” in *Proceedings of the International Conference of the IEEE Engineering in Medicine and Biology Society*, pp. 3143–3146, San Diego, California, USA, August–September 2012.
- [36] M. Llamedo Soria, J. P. Martinez, and P. Laguna, “A multilead wavelet-based ECG delineator based on the RMS signal,” in *Proceedings of the Computers in Cardiology 2006*, pp. 153–156, Valencia, Spain, September 2006.
- [37] K. M. Chang, “Arrhythmia ECG noise reduction by ensemble empirical mode decomposition,” *Sensors*, vol. 10, no. 6, pp. 6063–6080, 2010.
- [38] N. Sushma, T. D. Sunil, and M. Z. Kurian, “Implementation of QRS peak detector by morphological operation and ECG extraction method for arrhythmia detection,” *International Journal of Emerging Technology in Computer Science and Electronics*, vol. 14, no. 2, 2015.
- [39] M. Paoletti and C. Marchesi, “Model based signal characterisation for long-term personal monitoring,” in *Proceedings of the Computers in Cardiology 2001*, pp. 413–416, Rotterdam, Netherlands, 2001.
- [40] I. Silva, G. B. Moody, and L. Celi, “Improving the quality of ECGs collected using mobile phones,” in *Proceedings of the PhysioNet/Computing in Cardiology Challenge 2011*, pp. 273–276, Hangzhou, China, September 2011.
- [41] H. Kim, R. F. Yazicioglu, P. Merken, H. C. Van, and H. J. Yoo, “ECG signal compression and classification algorithm with quad level vector for ECG Holter system,” *IEEE Transactions on Information Technology in Biomedicine*, vol. 14, pp. 93–100, 2010.
- [42] P. C. Hii and W. Y. Chung, “A comprehensive ubiquitous healthcare solution on an Android™ mobile device,” *Sensors*, vol. 11, no. 7, pp. 6799–6815, 2011.

Research Article

A Study of the Effects of Daily Physical Activity on Memory and Attention Capacities in College Students

Dinh-Van Phan ^{1,2,3} Chien-Lung Chan ^{1,2} Ren-Hao Pan,^{1,2} Nan-Ping Yang ^{4,5}
Hsiu-Chen Hsu,^{1,2} Hsien-Wei Ting,^{1,6} and K. Robert Lai ⁷

¹Department of Information Management, Yuan Ze University, Taoyuan, Taiwan

²Innovation Center for Big Data and Digital Convergence, Yuan Ze University, Taoyuan, Taiwan

³University of Economics, The University of Danang, Danang, Vietnam

⁴Department of Surgery & Orthopedics, Keelung Hospital, Ministry of Health and Welfare, Keelung, Taiwan

⁵Faculty of Medicine, School of Medicine, National Yang-Ming University, Taipei, Taiwan

⁶Department of Neurosurgery, Taipei Hospital, Ministry of Health and Welfare, New Taipei City, Taiwan

⁷Department of Computer Science and Engineering, Yuan Ze University, Taoyuan, Taiwan

Correspondence should be addressed to Chien-Lung Chan; clchan@saturn.yzu.edu.tw

Received 11 October 2017; Revised 16 January 2018; Accepted 12 February 2018; Published 22 March 2018

Academic Editor: Yi Su

Copyright © 2018 Dinh-Van Phan et al. This is an open access article distributed under the Creative Commons Attribution License, which permits unrestricted use, distribution, and reproduction in any medium, provided the original work is properly cited.

This study evaluated the relationship between daily physical activity (DPA) and memory capacity, as well as the association between daily activity and attention capacity, in college students in Taiwan. Participants (mean age = 20.79) wore wearable trackers for 106 days in order to collect DPA. These data were analyzed in association with their memory and attention capacities, as assessed using the spatial span test (SST) and the trail making test (TMT). The study showed significant negative correlations between memory capacity, time spent on the attention test (TSAT), calories burnt, and very active time duration (VATD) on the day before testing ($r = -0.272$, $r = -0.176$, $r = 0.289$, $r = 0.254$, resp.) and during the week prior to testing ($r = -0.364$, $r = -0.395$, $r = 0.268$, $r = 0.241$, resp.). The calories burnt and the VATD per day thresholds, which at best discriminated between normal-to-good and low attention capacity, were ≥ 2283 calories day⁻¹, ≥ 20 minutes day⁻¹ of very high activity (VHA) on the day before testing, or $\geq 13,640$ calories week⁻¹, ≥ 76 minutes week⁻¹ of VHA during the week prior to testing. Findings indicated the short-term effects that VATD and calories burnt on the day before or during the week before testing significantly and negatively associated with memory and attention capacities of college students.

1. Introduction

Many studies have demonstrated that daily activity affects the physical and mental health of humans [1–6]. Therefore, from kindergarten to universities worldwide, physical education study or fitness events are held to improve student health and increase their learning efficiency. However, the search for strategies to improve health and increase study or work efficiency is laden with difficulties; there is a need to examine several, possibly interacting factors such as sex, age, environment, and living conditions, as well as examine historical data and investigate useful technologies.

Today, as quality of life has improved, people increasingly pay more attention to their personal health and personal development in order to enhance their life and improve their efficiency in terms of learning and work [7]. In conjunction, the development of mobile devices has also affected the lives of human beings. For example, special high-tech wearable equipment with sensors that can accurately collect information about human daily activity have increased in popularity and are now used widely. This has created an opportunity to study human activity more easily and accurately. The development of mobile technologies that utilize the Internet has brought people closer together; the

world is narrowing, and almost everywhere is now in communication range via a mobile phone or a smart watch. Consequently, people have become more sedentary [8], due to objective and subjective reasons. In light of the above-mentioned trends and observations, we explored the relationship between daily activity and memory capability, as well as daily activity and attention capacity, in college students using wrist-worn trackers.

2. Methods

The study involved 39 participants who were first-year college students in Taiwan (15 females, mean age 20.79 years, SD 1.03), each of whom voluntarily signed an agreement to join the study. The participants wore wrist-worn trackers over a period of 106 days (from March 10, 2016, to June 23, 2016) to collect daily activity data under free-living conditions. The trackers collected data and synchronized to the Cloud via a Bluetooth 4.0 connection to a computer or mobile phone. Daily activity data of all participants were collected automatically from the Cloud and stored in an Impala data system, and our assessment tool was developed using Java programming language and an API (application programming interface). We performed SST and TMT, twice per participant, to examine participants' memory capacity and attention capacity; these test batteries were repeated 14 times during the study period. The results of the tests were divided into two levels: low values (<25th percentile) and normal-to-high values (\geq 25th percentile). This study was approved by the Institutional Review Board (IRB) with IRB number TH-IRB-0015-0016.

The wrist-worn tracker used in this study was the Fitbit Charge HR™ device manufactured by Fitbit Inc. This device can track daily personal activity and measures variables such as heart rate, calories burnt, steps taken, distance travelled, floors climbed, physical active minutes, exercise, and sleep characteristics. It has PurePulse LED lights that reflect onto the skin to detect capillary expansion based on blood volume change in order to measure heart rate [9, 10]. Activities were divided into the following levels according to the physical activity level (PAL): sedentary activity ($1.0 \leq \text{PAL} < 1.4$), light activity ($1.4 \leq \text{PAL} < 1.6$), fair activity ($1.6 \leq \text{PAL} < 1.9$), and high activity ($1.9 \leq \text{PAL} < 2.5$) [11]. Moderate-to-vigorous physical activity (MVPA) consisted of fair and high activities. The rate of calories burnt at rest just to maintain vital body functions such as breathing, heartbeat, and brain activity was calculated as the basal metabolic rate. The daily physical data collected were adjusted by gender, age, height, and weight [11, 12]. Therefore, we did not need to adjust data on an individual basis in this study.

The attention capacity of the participants was evaluated using the TMT, which is one of the most popular neuropsychological tests. It can measure executive functions, such as visual search speed, scanning, mental flexibility, and speed of processing [13–16]. TMTs have been developed for use with computers and tablets, which have the advantages of simplicity, accuracy, and random transformation of positional repeatability measurement [17, 18]. A computerized version of TMT was also built for this study using Java

programming language to automatically collect results with high accuracy time (Figure 1).

The TMT consists of two parts. TMT-A requires participants to click sequentially connecting 25 consecutive digits from 1 to 25 (1, 2, ..., 25) displayed at random positions on the interface. TMT-B requires testers to click sequentially connecting alternate values between 13 numbers and 12 alphabet letters (A, B, ..., L) (e.g., 1, A, 2, B, 3, and C), which are also displayed at random positions on the interface. The test result was recorded as the time required to complete the test [13], this time spent on the attention test (TSAT) representing attention capacity; that is, the longer the time taken, the lower the attention capacity [19].

The SST was a computerized version provided by Cambridge Brain Sciences (<http://www.cambridgebrainsciences.com>). It consists of squares that light up on the interface, which are used to assess memory capacity. A participant sees squares lighting up and clicks the sequence in the same order. If the participants respond incorrectly, the previous level is presented. The test is terminated when the participant responds incorrectly three consecutive times. The memory capacity of the participant was calculated as the maximum number of squares to which the participant responded correctly [20, 21].

According to the recommendations of the manufacturer, the trackers used in this study should be recharged after several days and taken off while bathing or swimming, so the raw data need filtering before analysis. This study was based on heart rate data collected every five seconds by the trackers, and the filter conditions were as follows: (1) data were excluded if heart rate data at the same time were lacking; (2) if data had not been collected for at least 20 hours per day, the participant was excluded—fourteen memory and attention test data were continuously combined with daily activity data on the day before the test date and data collected during the week prior to the test date; (3) after combining the data, participants for whom fewer than four days of data were obtained were excluded. Finally, this study included two data groups for analysis: data obtained on the day before the test date ($N = 27$; 279 DPs) and data obtained during the week prior to the test date ($N = 15$; 125 DPs). This study focuses only on short-term physical activities associated with attention and memory capacity of college students. We tried to determine which activity precisely on one day before the test date will immediately associate with memory and attention capacity. Therefore, we analyzed the physical activities one day before the test date. Nevertheless, there could be a chance that participants altered their behaviors in the day immediately before the test date. Hence, we also analyzed physical activities during one week prior to the test date to eliminate this factor.

2.1. Statistical Analysis. The memory and attention test data (fourteen measurements—once per week) were combined with the DPA data obtained on the day before the test date and during the week prior to the test date; so the final data were measured repeatedly, but the number of measurements for each participant was different. Therefore, the PROC MIXED model (SAS 9.4 program) was applied in this study

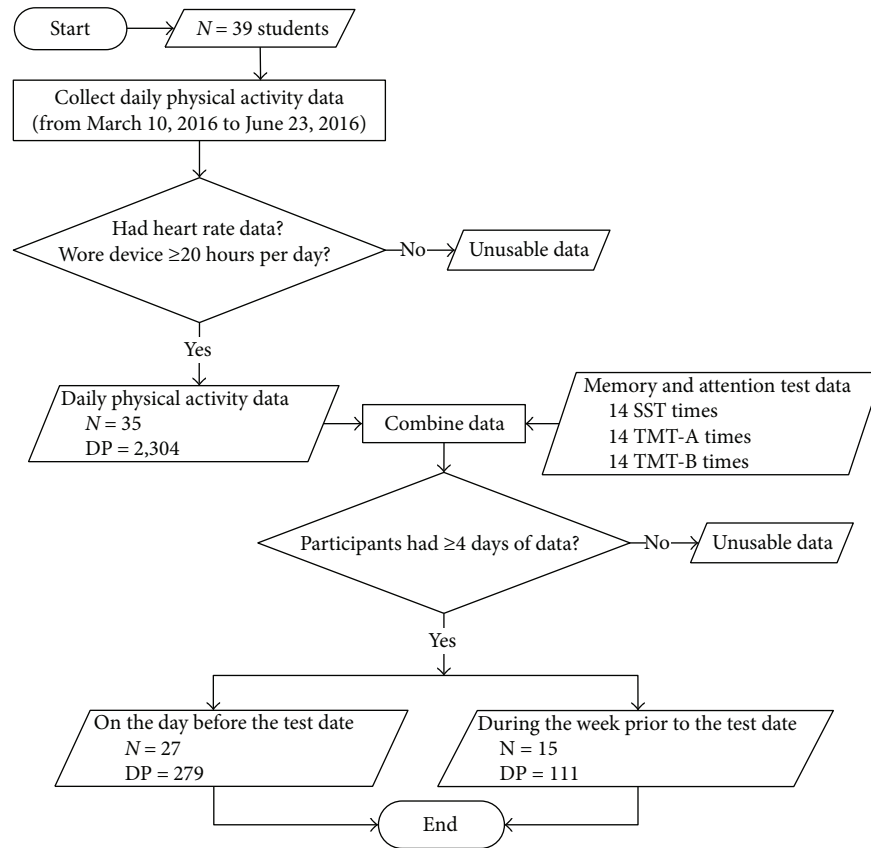


FIGURE 1: Study sample flowchart. DP: day-participant; SST: spatial span test; TMT: trail making test.

to analyze the correlations of DPA with memory and attention capacities [22–26]. This model is recommended for repeated measures and missing data [27]. The mixed model used the maximum likelihood (ML), DDFM = KR, and the TYPE = UN specifies a general variance-covariance matrix. The correlation coefficient was estimated by VCORR, and the bootstrap method was used to estimate 95% confidence intervals (CIs). This study also employed IBM SPSS Statistics Version 22 program to analyze quartile and descriptive statistics, in addition to the linear trend test. The receiver operating characteristic (ROC) was used to calculate the optimal cut-off points for calories burnt and the VATD based on optimizing the difference between sensitivity and specificity.

3. Results and Discussion

There were 33 participants in our study initially; however, during the period of the study, six more participants joined, and one participant dropped out. After the data were filtered, there remained 35 participants (89.74%) who wore a tracker for greater than or equal to 20 hours per day, which therefore accounted for 2304 day-participants (DPs). These data continuously combined fourteen memory and attention tests on the day before the test date, and every participant had data for more than or equal to four days. The final data consisted of 27 (16 male, 69.23%) participants (279 DPs). The daily activity data were combined with data obtained from fourteen memory and attention tests during the week before the

test date (who had at least seven days' data), and every participant had more than or equal to four days of data. The results represented 15 (10 male, 38.46%) participants in total (111 DPs). Table 1 shows the means (SDs) of DPA, memory capacity, and attention capacity on the day before the test date and during the week prior to the test date.

A mixed-model analysis showed a significant negative correlation between memory capacity and calories burnt on the day before the test date and during the week prior to the test date [$r = -0.272$ (95% CI: $-0.342, -0.160$), $r = -0.364$ (95% CI: $-0.476, -0.179$), resp.]. The analysis results also showed a significant negative correlation between memory capacity and the VATD on the day before the test date and during the week before the test date [$r = -0.176$ (95% CI: $-0.270, -0.079$), $r = -0.395$ (95% CI: $-0.524, -0.237$), resp.] (Table 2).

Regarding attention capacity, the analysis results showed a significant positive correlation between the TSAT and calories burnt (meaning that there existed a negative correlation between attention capacity and calories burnt) on the day before the test date and during the week prior to the test date [$r = 0.289$ (95% CI: $0.207, 0.366$), $r = 0.268$ (95% CI: $0.095, 0.361$), resp.]. The study results also demonstrated a significant positive correlation between the TSAT and the VATD (meaning that there was a negative correlation between the VATD and attention capacity) on the day before the test date and during the week prior to the test date [$r = 0.254$ (95% CI: $0.164, 0.351$), $r = 0.241$ (95% CI: $0.091,$

TABLE 1: Descriptive statistics of DPA, memory capacity, and attention capacity.

Measure		On the day before the test date	During the week before the test date
		<i>N</i> = 27 (Male = 16) DPs = 279 Mean (SD)	<i>N</i> = 15 (Male = 10) DPs = 111 Mean (SD)
Daily physical activity			
Calories	Calories	2347.27 (490.97)	16,435.97 (2920.77)
Steps	Steps	9084.68 (3467.87)	63,828.14 (21,894.72)
Distance	km	06.36 (02.45)	44.47 (15.54)
Floors	Floors	21.74 (13.96)	136.54 (68.24)
Elevation	Miles	65.74 (42.52)	412.97 (207.80)
Sedentary time duration	Minutes	795.42 (186.21)	5336.23 (759.71)
LATD	Minutes	168.80 (87.41)	1337.76 (411.19)
FATD	Minutes	22.25 (20.05)	176.52 (137.58)
VATD	Minutes	24.08 (22.75)	138.18 (109.42)
Memory and attention tests			
SST	Capability	07.04 (00.84)	07.05 (00.83)
TMT-A	Minutes	45.00 (10.58)	43.18 (11.03)
TMT-B	Minutes	56.59 (16.25)	53.13 (16.55)

DPs: day-participants; LATD: lightly active time duration; FATD: fairly active time duration; VATD: very active time duration; SST: spatial span test; TMT: trail making test.

0.405), resp.]. Additionally, MVPA on the day before the test date positively associated with the TSAT (and negatively associated with attention capacity), with $r = 0.198$ (95% CI: 0.090, 0.305) (Table 2).

Quartile analysis of physical activity also confirmed that a linear association existed between memory capacity and the TSAT and calories burnt, the VATD on the day before the test date (p for trend < 0.05) (Figure 2). A linear association also existed between memory capacity and the TSAT and calories burnt, the VATD during the week before the test date (p for trend < 0.05) (Figure 3).

Previous studies have indicated that daily moderate-to-vigorous physical activity (MVPA) positively affects the memory [28–30] and attention capacities of humans [31–34]. For example, higher academic performance is strongly and consistently related to a greater sedentary duration [35, 36]. Physical activity during the school day improves attention to tasks among elementary students [37, 38]. However, our study indicated that vigorous activity negatively associated with memory and attention capacities [39].

Galioto et al. studied 122 adults from the Longitudinal Assessment of Bariatric Surgery-2 parent project and identified weak correlations of self-reported aerobic physical activity with lower attention capacity ($r = -0.21$, $p = 0.04$) and execution capacity ($r = -0.27$, $p < 0.01$), and both self-reported aerobic physical activity and objectively determined MVPA min/week were negatively correlated with memory capacity ($r = -0.20$, $p = 0.04$; $r = -0.46$; $p = 0.02$, resp.) [40]. Indeed, our study of college students also showed that both the VATD on the day before the test date and the VATD during the week prior to the test date were negatively correlated with memory capacity [$r = -0.176$ (95% CI: -0.270 , -0.079), $r = -0.395$ (95% CI: -0.524 , -0.237), resp.], and both the

VATD on the day before the test date and the VATD during the week prior to the test date were positively correlated with the TSAT (and negatively correlated with attention capacity) [$r = 0.254$ (95% CI: 0.164, 0.351), $r = 0.241$ (95% CI: 0.091, 0.405), resp.].

A study of 74 children (mean age = 8.6 years, SD = 0.58, 46% girls) from 7 schools in East Central Illinois, US, from October 2013 to 2014 indicated no significant associations between MVPA and inhibition, working memory, or academic achievement [41]. Another study of 80 typically developing children (aged 8–12 years, 44 girls) in The Netherlands also demonstrated no significant associations between MVPA and visual memory span or TMT [42]. A study of the Healthy Lifestyle in Europe by Nutrition in Adolescence from 2006 to 2007 indicated that adolescents' attention capacity test performances were significantly and positively associated with a longer time spent performing moderate activity or MVPA under free-living conditions ($p < 0.05$). Promoting MVPA may have a beneficial effect on attention capacity. That study used the d2 test of attention to assess attention capacity prior to the participants (273 adolescents, aged 12.5–17.5 years) being monitored in terms of daily activity under free-living conditions using GT1M devices for 7 days, 8 hours per day [43]. However, our study assessed 39 students (mean age 20.79 years, SD = 1.03, 38.46% female) over a period of 106 days and filtered subjects for whom data were available ≥ 20 hours per day under free-living conditions for analysis; the participants were tested 14 times during this period, and every participant included in the final analysis had more than or equal to four days' worth of data. Our results showed that students' memory and attention capacities were significantly and negatively associated with a longer VATD and higher

TABLE 2: Correlation coefficients between DPA and the SST and TSAT.

Daily physical activity	On the day before the test date <i>N</i> = 279, <i>r</i> (95% CI)*		During the week before the test date <i>N</i> = 111, <i>r</i> (95% CI)*					
	SST	TMT-A	TMT-B	Mean of TMT	SST	TMT-A	TMT-B	Mean of TMT
Calories	-0.272 (-0.342, -0.160)	0.226 (0.136, 0.310)	0.288 (0.205, 0.358)	0.289 (0.207, 0.366)	-0.364 (-0.476, -0.179)	0.220 (0.038, 0.300)	0.270 (0.095, 0.373)	0.268 (0.095, 0.361)
Steps	-0.025 (-0.134, 0.078)	0.032 (-0.092, 0.155)	0.068 (-0.035, 0.170)	0.059 (-0.054, 0.168)	-0.041 (-0.226, 0.141)	-0.131 (-0.309, 0.041)	0.011 (-0.179, 0.210)	-0.050 (-0.239, 0.150)
Distance	-0.031 (-0.136, 0.077)	0.015 (-0.104, 0.137)	0.045 (-0.059, 0.151)	0.037 (-0.075, 0.149)	-0.098 (-0.252, 0.085)	-0.159 (-0.317, -0.011)	-0.040 (-0.205, 0.149)	-0.096 (-0.269, 0.077)
Floors	0.005 (-0.116, 0.113)	-0.082 (-0.186, 0.008)	-0.024 (-0.100, 0.056)	-0.051 (-0.130, 0.026)	0.111 (-0.033, 0.274)	-0.190 (-0.341, -0.053)	-0.049 (-0.189, 0.103)	-0.115 (-0.259, 0.028)
Elevation	0.005 (-0.117, 0.113)	-0.082 (-0.186, 0.009)	-0.024 (-0.100, 0.056)	-0.051 (-0.130, 0.026)	0.111 (-0.033, 0.274)	-0.190 (-0.341, -0.053)	-0.049 (-0.189, 0.102)	-0.115 (-0.259, 0.028)
Sedentary time duration	0.046 (-0.061, 0.150)	-0.038 (-0.137, 0.058)	-0.042 (-0.129, 0.043)	-0.044 (-0.135, 0.040)	-0.071 (-0.241, 0.094)	-0.078 (-0.222, 0.098)	-0.100 (-0.282, 0.051)	-0.098 (-0.265, 0.061)
LATD	-0.077 (-0.167, 0.019)	-0.073 (-0.161, 0.027)	-0.070 (-0.147, 0.014)	-0.077 (-0.154, 0.010)	-0.152 (-0.313, 0.041)	-0.208 (-0.369, -0.035)	-0.151 (-0.314, 0.052)	-0.190 (-0.359, 0.004)
FATD	0.062 (-0.059, 0.180)	0.059 (-0.059, 0.172)	0.051 (-0.079, 0.183)	0.059 (-0.068, 0.184)	0.092 (-0.044, 0.245)	-0.036 (-0.220, 0.142)	0.043 (-0.181, 0.298)	0.012 (-0.207, 0.252)
VATD	-0.176 (-0.270, -0.079)	0.222 (0.124, 0.327)	0.237 (0.146, 0.332)	0.254 (0.164, 0.351)	-0.395 (-0.524, -0.237)	0.188 (0.062, 0.332)	0.244 (0.081, 0.415)	0.241 (0.091, 0.405)
MVPA	-0.079 (-0.188, 0.031)	0.178 (0.069, 0.286)	0.183 (0.075, 0.290)	0.198 (0.090, 0.305)	-0.161 (-0.321, 0.020)	0.080 (-0.066, 0.231)	0.166 (-0.024, 0.381)	0.144 (-0.038, 0.343)

*95% CI: 95% bootstrap confident interval; SST: spatial span test; TMT: trail making test; Mean of TMT: mean of TMT-A and TMT-B; LATD: lightly active time duration; FATD: fairly active time duration; VATD: very active time duration; MVPA: moderate-to-vigorous physical activity.

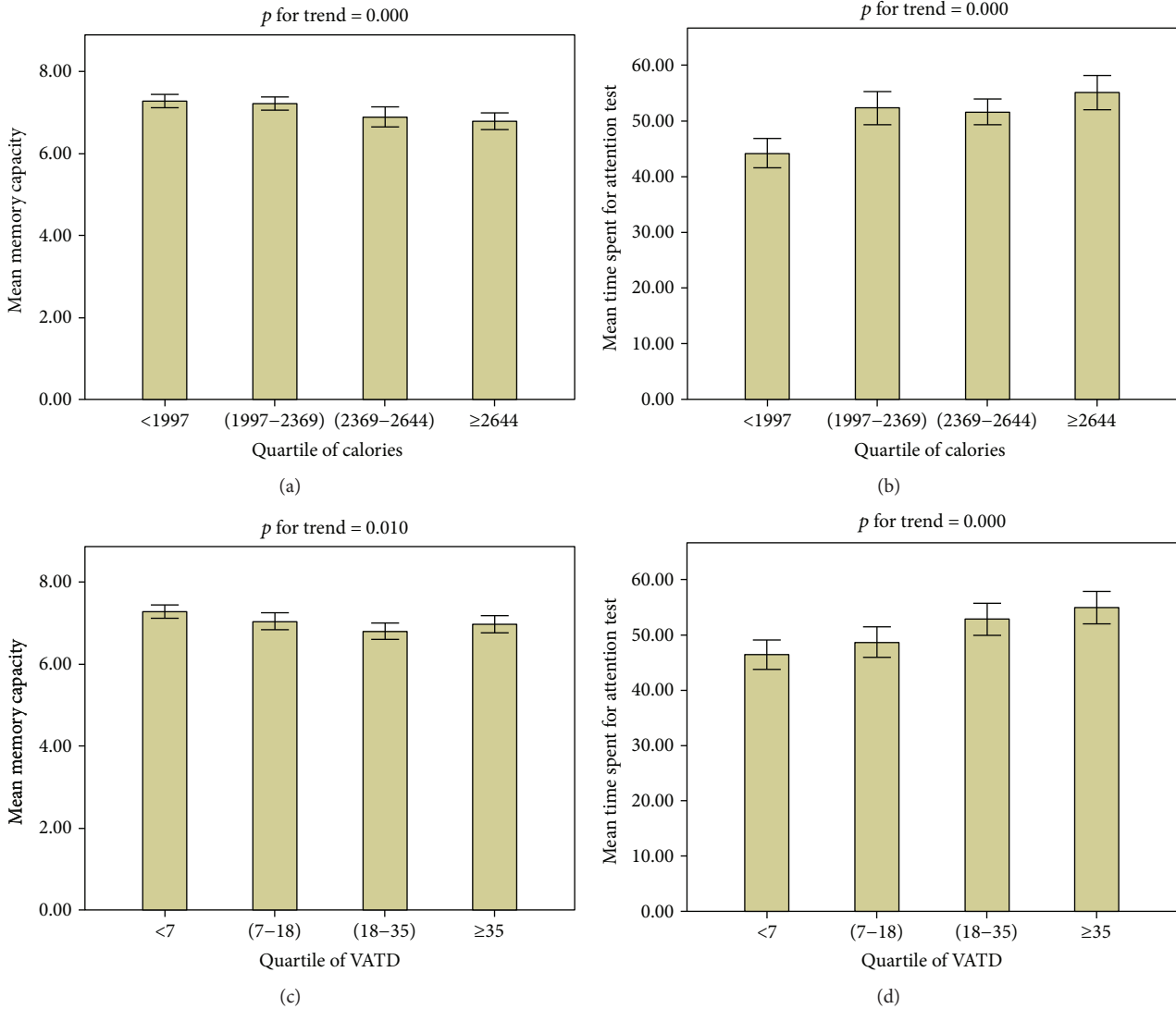


FIGURE 2: Mean of memory capacity and TSAT according to quartile of calories and the VATD on the day before the test date. (a) Memory capacity and calories, (b) TSAT and calories, (c) memory capacity and VATD, and (d) TSAT and VATD.

calories burnt. We also share the same view as Vanhelst et al. [43] in that increasing the VATD of students may lead to fatigue, and hence reduced cognitive functions such as memory and attention capacities. Therefore, moderate daily activity or light activity may improve memory and attention capacities [36, 37].

Vanhelst indicated that spending more than 58 minutes per day in MVPA was associated with a better attention capacity [43]. However, in the short term, our study found that more than 2283 calories burnt and more than 20 minutes of VATD on the day before the test, and 13,640 calories burnt and 76 minutes of VATD during the week prior to the test date, were associated with a poorer attention capacity (Table 3). This VATD cut-off point was consequently recommended by the American Heart Association, in that adults should spend at least 75 minutes per week participating in vigorous physical exercise [44]. The reported association between lower attention capacities in the short-term following vigorous activity might suggest that it was

due to fatigue [43]. A study of Davis and Bailey also indicated that fatigue during prolonged exercise obviously is influenced by central nervous system because prolonged exercise released ammonia into the blood that could alter central nervous system function [45]. Therefore, during the fatigue time, subjects may be less attentive and have less cognitive resources available to the individual concerned, and it requires additional time for recovery.

In this study, data were collected via wearable trackers in free-living conditions, and the advantage was continuous data collection without intrusion of subjects' daily lives. However, these data can be influenced by individual characteristics and external factors. For instance, physical activity level depends on demographic characteristics [46, 47]. Each participant may have different personal behavior and habit; therefore, personal physical activities are also different. The health of participants before the test such as sleepiness and napping also may affect their memory and attention capacities [48, 49] on which we had not tested before the test. In

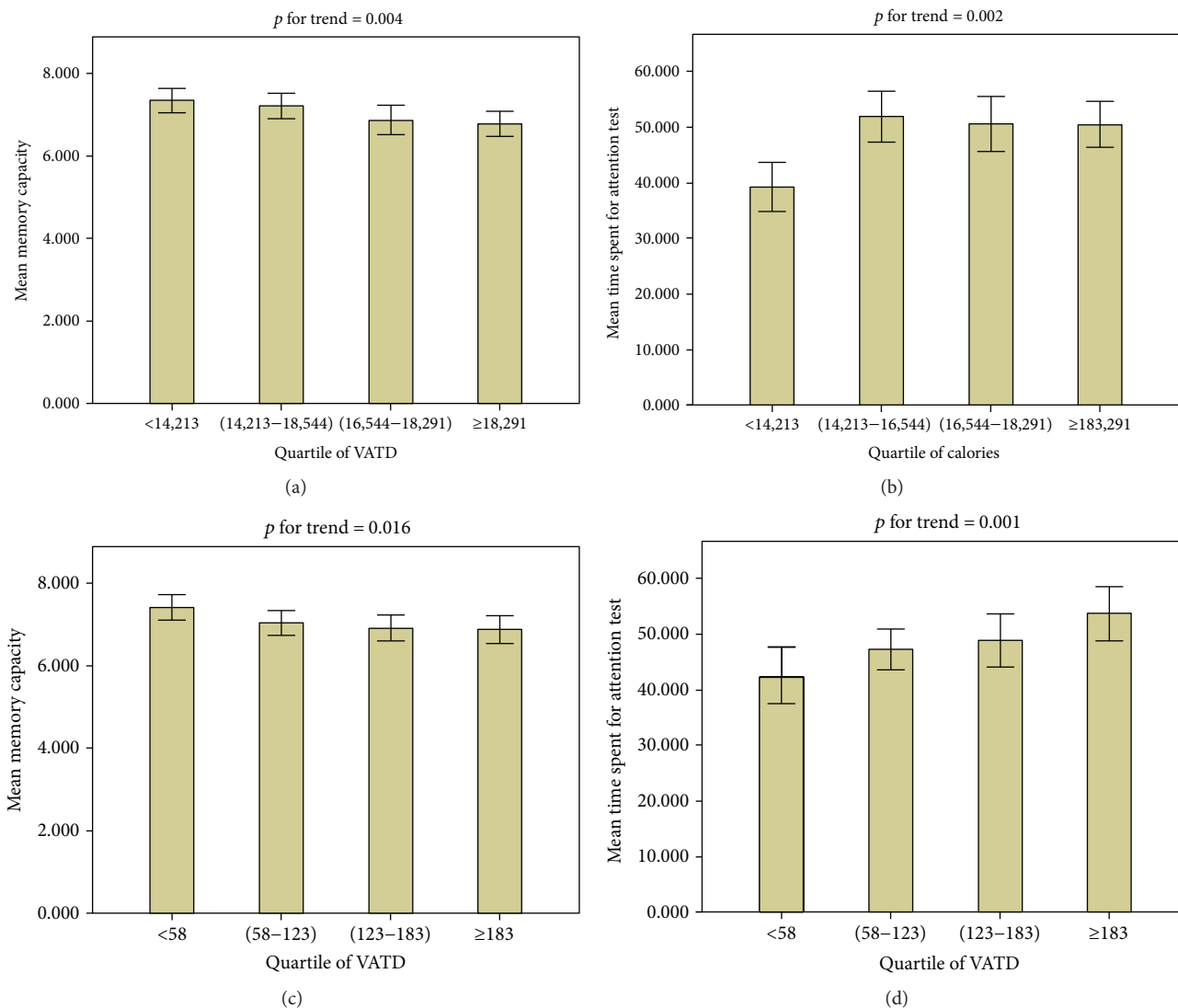


FIGURE 3: Mean of memory capacity and TSAT according to quartile of calories and VATD during the week prior to the test date. (a) Memory capacity and calories, (b) TSAT and calories, (c) memory capacity and VATD, and (d) TSAT and VATD.

TABLE 3: Physical activity cut-off points to predict good attention capacity according to the ROC.

	Unit/d	On the day before the test				p value	During the week before the test			
		SE	SP	AUC	Unit/d		SE	SP	AUC	p value
Calories burnt (calories)	2283	0.649	0.676	0.698	0.000	13,640	0.917	0.593	0.794	0.000
VATD (minutes)	20	0.540	0.765	0.662	0.000	76	0.798	0.667	0.791	0.000

Unit/d: unit per day; SE: sensitivity; SP: specificity; AUC: area under the receiver operating characteristic curve.

addition, the wearable trackers needed recharging after several days and taking off while participants were bathing and swimming.

It is likely that participants might have inadvertently altered their behavior while wearing the devices (as compared to the baseline when no such devices were being worn). These factors may influence the physical activity. However, this study indicated a convenient application based on wearable devices to monitor daily physical activities for getting memory and attention benefits.

4. Conclusions

Our exploratory study assessed the relationships between daily activity and memory capacity, and daily activity and the TSAT. Higher calories burnt or a greater VATD on the day before and during the week before a certain day is associated with a lower memory capacity and a lower attention capacity on that day. In addition, it was also found in this study that the calories burnt and the VATD on the day before (≥ 2283 calories, ≥ 20 minutes, resp.) and the calories burnt

and the VATD during the week before ($\geq 13,640$ calories, ≥ 76 minutes, resp.) a certain day were associated with a poorer attention capacity.

Our results were obtained from an exploratory study and not a random control trial, and hence, no comparisons were made between two independent groups. As the study was performed in a free-living environment, it was influenced by external factors and personal physiological characteristics of the participants. The findings have little supporting evidence, and few studies have been performed that produced the same results. Further studies will be designed as random control trials in order to compare two groups and control external impacting factors in a free-living environment.

Conflicts of Interest

The authors declare that they have no competing interests.

Authors' Contributions

Dinh-Van Phan, Chien-Lung Chan, and Ren-Hao Pan contributed equally to this work.

Acknowledgments

The authors acknowledge the financial support from the Ministry of Science and Technology, Taiwan (<http://www.most.gov.tw/>), MOST 104-3115-E-155-002 and MOST 105-2221-E-155-041-MY3.

References

- [1] I. Dore, J. L. O'Loughlin, G. Beauchamp, M. Martineau, and L. Fournier, "Volume and social context of physical activity in association with mental health, anxiety and depression among youth," *Preventive Medicine*, vol. 91, pp. 344–350, 2016.
- [2] E. Füzéki and W. Banzer, "Activities of daily living and health," *Public Health Forum*, vol. 21, no. 2, 2013.
- [3] N. Kondo, M. Kazama, K. Suzuki, and Z. Yamagata, "Impact of mental health on daily living activities of Japanese elderly," *Preventive Medicine*, vol. 46, no. 5, pp. 457–462, 2008.
- [4] K. A. Leger, S. T. Charles, J. Z. Ayanian, and D. M. Almeida, "The association of daily physical symptoms with future health," *Social Science & Medicine*, vol. 143, pp. 241–248, 2015.
- [5] J. Ohrnberger, E. Fichera, and M. Sutton, "The dynamics of physical and mental health in the older population," *The Journal of the Economics of Ageing*, vol. 9, pp. 52–62, 2017.
- [6] S. Gomes da Silva and R. M. Arida, "Physical activity and brain development," *Expert Review of Neurotherapeutics*, vol. 15, no. 9, pp. 1041–1051, 2015.
- [7] W. B. Strong, R. M. Malina, C. J. R. Blimkie et al., "Evidence based physical activity for school-age youth," *The Journal of Pediatrics*, vol. 146, no. 6, pp. 732–737, 2005.
- [8] J. E. Barkley and A. Lepp, "Mobile phone use among college students is a sedentary leisure behavior which may interfere with exercise," *Computers in Human Behavior*, vol. 56, pp. 29–33, 2016.
- [9] F. Inc, *How Does My Tracker Detect My Heart Rate?*, 2017, https://help.fitbit.com/articles/en_us/help_article/1565?q=heart-rate&l=en_US&fs=Search&pn=1#How.
- [10] R. F. Gardner, C. Voss, P. H. Dean, and K. C. Harris, "Validation of the Fitbit Charge Heart Rate™ device to monitor physical activity in children with congenital heart disease," *Canadian Journal of Cardiology*, vol. 32, no. 10, Supplement 1, p. S130, 2016.
- [11] S. Gerrior, W. Juan, and B. Peter, "An easy approach to calculating estimated energy requirements," *Preventing Chronic Disease*, vol. 3, no. 4, article A129, 2006.
- [12] Fitbit Inc, *How Does Fitbit Estimate How Many Calories I've Burned?*, 2017, https://help.fitbit.com/articles/en_US/Help_article/1381?q=calories&l=en_US&c=Products%3ACharge_HR&fs=Search&pn=1.
- [13] T. Tombaugh, "Trail making test A and B: normative data stratified by age and education," *Archives of Clinical Neuropsychology*, vol. 19, no. 2, pp. 203–214, 2004.
- [14] K. B. Kortte, M. D. Horner, and W. K. Windham, "The trail making test, part B: cognitive flexibility or ability to maintain set?," *Applied Neuropsychology*, vol. 9, no. 2, pp. 106–109, 2002.
- [15] J. A. Perianez, M. Rios-Lago, J. M. Rodriguez-Sanchez et al., "Trail making test in traumatic brain injury, schizophrenia, and normal ageing: sample comparisons and normative data," *Archives of Clinical Neuropsychology*, vol. 22, no. 4, pp. 433–447, 2007.
- [16] R. M. Reitan and D. Wolfson, "The trail making test as an initial screening procedure for neuropsychological impairment in older children," *Archives of Clinical Neuropsychology*, vol. 19, no. 2, pp. 281–288, 2004.
- [17] M. Kubo, C. Shoshi, T. Kitawaki et al., "Increase in prefrontal cortex blood flow during the computer version trail making test," *Neuropsychobiology*, vol. 58, no. 3–4, pp. 200–210, 2009.
- [18] T. Nakahachi, R. Ishii, M. Iwase et al., "Frontal cortex activation associated with speeded processing of visuospatial working memory revealed by multichannel near-infrared spectroscopy during advanced trail making test performance," *Behavioural Brain Research*, vol. 215, no. 1, pp. 21–27, 2010.
- [19] D. T. Stuss and B. Levine, "Adult clinical neuropsychology: lessons from studies of the frontal lobes," *Annual Review of Psychology*, vol. 53, no. 1, pp. 401–433, 2002.
- [20] R. A. A. Teixeira, E. C. Zachi, D. T. Roque, A. Taub, and D. F. Ventura, "Memory span measured by the spatial span tests of the Cambridge Neuropsychological Test Automated Battery in a group of Brazilian children and adolescents," *Dementia & Neuropsychologia*, vol. 5, no. 2, pp. 129–134, 2011.
- [21] M. Luciana and C. A. Nelson, "Assessment of neuropsychological function through use of the Cambridge Neuropsychological Testing Automated Battery: performance in 4- to 12-year-old children," *Developmental Neuropsychology*, vol. 22, no. 3, pp. 595–624, 2002.
- [22] J. M. Bland and D. G. Altman, "Correlation, regression, and repeated data," *BMJ*, vol. 308, no. 6933, pp. 896–896, 1994.
- [23] J. M. Bland and D. G. Altman, "Calculating correlation coefficients with repeated observations: part 2—correlation between subjects," *BMJ*, vol. 310, no. 6980, p. 633, 1995.
- [24] J. M. Bland and D. G. Altman, "Statistics notes: calculating correlation coefficients with repeated observations: part 1—correlation within subjects," *BMJ*, vol. 310, no. 6977, p. 446, 1995.
- [25] A. Hamlett, "On the use of PROC MIXED to estimate correlation in the presence of repeated measures," in *Proceedings of the Twenty-Ninth Annual SAS Users Group International Conference*, pp. 198–129, SAS Institute Inc., Cary NC USA, 2004.

- [26] A. Hamlett, L. Ryan, P. Serrano-Trespacios, and R. Wolfinger, "Mixed models for assessing correlation in the presence of replication," *Journal of the Air & Waste Management Association*, vol. 53, no. 4, pp. 442–450, 2003.
- [27] M. G. Kenward and J. H. Roger, "Small sample inference for fixed effects from restricted maximum likelihood," *Biometrics*, vol. 53, no. 3, pp. 983–997, 1997.
- [28] F. Candela, G. Zucchetti, D. Magistro, and E. Rabaglietti, "The effects of a physical activity program and a cognitive training program on the long-term memory and selective attention of older adults: a comparative study," *Activities, Adaptation & Aging*, vol. 39, no. 1, pp. 77–91, 2015.
- [29] G. W. Rebok and D. J. Plude, "Relation of physical activity to memory functioning in older adults: the memory workout program," *Educational Gerontology*, vol. 27, no. 3-4, pp. 241–259, 2001.
- [30] J. M. Bugg, E. L. DeLosh, and B. A. Clegg, "Physical activity moderates time-of-day differences in older adults' working memory performance," *Experimental Aging Research*, vol. 32, no. 4, pp. 431–446, 2006.
- [31] M. Felez-Nobrega, C. H. Hillman, E. Cirera, and A. Puig-Ribera, "The association of context-specific sitting time and physical activity intensity to working memory capacity and academic achievement in young adults," *European Journal of Public Health*, vol. 27, no. 4, pp. 741–746, 2017.
- [32] Y. K. Chang, S. Liu, H. H. Yu, and Y. H. Lee, "Effect of acute exercise on executive function in children with attention deficit hyperactivity disorder," *Archives of Clinical Neuropsychology*, vol. 27, no. 2, pp. 225–237, 2012.
- [33] J. W. Li, H. O'Connor, N. O'Dwyer, and R. Orr, "The effect of acute and chronic exercise on cognitive function and academic performance in adolescents: a systematic review," *Journal of Science and Medicine in Sport*, vol. 20, no. 9, pp. 841–848, 2017.
- [34] P. J. Smith, J. A. Blumenthal, B. M. Hoffman et al., "Aerobic exercise and neurocognitive performance: a meta-analytic review of randomized controlled trials," *Psychosomatic Medicine*, vol. 72, no. 3, pp. 239–252, 2010.
- [35] C. Maher, L. Lewis, P. T. Katzmarzyk, D. Dumuid, L. Cassidy, and T. Olds, "The associations between physical activity, sedentary behaviour and academic performance," *Journal of Science and Medicine in Sport*, vol. 19, no. 12, pp. 1004–1009, 2016.
- [36] J. Kerr, S. J. Marshall, R. E. Patterson et al., "Objectively measured physical activity is related to cognitive function in older adults," *Journal of the American Geriatrics Society*, vol. 61, no. 11, pp. 1927–1931, 2013.
- [37] M. T. Mahar, "Impact of short bouts of physical activity on attention-to-task in elementary school children," *Preventive Medicine*, vol. 52, Supplement 1, pp. S60–S64, 2011.
- [38] T. M. Altenburg, M. J. Chinapaw, and A. S. Singh, "Effects of one versus two bouts of moderate intensity physical activity on selective attention during a school morning in Dutch primary schoolchildren: a randomized controlled trial," *Journal of Science and Medicine in Sport*, vol. 19, no. 10, pp. 820–824, 2016.
- [39] J. Wilbur, D. X. Marquez, L. Fogg et al., "The relationship between physical activity and cognition in older Latinos," *The Journals of Gerontology Series B: Psychological Sciences and Social Sciences*, vol. 67, no. 5, pp. 525–534, 2012.
- [40] R. Galioto, W. C. King, D. S. Bond et al., "Physical activity and cognitive function in bariatric surgery candidates," *International Journal of Neuroscience*, vol. 124, no. 12, pp. 912–918, 2014.
- [41] D. M. Pindus, E. S. Drollette, M. R. Scudder et al., "Moderate-to-vigorous physical activity, indices of cognitive control, and academic achievement in preadolescents," *The Journal of Pediatrics*, vol. 173, pp. 136–142, 2016.
- [42] A. G. van der Niet, J. Smith, E. J. A. Scherder, J. Oosterlaan, E. Hartman, and C. Visscher, "Associations between daily physical activity and executive functioning in primary school-aged children," *Journal of Science and Medicine in Sport*, vol. 18, no. 6, pp. 673–677, 2015.
- [43] J. Vanhelst, L. Béghin, A. Duhamel et al., "Physical activity is associated with attention capacity in adolescents," *The Journal of Pediatrics*, vol. 168, pp. 126–131.e2, 2016.
- [44] American Heart Association, *American Heart Association Recommendations for Physical Activity in Adults*, 2014, http://www.heart.org/HEARTORG/HealthyLiving/PhysicalActivity/FitnessBasics/American-Heart-Association-Recommendations-for-Physical-Activity-in-Adults_UCM_307976_Article.jsp#.WTefQB82s2w.
- [45] J. M. Davis and S. P. Bailey, "Possible mechanisms of central nervous system fatigue during exercise," *Medicine & Science in Sports & Exercise*, vol. 29, no. 1, pp. 45–57, 1997.
- [46] A. P. Hills, N. Mokhtar, and N. M. Byrne, "Assessment of physical activity and energy expenditure: an overview of objective measures," *Frontiers in Nutrition*, vol. 1, p. 5, 2014.
- [47] S. M. Mohnen, B. Völker, H. Flap, and P. P. Groenewegen, "Health-related behavior as a mechanism behind the relationship between neighborhood social capital and individual health—a multilevel analysis," *BMC Public Health*, vol. 12, no. 1, p. 116, 2012.
- [48] H. Lau, M. A. Tucker, and W. Fishbein, "Daytime napping: effects on human direct associative and relational memory," *Neurobiology of Learning and Memory*, vol. 93, no. 4, pp. 554–560, 2010.
- [49] F. J. van Schalkwijk, C. Sauter, K. Hoedlmoser et al., "The effect of daytime napping and full-night sleep on the consolidation of declarative and procedural information," *Journal of Sleep Research*, 2017.

Research Article

A Novel Neural Network Model for Blood Pressure Estimation Using Photoplethysmography without Electrocardiogram

Ludi Wang ¹, Wei Zhou,² Ying Xing ¹ and Xiaoguang Zhou ¹

¹Automation School, Beijing University of Posts and Telecommunications, Beijing 100876, China

²Functional Pharmacology, Department of Neuroscience, Uppsala University, Uppsala, Sweden

Correspondence should be addressed to Xiaoguang Zhou; zxg_bupt@126.com

Received 10 August 2017; Revised 7 November 2017; Accepted 28 November 2017; Published 7 March 2018

Academic Editor: Chengyu Liu

Copyright © 2018 Ludi Wang et al. This is an open access article distributed under the Creative Commons Attribution License, which permits unrestricted use, distribution, and reproduction in any medium, provided the original work is properly cited.

The prevention, evaluation, and treatment of hypertension have attracted increasing attention in recent years. As photoplethysmography (PPG) technology has been widely applied to wearable sensors, the noninvasive estimation of blood pressure (BP) using the PPG method has received considerable interest. In this paper, a method for estimating systolic and diastolic BP based only on a PPG signal is developed. The multitaper method (MTM) is used for feature extraction, and an artificial neural network (ANN) is used for estimation. Compared with previous approaches, the proposed method obtains better accuracy; the mean absolute error is 4.02 ± 2.79 mmHg for systolic BP and 2.27 ± 1.82 mmHg for diastolic BP.

1. Introduction

Blood pressure (BP) is the driving force for the flow of blood through the blood vessels and reflects the cardiovascular health of the human body. At present, hypertension is the most significant risk factor for cardiovascular and cerebrovascular diseases, identified by the World Health Organization [1] as the main cause of death and disability among the elderly. Poorly controlled hypertension increases the risk of heart attacks, strokes, kidney failure, and heart failure.

Table 1 lists the classification criteria for hypertension in adults (age > 18 years). A normal BP for an adult human is 120/80 mmHg. A systolic blood pressure (SBP) of between 140 and 159 mmHg or diastolic blood pressure (DBP) of between 90 and 99 mmHg is defined as the first stage of hypertension, while the second stage is when SBP is higher than 159 mmHg, or DBP is higher than 99 mmHg [2].

Invasive BP measurement has the highest accuracy of several methods available for measuring BP, but it is not widely applied because of its difficulty and high risk. Using Korotkoff sounds to estimate SBP and DBP is another auscultatory measurement, and this has been widely accepted as the gold standard [3, 4]. Despite its high degree of accuracy and reliability, the auscultatory method does not apply to

home blood pressure measurement (HBPM) [5], as it requires a trained professional [6]. Furthermore, the mercury sphygmomanometer is gradually being removed from clinical use [6]. Oscillometric blood pressure measurement has become increasingly popular in automated blood pressure measurement devices [7]. This method uses an electronic pressure sensor to observe the pressure oscillation in the cuff, during its gradual deflation from above SBP to below DBP. The oscillation amplitude increases to its maximum value when the cuff pressure reaches the mean arterial pressure and then gradually decreases with subsequent deflation of the cuff pressure [8]. However, it cannot provide continuous beat-to-beat BP measurement with its periodic features, and it is not appropriate for home healthcare or easing the workload of clinicians at hospitals.

For cuffless BP measurement, the pulse transit time (PTT) method and photoplethysmography (PPG) are widely used techniques [9]. PTT is defined as the time taken for the arterial pulse pressure wave to travel from the aortic valve to the periphery [10], and some researchers have used it to estimate BP indirectly [11]. However, there are two parameters required to calculate PTT, electrocardiogram (ECG), and PPG. As a result, calculation of PPT commonly requires two devices to obtain these two parameters—the ECG is

measured at the wrist or chest, and the PPG is measured from the index finger [12].

Wearable pulse rate sensors based on PPG have become increasingly popular, with more than ten companies producing these sensors commercially [13]. To take advantage of this technology, some researchers have experimented with using only a single PPG waveform for estimating BP. A continuous PPG waveform and one single PPG waveform extracted from it are shown in Figure 1. Shin et al. [14] presented a pressure index (PI) extracted from a single PPG signal to estimate BP. Teng et al. [15] extracted four features of PPG signals to find an optimal feature for BP estimation: width of 2/3 pulse amplitude, width of 1/2 pulse amplitude, systolic upstroke time, and diastolic time. This method established a linear regression model and found that systolic upstroke time and diastolic upstroke time from the PPG wave have higher correlations with BP. However, tests show that such a correlation is not always linear. Gao et al. [16] developed a method for BP estimation using the regression support vector machine (RSVM) method, with RBF kernel and discrete wavelet transform, and obtained better performance.

In this paper, a new approach for beat-to-beat BP estimation based on artificial neural networks (ANNs) is presented. Yi et al. [17] have proved that for BP estimation, ANNs have better performance compared to regression analysis using PTT. The presented method uses a multitaper method (MTM) [18] to obtain the spectral components and combines them with two morphological features of a PPG signal, to constitute the input parameters. For wide representation of possible PPG signal and correspondent beat-to-beat BP, we extract the signal from the Multiparameter Intelligent Monitoring in Intensive Care (MIMIC) database [19, 20] for network training and testing. The results show that the presented method achieves better performance using only the PPG signal. Figure 2 shows the schematic illustration of presented BP estimation frameworks.

The paper is organized as follows: Section 2 describes the overview of the MIMIC database, Section 3 explains the features extracted from a PPG signal and the presentation of the architecture of the ANN, and Section 4 shows the results using different methods. Finally, the conclusion summarizes the paper proposal and briefly anticipates future work.

2. Data Description

The MIMIC database is a collection of multiparameter recordings from over 90 ICU patients. The data in each case includes signals and periodic measurements obtained from a bedside monitor, as well as clinical data obtained from the patient's medical record. The recordings vary in length; almost all of them are at least 20 hours, and many are 40 hours or more. In total, the database contains nearly 200 patient-days of real-time signals and accompanying data [21].

The database contains data of ECG (leads I, III, and V), ABP, PAP, PPG, and respiratory signals recorded simultaneously with a 125 Hz sampling rate. In this paper, only the

TABLE 1: Classification of hypertension in adults (age > 18 years).

Blood pressure classification	BP (mmHg)	
	Systolic	Diastolic
Normal	<120	And <80
Prehypertension	120–139	Or 80–89
Stage 1 hypertension	140–159	Or 90–99
Stage 2 hypertension	≥160	Or ≥100

records with both ABP and PPG were extracted. Figure 3 shows an example record.

In total, there are 58,795 valid intervals of PPG signal (subject number is 72) and corresponding BP values for different people and different time instances. In order to avoid overfitting, we use 70% of them for network training, 15% of them for validation, and 15% of them for testing. The training dataset is presented to the network during training, and the network is adjusted according to its error. The validation dataset is used to measure network generalization and to halt training when generalization stops improving. The test dataset has no effect on training and so provides an independent measure of network performance during and after training. The Levenberg-Marquardt algorithm was chosen for training the ANN. In this algorithm, training automatically stops when generalization stops improving, as indicated by an increase in the mean square error of the validation samples.

3. ANN-Based BP Estimation

3.1. Multitaper Method. The multitaper method (MTM) [22] takes advantage of an extended version of the spectral representation as follows:

$$x_t = \int_{-1/2}^{1/2} e^{-i\omega t} dz(t). \quad (1)$$

In this case, the x_t may contain a number of periodic components in addition to the underlying stationary process as follows:

$$x_t = \sum_j C_j \cos(\omega_j t + \phi_j) + \xi_t = \sum_j \mu_j e^{i\omega_j t} + \mu_j^* e^{-i\omega_j t} + \xi_t, \quad (2)$$

where ξ_t is a zero-mean stationary process with $S(f)$ not necessarily constant [18]. The above types of processes, called central stationary or conditional stationary processes, are often referred to as having mixed spectra [23]. For these processes, the expected value of the discrete orthogonal increment process $dZ(f)$ is no longer zero and can be calculated as follows:

$$E\{dZ(f)\} = \sum_j \mu_j \delta(f - f_j) df, \quad (3)$$

where δ is the Dirac delta function. The second central moment of $dZ(f)$ can be obtained as follows:

$$E\{|dZ(f) - E\{dZ(f)\}\|^2\} = S(f) df. \quad (4)$$

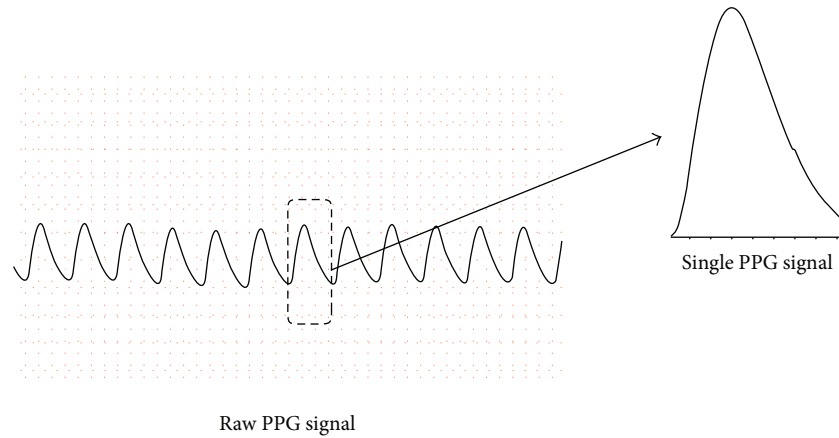


FIGURE 1: The continuous PPG waveform and one single PPG waveform extracted from it.

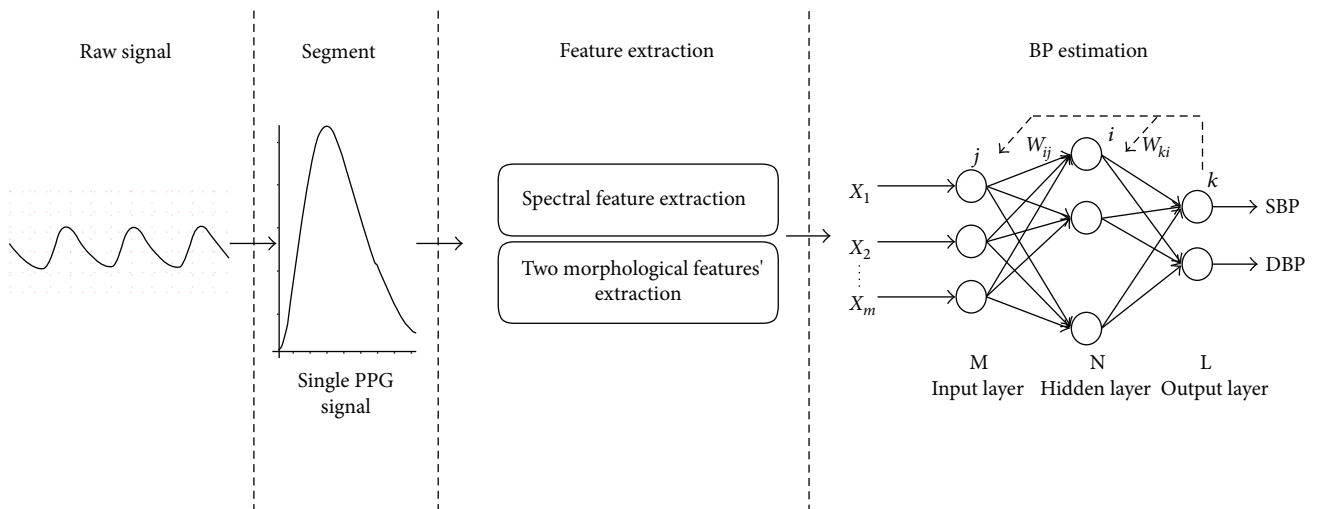


FIGURE 2: Schematic illustration of presented BP estimation frameworks.

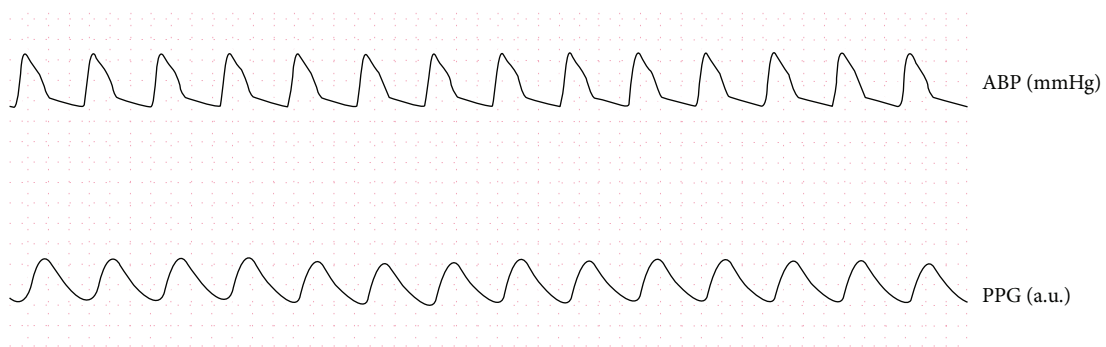


FIGURE 3: An example record.

For processes with mixed spectra, the first moment of $dZ(f)$ gives the deterministic component, while the second central moment of $dZ(f)$ gives the continuous nondeterministic component. The classical method has been centered on the estimation of the second moment of $dZ(f)$, which gives the continuous component of the spectrum. However, the estimation of the first moment of $dZ(f)$ was initially also required. Major opposition to the classical method is

predicated on the fact that there is no separation between the deterministic component and nondeterministic component; spurious peaks in the spectrum can be identified as the deterministic component without an objective criterion for differentiating between real and spurious lines [24].

In the MTM spectral estimation, a useful, yet simple, likelihood ratio test for the significance of periodic components is offered by the multiwindow method. This method

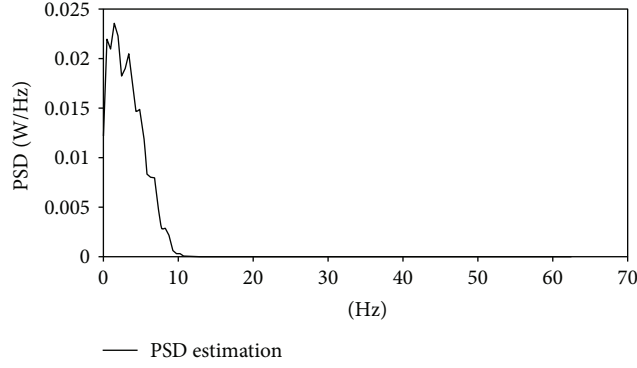


FIGURE 4: Frequency of single PPG signal.

TABLE 2: Performance results of different number of the input parameters.

Number of the input parameters	SBP		DBP	
	e (mmHg)	e_r (%)	e (mmHg)	e_r (%)
3 parameters (10 Hz interval)	8.29 ± 6.60	6.00 ± 5.28	6.19 ± 6.63	9.14 ± 7.45
4 parameters (5 Hz interval)	7.62 ± 6.08	5.49 ± 4.77	4.31 ± 3.83	3.84 ± 3.39
7 parameters (2 Hz interval)	6.59 ± 5.25	4.72 ± 4.02	4.34 ± 5.23	4.72 ± 3.91
12 parameters (1 Hz interval)	4.64 ± 3.63	3.42 ± 2.61	3.69 ± 2.74	3.12 ± 4.11
22 parameters (0.5 Hz interval)	4.02 ± 2.79	2.84 ± 2.00	2.27 ± 1.82	4.39 ± 3.60

makes use of multiple data windows, referred to as ‘‘Slepian sequences’’ and ‘‘discrete prolate spheroidal sequences.’’ They are defined as follows:

$$\lambda_k v_n^{(k)}(N, W) = \sum_{m=0}^{N-1} \frac{\sin\{2\pi W(n-m)\}}{\pi(n-m)} v_m^{(k)}(N, W), \quad (5)$$

where N is the number of sampling points of a single PPG wave (the sampling rate is 125 Hz), W is the spectral bandwidth, and λ_k are the eigenvalues associated with the Slepian sequences $v_n^{(k)}(N, W)$, which can be calculated numerically [25]. After Fourier transformation, the Slepian functions can be calculated as follows:

$$v_k(f) = \sum_{n=0}^{N-1} v_n^{(k)}(N, W) e^{-i2\pi f n}. \quad (6)$$

In the interval $(f - W, f + W)$, the energy concentration of the above Slepian functions is maximum. Furthermore, the bias from all frequencies is remote from the frequency of the window width times the number of observations, and thus the use of these sequences is very effective in eliminating window leakage [26].

The MTM calculates the expansion or eigen coefficients of input X_t as a first step as follows:

$$y_k(f) = \sum_{t=0}^{N-1} x_t v_t^{(k)}(N, W) e^{-i2\pi f t}. \quad (7)$$

Combining the above equations, the expected value of $y_k(f)$ can be obtained as follows:

$$E\{y_k(f)\} = \mu V_k(f - f_0) + \mu^* V_k(f + f_0). \quad (8)$$

At $f = f_0$,

$$E\{y_k(f_0)\} = \mu V_k(0) + \mu^* V_k(2f_0) \approx \mu V_k(0), \quad (9)$$

assuming $2f_0 > W$ and thus neglecting the second term in (9), since V_k is highly concentrated in the interval $(f - W, f + W)$.

By minimizing the residual local squared error, that is, when $f = f_0$, the μ can be estimated. The squared error can be described as follows:

$$e^2(\mu, f) = \sum_{k=0}^{N-1} |y_k(f) - \mu V_k(0)|^2. \quad (10)$$

The result is given as follows:

$$\hat{\mu}(f) = \frac{\sum_{k=0}^{K-1} V_k^*(0) y_k(f)}{\sum_{k=0}^{K-1} |V_k(0)|^2}. \quad (11)$$

An F test can be used to test for the significance of a line component at f , and the location of its maximum value provides an estimation of the line frequency.

In this paper, the periods of interest are nearly as long as the data. Thus, a line component at zero frequency is included and the estimation of $\mu(0)$ from (11) is used as an alternative estimation of the mean, which will result in the

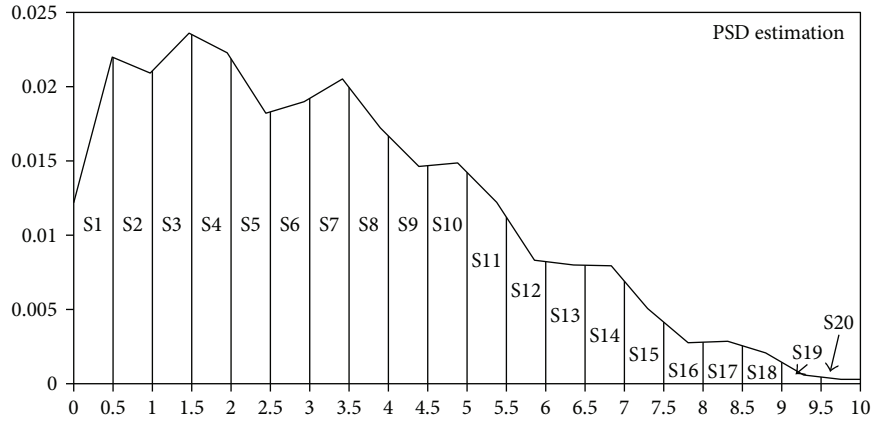


FIGURE 5: Spectral features extracted from single PPG signal.

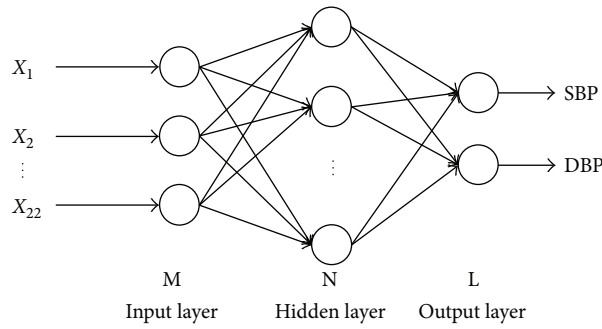


FIGURE 6: The architecture of ANN.

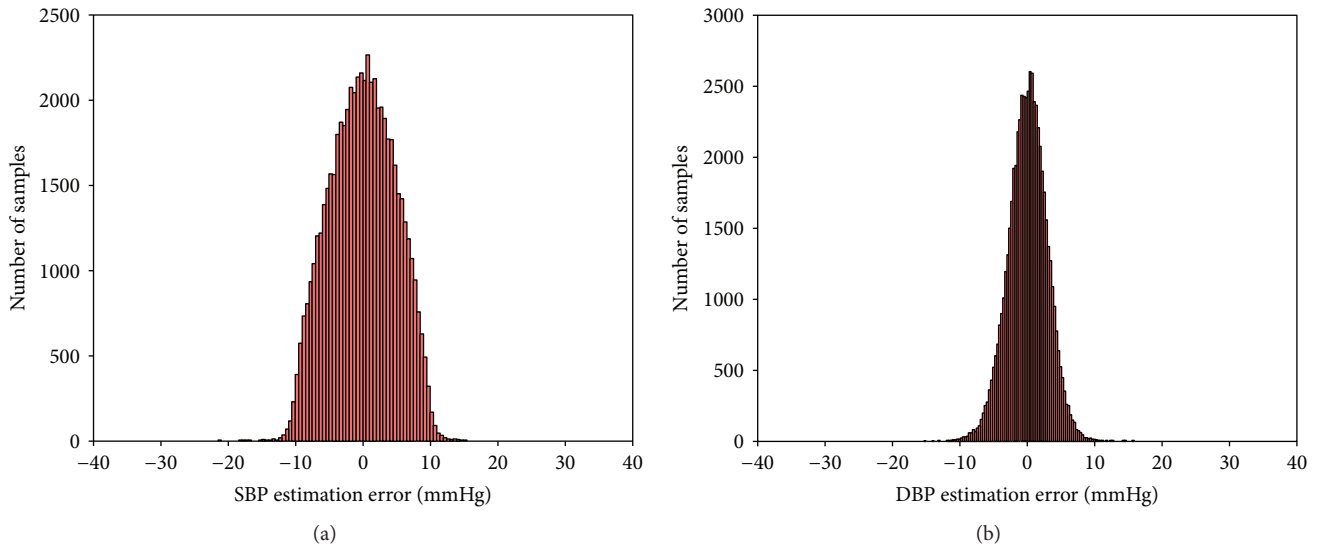


FIGURE 7: Histograms of error: (a) SBP estimation error and (b) DBP estimation error.

preservation of the continuous part of the spectrum at zero frequency [23]. The continuous part of the spectrum can be calculated as follows:

$$\hat{S}(f) = \frac{1}{K} \sum_{k=0}^{K-1} |y_k(f)|^2. \quad (12)$$

TABLE 3: Number of subjects in different methods.

Method	Number of subjects
Linear regression [15]	15
RSVM based [16]	65
Proposed method	72

TABLE 4: Performance results of the linear regression, SVRM-based method, and ANN-based method with different feature extraction technique on the test database.

Method	Number of input parameters	SBP		DBP	
		e (mmHg)	e_r (%)	e (mmHg)	e_r (%)
Linear regression [15]	2	9.80 ± 8.09	8.94 ± 7.57	5.88 ± 5.11	10.26 ± 8.83
RSVM based [16]	13 for SBP 22 for DBP	5.07 ± 4.84	4.32 ± 3.59	4.31 ± 3.83	3.84 ± 3.39
ANN based (this method)	22	4.02 ± 2.79	2.84 ± 2.00	2.27 ± 1.82	4.39 ± 3.60

However, according to (4), the spectrum near a significant line component with frequency f_0 must be reconstructed, by subtracting the contribution of the line component as follows [27]:

$$\hat{S}_r(f) = \frac{1}{K} \sum_{k=0}^{K-1} |y_k(f) - \tilde{\mu}(f_0)V_k(f - f_0)|^2. \quad (13)$$

3.2. Feature Extraction. Several spectral and morphological features are used to characterize the single PPG signal. The systolic upstroke time (ST) and diastolic time (DT) presented in [15] are used as the two morphological features. Then the MTM is used to extract the spectral features.

As shown in Figure 4, the dominant frequency of single PPG waveform is mostly focused in the interval of low frequency (0.1~10 Hz).

As a result, this method tries to extract the spectral character in the interval of low frequency (0.1~10 Hz). We calculate the power of every 0.5, 1, 2, 5, and 10 Hz interval. Then, we use them as input separately to determine the optimal number of input parameters, and the results are as listed in Table 2 of Section 4. The best results are obtained when the interval is 0.5 Hz, as presented in Figure 5.

In total, the 22 parameters, including the times of systolic and diastolic parts and spectral features, are used to train the ANN.

3.3. Artificial Neural Network Architecture. There are various ANN architectures for fitting the input data to target, such as counter propagation, learning vector quantization, and radial basis function. Despite good performance, these architectures require large numbers of neurons and cannot be applied in the case of a big training set, due to their substantial memory requirements.

In this paper, PPG features are fed to a multilayer perceptron architecture, which has 22 input neurons (the number of input parameters, as mentioned above) and 2 output neurons, to simultaneously estimate SBP and DBP. This architecture is shown in Figure 6.

4. Experimental Results and Discussion

Figure 7 shows the histograms of the errors, calculated as the difference between real SBP/DBP and the output of the ANN, for the proposed method. The mean difference and standard deviation between the estimated BP and measured BP are -0.0217 ± 4.8950 mmHg for SBP and 0.0975 ± 2.9160 mmHg for DBP.

To further evaluate the performance of the presented method, other two BP [15, 16] estimation methods are chosen for comparison in this paper. Table 3 lists the number of subjects in the above studies.

As indicated earlier, performance is assessed on effective records from the MIMIC database and is processed in a MATLAB (MathWorks, Natick, MA, USA) environment. Absolute error e and relative error e_r are used to evaluate the performance, which are, respectively, defined as

$$e = \text{BP}_{\text{estimated}} - \text{BP}, \quad (14)$$

$$e_r = \frac{\text{BP}_{\text{estimated}} - \text{BP}}{\text{BP}}.$$

Table 2 lists the performance results of different numbers of input parameters, and Table 4 lists the results of performance on the test database for the linear regression, RSVM-based method, and ANN-based method with different feature extraction techniques. The results are presented as mean and standard deviation of absolute error e and relative error e_r , among reference SBP/DBP and estimated values. For evaluation of the performance of this model in a single individual, test data is divided into individual subsets by index provided by PhysioNet [21] and is used to test performance on each subset, respectively. The estimated performance of the method applied to single individuals is listed in Table 5.

Compared with the other methods, our method has better performance and can be confidently said to provide an effective detection technique for wearable devices and mobile software in the field of hypertension.

5. Conclusion and Future Work

In this study, we propose a noninvasive and beat-to-beat method of BP estimation determined only from PPG signal. The MTM is used to extract representative features to improve precision and velocity. This is achieved using a typical-structure feed forward ANN. With the wearable PPG sensor becoming an increasingly popular technology, this method has practical significance as part of a big data solution.

According to the Association for the Advancement of Medical Instrumentation (AAMI), the mean and deviation absolute error between the device and the mercury standard sphygmomanometer can be larger than 5 ± 8 mmHg as well as the number of simultaneous readings agrees within 10 mmHg for 95% or more of the recordings and within

TABLE 5: The performance results based on individual measurements.

Record	SBP		DBP	
	e (mmHg)	e_r (%)	e (mmHg)	e_r (%)
Subject number 211 (F, 67)	4.68 ± 4.05	4.64 ± 4.62	2.60 ± 1.59	4.49 ± 2.70
Subject number 212 (M, 84)	5.10 ± 4.32	3.65 ± 3.25	2.95 ± 1.98	5.44 ± 3.88
Subject number 213 (F, 82)	3.03 ± 2.71	3.00 ± 2.56	3.12 ± 1.98	5.50 ± 3.43
Subject number 214 (F, 72)	4.10 ± 2.72	2.91 ± 1.92	2.50 ± 1.64	5.48 ± 3.65
Subject number 216 (M, 67)	3.35 ± 2.32	3.28 ± 2.29	1.91 ± 1.58	4.52 ± 3.33
Subject number 224 (M, 21)	2.89 ± 2.15	2.37 ± 1.82	2.16 ± 1.59	4.12 ± 3.04
Subject number 225 (M, 73)	4.51 ± 2.79	3.79 ± 2.39	2.08 ± 1.52	4.92 ± 3.64
Subject number 226 (M, 68)	4.44 ± 2.81	3.49 ± 2.20	2.32 ± 1.70	4.18 ± 3.50
Subject number 230 (F, 75)	5.18 ± 3.63	3.24 ± 2.28	1.82 ± 1.42	4.66 ± 3.51
Subject number 235 (F, 67)	3.55 ± 2.59	2.47 ± 1.80	2.09 ± 1.39	3.81 ± 2.98
Subject number 237 (F, 63)	6.14 ± 4.29	4.10 ± 2.68	2.92 ± 2.06	4.14 ± 2.69
Subject number 240 (M, 68)	4.55 ± 3.26	3.65 ± 2.56	1.84 ± 1.76	3.87 ± 3.09
Subject number 241 (F, 76)	3.95 ± 2.59	3.23 ± 2.20	3.45 ± 2.19	5.71 ± 3.97
Subject number 243 (M, 90)	5.21 ± 3.28	4.41 ± 2.78	2.92 ± 1.88	4.99 ± 3.15
Subject number 245 (F, 63)	4.03 ± 2.84	3.01 ± 2.12	3.40 ± 2.12	5.77 ± 3.65
Subject number 252 (M, 52)	6.08 ± 2.96	5.30 ± 2.68	2.70 ± 2.07	5.58 ± 3.42
Subject number 259 (F, 76)	4.57 ± 3.07	3.45 ± 2.33	3.26 ± 2.10	4.51 ± 3.34
Subject number 262 (F, 65)	5.15 ± 3.60	4.36 ± 3.15	2.77 ± 1.93	5.36 ± 3.43
Subject number 264 (M, 65)	4.11 ± 2.66	3.14 ± 2.04	2.79 ± 1.91	4.64 ± 3.21
Subject number 267 (M, 67)	3.72 ± 2.56	2.84 ± 1.94	2.56 ± 1.82	4.66 ± 3.06
Subject number 269 (F, 82)	4.34 ± 2.95	3.26 ± 2.22	3.39 ± 2.20	4.28 ± 2.91
Subject number 276 (F, 66)	3.76 ± 2.53	3.11 ± 2.13	2.78 ± 1.95	4.01 ± 3.07
Subject number 277 (F, 71)	4.33 ± 2.85	3.51 ± 2.31	2.85 ± 2.00	3.94 ± 2.74
Subject number 279 (F, 85)	4.15 ± 2.65	3.40 ± 2.21	3.03 ± 2.06	4.13 ± 2.90
Subject number 280 (M, 60)	4.50 ± 2.84	3.93 ± 2.54	3.57 ± 2.52	4.06 ± 2.78
Subject number 281 (M, 61)	5.02 ± 3.58	4.35 ± 3.19	2.70 ± 1.83	5.16 ± 3.53
Subject number 284 (F, 59)	4.73 ± 3.19	3.37 ± 2.37	3.15 ± 2.16	4.96 ± 3.45
Subject number 285 (M, 55)	5.70 ± 4.73	4.11 ± 4.04	2.66 ± 1.97	5.12 ± 3.42
Subject number 286 (F, 34)	4.30 ± 3.01	3.59 ± 2.52	2.86 ± 1.82	4.40 ± 2.77
Subject number 288 (F, 59)	4.84 ± 3.00	3.70 ± 2.33	3.27 ± 2.01	5.40 ± 4.28
Subject number 289 (F, 61)	5.10 ± 3.77	4.67 ± 3.49	2.85 ± 1.83	6.12 ± 4.38
Subject number 293 (F, 71)	4.44 ± 3.82	3.86 ± 2.51	2.92 ± 2.12	4.20 ± 2.98
Subject number 401 (F, 64)	7.11 ± 5.64	5.54 ± 4.58	3.97 ± 2.91	4.32 ± 3.27
Subject number 404 (F, 87)	4.01 ± 3.78	2.73 ± 1.91	2.07 ± 2.73	5.03 ± 3.38
Subject number 408 (M, 45)	4.10 ± 2.70	2.88 ± 1.89	3.01 ± 2.01	6.08 ± 4.20
Subject number 410 (M, 57)	3.53 ± 3.48	3.10 ± 3.15	3.18 ± 2.13	5.69 ± 3.56
Subject number 411 (F, 82)	3.40 ± 3.33	3.42 ± 2.38	3.45 ± 2.36	5.07 ± 3.41
Subject number 415 (F, 54)	3.06 ± 2.03	2.99 ± 2.00	2.66 ± 1.97	4.71 ± 3.39
Subject number 417 (M, 86)	3.13 ± 2.14	2.95 ± 2.03	3.74 ± 2.08	7.10 ± 3.97
Subject number 418 (M, 52)	3.59 ± 3.41	3.54 ± 2.39	2.65 ± 1.86	5.74 ± 3.77
Subject number 422 (F, 84)	3.97 ± 3.29	4.03 ± 4.40	3.18 ± 2.13	4.30 ± 3.09
Subject number 430 (M, 91)	2.68 ± 2.06	2.61 ± 2.00	3.62 ± 2.35	5.52 ± 4.04
Subject number 434 (F, 52)	6.54 ± 6.35	4.30 ± 4.38	3.29 ± 2.00	4.32 ± 4.11
Subject number 436 (F, 87)	7.59 ± 6.80	4.92 ± 4.61	2.97 ± 1.91	5.19 ± 4.75
Subject number 437 (M, 75)	8.36 ± 7.79	5.57 ± 5.37	2.89 ± 2.04	4.41 ± 3.18
Subject number 438 (M, 78)	3.73 ± 2.67	3.48 ± 2.50	2.31 ± 1.64	3.89 ± 2.86
Subject number 439 (F, 75)	4.44 ± 3.87	3.60 ± 2.30	2.14 ± 1.51	5.85 ± 3.58
Subject number 443 (M, 75)	4.52 ± 3.75	3.82 ± 3.36	2.34 ± 1.66	4.82 ± 3.48

TABLE 5: Continued.

Record	SBP		DBP	
	e (mmHg)	e_r (%)	e (mmHg)	e_r (%)
Subject number 446 (M, 73)	4.97 ± 4.90	3.91 ± 2.31	2.09 ± 1.51	5.82 ± 3.67
Subject number 447 (M, 50)	4.01 ± 3.65	3.32 ± 2.21	3.76 ± 2.35	4.13 ± 2.92
Subject number 449 (M, 75)	3.93 ± 3.74	2.91 ± 2.01	3.45 ± 2.23	5.69 ± 3.70
Subject number 450 (F, 76)	4.73 ± 3.69	3.21 ± 2.39	3.53 ± 2.27	4.66 ± 3.22
Subject number 452 (M, 73)	4.34 ± 3.73	3.61 ± 3.28	2.90 ± 2.13	6.73 ± 3.95
Subject number 455 (M, 49)	4.19 ± 3.69	3.48 ± ± 2.18	2.16 ± 2.96	5.47 ± 3.41
Subject number 456 (M, 84)	3.69 ± 3.52	2.77 ± 1.89	3.67 ± 2.13	5.38 ± 3.89
Subject number 457 (F, 80)	4.28 ± 3.91	3.36 ± 2.39	2.52 ± 1.81	4.47 ± 3.41
Subject number 458 (F, 73)	3.87 ± 2.85	3.32 ± 2.48	2.40 ± 1.72	5.83 ± 3.96
Subject number 464 (F, 49)	4.05 ± 2.86	3.43 ± 2.51	2.58 ± 1.79	5.32 ± 3.63
Subject number 466 (M, 70)	4.42 ± 3.55	3.69 ± 2.18	2.10 ± 1.92	6.73 ± 3.95
Subject number 468 (F, 76)	3.49 ± 2.32	2.95 ± 1.98	2.63 ± 1.89	5.47 ± 3.41
Subject number 471 (F, 78)	3.72 ± 2.57	3.16 ± 2.21	3.99 ± 2.25	5.83 ± 3.39
Subject number 472 (M, 79)	3.29 ± 2.21	2.66 ± 2.84	3.30 ± 2.06	4.78 ± 3.60
Subject number 474 (M, 75)	5.04 ± 3.62	4.20 ± 4.06	3.64 ± 2.49	5.12 ± 3.67
Subject number 476 (F, 72)	4.20 ± 3.72	3.48 ± 4.18	3.24 ± 2.34	4.47 ± 3.45
Subject number 477 (M, 67)	4.07 ± 3.68	3.17 ± 2.80	3.17 ± 2.08	4.12 ± 3.67
Subject number 478 (M, age not recorded)	4.44 ± 2.79	3.82 ± 2.37	2.95 ± 1.99	5.93 ± 4.12
Subject number 479 (F, 77)	4.78 ± 4.04	3.43 ± 3.91	3.23 ± 2.08	4.96 ± 4.71
Subject number 480 (M, 52)	5.20 ± 4.81	4.25 ± 3.99	3.17 ± 2.08	5.18 ± 3.78
Subject number 481 (F, 73)	2.91 ± 3.76	3.55 ± 4.01	2.76 ± 1.94	5.44 ± 3.81
Subject number 482 (F, 92)	3.88 ± 2.67	3.34 ± 2.44	2.51 ± 1.83	4.47 ± 3.45
Subject number 484 (M, 60)	4.52 ± 2.74	3.81 ± 4.74	2.82 ± 2.00	4.94 ± 4.12
Subject number 485 (M, 69)	4.73 ± 3.89	3.54 ± 2.50	2.34 ± 1.74	4.18 ± 3.68
Subject number 488 (age and gender not recorded)	4.04 ± 2.75	3.24 ± 2.24	3.12 ± 2.16	4.92 ± 3.24

5 mmHg for 85% or more of simultaneous observations [13, 28]. Our future research will investigate how to improve the efficiency of the estimation algorithm, especially in a single individual. We will combine the method with data such as patient age, sex, and previous medical disorders. Hybrid and adaptable methods will also be considered.

Conflicts of Interest

The authors declare that there are no competing interests regarding the publication of this paper.

Acknowledgments

This work is supported by 2015 China Special Fund for Grain-Scientific Research in Public Interest (201513002).

References

- [1] World Heart Federation, "Hypertension," August 2017, <http://www.world-heart-federation.org/cardiovascular-health/cardiovascular-disease-risk-factors/hypertension/?sid=ISI:WoS>.
- [2] BC Guidelines & Protocols Advisory Committee, *Hypertension – Diagnosis and Management*, BC Ministry of Health, 2016.
- [3] J. R. Higgins and S. M. De, "Blood-pressure measurement and classification in pregnancy," *The Lancet*, vol. 357, no. 9250, pp. 131–135, 2001.
- [4] J. Landgraf, S. H. Wishner, and R. A. Kloner, "Comparison of automated oscillometric versus auscultatory blood pressure measurement," *The American Journal of Cardiology*, vol. 106, no. 3, pp. 386–388, 2010.
- [5] T. Ohkubo, Y. Imai, I. Tsuji et al., "Home blood pressure measurement has a stronger predictive power for mortality than does screening blood pressure measurement: a population-based observation in Ohasama, Japan," *Journal of Hypertension*, vol. 16, no. 7, pp. 971–975, 1998.
- [6] P. K. Lim, S. C. Ng, W. A. Jassim et al., "Improved measurement of blood pressure by extraction of characteristic features from the cuff oscillometric waveform," *Sensors*, vol. 15, no. 6, pp. 14142–14161, 2015.
- [7] T. G. Pickering, J. E. Hall, L. J. Appel et al., "Recommendations for blood pressure measurement in humans and experimental animals. Part 1: blood pressure measurement in humans: a statement for professionals from the Subcommittee of Professional and Public Education of the American Heart

- Association Council on High Blood Pressure Research," *Hypertension*, vol. 45, no. 1, pp. 142–161, 2005.
- [8] S. Lee, G. Jeon, and G. Lee, "On using maximum a posteriori probability based on a Bayesian model for oscillometric blood pressure estimation," *Sensors*, vol. 13, no. 10, pp. 13609–13623, 2013.
- [9] Z. Taha, L. Shirley, and M. A. M. Razman, "A review on non-invasive hypertension monitoring system by using photoplethysmography method," *Movement, Health & Exercise*, vol. 6, no. 1, pp. 47–57, 2017.
- [10] R. P. Smith, J. Argod, J. L. Pepin, and P. A. Levy, "Pulse transit time: an appraisal of potential clinical applications," *Thorax*, vol. 54, no. 5, pp. 452–457, 1999.
- [11] C. Ahlstrom, A. Johansson, F. Uhlin, T. Länne, and P. Ask, "Noninvasive investigation of blood pressure changes using the pulse wave transit time: a novel approach in the monitoring of hemodialysis patients," *Journal of Artificial Organs*, vol. 8, no. 3, pp. 192–197, 2005.
- [12] H. Gesche, D. Grosskurth, G. Kuchler, and A. Patzak, "Continuous blood pressure measurement by using the pulse transit time: comparison to a cuff-based method," *European Journal of Applied Physiology*, vol. 112, no. 1, pp. 309–315, 2012.
- [13] W. B. White, A. S. Berson, C. Robbins et al., "National standard for measurement of resting and ambulatory blood pressures with automated sphygmomanometers," *Hypertension*, vol. 21, no. 4, pp. 504–509, 1993.
- [14] H. Shin and S. D. Min, "Feasibility study for the non-invasive blood pressure estimation based on ppg morphology: normotensive subject study," *Biomedical Engineering Online*, vol. 16, no. 1, p. 10, 2017.
- [15] X. F. Teng and Y. T. Zhang, "Continuous and noninvasive estimation of arterial blood pressure using a photoplethysmographic approach," in *Proceedings of the 25th Annual International Conference of the IEEE Engineering in Medicine and Biology Society (IEEE Cat. No.03CH37439)*, vol. 4, pp. 3153–3156, Cancun, Mexico, 2003.
- [16] S. C. Gao, P. Wittek, L. Zhao, and W. J. Jiang, "Data-driven estimation of blood pressure using photoplethysmographic signals," in *2016 38th Annual International Conference of the IEEE Engineering in Medicine and Biology Society (EMBC)*, pp. 766–769, Orlando, FL, USA, 2016.
- [17] K. J. Yi, B. Hwan Cho, S. Mi Im, M. Ju Jeon, I. Young Kim, and S. Kim, "Comparative study on artificial neural network with multiple regressions for continuous estimation of blood pressure," in *2005 IEEE Engineering in Medicine and Biology 27th Annual Conference*, pp. 6942–6945, Shanghai, China, 2005.
- [18] P. Donaldb and A. Walden, *Spectral Analysis for Physical Applications*, Cambridge University Press, 1998.
- [19] G. B. Moody and R. G. Mark, "A database to support development and evaluation of intelligent intensive care monitoring," in *Computers in Cardiology, 1996*, pp. 657–660, Indianapolis, IN, USA, 1996.
- [20] A. L. Goldberger, L. A. Amaral, L. Glass et al., "PhysioBank, PhysioToolkit, and PhysioNet: components of a new research resource for complex physiologic signals," *Circulation*, vol. 101, no. 23, pp. e215–e220, 2000.
- [21] "MIMIC Database," August 2017, <https://physionet.org/physiobank/database/mimicdb/>.
- [22] D. J. Thomson, "Spectrum estimation and harmonic analysis," *Proceedings of the IEEE*, vol. 70, no. 9, pp. 1055–1096, 1982.
- [23] D. J. Thomson, "Time series analysis of Holocene climate data," *Philosophical Transactions of the Royal Society A: Mathematical Physical and Engineering Sciences*, vol. 330, no. 1615, pp. 601–616, 1990.
- [24] D. J. Thomson, "Quadratic-inverse spectrum estimates: applications to paleoclimatology," *Philosophical Transactions of the Royal Society A: Mathematical Physical and Engineering Sciences*, vol. 332, no. 1627, pp. 539–597, 1990.
- [25] D. Slepian, "Prolate spheroidal wave functions, fourier analysis, and uncertainty — V: the discrete case," *Bell System Technical Journal*, vol. 57, no. 5, pp. 1371–1430, 1978.
- [26] A. R. Rao and K. Hamed, "Multi-taper method of analysis of periodicities in hydrologic data," *Journal of Hydrology*, vol. 279, no. 1-4, pp. 125–143, 2003.
- [27] Association for the Advancement of Medical Instrumentation, "American national standard for electronic or automated sphygmomanometers," in *ANSI/AAMI SP10-1992/A1*, Arlington, VA, USA, 1996.
- [28] T. Tamura, Y. Maeda, M. Sekine, and M. Yoshida, "Wearable photoplethysmographic sensors—past and present," *Electronics*, vol. 3, no. 2, pp. 282–302, 2014.

Research Article

Earable RCC: Development of an Earphone-Type Reliable Chewing-Count Measurement Device

Kazuhiro Taniguchi ¹, Hisashi Kondo,² Toshiya Tanaka,³ and Atsushi Nishikawa ⁴

¹Graduate School of Information Sciences, Hiroshima City University, 3-4-1 Ozukahigashi, Asaminami-ku, Hiroshima, Hiroshima 731-3194, Japan

²Wearable Media Laboratory, eRCC Co. Ltd., 21-3 Motomachi, Naka-ku, Hiroshima, Hiroshima 730-8504, Japan

³SAGA-KEN Medical Centre KOSEIKAN, 400 Nakabaru, Kasemachi, Saga, Saga 840-8571, Japan

⁴Faculty of Textile Science and Technology, Shinshu University, 3-15-1 Tokida, Ueda, Nagano 386-8567, Japan

Correspondence should be addressed to Kazuhiro Taniguchi; taniguti@hiroshima-cu.ac.jp

Received 2 November 2017; Accepted 25 December 2017; Published 12 February 2018

Academic Editor: Feng Liu

Copyright © 2018 Kazuhiro Taniguchi et al. This is an open access article distributed under the Creative Commons Attribution License, which permits unrestricted use, distribution, and reproduction in any medium, provided the original work is properly cited.

Gastric cancer patients having undergone gastrectomy are at a high risk of becoming malnourished owing to decreased gastric function. To prevent malnutrition, patients need to thoroughly chew a mouthful of food at least 30 times. For these gastrectomy patients requiring dietary support, we developed a chewing-count measurement device named earable RCC using an earphone-type sensor. Experiments to evaluate the performance of this device were conducted on six healthy volunteers who participated in “gum-chewing tests” and “almond-eating tests.” The precision calculated based on the results was ≥ 0.958 , indicating that the earphone-type chewing-count measurement device could experimentally distinguish chewing from other actions. In addition, the recall calculated from the test results was ≥ 0.937 , showing that the device does not miss chewing actions and can accurately count the number of chews with high probability at the timing of chewing. The experimental results also imply that earphone-type sensors may be used to measure swallowing, occlusal force, and tongue motion. Our future plans include clinical testing of the earphone-type chewing-count measurement device to determine its utility in patients who have undergone gastrectomy. We also intend to expand the application of this device for use in other patients to aid in dementia prevention and dietary support.

1. Introduction

Gastric cancer patients who have undergone gastrectomy surgery are at a high risk of becoming malnourished because of decreased gastric function [1]. To prevent malnutrition, improvements in the method of meal intake are important. One such improvement is to slowly and thoroughly chew a mouthful of food about 30 times before ingesting it. Verbal instructions accompanied by materials such as pamphlets on chewing carefully are given to the patients; however, chewing depends subjectively on the patient and conducting the actual practice of slowly and thoroughly chewing before ingestion is often difficult. If a patient cannot slowly and thoroughly chew before swallowing, problems such as food quickly flowing into the intestines, inability of the body to adapt, and early dumping syndrome arise. By being able to

visualize the practice of chewing thoroughly and applying it for patient support, the quality of life of patients having undergone gastrectomy (postgastrectomy patients) may be improved. We believe that visualizing the practice of chewing thoroughly can enhance the eating habits of patients and are trying to implement this at clinical sites. Meeting the “chewing thoroughly” metric can be made possible by quantifying the number of chews.

To improve the meal intake method and determine the number of chews, data obtained and recorded, using a chewing-count measurement device is preferable over that obtained and recorded by the patients themselves. This is because gathering and recording of data by the patients place undue burden on them, and the data may not be objective. Current devices to measure the number of chews include a camera that records mouth movements [2]; tooth-

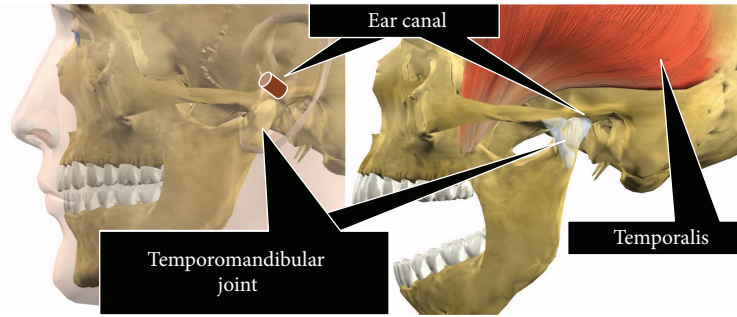


FIGURE 1: Relationship between chewing and changes in ear canal shape.

embedded sensors [3], EMG [4], and piezoelectric strain gauge sensors [5] attached to the skin surface; microphones that detect chewing noises [6–9]; and accelerometers that recognize the movement of skin caused by chewing [10, 11]. However, these devices were not developed specifically for dietary support of postgastrectomy patients, and each tool has drawbacks when applied to such patients. For instance, capturing mouth movements by a camera to measure chewing activity impinges on a patient’s privacy. Tooth-embedded sensors to capture the number of chews are invasive and not well accepted by patients. EMG and piezoelectric strain gauge sensors that measure the number of chews dependent on muscle and skin movements require the sensors to be placed on the patient’s skin, increasing the discomfort of patients and impeding their ability to eat meals. In addition, microphones that detect chewing noises tend to be ineffective due to ambient background noise. Accelerometers can detect whether meal intake is occurring or not but are unsuitable for accurately measuring the number of chews. Moreover, the design of all of these devices does not permit chewing measurement results to be attainable in real time to patients and physicians.

Therefore, we have been conducting research and development with respect to a chewing-count measurement device that uses an earphone-type sensor to provide dietary support for postgastrectomy patients [12–14]. In this paper, we describe the mechanics of the device and present the results from performance evaluation experiments. In our previous research, we focused on the distinctive pattern of variation associated with consuming meals (chewing), mainly with the aim of healthcare monitoring. We developed an earphone-type sensor (wearable device) and demonstrated its effectiveness in obtaining robust measurements during meals [15].

2. Materials and Methods

2.1. Earphone-Type Chewing-Count Measurement Device. In this research, we aimed to develop a chewing-count measurement device that met the following five criteria:

- (i) Providing a measurement accuracy (precision and recall) of $\geq 90\%$
- (ii) Not impeding the patient’s eating activities: less burden of wearing the device, number of chews

measured without placing the sensor or device in the mouth (measurements can be taken even if there is food in the mouth), movements of the muscles and joints used for chewing (e.g., cheek joints and temporalis muscle) not obstructed by the device, and small and lightweight devices

- (iii) Protecting patient privacy
- (iv) Being easy to operate and facilitating handling without specialized knowledge
- (v) Revealing the number of chews in real time to patients and physicians, recording meal contents as images, and presenting past meal contents (images) and measurements in graphical format concurrently

Chewing occurs via the movement of the temporalis muscle and temporomandibular joint. Based on the anatomical positional relationship between the temporalis muscle and temporomandibular joint shown in Figure 1, chewing activity changes the shape of the ear canal near the temporalis muscle and temporomandibular joint. We measured the change in shape of the ear canal due to chewing with an earphone-type sensor, and using the obtained results, we developed a device that determines the number of chews. The earphone-type sensor contains an optical distance sensor that uses light for taking measurements. Using this method, chewing count can be obtained without irritating sensitive ears.

The outer appearance of the earphone-type chewing-count measurement device named earable RCC is shown in Figure 2. The configuration of the device is shown in Figure 3. In this device, the earphone-type sensor is attached to either the right or left ear, and the movement of the ear canal is measured. The earphone-type sensor has the same shape as an inner-ear-type earphone and is fitted with an optical distance sensor, QRE1113 (Fairchild Semiconductor International Inc., California, USA), which has an infrared LED and a phototransistor built in. Infrared light emitted from LED is transmitted within the ear canal, and the reflected light is captured by the phototransistor. From the obtained data, movements of the ear canal during chewing can be measured (Figure 4). The electronic circuitry around the optical distance sensor is shown in Figure 5. In this diagram, when distance d between the eardrum and optical distance sensor is short, the amount of light reflected from

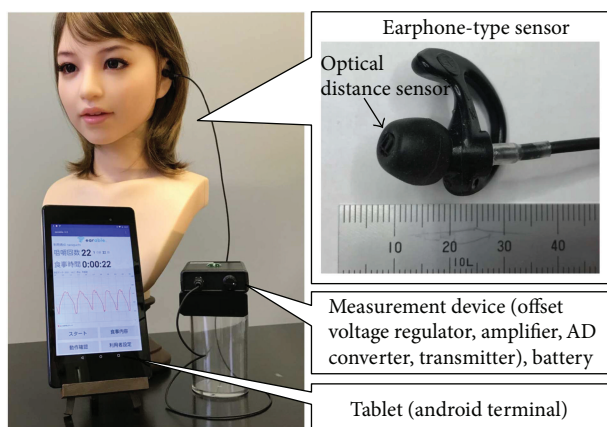


FIGURE 2: Outer appearance of earphone-type chewing-count measurement device (earable RCC).

the eardrum is large and the output voltage increases. Similarly, when distance d is long, the amount of reflected light is small and the output voltage decreases.

The earphone-type sensor to be inserted into the ear canal was made in two sizes, small and medium, based on the sensors that are commercially available. The sensor was also constructed for both the right and the left ears for each size.

The earphone-type sensor was connected to a measurement instrument with a cable. The instrument was $110 \times 75 \times 25$ mm in size and weighed 115 g; it was small enough to be unobtrusive on a dining table. A voltage of 3.3 V DC was supplied from the instrument to the earphone-type sensor, and the output data from the sensor were detected by the offset voltage regulator of the instrument. The amount of offset voltage measured by the sensor was adjusted to a central value after analog to digital (AD) conversion of the signal received by the offset voltage regulator of the instrument. The adjustment was based on the following formula: central value of AD convertible range = 3.3 V (power supply voltage of the AD converter) $\div 2 = 1.65 \text{ V}$. The offset voltage adjustment is required to correct for differences in this parameter caused by dissimilarities in ear canal shape among individuals. The value (waveform) measured by the sensor is an amplitude based on the offset voltage. Only the amplitudes were magnified in the signal after offset voltage adjustment because the offset voltage was kept fixed by the amplifier. The amplification level could be magnified up to 40 times by a knob (variable resistor) on the measurement instrument. The analog signal after amplification was converted to a digital signal by the AD converter with a sampling frequency of 250 Hz and a 10-bit resolution. The converted digital signal was sent by a transmitter (Bluetooth 2.1) to a tablet (ASUS Nexus 7, Bluetooth 3.0). By the aid of an application software that we built, the tablet displayed and recorded the waveforms of values sent from the transmitter, number of chews, and duration of measurement. The software can be installed on an android terminal (e.g., tablets and smartphones) supporting version 5.0 and above. When chewing is detected by this software, the information is displayed on the tablet with concurrent sounds emitted

through the speaker to the user. In this software, one chew was deemed to have occurred when the peak-to-peak waveform value exceeded 0.4 V ($1.65 \pm 0.2 \text{ V}$). We chose this threshold of 0.4 V based on trial and error. Before measuring the number of chews using the earphone-type chewing-count measurement device, the amplification level was adjusted using the knob on the instrument such that the peak-to-peak waveform on the tablet was 0.4 V or more. This adjustment was made while the subjects moved their mouths when empty as if chewing and when eating foods used for testing.

The software that we developed manages patient information via ID numbers, thereby protecting the privacy of patients. Using a camera embedded in the android terminal, images of the meal contents can be taken and recorded. This information can be linked to the measurements of chewing counts. The chewing-count data can be searched by patient ID, and the measurements can also be displayed in a graphical format. The software and hardware are designed for intuitive operation, and the device can easily be handled without specialized knowledge. These functions of the chewing-count measurement device are useful for the dietary support of patients and were implemented according to requests from clinicians.

We conducted experiments to evaluate the measurement accuracy (precision and recall) of the chewing-count measurement device involving subjects described in Section 2.2 for evaluation experiments outlined in Section 2.3.

2.2. Subjects. Six volunteers (men and women between 21 and 43 years of age; mean age, 28.2 years) served as subjects and were individually identified as A to F. All subjects were healthy, had no history of surgery such as gastrectomy, and had never received dietary counselling. Subjects were those who could chew without problems, did not have pain in their teeth or jaws, and did not have subjective symptoms of fatigue; volunteers who were undergoing orthodontic or medical treatment were excluded. Furthermore, the ear sensor had to fit on the subjects without it being too large or small; subjects who did not have symptoms of ear pain or fatigue were selected, whereas those under treatment were excluded.

This study was approved by the Shinshu University Ethical Committee on Human Science Research. An adequate explanation of the study was given to the subjects in advance, and consent for research participation was obtained.

2.3. Evaluation Experiments. Subjects participated in experiments involving chewing two types of food. Prior to the experiment, the subjects selected either a small or medium earphone-type sensor that fit on their left or right ear.

For the gum-chewing experiment, subjects were requested to refrain from other actions such as taking food into their mouth or swallowing and to focus on chewing the gum only. According to a report by the Chewing Gum Association of Japan, the number of chews for one 3 g stick of gum is approximately 550. Gum sold in Japan is often in the form of 1.5 g sticks; thus, we assumed that the number of chews for this type of gum would be half that for a 3 g stick or approximately 275. Xylitol Oratect Gum (Lotte Co. Ltd.,

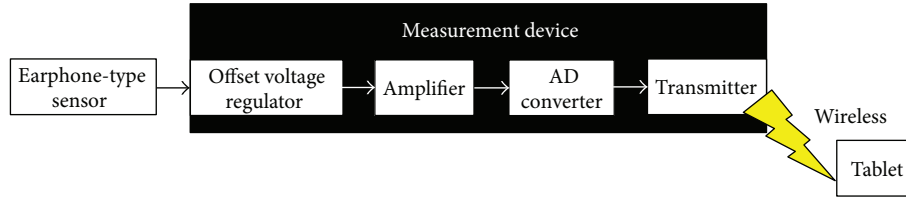


FIGURE 3: Configuration of the chewing-count measurement device.

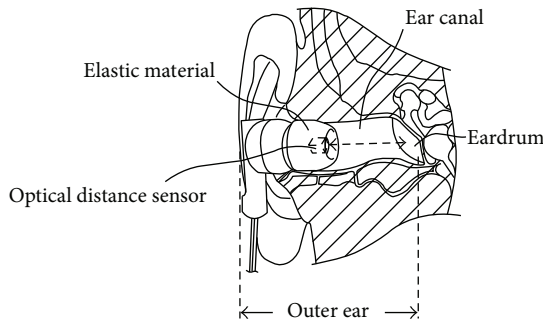


FIGURE 4: Measurement principle for changes in the shape of the ear canal.

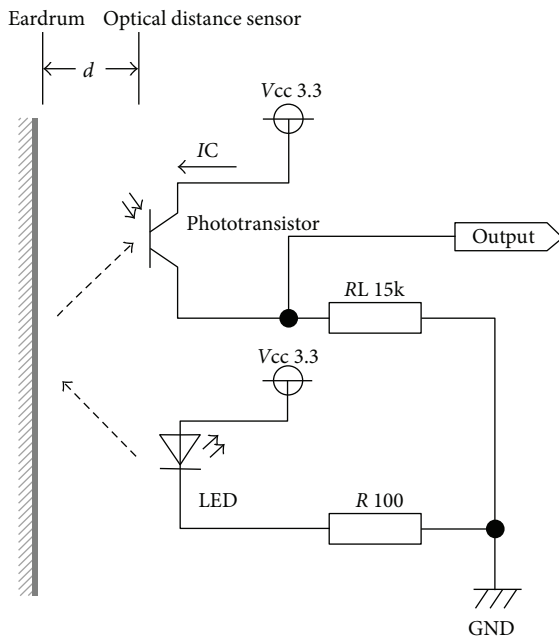


FIGURE 5: Electronic circuit around the optical distance sensor.

Tokyo, Japan) was used in this experiment. Prior to measuring the number of chews, the subjects, while using the earphone-type chewing-count measurement device, placed a 1.5 g stick of gum in their mouth and started chewing. At that time, the researcher adjusted the amplification level by turning the knob on the measuring instrument such that the peak-to-peak waveform displayed on the tablet was $\geq 0.4V$. Once this adjustment had been made, the subjects expelled and disposed of the gum. For the experiment, one fresh 1.5 g stick of gum was taken in the mouth and chewed

300 times; during this period, the number of chews was measured by the earphone-type chewing-count measurement device. Concurrently, the subjects reported the number of chews they made with a manual counter. The researcher also used a manual counter to note the number of times that the chewing-count measurement device indicated chewing, although the subject was not chewing.

For the eating experiment, the subjects ate 10 almonds one by one. We chose to use almonds because one almond can be eaten in a mouthful, and because the size and hardness of almonds do not vary much compared with those of other foods, they are readily available as size-selected products. Almonds are crushed by chewing, and their hardness changes greatly by chewing. Therefore, in this experiment, it was possible to include actions such as taking food in the mouth, chewing the food hard until soft, and swallowing food. Unsalted roasted almonds obtained from a convenience store (7-Eleven Japan Co. Ltd., Tokyo, Japan) were used. A preliminary experiment conducted with subject A indicated that the number of almonds that could be eaten by chewing approximately 300 times (the same number as for gum chewing) was 10; therefore, 10 almonds were used to minimize differences in the number of chews between the gum-chewing and almond-eating experiments. Furthermore, dietary support instructions to postgastrectomy patients indicated that they should chew a mouthful of food about 30 times. Thus, when subjects chew one almond 30 times, the total number of chews for 10 almonds eaten one by one is 300 times. Prior to measuring the number of chews, the subjects, while using the earphone-type chewing-count measurement device, chewed one almond. At that time, the researcher adjusted the amplification level by turning the knob on the measuring instrument such that the peak-to-peak waveform displayed on the tablet was $\geq 0.4V$. For the experiment, 10 almonds were eaten one by one until fully consumed; during this period, the number of chews was measured by the earphone-type chewing-count measurement device. Concurrently, the subjects reported the number of chews they made with a manual counter. The researcher also used a manual counter to note the number of times that the chewing-count measurement device indicated chewing, although the subject was not chewing.

After all the experiments, a survey was administered by interviewing the subjects. All of the experiments were performed with the subjects sitting in a chair, with a table placed in front of them. On this table, one dish containing two sticks of gum, a second dish with 11 almonds, the measuring instrument, one android tablet, and one manual counter were placed.

Prior to the experiment, the researcher informed the subjects about ingredients in the gum to be used and explained that the gum contained gelatin, which can be an allergen. In addition, the researcher notified the subjects that the almonds to be used had been processed in a manufacturing facility where products, including eggs, milk, wheat, peanuts, and shrimp, were handled. Moreover, after notification, the researcher confirmed with the subjects that they did not have allergic reactions to the gum or almonds used.

During all experiments, the subjects were requested not to drink fluids such as water. If fluids were ingested during the chewing measurement experiment, the results were invalidated, and the experiment was reperformed. The earphone-type sensor was cleaned and disinfected with ethanol before and after use in the experiments.

3. Results

We conducted the gum-chewing and almond-eating experiments outlined above and obtained results on the number of chews determined by the chewing-count measurement device (recorded in the internal memory of the device) and the number of chews the subjects reported with a manual counter. In addition, the number of times that the chewing-count measurement device indicated chewing despite the subject not chewing was noted by the researcher using a manual counter. Results from a survey administered to the subjects in an interview format by the researcher were also acquired. Furthermore, the subject's chewing condition, waveform displayed on the measuring device, and the number of chews were visually observed, and the results were recorded by the researcher.

Table 1 shows the results from each subject when chewing one 1.5 g stick of gum 300 times. Precision p values in Table 1 were calculated using (1) and indicated the ratio of “the number of times chewing was indicated by the device when the subject was chewing” to “the number of times chewing was indicated by the device.”

$$p = \frac{TP}{TP + FP}. \quad (1)$$

Here, “true positive (TP)” represents the number of times the device indicated chewing when the subject was actually chewing, and “false positive (FP)” represents the number of times the device indicated chewing despite the subject not chewing. In other words, TP is the number of times the device indicated chewing subtracted by the number of times the researcher recorded on the manual counter that the device indicated chewing despite the subject not chewing. FP is the number of times the researcher recorded on the manual counter that the device indicated chewing despite the subject not chewing.

Recall r values in Table 1 were calculated using (2) and indicated the ratio of “the number of times the device indicated chewing when the subject was actually chewing” to “the number of times the subject was actually chewing.”

$$r = \frac{TP}{TP + FN}. \quad (2)$$

TABLE 1: Results from chewing experiment. Results from chewing one 1.5 g stick of gum 300 times. For precision, the numerator is TP and the denominator is the sum of TP and FP. For recall, the numerator is TP and the denominator is the sum of TP and FN.

Subject	Precision	Recall
A	1.000 = 300/300	1.000 = 300/300
B	1.000 = 281/281	0.937 = 281/300
C	1.000 = 300/300	1.000 = 300/300
D	1.000 = 298/298	0.993 = 298/300
E	1.000 = 300/300	1.000 = 300/300
F	0.987 = 300/304	1.000 = 300/300

TABLE 2: Results from eating experiment. Results from eating 10 almonds one by one. For precision, the numerator is TP and the denominator is the sum of TP and FP. For recall, the numerator is TP and the denominator is the sum of TP and FN.

Subject	Precision	Recall
A	0.984 = 300/305	1.000 = 300/300
B	1.000 = 331/331	0.974 = 331/340
C	0.958 = 207/216	1.000 = 207/207
D	0.996 = 255/256	0.988 = 255/258
E	0.990 = 291/294	0.980 = 291/297
F	0.966 = 230/238	1.000 = 230/230

Here, “false negative (FN)” represents the number of times that the device failed to count the subject's actual chewing and is equal to the number of times the subject recorded on the manual counter that he/she was chewing subtracted by the number of times the chewing-count measurement device indicated chewing and added by the number of times the researcher recorded on the manual counter that the device indicated chewing despite the subject not chewing.

Table 2 shows a summary of the results from each subject when 10 almonds were eaten one by one. The same calculation methods as used for constructing Table 1 were used.

There was no need to reperform any of the chewing measurement experiments due to the ingestion of fluids by the subjects. In addition, all subjects selected an earphone-type sensor that fits in the right ear. Subjects A and B chose the small size, and subjects C to F chose the medium size.

4. Discussion

Based on Tables 1 and 2, precision was shown to be ≥ 0.958 , indicating that the earphone-type chewing-count measurement device incorrectly identified chewing occurrences only a few times. In addition, based on Tables 1 and 2, recall was shown to be ≥ 0.937 , indicating that after chewing was finished, the device could accurately count the number of chews with a high probability of not missing chews.

Based on Table 1, the chewing results from each subject were evaluated. First, the results for subject A indicate precision to be 1.000; thus, when subject A was not chewing, the chewing-count measurement device correctly identified that chewing was not occurring. The precision in results obtained

from subjects B to E was the same as that for subject A. The precision in results acquired from subject F was 0.987. At this instance, the device incorrectly recognized chewing when subject F swallowed saliva while chewing gum. The cause of erroneously identifying swallowing as chewing appears to be that the measured change in shape of the ear canal (peak-to-peak waveform in the earphone-type sensor) during swallowing was larger in subject F than that in the other participants. The value quantified for swallowing in the other subjects was less than or equal to the threshold value set using the measurement instrument, whereas the value exceeded the threshold value in subject F, resulting in the misidentification of chewing. These results from subject F were obtained by the earphone-type sensor, suggesting that the technology can be used to measure swallowing in addition to chewing. Chewing is often conducted in succession, but swallowing is intermittent. Based on this, we believe that chewing could be distinguished from swallowing by amplifying the measurement waveform of the sensor and conducting frequency analysis of the waveform. Thus, in the future, we plan to clarify and quantify the relationship between swallowing and changes in the shape of the ear canal and to conduct research on swallowing measurements using the earphone-type sensor.

The chewing-count measurement device did not fail even once in detecting chewing in subjects A, C, E, and F, as evidenced by the finding of recall = 1.00 shown in Table 1. Recall values were 0.937 and 0.993 for subjects B and D, respectively. Compared with subject D, results from subject B indicated that a large number of chews (19 out of 300) were unrecognized by the device. These 19 undetected chews occurred consecutively in the latter half of the experiment. During this time, the waveform on the device was synchronized with chewing performed by subject B; however, the peak-to-peak value of the waveform fell below the threshold of 0.4 V; thus, the device did not recognize chewing. Based on the results of the postexperiment survey, it was discovered that subject B experienced fatigue near the end of chewing gum 300 times consecutively without rest and found it difficult to continue exerting occlusal force. Therefore, we need to take into consideration chewing fatigue when using the chewing-count measurement device for the dietary support of gastric cancer patients. The results also suggest that the device could be employed to measure occlusal force; thus, we have started research on this issue [16].

Based on Table 2, the eating results from each subject were evaluated. The results for subject B indicated precision to be 1.000; thus, when subject B was not chewing, the chewing-count measurement device correctly identified this. Precision values were 0.984, 0.958, 0.996, 0.990, and 0.966 for subjects A and C to F, respectively. Based on the results of the postexperiment survey, it was discovered that subject A had used his/her tongue to remove a piece of almond stuck to the back of a tooth, and the device had erroneously indicated this action as chewing. This result suggests that an earphone-type sensor is potentially applicable to the measurement of tongue movement. In addition, the results from subjects C–F revealed that swallowing was misidentified as chewing by the device.

The chewing-count measuring device did not fail even once in detecting chewing in subjects A, C, and F, as evidenced by the recall value being 1.00 in Table 2. Recall values were 0.974, 0.988, and 0.980 for subjects B, D, and E, respectively. In these instances, the device could not detect chewing on the brink of swallowing. This was probably due to the use of almonds as test food; because the almonds were crushed by chewing, the occlusal force needed for chewing decreased, and the values measured by the device on the brink of swallowing reached the threshold value or lower. Therefore, we plan to build on the above occlusal force measurement study not only toward the application of the device for occlusal force measurement but also toward device improvement to address the decreases in the accuracy of chewing measurements associated with changes in occlusal force due to jaw fatigue caused by chewing, eating, and grinding of food. In this experiment, the amplification level of the signal was set by turning the knob of the measurement instrument before the experiment. However, the signal amplitude was found to change depending on the extent of the subject's fatigue; thus, we need to reexamine how the amplification level is set when operating the device.

We developed an earphone-type chewing-count measurement device that is hands-free because the sensor is worn in the ear. Thus, the apparatus does not obstruct vision or require electrodes placed on the face, as in the past, and regular meal intake is possible. In addition, the device consists only of an earphone-type sensor, a small, lightweight measurement instrument (110 × 75 × 25 mm, 115 g weight), and a tablet terminal; therefore, it takes up little space and is not an obstacle when eating meals. The device displays in real time not only the number of chews but also the ear canal motion accompanying chewing as a waveform on the tablet terminal. The waveform associated with ear canal movements due to chewing can be considered a visual representation of the chewing action (jaw movements). In other words, subjects can “visualize” their chewing in real time while eating meals. The device can also record and retain in its memory the number of chews and waveforms of ear canal movements associated with chewing; thus, accumulation and analysis of the measurement results are subsequently possible. The device can emit sounds as each chew occurs. Because of the combination of visual display and sound, it is possible to recognize chewing action visually and aurally. This enables a subject to receive feedback on chewing movements aurally even if he/she is visually occupied with another action (e.g., common activities during mealtimes such as watching TV or reading the newspaper). We believe that by visualizing chewing movements and number of chews, postgastrostomy patients can direct their own chewing behavior in real time, resulting in improvement of dietary habits (an increase of the number of chews) and overcoming of postoperative complications.

Future plans include improving the accuracy of the earphone-type chewing-count device, developing the same earphone-type sensor for swallowing and occlusal force quantification [16], and conducting further research on measurements of tongue movement. To confirm the usefulness of the device, we plan to deploy it for postgastrostomy patients.

In addition, because improvement in chewing is desirable for dementia prevention and diet support, the device will also be applied to these fields.

5. Conclusions

To aid the recovery of postgastrectomy patients, we developed a chewing-count measurement device that provides real-time visualization of chewing movements and the number of chews to the patient. This information is necessary for patients to self-monitor and improve their meal-intake behavior by increasing the number of chews before swallowing.

We developed a device that measures the number of chews using a wearable earphone-type sensor and displays the information on a tablet terminal in real time. The device was tested on 6 healthy volunteers who chewed gum or ate almonds; the results confirmed that the instrument can accurately count chewing without missing any chewing occurrences and can correctly distinguish behaviors other than chewing. The experimental results also suggest that the earphone-type sensor can be used to measure swallowing, occlusal force, and tongue movement in addition to chewing.

The chewing-count measurement device requires the subject to only wear an earphone-type sensor to measure chewing and thus does not obstruct meal intake and allows “visualizing” and monitoring of the subject’s chewing actions on a tablet screen in real time while eating.

Future plans include clinical application of the measurement device for postgastrectomy patients. In the future, we will expand this study to include a larger sample, particularly to include a wider age range of subjects. Furthermore, we would like to include at-home use as a potential context of this device and conduct experiments in real-life scenarios such as talking or drinking while chewing to examine how these actions affect the measurement accuracy and make modifications to the device as necessary. Further, broader application of the device, such as for dementia prevention and dietary support, is being considered. The measurement range for the earphone-type sensor will also be expanded for the quantification of swallowing, occlusal force, and tongue movement in addition to chewing.

Conflicts of Interest

The authors declare that there is no conflict of interests regarding the publication of this paper.

Acknowledgments

The authors would like to thank Welltone Co. Ltd., for their cooperation in developing the earphone-type chewing-count measurement device. They also express their gratitude to Dr. Yutaka Kimura, Health Science Center, Kansai Medical University, who provided guidance on the development of the earphone-type chewing-count measurement device. This research was supported in part by the Japanese Ministry of Internal Affairs and Communications, Strategic Information and Communications R&D Promotion Programme Project

(132308004), and the Japanese Ministry of Internal Affairs and Communications, Innovation Program, Wearable Ear-ring Computer Project.

References

- [1] J. Chris Eagon, K. A. Kelly, and B. W. Miedema, “Postgastrectomy syndromes,” *Surgical Clinics of North America*, vol. 72, no. 2, pp. 445–465, 1992.
- [2] S. Cadavid, M. Abdel-Mottaleb, and A. Helal, “Exploiting visual quasi-periodicity for real-time chewing event detection using active appearance models and support vector machines,” *Personal and Ubiquitous Computing*, vol. 16, no. 6, pp. 729–739, 2012.
- [3] C. Y. Li, Y.-C. Chen, W.-J. Chen, P. Huang, and H.-h. Chu, “Sensor-embedded teeth for oral activity recognition,” in *Proceedings of the 17th annual international symposium on International symposium on wearable computers - ISWC*, pp. 41–44, Zurich, Switzerland, September 2013.
- [4] R. Zhang and O. Amft, “Bite glasses: measuring chewing using Emg and bone vibration in smart eyeglasses,” in *Proceedings of the 2016 ACM International Symposium on Wearable Computers (ISWC '16)*, pp. 50–52, Heidelberg, Germany, September 2016.
- [5] E. S. Sazonov and J. M. Fontana, “A sensor system for automatic detection of food intake through non-invasive monitoring of chewing,” *IEEE Sensors Journal*, vol. 12, no. 5, pp. 1340–1348, 2012.
- [6] S. Päßler and W. J. Fischer, “Evaluation of algorithms for chew event detection,” in *Proceedings of the 7th International Conference on Body Area Networks*, pp. 20–26, Oslo, Norway, February 2012.
- [7] O. Amft, M. Stäger, P. Lukowicz et al. M. Beigl, S. Intille, J. Rekimoto et al., “Analysis of chewing sounds for dietary monitoring,” in *UbiComp 2005: Ubiquitous Computing. UbiComp 2005. Lecture Notes in Computer Science*, vol. 3660, pp. 56–72, Springer, Berlin, Heidelberg, 2005.
- [8] K. Yatani and K. N. Truong, “Bodyscope: a wearable acoustic sensor for activity recognition,” in *Proceedings of the 2012 ACM Conference on Ubiquitous Computing*, pp. 341–350, Pittsburgh, Pennsylvania, September 2012.
- [9] Y. Gao, N. Zhang, H. Wang et al., “iHear food: eating detection using commodity bluetooth headsets,” in *2016 IEEE First International Conference on Connected Health: Applications, Systems and Engineering Technologies (CHASE)*, pp. 163–172, Washington, DC, USA, June 2016.
- [10] S. Wang, G. Zhou, L. Hu, Z. Chen, and Y. Chen, “CARE: chewing activity recognition using noninvasive single axis accelerometer,” in *Proceedings of the 2015 ACM International Joint Conference on Pervasive and Ubiquitous Computing and Proceedings of the 2015 ACM International Symposium on Wearable Computers - UbiComp '15*, pp. 109–112, Osaka, Japan, September 2015.
- [11] A. Bedri, R. Li, M. Haynes et al., “EarBit: using wearable sensors to detect eating episodes in unconstrained environments,” *Proceedings of the ACM on Interactive, Mobile, Wearable and Ubiquitous Technologies*, vol. 1, no. 3, pp. 1–20, 2017.
- [12] M. Kurosawa, K. Taniguchi, and A. Nishikawa, “Earable: a novel earphone-type wearable sensor and its applications,” in *Proceedings of the 5th Annual Conference of AnalytiX-2017 (AnalytiX-2017)*, p. 400, Fukuoka, Japan, 2017.

- [13] K. Taniguchi, Y. Horise, A. Nishikawa, and S. Iwaki, "A novel wearable input device using movement of ear-canals," in *Proceedings of Textile Bioengineering and Informatics Symposium (TBIS) 2012*, pp. 166–174, Ueda, Japan, 2012.
- [14] *Input Device, Wearable Computer, and Input Method*, 2015, US Patent No.US8994647.
- [15] K. Taniguchi, H. Chiaki, M. Kurosawa, and A. Nishikawa, "A novel earphone type sensor for measuring mealtime: consideration of the method to distinguish between running and meals," *Sensors*, vol. 17, no. 2, p. 252, 2017.
- [16] M. Kurosawa, K. Taniguchi, and A. Nishikawa, "A basic study of occlusal force measured using a wearable ear sensor," in *Proceedings of the 14th International Conference on Ubiquitous Healthcare (uHealthcare 2017)*, p. 85, Seoul, Korea, 2017.

Research Article

Noninvasive Estimation of Joint Moments with Inertial Sensor System for Analysis of STS Rehabilitation Training

Kun Liu , Jianchao Yan , Yong Liu , and Ming Ye 

School of Mechanical Science and Engineering, Jilin University, Jilin 130025, China

Correspondence should be addressed to Yong Liu; liuyong16@mails.jlu.edu.cn

Received 5 August 2017; Accepted 11 December 2017; Published 11 February 2018

Academic Editor: Li Zhang

Copyright © 2018 Kun Liu et al. This is an open access article distributed under the Creative Commons Attribution License, which permits unrestricted use, distribution, and reproduction in any medium, provided the original work is properly cited.

An original approach for noninvasive estimation of lower limb joint moments for analysis of STS rehabilitation training with only inertial measurement units was presented based on a piecewise three-segment STS biomechanical model and a double-sensor difference based algorithm. Joint kinematic and kinetic analysis using a customized wearable sensor system composed of accelerometers and gyroscopes were presented and evaluated compared with a referenced camera system by five healthy subjects and five patients in rehabilitation. Since there is no integration of angular acceleration or angular velocity, the result is not distorted without offset and drift. Besides, since there are no physical sensors implanted in the lower limb joints based on the algorithm, it is feasible to noninvasively analyze STS kinematics and kinetics with less numbers and types of inertial sensors than those mentioned in other methods. Compared with the results from the reference system, the developed wearable sensor system is available to do spatiotemporal analysis of STS task with fewer sensors and high degree of accuracy, to apply guidance and reference for rehabilitation training or desired feedback for the control of powered exoskeleton system.

1. Introduction

Sit-to-stand (STS) movement is one of the most commonly performed functional activities [1, 2], which requires both relatively large joint moments and precise balance control [3, 4]. STS movement is also a complex dynamic task that requires regulation of lower limb muscles to drive the human body while rising from a chair from a stable seated position to a relatively unstable upright stance [5–8]. However, for dependent people having lost part of their lower limb functionalities without adequate joint moment, the activity becomes tiring and cannot be accomplished without the help of external assistance [9]. Therefore, the ability to perform STS transfer in a reliable and safe manner with adequate joint moment [10] becomes a key element of movement rehabilitation in orthopedically or neurologically impaired individuals.

Ambulatory estimation and analysis of STS movement with wearable sensors is a promising clinical tool to diagnose human motion. Quantitative kinetic and kinematic information of STS is crucial for the clinical evaluation and

therapeutic treatment comparisons in the orthopedic and rehabilitation fields. However, since the camera-based human motion analysis system is bulky, expensive, and complex, it restricts the user to a constrained environment where cameras are installed; therefore, it is not applicable for out-lab ambulatory measurement of lower limb posture in ordinary life [11]. Recently, small inertial sensor measurement modules (IMUs) comprised of accelerometers, gyroscopes, and (or) magnetometers were developed and appear to be promising for estimating human movement. Various methods using inertial sensors were available for assessing 3D human posture in motion [12–14]; however, few papers proposed methods to estimate kinetics of lower limb joints using wearable inertia sensors and also few detailed applications of inertia sensors for noninvasive analysis and diagnosis of STS rehabilitation training.

In order to make full use of the remaining muscle power of the patient, assistant systems such as exoskeleton/orthosis and partial body weight support (PBWS) rehabilitation robot were designed to make up for the lack of joint moment with external assistance [15–18]. One of the key technical

problems of assistant system is how to noninvasively estimate the joint moment with wearable sensors especially for the control of wearable exoskeleton/orthosis. Furthermore, monitored rehabilitation exercises have been shown to be more effective than practice without feedback [19]. Thence, the wearable monitoring of any STS rehabilitation program is desirable to ensure the correct execution of the exercise by patients and also to quantify the progress toward the recovery of muscle strength, endurance, and increase in the range of motion. Bonnet et al. [20] investigated the possibility of estimating 3D lower limb joint kinematics using a single inertial measurement unit during lower limb rehabilitation. But they only monitored the hip and knee joint angles without any kinetic analysis of human motion. Stieglitz et al. [21] designed a setup to noninvasively measure the joint torque development at given ankle positions in an intact leg, but it is only applicable to test the isometric torque development in accordance to the anatomical features of the rat model, not a human biomechanical model. Inkster et al. [22] analyzed the joint moment for postural control during STS task by individuals with mild Parkinson's disease. But all of the kinematic and kinetic data were obtained from nonwearable imaging systems and force plate in the lab, which were only suitable for offline processing and analysis. Yoshioka et al. [23, 24] did biomechanical kinematic and kinetic analyses of STS movements and computed minimum peak joint moments and analyzed the relation between movement time and joint moment development during a STS task. Although their presented research has practical applications in STS rehabilitations and exercise prescription, the required muscle strength was quantitatively estimated based on optical motion capture system with 7 cameras, which occupied a lot of space and was not convenient for portable systems with real-time control. Wang et al. [25] presented a method to predict the joint moment using wearable EMG sensors with a neural network model of muscle activations, but it was validated at the elbow, not the lower limb joints. Karatsidis et al. [26] demonstrated that estimation of 3D ground reaction force and moments during gait using only kinematic information obtained from inertial sensors agreed with "gold-standard" force plate measurements, but there was no further analysis of the joint kinetics.

The purpose of this study is to noninvasively estimate the joint moments using wearable IMUs to provide reference for making exercise prescription of STS rehabilitation training. The kinematic and kinetic profiles underlying the STS movement were analyzed with two groups: (1) patients with lower limb muscle dysfunction but in rehabilitation and could perform STS task independently and (2) age-matched healthy controls that could perform in fluent STS motion task independently. Compared with the healthy subjects, it was hypothesized that patients in STS rehabilitation would exhibit altered anticipatory postural control which would include an increased preparatory hip flexion and forward displacement of the COM prior to seat-off. By comparing with the kinematic and kinetic data derived from the IMUs and referenced camera system and force plate, the accuracy and availability of the developed wearable

sensor system were verified. By comparing and analyzing the calculated joint moments of two groups of the subjects, the rehabilitation condition of the patients with lower limb muscle dysfunction during the STS training were more explicit. It has the extensive applicability and practical significance for making exercise prescription of STS rehabilitation training. Also, the presented method to noninvasively estimate the lower limb joint moments using IMUs was useful and crucial for the real-time control of wearable exoskeleton/orthosis.

2. Methods

As we presented [27], the segment rotational angles (joint angles) in sagittal plane could be calculated using the sensor-measured accelerations based on a double-sensor difference based algorithm. Then the angular acceleration of each segment based on the calculated joint angles and measured accelerations was calculated. In order to do kinematic and kinetic analyses of STS movement using wearable IMUs, a piecewise two-dimensional (2D) three-segment STS biomechanical model of the human body is needed. A piecewise biomechanical model for STS kinematic analysis was presented in our previous work [28] just for a control strategy research, but there was no kinetic analysis of STS. Here the model is further developed for the STS joint kinetic analysis using IMUs as shown in Figure 1 and Figure 2. Then we did the kinetics and kinematics analysis of the STS movement and proposed the angular accelerations of the shank, thigh, and HAT (α_1 , α_2 , and α_3) and the joint moments (M_i , where $i = 1, 2, 3$) based on the further developed model of that which we presented in our previous work [28]

Before the buttocks leaved the chair (seat-off), the lower limb segment remained stationary, and the main movement was that the HAT (head, neck, arms, and torso) rotated forward around the hip joint with a certain spinal curvature. That the spinal curvature would lead to length variation of the HAT and location change of the COM of HAT will make the calculated result deviate from the true value. Therefore, in the experiment, the subjects would be told to minimize the spinal curvature as possible as they could and the spinal curvature was not taken into account in the STS biomechanical model. Therefore, based on the piecewise 2D three-segment STS biomechanical model as proposed in Figure 1, we calculated the angular acceleration (α_3) of center of mass (COM) of the HAT before seat-off.

$$\alpha_3 = \ddot{\theta}_3 = \frac{g \cos \theta_3 - a_{3y_3}}{k_3 l_3}. \quad (1)$$

After seat-off as shown in Figure 1, the three segments of the whole body rotated about their corresponding joints until the whole body stretched to the upright static posture finally. We calculated the angular accelerations of the shank, thigh, and HAT (α_1 , α_2 , and α_3) based on the calculated joint angles and angular velocities as shown in

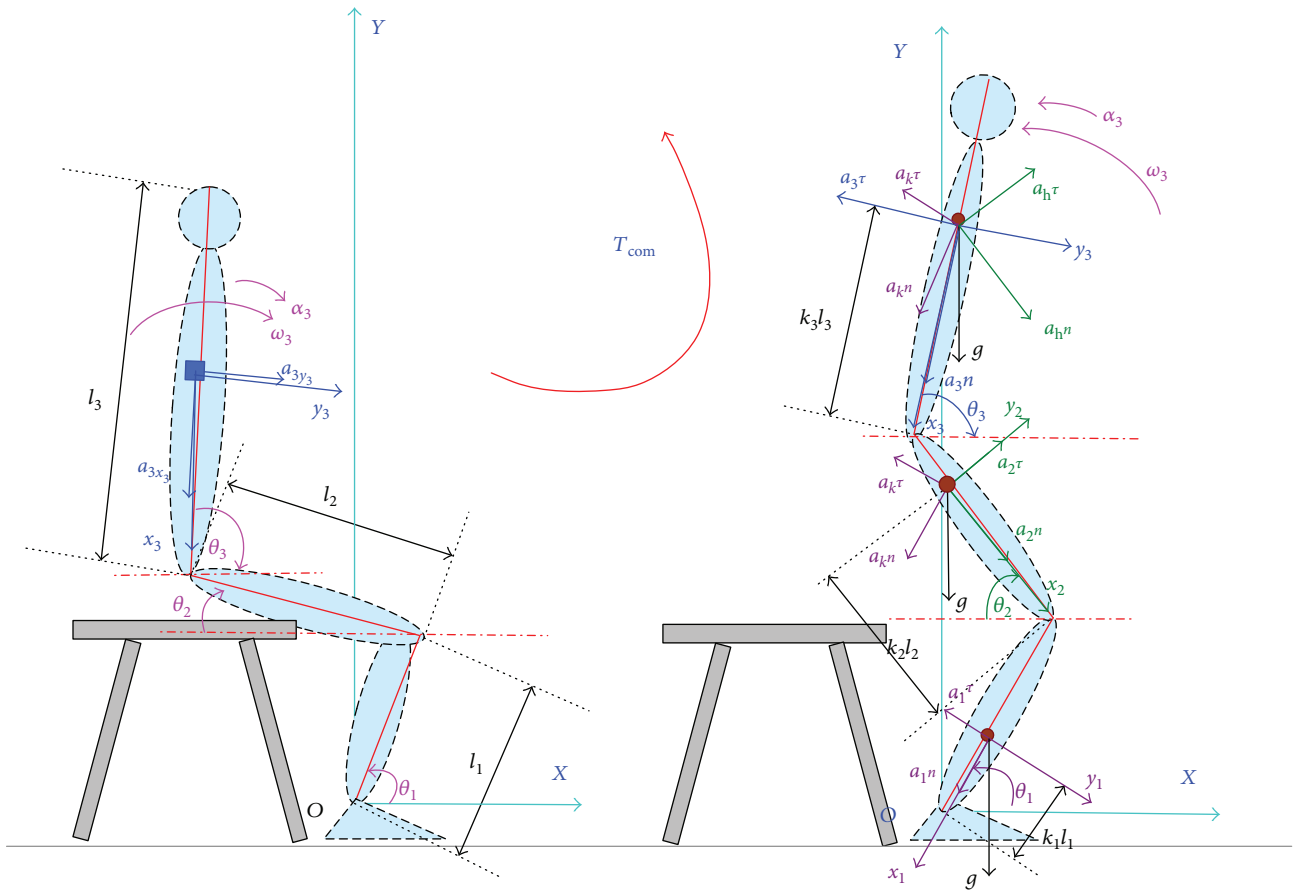


FIGURE 1: Kinematic analysis of STS movement in sagittal plane based on a piecewise 2D three-segment STS biomechanical model of the human body.

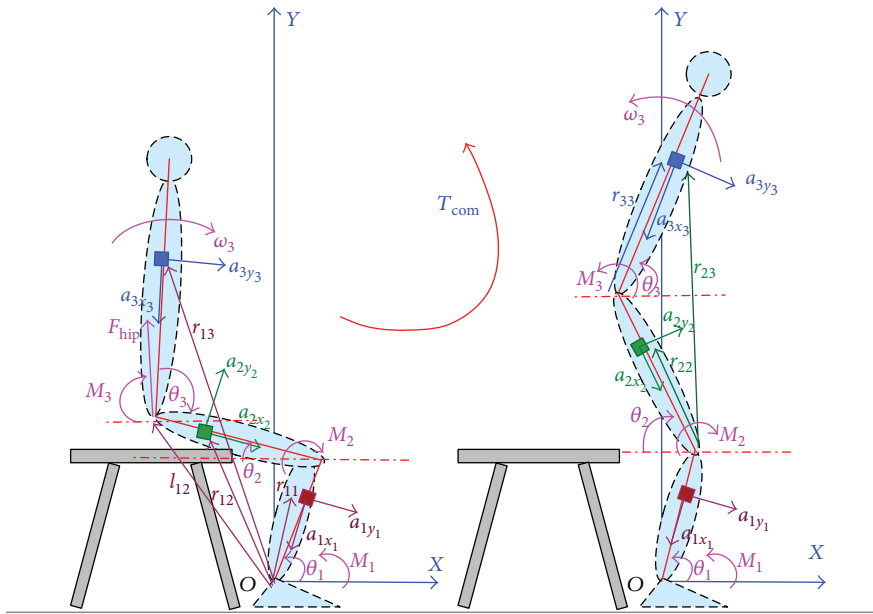


FIGURE 2: Kinetic analysis of STS movement in sagittal plane based on a piecewise 2D three-segment STS biomechanical model of the human body.

$$\begin{aligned}
\alpha_1 &= \ddot{\theta}_1 = k_1 l_1^{-1} \left(g \cos \theta_1 - a_{1y_1} \right), \\
\alpha_2 &= \ddot{\theta}_2 = (k_2 l_2)^{-1} \left(a_{2y_2} + l_1 \omega_1^2 \sin(\theta_1 + \theta_2) \right. \\
&\quad \left. - k_1^{-1} \left(g \cos \theta_1 - a_{1y_1} \right) \cos(\theta_1 + \theta_2) + g \cos \theta_2 \right), \\
\alpha_3 &= \ddot{\theta}_3 = (k_3 l_3)^{-1} \left\{ k_2^{-1} \left(a_{2y_2} + l_1 \omega_1^2 \sin(\theta_1 + \theta_2) \right) \right. \\
&\quad \left. - k_1^{-1} \left(g \cos \theta_1 - a_{1y_1} \right) \cos(\theta_1 + \theta_2) \right. \\
&\quad \left. + g \cos \theta_2 \right\} \cos(\theta_2 + \theta_3) \\
&\quad + a_{3y_3} - g \cos \theta_3 + l_1 \omega_1^2 \sin(\theta_3 - \theta_1) \\
&\quad + k_1^{-1} \left(g \cos \theta_1 - a_{1y_1} \right) \cos(\cos \theta_3 - \theta_1) \\
&\quad \left. - l_2 \omega_2^2 \sin(\theta_2 + \theta_3) \right\}, \tag{2}
\end{aligned}$$

where l_i , $i = 1, 2, 3$, is the length of the shank, thigh, and HAT, θ_i , $i = 1, 2, 3$, is the ankle, knee, and hip joint angles which were calculated based on a double-sensor difference based algorithm [23], and ω_i , $i = 1, 2, 3$, is the angular velocities of the shank, thigh, and HAT about the corresponding joint. T_{com} is the STS trajectory of COM.

Based on kinetic analysis of STS as shown in Figure 2, we calculated the joint moments (M_i , $i = 1, 2, 3$) before seat-off as follows:

$$\begin{aligned}
\vec{M}_3 &= J_3 \cdot \vec{\alpha}_3 + \vec{r}_{33} \times (m_3 \cdot \vec{a}_3), \\
\vec{M}_2 &= J_3 \cdot \vec{\alpha}_3 + \vec{r}_{23} \times (m_3 \cdot \vec{a}_3) + \vec{r}_{22} \times (m_2 \cdot \vec{g}) \\
&\quad - \vec{l}_{22'} \times \vec{F}_{\text{hip}}, \\
\vec{M}_1 &= J_3 \cdot \vec{\alpha}_3 + \vec{r}_{13} \times (m_3 \cdot \vec{a}_3) + \vec{r}_{12} \times (m_2 \cdot \vec{g}) \\
&\quad + \vec{r}_{11} \times (m_1 \cdot \vec{g}) + \vec{l}_{12'} \times \vec{F}_{\text{hip}}. \tag{3}
\end{aligned}$$

Then the joint moments before seat-off were reformulated in detail as follows:

$$\begin{aligned}
M_3 &= J_3 (k_3 l_3)^{-1} \left(a_{3y_3} - g c_3 \right) + m_3 a_{3y_3} k_3 l_3, \\
M_2 &= F_{\text{hip}} l_2 c_2 - J_3 (k_3 l_3)^{-1} \left(a_{3y_3} - g c_3 \right) - m_2 g k_2 l_2 c_2 \\
&\quad - m_3 a_{3x_3} (2k_3 l_3)^{-1} (2l_2^2 - 2l_2 k_3 l_3 c_{2+3}) \\
&\quad - m_3 a_{3y_3} (2k_3 l_3)^{-1} (2k_3^2 l_3^2 - 2l_2 k_3 l_3 c_{2+3}), \\
M_1 &= J_3 (k_3 l_3)^{-1} \left(a_{3y_3} - g c_3 \right) + m_1 g k_1 l_1 c_1 \\
&\quad + F_{\text{hip}} (l_2 c_2 - l_1 c_1) + m_3 a_{3x_3} (2k_3 l_3)^{-1} \\
&\quad \cdot \left((2l_1^2 + 2l_2^2 + l_3^2 - 4l_1 l_2 c_{1+2} + 2l_1 k_3 l_3 c_{1-3} \right. \\
&\quad \left. - 2l_2 k_3 l_3 c_{2+3})^{1/2} - k_3^2 l_3^2 \right) - m_3 a_{3y_3} (2k_3 l_3)^{-1} \\
&\quad \cdot (k_3^2 l_3^2 + l_3^2 + 2l_1 k_3 l_3 c_{1-3} - 2l_2 k_3 l_3 c_{2+3}). \tag{4}
\end{aligned}$$

We also calculated the moments of the hip, knee, and ankle joint after seat-off as follows:

$$\begin{aligned}
\vec{M}_3 &= J_3 \cdot \vec{\alpha}_3 + \vec{r}_{33} \times (m_3 \cdot \vec{a}_3), \\
\vec{M}_2 &= -J_3 \cdot \vec{\alpha}_3 - J_2 \cdot \vec{\alpha}_2 - \vec{r}_{23} \\
&\quad \times (m_3 \cdot \vec{a}_3) - \vec{r}_{22} \times (m_2 \cdot \vec{a}_2), \\
\vec{M}_1 &= J_3 \cdot \vec{\alpha}_3 + J_2 \cdot \vec{\alpha}_2 + J_1 \cdot \vec{\alpha}_1 + \vec{r}_{13} \\
&\quad \times (m_3 \cdot \vec{a}_3) + \vec{r}_{12} \times (m_2 \cdot \vec{a}_2) \\
&\quad + \vec{r}_{11} \times (m_1 \cdot \vec{a}_1). \tag{5}
\end{aligned}$$

Then the joint moments after seat-off were reformulated in detail as follows:

$$\begin{aligned}
M_3 &= J_3 (k_3 l_3)^{-1} \left(k_2^{-1} \left(a_{2y_2} + l_1 \omega_1^2 s_{1+2} \right) \right. \\
&\quad \left. - k_1^{-1} \left(g c_1 - a_{1y_1} \right) c_{1+2} + g c_2 \right) c_{2+3} \\
&\quad + a_{3y_3} - g c_3 + l_1 \omega_1^2 s_{3-1} + k_1^{-1} \\
&\quad \cdot \left(g c_1 - a_{1y_1} \right) c_{3-1} - l_2 \omega_2^2 s_{2+3} \Big) + m_3 a_{3y_3} k_3 l_3, \\
M_2 &= -J_2 (k_2 l_2)^{-1} \left(a_{2y_2} + l_1 \omega_1^2 s_{1+2} \right) \\
&\quad - k_1^{-1} \left(g c_1 - a_{1y_1} \right) c_{1+2} + g c_2 \\
&\quad - J_3 (k_3 l_3)^{-1} \left(k_2^{-1} \left(a_{2y_2} + l_1 \omega_1^2 s_{1+2} \right) \right. \\
&\quad \left. - k_1^{-1} \left(g c_1 - a_{1y_1} \right) c_{1+2} + g c_2 \right) c_{2+3} + a_{3y_3} - g c_3 \\
&\quad + l_1 \omega_1^2 s_{3-1} + k_1^{-1} \left(g c_1 - a_{1y_1} \right) c_{3-1} - l_2 \omega_2^2 s_{2+3} \Big) \\
&\quad - m_2 a_{2y_2} k_2 l_2 - m_3 a_{3x_3} (2k_3 l_3)^{-1} (2l_2^2 - 2l_2 k_3 l_3 c_{2+3}) \\
&\quad - m_3 a_{3y_3} (2k_3 l_3)^{-1} (2k_3^2 l_3^2 - 2l_2 k_3 l_3 c_{2+3}), \\
M_1 &= J_1 (k_1 l_1)^{-1} \left(g c_1 - a_{1y_1} \right) + J_2 (k_2 l_2)^{-1} \\
&\quad \cdot \left\{ a_{2y_2} + l_1 \omega_1^2 s_{1+2} - k_1^{-1} \left(g c_1 - a_{1y_1} \right) c_{1+2} + g c_2 \right\} \\
&\quad + J_3 (k_3 l_3)^{-1} \left\{ k_2^{-1} \left\{ a_{2y_2} + l_1 \omega_1^2 s_{1+2} \right. \right. \\
&\quad \left. \left. - k_1^{-1} \left(g c_1 - a_{1y_1} \right) c_{1+2} + g c_2 \right\} c_{2+3} + a_{3y_3} - g c_3 \right. \\
&\quad \left. + l_1 \omega_1^2 s_{3-1} + k_1^{-1} \left(g c_1 - a_{1y_1} \right) c_{3-1} - l_2 \omega_2^2 s_{2+3} \right\} \\
&\quad + m_1 a_{1y_1} k_1 l_1 + m_2 a_{2x_2} (2k_2 l_2)^{-1} (2l_1^2 - 2l_1 k_2 l_2 c_{1+2}) \\
&\quad + m_2 a_{2y_2} (2k_2 l_2)^{-1} (2k_2^2 l_2^2 - 2l_1 k_2 l_2 c_{1+2}) \\
&\quad + m_3 a_{3x_3} (2k_3 l_3)^{-1} \left((2l_1^2 + 2l_2^2 + l_3^2 - 4l_1 l_2 c_{1+2} \right. \\
&\quad \left. + 2l_1 k_3 l_3 c_{1-3} - 2l_2 k_3 l_3 c_{2+3})^{1/2} - k_3^2 l_3^2 \right) \\
&\quad - m_3 a_{3y_3} (2k_3 l_3)^{-1} (k_3^2 l_3^2 + l_3^2 + 2l_1 k_3 l_3 c_{1-3} - 2l_2 k_3 l_3 c_{2+3}). \tag{6}
\end{aligned}$$

As shown in all the equations, the joint moments were calculated from the sensor-measured data without any integral or differential operations.

The mass and dimension of each segment of the subjects were estimated based on the average current Chinese male inertial parameters of body segments according to Chinese

TABLE 1: Average inertia parameters of body segments of current Chinese male adults according to Chinese national standards.

Segments (definition)	Segment length/height (%)	Segment mass/whole body mass (%)	Center of mass/segment length distal	Moment of inertia (kg·m ²)
Foot (lateral malleolus/head metatarsal)	14.77	3.6	0.5	0.0044
Shank (femoral condyles/medial malleolus)	23.86	10.6	0.567	0.0385
Thigh (greater trochanter/femoral condyles)	28.13	22.7	0.567	0.1978
HAT (greater trochanter/glenohumeral joint)	50.17	63.1	0.374	0.9180

national standards [29] as shown in Table 1. The moment of inertia of each segment was estimated based on the height and total mass of the subject [30] and shown in Table 1. All segments were assumed to be rigid, and the STS movement was performed only in the sagittal plane.

3. Experiment

Two force plates were developed with pressure sensors (YZC-1B) and sampled at 100 Hz using a microcontroller (Arduino UNO). One force plate (force plate A) was placed on the anterior section of the chair to measure the vertical chair reaction force (VCRF) before subjects' thighs left the seat (seat-off). Another force plate (force plate B) was fixed on the ground under subjects' feet to measure the vertical ground reaction force (VGRF) throughout the STS process. To measure the accelerations and angular velocities of the segments for calculating the joint angles, angular accelerations, and joint moments, three customized IMUs (wearable sensor JY-901B, 1.1 × 1.1 × 0.5 inches with battery and Bluetooth communication) were attached on the lateral surface of shank, thigh, and HAT with elastic straps, coinciding with the COM of each segment in the sagittal plane as shown in Figure 2 as possible. A microcontroller (Arduino UNO) was used to capture accelerations and angular velocity data from the IMUs at 100 Hz, store data, and communicate with a PC in real time. During the initial calibration, the two force plates were positioned horizontally under the feet and on the chair with calibration errors of 0.53% and 0.61% in the vertical direction. The orientation of segments was estimated by combining the orientations of individual IMUs with the STS biomechanical model of the human body. To relate the sensor orientations to segment orientations, a sensor-to-segment calibration procedure is performed referring to [26]. Each of the three IMUs was repeatedly adjusted in the sagittal plane with the x -axis coinciding with the axial direction of its corresponding segment in the segment coordinate frames based on the recommendations of the International Society of Biomechanics [31]. Simultaneously, a commercial optical motion analysis system, NAC Hi-Dcam II Digital High Speed Camera Systems (NAC Image Technology, Japan), was used to track and measure the 3D trajectories of the retroreflective markers on the segments of the subjects, with sampling frequency of 100 Hz and calibration error 0.22%. Then the referenced angle, angular velocity, and acceleration of the segments were obtained from the referenced camera system by analyzing the motion parameters of the markers and then were used to calculate the angular

accelerations and joint moments based on the developed method offline.

Five healthy male subjects (age = 28.1 ± 6.3 years; mass = 67.3 ± 8.5 kg; height = 173.5 ± 6.7 cm) without known lower limb musculoskeletal or neurological dysfunction and five male patients in STS rehabilitation (age = 29.5 ± 7.5 years; mass = 65.4 ± 6.3 kg; height = 172.5 ± 7.6 cm) with mild lower limb dyskinesia but without affecting their ability of performing STS movement participated in this study by two groups and received informed consent. The experimental protocol was approved by the Human Ethical Review Committee of Jilin University. After familiarization, each of the ten participants reported no serious impediment of either IMUs or force plates and performed three STS trials as a task at self-selected appropriate speed (healthy subjects' STS within 3 s and patients' STS within 7 s) wearing the developed sensor system in the working space of the referenced optical motion capture system (RCS). Finally, 30 trials (3 trials × 1 task per subject × 10 subjects) were achieved for analysis. Although a task of three STS trials were performed by one subject, the STS time and the amount of captured data of each trial could not be absolutely the same. Therefore, the time of zero VCRF (time of seat-off) was so important that it was designated as the referenced standard point (RSP) within whole STS to synchronize the three trials of a task to the same percentage metric, then the ensemble averages of the captured angular velocities and accelerations of the three STS trails in a task performed by one subject were got for calculating the composite joint angles and angular accelerations of each segment's COM in the STS movement. By comparing with the processed kinematic and kinetic data of the ten tasks achieved from the IMUs and RCS, the accuracy and availability of the developed wearable sensor system could be verified. Furthermore, the joint moments of ankle, knee, and hip joints of each subject of the ten were calculated based on the corresponding ensemble averages of all the original inertial parameters of a task derived from the sensor system. Five groups of hip, knee, and ankle joint moments of the five healthy subjects were, respectively, synchronized again to get a group of ensemble average joint moments as references for comparing and analyzing the STS rehabilitation conditions of the five patients. Figure 3 shows a healthy male subject performing a STS trial with the developed sensor system in the working space of the RCS.

4. Result

All signals captured by the developed sensor system (IMUs and force plates) and the RCS were offline processed by



FIGURE 3: Experiment using the developed sensor system in the working space of the RCS.

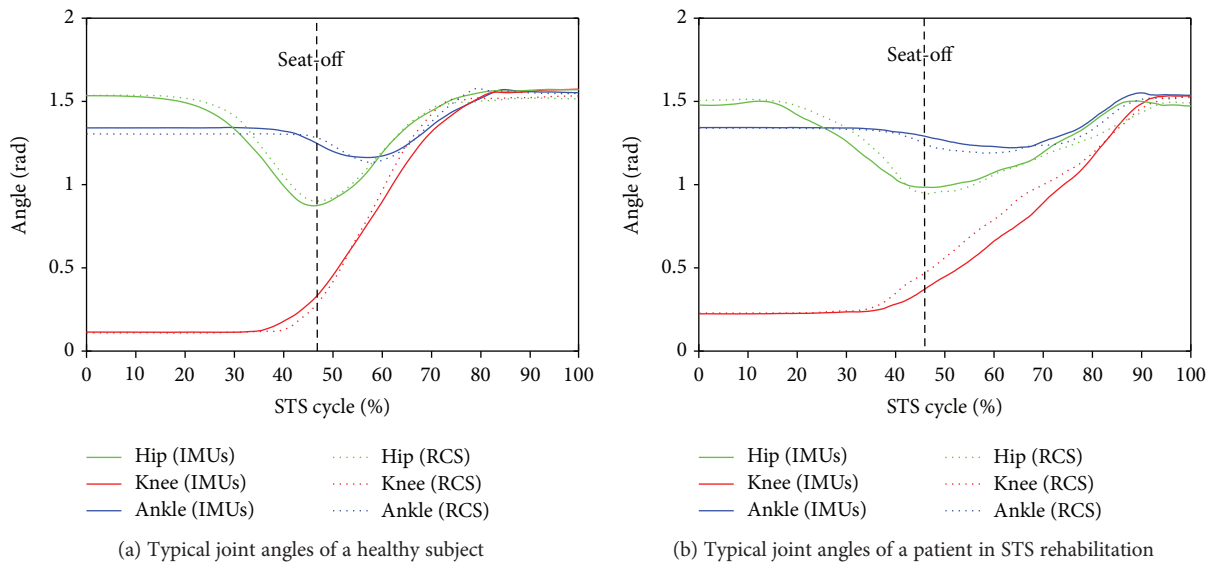


FIGURE 4: Typical hip, knee, and ankle joint angles during the STS tasks performed by a healthy subject and a patient.

Matlab. A low-pass filter with a cutoff frequency of 20 Hz was used to remove noise from all the raw data. A typical group of the calculated compositive hip, knee, and ankle joint angles (green, red, and blue lines correspondingly) and COM angular accelerations of the HAT, thigh, and shank (green, red, and blue lines correspondingly) derived from one of the five healthy subjects using the IMUs (dotted lines) and the RCS (solid lines) were compared as shown in Figure 4(a) and Figure 5(a), and the same parameters acquired from one of

the five patients in STS rehabilitation were compared as shown in Figure 4(b) and Figure 5(b). The corresponding VCRF and VGRF in the same STS task performed by the healthy subject and the patient in STS rehabilitation were, respectively, shown in Figures 6(a) and 6(b), which were used to offer the referenced standard point (seat-off) within whole STS to synchronize the three trials of a task to the same percentage metric. The entire STS cycles of all the trials were synchronized by a percentage metric.

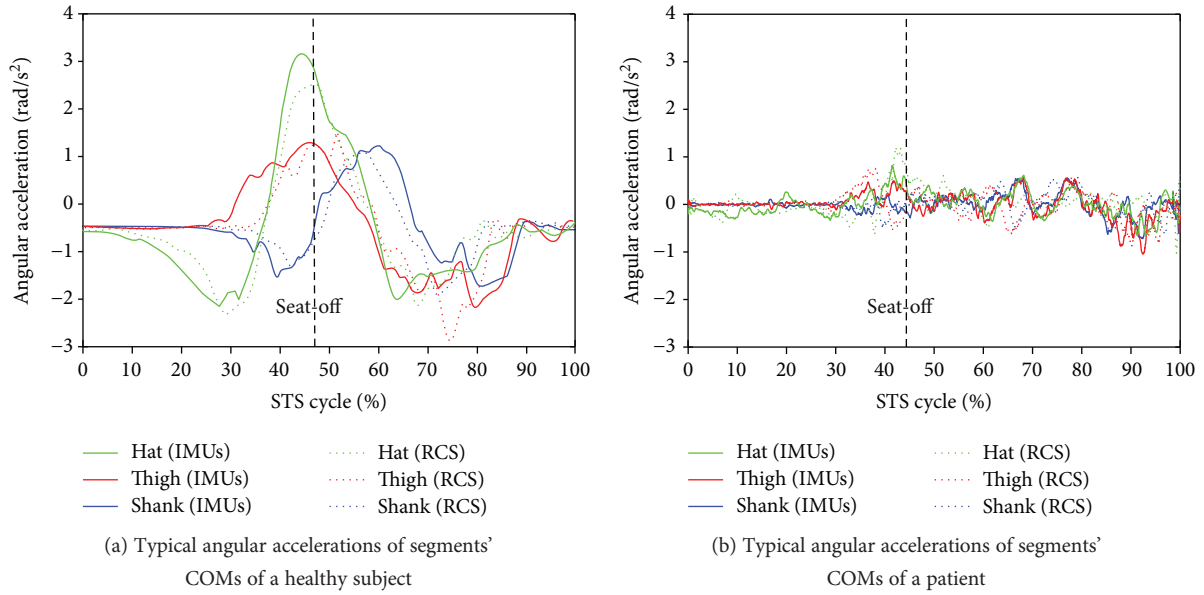


FIGURE 5: Typical angular accelerations of the COMs of HAT, thigh, and shank segments during the STS task performed by a healthy subject and a patient.

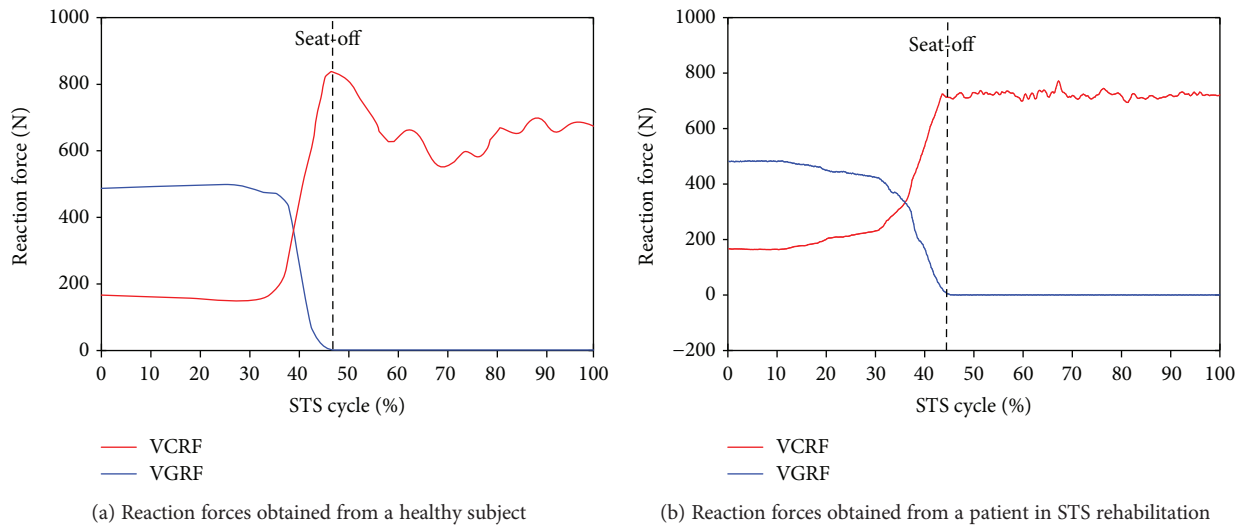


FIGURE 6: Typical VCRF from plate A (red line) under the feet and VGRF from force plate B (blue line) on the chair in the STS tasks performed by a healthy subject and a patient in STS rehabilitation.

The accuracy of the developed sensor system should be evaluated by comparing the measured original inertial data (joint angular velocities and accelerations of the segments' COM) with those captured by the RCS, but not by comparing the joint moments, which were calculated from the original inertial data. However, since the previous calculated composite joint angles (θ_1 , θ_2 , and θ_3) and angular accelerations of each segment's COM (α_1 , α_2 , and α_3) were derived from the synchronized ensemble averages of the measured original angular velocities and accelerations of three STS trails in a task, the accuracy of the sensor system could be more sufficiently evaluated by comparing θ_1 , θ_2 , θ_3 , α_1 , α_2 , and α_3 based on more groups of measured original data between the two different systems. All the analysis parameters between the referenced and calculated

composite joint angles (θ_1 , θ_2 , and θ_3) and angular accelerations of each segment's COM (α_1 , α_2 , and α_3) of the five healthy subjects are, respectively, shown in Table 2 and Table 3, where RMSE was the root mean square of the differences between the referenced and calculated values, R was Pearson's correlation coefficients, and e_{\max} was the maximum error. The same analysis parameters of the five patients are shown in Table 4 and Table 5. The two groups of the subjects in the four tables were numbered according to their STS times from short to long. The agreement between the data of the IMUs and RCS synchronized and normalized to the STS cycle was derived from R , which were categorized as weak ($R \leq 0.35$), moderate ($0.35 < R \leq 0.67$), strong ($0.67 < R \leq 0.9$), and excellent ($R > 0.9$), according to [26].

TABLE 2: Analysis and comparison of compositive joint angles (θ_1 , θ_2 , and θ_3) derived from the IMUs and RCS in STS tasks performed by healthy subjects.

Healthy subjects	Ankle joint angle θ_1 (rad)			Knee joint angle θ_2 (rad)			Hip joint angle θ_3 (rad)		
	RMSE	R	e_{\max}	RMSE	R	e_{\max}	RMSE	R	e_{\max}
1	0.079	0.951	0.094	0.068	0.919	0.166	0.031	0.933	0.120
2	0.092	0.939	0.101	0.069	0.902	0.198	0.039	0.929	0.124
3	0.112	0.926	0.114	0.085	0.869	0.201	0.046	0.928	0.157
4	0.117	0.919	0.179	0.094	0.853	0.229	0.054	0.915	0.195
5	0.123	0.917	0.198	0.112	0.808	0.286	0.060	0.901	0.287
Average	0.105	0.930	0.137	0.087	0.870	0.216	0.046	0.921	0.177

TABLE 3: Analysis and comparison of compositive angular accelerations of each segment's COM (α_1 , α_2 , and α_3) derived from the IMUs and RCS in STS tasks performed by healthy subjects.

Healthy subjects	Ankle joint angular acceleration α_1 (rad/s ²)			Knee joint angular acceleration α_2 (rad/s ²)			Hip joint angular acceleration α_3 (rad/s ²)		
	RMSE	R	e_{\max}	RMSE	R	e_{\max}	RMSE	R	e_{\max}
1	3.056	0.885	0.725	2.998	0.912	0.924	1.646	0.824	0.724
2	3.243	0.843	0.953	3.054	0.895	0.742	1.850	0.815	0.753
3	3.562	0.821	0.966	3.155	0.852	0.977	2.096	0.795	0.868
4	3.982	0.796	1.028	3.432	0.824	1.124	2.554	0.801	0.902
5	4.244	0.730	1.150	3.752	0.810	1.109	2.730	0.765	0.890
Average	3.617	0.815	0.964	3.278	0.859	0.975	2.175	0.800	0.827

TABLE 4: Analysis and comparison of compositive joint angles (θ_1 , θ_2 , and θ_3) derived from the IMUs and RCS in STS tasks performed by patients.

Patients	Ankle joint angle θ_1 (rad)			Knee joint angle θ_2 (rad)			Hip joint angle θ_3 (rad)		
	RMSE	R	e_{\max}	RMSE	R	e_{\max}	RMSE	R	e_{\max}
1	0.117	0.805	0.103	0.069	0.808	0.217	0.049	0.848	0.180
2	0.159	0.819	0.124	0.075	0.751	0.324	0.051	0.741	0.184
3	0.235	0.740	0.131	0.087	0.748	0.255	0.054	0.788	0.232
4	0.257	0.737	0.205	0.090	0.745	0.207	0.063	0.692	0.243
5	0.362	0.625	0.166	0.096	0.713	0.269	0.070	0.715	0.199
Average	0.226	0.745	0.146	0.083	0.753	0.254	0.057	0.757	0.208

TABLE 5: Analysis and comparison of compositive angular accelerations of each segment's COM (α_1 , α_2 , and α_3) derived from the IMUs and RCS in STS tasks performed by patients.

Patients	Ankle joint angular acceleration α_1 (rad/s ²)			Knee joint angular acceleration α_2 (rad/s ²)			Hip joint angular acceleration α_3 (rad/s ²)		
	RMSE	R	e_{\max}	RMSE	R	e_{\max}	RMSE	R	e_{\max}
1	0.124	0.524	0.195	0.122	0.563	0.143	0.189	0.621	0.132
2	0.182	0.542	0.220	0.147	0.522	0.213	0.201	0.608	0.237
3	0.167	0.601	0.172	0.261	0.512	0.249	0.227	0.534	0.258
4	0.201	0.491	0.253	0.166	0.509	0.197	0.186	0.522	0.355
5	0.230	0.483	0.279	0.245	0.504	0.288	0.223	0.499	0.306
Average	0.181	0.528	0.224	0.188	0.522	0.218	0.205	0.557	0.258

Furthermore, to analyze and evaluate the availability of the developed sensor system for noninvasively analyzing the kinetics of the STS movement, the joint moments of ankle, knee, and hip joints of the ten subjects were, respectively, calculated according to the presented method based

on the corresponding synchronized ensemble averages of the measured original inertial data from IMUs. Thereinto, the five groups of hip, knee, and ankle joint moments of the five healthy subjects were further synchronized to get one group of ensemble average joint moments as the reference

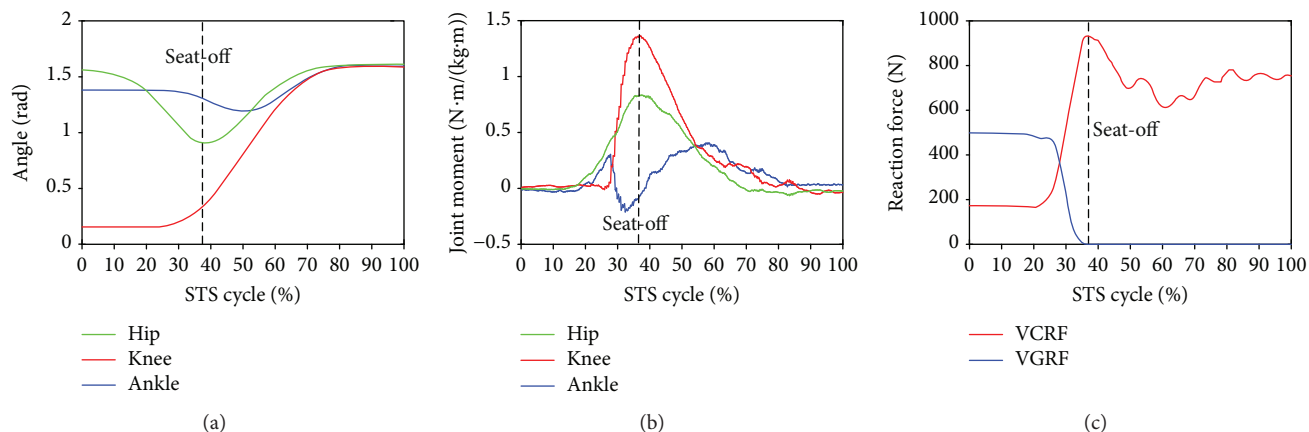


FIGURE 7: Percentage synchronized ensemble averages of the three joint angles (a), three joint moments (b), and two reaction forces (c) out of the 15 trials (3 trials \times 1 task per subject \times 5 healthy male subjects) as the reference (JMr) for comparing and analyzing the STS rehabilitation training of the five patients in rehabilitation.

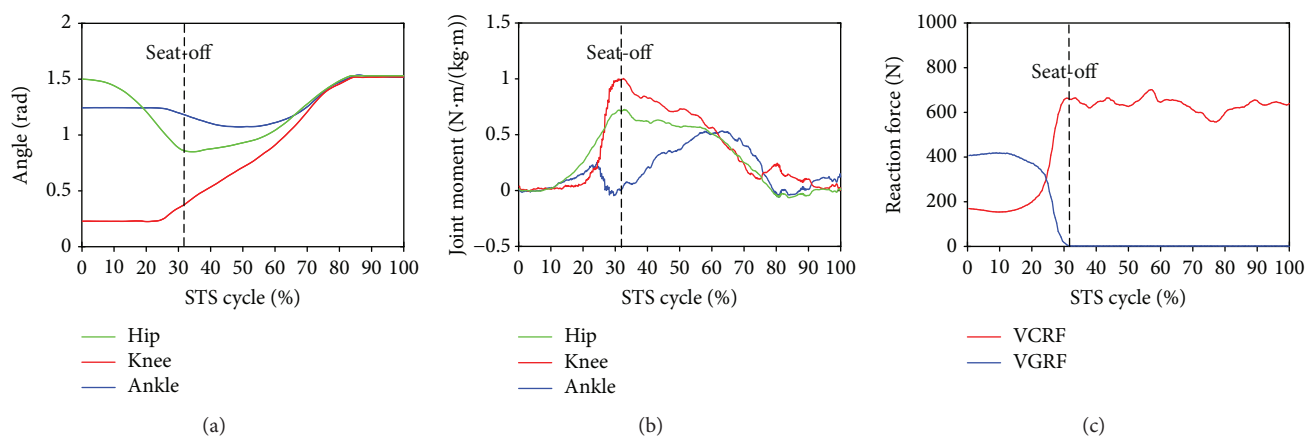


FIGURE 8: Percentage synchronized ensemble averages of the three joint angles (a), three joint moments (b) and two reaction forces (c) out of the 3 trials of a task performed by patient 1 (P1).

(JMr) for comparing and analyzing the STS rehabilitation training of the five patients and were shown in Figure 7. To compare the same joint moment of different STS tasks performed by different subjects, it was normalized to per Nm/kg·m divided by the height and mass of the corresponding subjects. All the corresponding curves of the patients were also shown in Figures 8–12. To do quantitative analysis of the STS movement, the peak-valley value of JMr and patient's joint moments (JMp), the peak value of VGRF and VCRF, as crucial quantitative characteristics, were shown in Table 6 and compared in Figure 13. Finally, to compare and analyze the STS rehabilitation status of each patient, the agreement between JMr and JMp synchronized to the STS cycle referred to the RSP was also derived from Pearson's correlation coefficients (R) and shown in Table 7.

5. Discussion and Conclusion

Comparing the same kinematic parameters (θ , α) derived from the developed IMUs (dotted lines) and the RCS (solid lines) curved by the same color but different lines in the same figure in Figure 4 and Figure 5, it was found that the

corresponding parameters were basically the same except for a few subtle differences. Because the shape of each lower limb segment was an irregular approximate cone-cylinder, although a sensor-to-segment calibration procedure to relate the sensor orientations to segment orientations is performed, it was difficult to guarantee two axes of the IMUs absolutely in the sagittal plane in initial setting up. Therefore, the measured angular velocities and accelerations for calculating the joint angles, angular accelerations, and joint moments was not exactly the data needed in the equations but that with certain systematic errors and noise. Especially referred to all the analysis parameters between the referenced and calculated joint angles (θ_1 , θ_2 , and θ_3) and angular accelerations of each segment's COM (α_1 , α_2 , and α_3) of the five healthy subjects and five patients in Tables 2–5, faster and more fluent STS movements performed by either healthy subjects or patients resulted in lower e_{\max} and RMSE and greater correlation coefficient. As it was more difficult to firmly fix the IMUs on the soft human body segments than on a rigid body without any slight movement, the errors were predictable and inevitable. Especially in lower-speed STS motion, long duration of skin motion artifact due to impact loading and

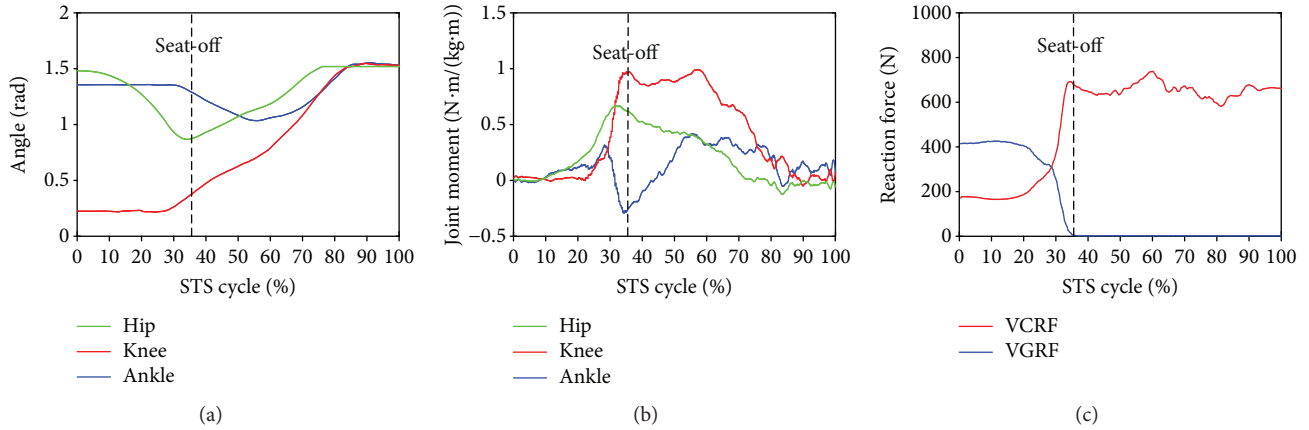


FIGURE 9: Percentage synchronized ensemble averages of the three joint angles (a), three joint moments (b), and two reaction force (c) out of the 3 trials of a task performed by patient 2 (P2).

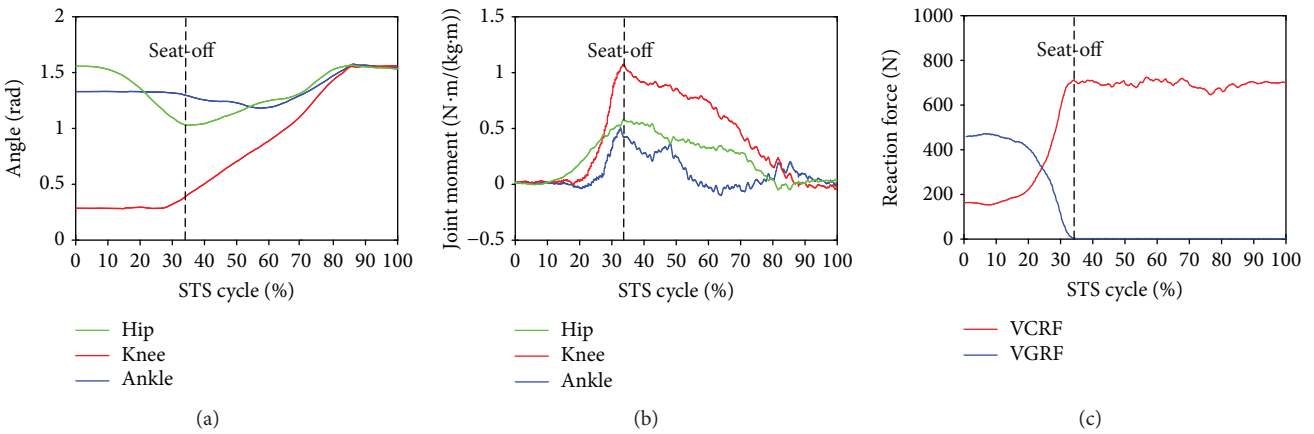


FIGURE 10: Percentage synchronized ensemble averages of the three joint angles (a), three joint moments (b), and two reaction force (c) out of the 3 trials of a task performed by patient 3 (P3).

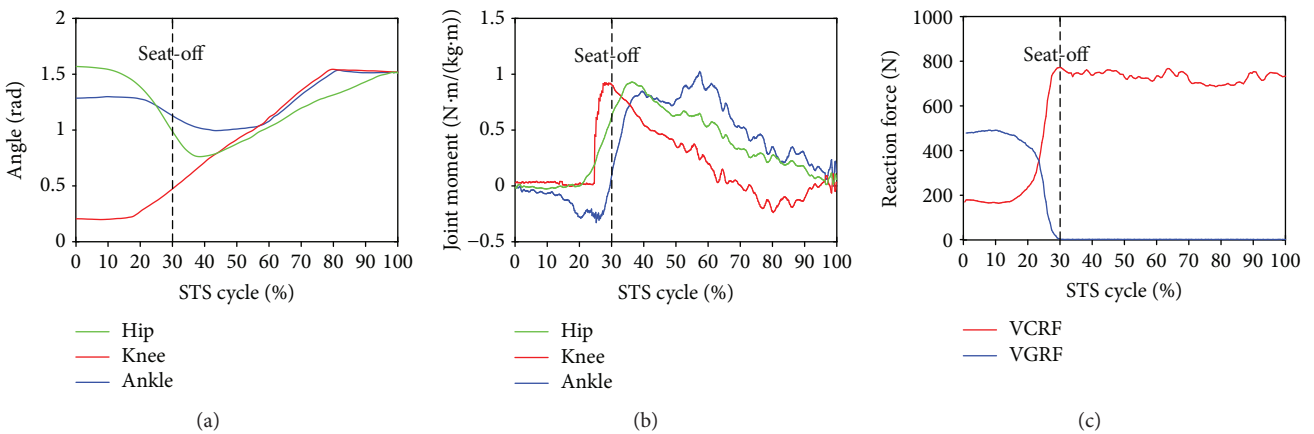


FIGURE 11: Percentage synchronized ensemble averages of the three joint angles (a), three joint moments (b), and two reaction force (c) out of the 3 trials of a task performed by patient 4 (P4).

muscle activation, body-sway motion in nonfluent STS trials would inevitably contaminate the measured original angular velocities and accelerations and then bring errors to the

calculated joint angles and angular accelerations. Compared to the e_{max} , RMSE, and R of the patients in rehabilitation and those of the healthy subjects, it suggests that the STS

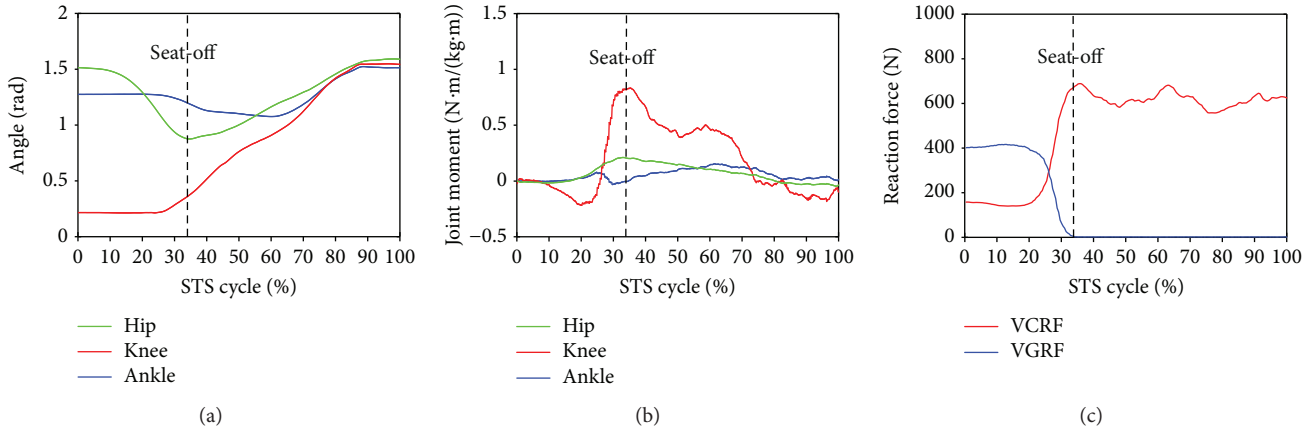


FIGURE 12: Percentage synchronized ensemble averages of the three joint angles (a), three joint moments (b), and two reaction force (c) out of the 3 trials of a task performed by patient 5 (P5).

TABLE 6: Kinetic analysis based on the data derived from the healthy subjects and patients using the developed wearable sensor system.

Synchronized ensemble averages		Healthy subjects	Patient 1	Patient 2	Patient 3	Patient 4	Patient 5
Peak-valley joint moments (Nm/kg·m)	Ankle dorsiflexion	-0.2112	-0.0462	-0.2853	-0.0648	-0.3285	-0.0309
	Ankle plantarflexion	0.4106	0.5309	0.4025	0.5073	0.8428	0.1504
	Knee flexion	-0.0235	-0.0388	-0.0235	-0.0321	-0.2385	-0.2175
	Knee extension	1.3507	0.9996	0.9703	1.0551	0.8207	0.8298
	Hip flexion	-0.0849	-0.0592	-0.0085	-0.0341	-0.0119	-0.0431
	Hip extension	0.8351	0.7239	0.6617	0.5536	0.9296	0.1911
Peak force (N)	VGRF	930.7	635.5	720.3	703.2	761.3	671.1
	VCRF	499.7	419.8	420.9	482.9	485.6	420.9

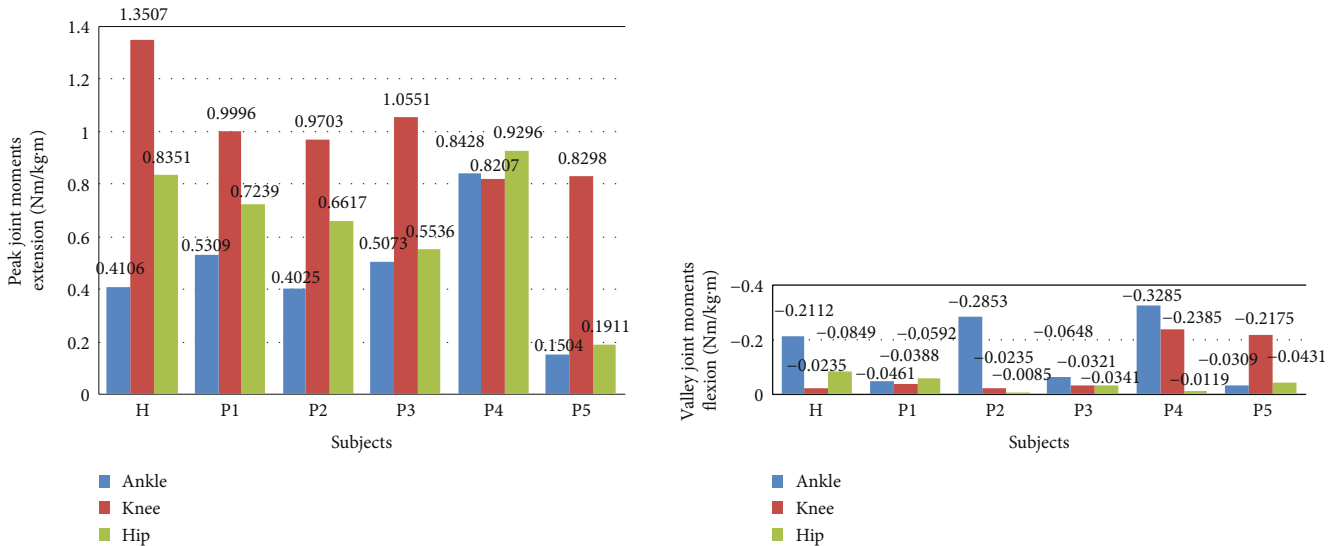


FIGURE 13: Comparison of the synchronized ensemble averages of the peak-valley joint moments in extension and flexion movements by the healthy subjects (H) and patients (P1, P2, P3, P4, and P5).

motion performed by the patients at a lower speed implicated more muscle tremble or body-sway motion which also contaminated the measured signal and resulted in greater e_{max} and RMSE and lower correlation coefficient.

The presented method used a rigid-body linked-segment model in which the positions of the end points and joints were estimated through predefined measured lengths and IMU-derived segment orientations. The moment of inertia

TABLE 7: The correlation coefficient of joint angles and moments of each patient compared with the reference.

Parameters		R of the patients				
		R_1	R_2	R_3	R_4	R_5
Angles	Hip (θ_1)	0.8521	0.6133	0.5970	0.4428	0.5054
	Knee (θ_2)	0.5257	0.4319	0.4720	0.3168	0.4722
	Ankle (θ_3)	0.8071	0.7758	0.6943	0.5480	0.6012
Moments	Hip (M_3)	0.3001	0.2965	0.3546	0.2219	0.0904
	Knee (M_2)	0.2909	0.2725	0.1073	0.1928	0.1050
	Ankle (M_1)	0.3460	0.2853	0.0648	0.1825	0.0309

of each segment, initial segment mass, segment lengths, and the position of COM were estimated or manually measured before each task individually as show in Table 1. Moreover, calibration limitations, such as a mismatch between the pose performed by the subject and the pose that the computational model is assuming, can cause errors. However, the results in Table 2 and Table 3 showed that the joint angles and angular accelerations derived from the IMUs were closed to those from the RCS with strong ($0.67 < R \leq 0.9$) and even excellent correlation coefficient (all $R > 0.93$) by healthy subjects. It suggests that the developed wearable sensor system based on the presented method was available for noninvasive estimation of the kinematic parameters to calculate joint moments and do kinetic analysis of STS. Although the parameters in Tables 4 and 5 derived from the patients in STS rehabilitation was less satisfactory compared with the parameters derived from the healthy subjects with the least $R = 0.522$, it still was moderate and suggests that the developed wearable sensor system was more accurate to evaluate a more fluent and coherent STS movement performed by healthy subjects with sufficient muscle force, but it was also suitable for estimating the STS movement of a patient who can perform a complete STS task independently.

Comparing the two groups of typical joint angles of a healthy subject and a patient in Figure 4, it suggests that the HAT took action first in the three segments of both subjects. When the HAT swung forward without reaching the maximum hip joint angle, the knee joint angle had begun to increase (seat-off, 47% for healthy subjects, 45% for patients), then the HAT continued to move forward after the knee joint started to extend. However, the difference was that the HAT of the patients in rehabilitation swung more forward with greater hip joint angle than the healthy subjects. Because the inertia joint moments of the patients with lower STS speed was smaller than those of the healthy subjects with higher STS speed, the patients needed to adjust their center of gravity exactly above the feet with an exaggerated hip flexion strategy than the healthy subjects. The strategy could potentially compensate for the inability to generate lower extremity muscle force, so that the COM could be placed further ahead and the lower extremity moments could be redistributed potentially for easy STS. The ankle joint angles of both the healthy subject and the patient began to decrease first and then increase after seat-off. Larger moment of momentum of the HAT of the healthy subject would promote more obvious motion of the thigh and shank then

resulted in exaggerated flexion angle of the ankle joint, while it was different in the patients in rehabilitation.

As shown in Figure 5, the angular accelerations of all segments' COMs during the STS trial performed by the patient varied less obviously and the peak value was also significantly less than those of the healthy subjects. It suggests that the patient in rehabilitation could not yet stand up in relative shorter time fluently and coherently as a healthy subject stood up with sufficient muscle force. And the lower limb muscles of the patients in rehabilitation still suffered activation trembles which contaminated the IMUs' signal and resulted in errors. Based on all the trials, if the STS movement was performed longer than 7 seconds, regarded as a quasi-static state, all the kinematic data measured by IMUs fluctuated even close to zero, which was almost of no availability. In this case, the joint moments resulted from the kinematic factors could be almost disregarded and it should be directly estimated with the moments contributed by the gravities of all the body segments. Therefore, the developed sensor system was almost inapplicable to estimate the joint moments of quasistatic STS movement.

Comparing the moments of the same joint of the healthy subjects (JMr) and patients (JMp) in Figures 7–12, it suggests that the inertia joint moment component played an important role in the resultant joint moment to contribute more fluent and successful STS movement for healthy subjects. That the knee joint moments (red line) of both the healthy subjects and patients had been increasing before seat-off suggests the existence of the static component of the knee joint moment. In other words, before the knee joint angle changed, the knee joint moments had already been increasing to react the gravity moment acting on the knee joint for preparing to sit up and stretch. Then the VCRF vanished and the VGRF rapidly reached the maximum after the subject leaved the chair (seat-off) and started to stretch.

Referring to Figures 8 and 9 derived from P1 and P2, the variation tendency of hip, knee, and ankle joint angles in the left charts of Figures 8 and 9 were similar to those of the healthy subjects in the left chart of Figure 7 suggesting that the proprioception on the STS posture and the STS balance control ability of the patients has recovered well in the rehabilitation training. But the exaggerated long duration hip flexion (green line in Figure 9(a)) led to a greater dorsiflexion of the ankle angle (blue line in Figure 9(a)) and a greater valley value of ankle joint moment (blue line in Figure 9(b)). After consulting with P2, he was weak to control the muscles of the thigh and experienced shakes of the thigh after seat-off, which proved the vibration of the knee joint moment after seat-off (red line in Figure 9(b)). Referring to Figures 10 and 12, derive d from P3 and P5; the dorsiflexion angles of ankle joints of P3 and P5 were not so obvious and the valley values of the ankle joint angle emerged later than those of other patients. The hip joint angle of P3 swung forward the least in the five patients. Meanwhile, almost no dorsiflexion moments appeared in the ankle joint of P3 and P5 before seat-off but stretched slowly with moderate hip joint moments. After consulting with P3 and P5, P3 reported that it was difficult to swing HAT forward enough with some spinal trauma, so that the hip joint moment was not great and

the shank was almost not swung forward but just stretched after seat-off with dorsiflexion ankle joint moment; P5 reported to have difficulty in ankle joint that led to insufficient ankle joint moment for stretching off, so that he performed a low-speed STS movement with less swing of the shank (smaller ankle joint angle) and slow swing of HAT (smaller hip joint moment). Referring to Figure 11 derived from P4, the difference comparing Figure 7 derived from healthy subjects was that the HAT of P4 swung more forward with greater and later valley value of hip joint angle and with later peak value of hip joint moment after seat-off. Because P4's inertia knee joint moment at lower STS speed with leg muscle weakness was less than those of the healthy subjects, he needed to adjust his center of gravity exactly above the feet with an exaggerated hip flexion strategy than the healthy subjects. The strategy would cause a substantial increase of the plantar-flexion ankle joint moment (blue line in Figure 11(b)) and could potentially compensate for the inability to generate greater lower limb muscle force, so that the COM could be placed further ahead and the lower limb moments could be redistributed potentially for easy STS. Larger moment of momentum of the HAT of P4 promoted an obvious motion of the thigh and shank then resulted in exaggerated flexion angle of ankle joint (blue line in Figure 11(a)) and greater valley value of ankle joint moment before seat-off.

As shown in Table 6, peak-valley joint moments of the healthy subjects and patients were calculated from the data derived from the IMUs. The average peak knee extension moment was $1.3507 \text{ N}\cdot\text{m}\cdot\text{kg}^{-1}\cdot\text{m}^{-1}$, the average peak hip extension moment was $0.8351 \text{ N}\cdot\text{m}\cdot\text{kg}^{-1}\cdot\text{m}^{-1}$, and the average peak ankle plantar flexion moment was $0.4106 \text{ N}\cdot\text{m}\cdot\text{kg}^{-1}\cdot\text{m}^{-1}$ for healthy subjects. It suggests that greatest joint moment of the hip, knee, and ankle joints was generated on the knee joint around seat-off. And it also suggests that the knee joint plays the most important role in STS and the phase around seat-off in the STS rehabilitation should be paid more attention. The comparison histogram of the synchronized ensemble averages of the peak-valley joint moments in extension and flexion movements by the healthy subjects and patients in Figure 13 was imaged and intuitively suggests the rehabilitation situations of the lower limb muscle maximum capacity in STS movement. The correlation coefficient of joint angles and moments of each patient compared with the references indicates the agreement of STS movement between the patients and the healthy subjects, which is valuable for evaluating the recovery of the whole STS rehabilitation training.

As the subjects in the experiment were limited to only five patients in rehabilitation and five healthy males, the results could not cover all cases of patients in STS rehabilitation training. Therefore, to verify systematic errors and measuring errors of the developed wearable sensor system for estimate joint moments of rehabilitation, more studies are necessary to determine reliability and validity of the system for more diverse subjects, especially for clinical populations. Since there was no integration of acceleration or angular velocity in the calculation of the joint angles and joint moments, the results were not distorted without considering

drift errors. However, the results were still affected by off-set errors by misalignment of the inertial sensors with the reference system; it was small but inevitable. Customized IMUs were used in the experiment, which could test angular velocities and accelerations about three orthogonal axes and packaged in a single SMT ($1.1 \times 1.1 \times 0.50$ inches) with rechargeable batteries that was convenient to wear for patients. Especially compared with the RCS of high cost and large space occupation, the developed wearable sensor system could provide adequate and necessary quantitative analysis of joint moments noninvasively. Another advantage of this method is that the developed device is not model-dependent which is very practical to continuously monitor the kinetic characteristics of patients in rehabilitation in home or to provide real-time feedback joint moments for the wearable powered exoskeleton assistant system. With the miniaturization of the inertial sensors, we are working to promote the developed wearable sensor and analysis systems to clinical applications.

Consequently, although the developed prototype of the wearable sensor system was only tested in ideal conditions in the lab with ten subjects, it provided a methodological reference for noninvasively evaluating functional rehabilitation state in STS dysfunction patients by kinetic analysis with the piecewise 2D three-segment STS biomechanical model. We innovatively analyzed both kinematics and kinetics of STS motion noninvasively with wearable sensor system, especially creatively estimated the lower limb joint moments with wearable inertial sensors for STS rehabilitation training analysis. The results showed insight into the movement coordination of STS and had implications for the ongoing development of more effective training techniques in the clinic.

Notations

\vec{M}_i :	joint moment vector about joint i ($i = 1, 2, 3$; ankle joint, knee joint, and hip joint)
J_j :	moment of inertia of segment j about the center of mass ($j = 1, 2, 3$; shank, thigh, and HAT)
$\vec{\alpha}_j$:	actual angular acceleration vector of segment j about the center of mass, containing the acceleration of the center of gravity
\vec{r}_{ij} :	position vector from joint i to the center of gravity of segment j
m_j :	mass of segment j
k_j :	position of the COM of the segment j
\vec{a}_j :	acceleration vector of the center of gravity of segment j
g :	acceleration of the center of gravity
T_{com} :	STS trajectory of the COM
θ_i :	angle of joint i ($i = 1, 2, 3$; ankle joint, knee joint, and hip joint)
\vec{F}_{hip} :	is the equivalent external force acting on the hip joint from the chair.

Conflicts of Interest

The authors declare no conflict of interest.

Authors' Contributions

Kun Liu, Jianchao Yan, and Yong Liu conceived and designed the experiments; Kun Liu and Ming Ye helped to perform the experiments; Kun Liu, Jianchao Yan, and Yong Liu analyzed the data; Kun Liu, Jianchao Yan, and Yong Liu wrote the paper. In addition, Kun Liu, Jianchao Yan, and Yong Liu are responsible for the implementation of the proposed scheme.

Acknowledgments

The authors wish to acknowledge the support of the volunteer subjects of Robotics and Dynamics Research Lab in Jilin University. The work was partly supported by Youth Research Fund Project of the Department of Science and Technology of Jilin province (20160520066JH), Graduate Innovation Fund of Jilin University.

References

- [1] G. D. Baer and A. M. Ashburn, "Trunk movements in older subjects during sit-to-stand," *Archives of Physical Medicine and Rehabilitation*, vol. 76, no. 9, pp. 844–849, 1995.
- [2] Y. C. Pai and M. W. Rogers, "Control of body mass transfer as a function of speed of ascent in sit-to-stand," *Medicine & Science in Sports & Exercise*, vol. 22, no. 3, pp. 378–384, 1990.
- [3] C. A. Doorenbosch, J. Harlaar, M. E. Roebroek, and G. J. Lankester, "Two strategies of transferring from sit-to-stand; the activation of monoarticular and biarticular muscles," *Journal of Biomechanics*, vol. 27, no. 11, pp. 1299–1307, 1994.
- [4] M. M. Gross, P. J. Stevenson, S. L. Charette, G. Pyka, and R. Marcus, "Effect of muscle strength and movement speed on the biomechanics of rising from a chair in healthy elderly and young women," *Gait & Posture*, vol. 8, no. 3, pp. 175–185, 1998.
- [5] R. M. Enoka, *Neuromechanics of human movements*, IEEE Eng. Human Kinetics. Soc., 2007.
- [6] W. G. Janssen, H. B. Bussman, and H. J. Stam, "Determinants of the sit-to-stand movement: a review," *Physical Therapy*, vol. 82, no. 9, pp. 866–879, 2002.
- [7] S. Kawagoe, N. Tajima, and E. Chosa, "Biomechanical analysis of effects of foot placement with varying chair height on the motion of standing up," *Journal of Orthopaedic Science*, vol. 5, no. 2, pp. 124–133, 2000.
- [8] A. Kralj, R. J. Jaeger, and M. Munih, "Analysis of standing up and sitting down in humans: definitions and normative data presentation," *Journal of Biomechanics*, vol. 23, no. 11, pp. 1123–1138, 1990.
- [9] S. Mefoued, S. Mohammed, Y. Amirat, and G. Fried, "Sit-to-stand movement assistance using an actuated knee joint orthosis," in *2012 4th IEEE RAS & EMBS International Conference on Biomedical Robotics and Biomechatronics (BioRob)*, pp. 1753–1758, Rome, Italy, June 24–27, 2012.
- [10] P. T. Cheng, C. L. Chen, C. M. Wang, and W. H. Hong, "Leg muscle activation patterns of sit-to-stand movement in stroke patients," *American Journal of Physical Medicine & Rehabilitation*, vol. 83, no. 1, pp. 10–16, 2004.
- [11] K. Liu, Y. Inoue, and K. Shibata, "Physical sensor difference-based method and virtual sensor difference-based method for visual and quantitative estimation of lower limb 3D gait posture using accelerometers and magnetometers," *Computer Methods in Biomechanics and Biomedical Engineering*, vol. 15, no. 2, pp. 203–210, 2012.
- [12] R. J. de Asla, L. Wan, H. E. Rubash, and G. Li, "Six DOF in vivo kinematics of the ankle joint complex: application of a combined dual-orthogonal fluoroscopic and magnetic resonance imaging technique," *Journal of Orthopaedic Research*, vol. 24, no. 5, pp. 1019–1027, 2006.
- [13] J. Favre, R. Aissaoui, B. M. Jolles, J. A. de Guise, and K. Aminian, "Functional calibration procedure for 3D knee joint angle description using inertial sensors," *Journal of Biomechanics*, vol. 42, no. 14, pp. 2330–2335, 2009.
- [14] R. Takeda, S. Tadano, A. Natorigawa, M. Todoh, and S. Yoshinari, "Gait posture estimation using wearable acceleration and gyro sensors," *Journal of Biomechanics*, vol. 42, no. 15, pp. 2486–2494, 2009.
- [15] S. Yoshioka, A. Nagano, D. C. Hay, and S. Fukashiro, "The minimum required muscle force for a sit-to-stand task," *Journal of Biomechanics*, vol. 45, no. 4, pp. 699–705, 2012.
- [16] M. M. Van der heijden, K. Meijer, P. J. Willems, and H. H. Savelberg, "Muscles limiting the sit-to-stand movement: an experimental simulation of muscle weakness," *Gait & Posture*, vol. 30, no. 1, pp. 110–114, 2009.
- [17] T. F. Yan, M. Cempini, C. M. Oddo, and N. Vitiello, "Review of assistive strategies in powered lower-limb orthoses and exoskeletons," *Robotics and Autonomous Systems*, vol. 64, no. 64, pp. 120–136, 2015.
- [18] W. R. Eby and E. Kubica, "Modeling and control considerations for powered lower-limb orthoses: a design study for assisted STS," *Journal of Medical Devices*, vol. 1, no. 2, pp. 126–139, 2006.
- [19] A. W. Lam, A. HajYasien, and D. Kulic, "Improving rehabilitation exercise performance through visual guidance," in *2014 36th Annual International Conference of the IEEE Engineering in Medicine and Biology Society*, pp. 1735–1738, Chicago, IL, USA, 2014.
- [20] V. Bonnet, V. Joukov, D. Kulic, P. Fraise, N. Ramdani, and G. Venture, "Monitoring of hip and knee joint angles using a single inertial measurement unit during lower limb rehabilitation," *IEEE Sensors Journal*, vol. 16, no. 6, pp. 1557–1564, 2016.
- [21] T. Stieglitz, M. Schuettler, A. Schneider, E. Valderrama, and X. Navarro, "Noninvasive measurement of torque development in the rat foot: measurement setup and results from stimulation of the sciatic nerve with polyimide-based cuff electrodes," *IEEE Transactions on Neural Systems and Rehabilitation Engineering*, vol. 11, no. 4, pp. 427–437, 2003.
- [22] L. M. Inkster and J. J. Eng, "Postural control during a sit-to-stand task in individuals with mild Parkinson's disease," *Experimental Brain Research*, vol. 154, no. 1, pp. 33–38, 2004.
- [23] S. Yoshioka, A. Nagano, R. Himeno, and S. Fukashiro, "Computation of the kinematics and the minimum peak joint moments of sit-to-stand movements," *Biomedical Engineering Online*, vol. 6, no. 1, p. 26, 2007.
- [24] S. Yoshioka, A. Nagano, D. C. Hay, and S. Fukashiro, "Biomechanical analysis of the relation between movement time and joint moment development during a sit-to-stand task," *Biomedical Engineering OnLine*, vol. 8, no. 1, p. 27, 2009.
- [25] L. Wang and T. S. Buchanan, "Prediction of joint moments using a neural network model of muscle activations from

- EMG signals,” *IEEE Transactions on Neural Systems and Rehabilitation Engineering*, vol. 10, no. 1, pp. 30–37, 2002.
- [26] A. Karatsidis, G. Bellusci, H. M. Schepers, M. de Zee, M. S. Andersen, and P. H. Veltink, “Estimation of ground reaction forces and moments during gait using only inertial motion capture,” *Sensors*, vol. 17, no. 1, p. 75, 2017.
- [27] K. Liu, T. Liu, K. Shibata, Y. Inoue, and R. C. Zheng, “Novel approach to ambulatory assessment of human segmental orientation on a wearable sensor system,” *Journal of Biomechanics*, vol. 42, no. 16, pp. 2747–2752, 2009.
- [28] K. Liu, C. Li, P. F. Yan, and M. Ye, “Fuzzy PID control strategy based on piecewise biomechanical model for sit-to-stand movement,” in *2016 IEEE International Conference on Mechatronics and Automation*, pp. 1466–1471, Harbin, China, 2016.
- [29] General Administration of Quality Supervision, Inspection and Quarantine of the People’s Republic of China, *Standardization Administration of the People’s Republic of China, GB/T 17245—2004 [s], Inertial Parameters of Adult Human Body*, 2004.
- [30] M. R. Yeadon, “Kinetics of human motion,” *Journal of Biomechanics*, vol. 38, no. 6, pp. 1371–1372, 2005.
- [31] G. Wu, S. Siegler, P. Allard et al., “ISB recommendation on definitions of joint coordinate system of various joints for the reporting of human joint motion—part I: ankle, hip, and spine,” *Journal of Biomechanics*, vol. 35, no. 4, pp. 543–548, 2002.

Research Article

A Digital Compressed Sensing-Based Energy-Efficient Single-Spot Bluetooth ECG Node

Kan Luo ¹, Zhipeng Cai,² Keqin Du ¹, Fumin Zou,¹ Xiangyu Zhang,² and Jianqing Li ²

¹Fujian Key Laboratory of Automotive Electronics and Electric Drive and School of Information Science and Engineering, Fujian University of Technology, Fuzhou 350118, China

²School of Instrument Science and Engineering, Southeast University, Nanjing 210096, China

Correspondence should be addressed to Kan Luo; luok@foxmail.com

Received 31 August 2017; Accepted 5 December 2017; Published 11 January 2018

Academic Editor: Feng Liu

Copyright © 2018 Kan Luo et al. This is an open access article distributed under the Creative Commons Attribution License, which permits unrestricted use, distribution, and reproduction in any medium, provided the original work is properly cited.

Energy efficiency is still the obstacle for long-term real-time wireless ECG monitoring. In this paper, a digital compressed sensing (CS-) based single-spot Bluetooth ECG node is proposed to deal with the challenge in wireless ECG application. A periodic sleep/wake-up scheme and a CS-based compression algorithm are implemented in a node, which consists of ultra-low-power analog front-end, microcontroller, Bluetooth 4.0 communication module, and so forth. The efficiency improvement and the node's specifics are evidenced by the experiments using the ECG signals sampled by the proposed node under daily activities of lay, sit, stand, walk, and run. Under using sparse binary matrix (SBM), block sparse Bayesian learning (BSBL) method, and discrete cosine transform (DCT) basis, all ECG signals were essentially undistorted recovered with root-mean-square differences (PRDs) which are less than 6%. The proposed sleep/wake-up scheme and data compression can reduce the airtime over energy-hungry wireless links, the energy consumption of proposed node is 6.53 mJ, and the energy consumption of radio decreases 77.37%. Moreover, the energy consumption increase caused by CS code execution is negligible, which is 1.3% of the total energy consumption.

1. Introduction

Cardiovascular diseases (CVDs) are a major threat to human health. According to the report of WHO, about 17.5 million people died of heart disease every year around the world [1]. Furthermore, the cost for CVD-related treatment is substantial, which is estimated approximately to be 3.8 trillion U.S. dollars in all low- and middle-income countries during 2011–2025 [2]. The situation will be even more severe due to the increasing aging population. Many of CVD-related deaths and associated economic losses can be avoided if the diseases have been early prevented, diagnosed, and treated.

Electrocardiogram (ECG) can give an insight of heart status for diagnosis of CVDs, and it is a standard medical examination in clinical practices nowadays [3]. However, there still exist some limitations of traditional ECG instruments for early diagnosis of CVDs, such as in-hospital short-term examination, huge in volume, inconvenient movement,

wired connection, and low autonomy [4]. They cannot satisfy the requirement for long-term, real-time monitoring and feedback in mobile scenarios as most of the early stage CVDs are accidental during daily activity and out of a hospital. Development of inexpensive continuous ambulatory ECG monitoring device becomes a challenge in real-time, long-term, and convenient ECG monitoring.

In recent years, with the rapid development of wireless body sensor networks (WBSNs) and wearable techniques, lots of WBSN-enabled ambulatory ECG monitoring devices have been developed [1, 5, 6]. They could be seamlessly integrated into patients' life for heart status monitoring, providing early warning to avoid accidental adverse cardiovascular events. However, most of such existing devices need to be further improved to advance energy efficiency, which is the major obstacle for long-term wireless ECG monitoring.

Different studies for the energy-efficient node have been investigated from various aspects, including hardware,

communication protocol, scheme, coding technology, and data compression methods. Low-power hardware can directly reduce the energy consumption. Yazicioglu et al. [7] proposed mixed-signal design approaches to reduce overall power dissipation of the biopotential sensor node. Tsai et al. [8] fabricated a low-power analog front-end IC, using a $0.18\ \mu\text{m}$ CMOS standard, for effectively wireless ECG acquisition. Energy-efficient protocol or strategy can also prolong the node's lifetime. Nemati employed ANT protocol as a low-data-rate wireless module to reduce the power consumption of a wireless capacitive ECG node. Yan et al. [9] proposed a distance-based energy-efficient data strategy, which lowered the transmission power in both the sensor node level and the network level. Also, considering communication consumes more than 65% of the total energy [10], lots of coding or compression approaches were proposed to optimize the radio energy consumption. A proper compression technology can reduce the amount of the transmitted data, thus improving the node's energy efficiency. As most of the high-performance compression schemes are not compatible with resource-constraint node [11, 12], low computational complexity coding or compression methods were investigated, such as the Walsh transform based variable-word-length coding [13], nonuniform sampling-based dynamic compression [1], and compressed sensing- (CS-) based method [14–16]. Particularly, as a novel sampling paradigm, CS combines the sampling and compression into one step. It efficiently collects signal following the “information rate” instead of the traditional “Nyquist rate” [17–19]. The reported CS-enabled wireless ECG monitoring [14, 15, 20, 21] shows the advantages of CS method in low complexity, low-cost, and energy efficiency.

Existing literature has shown that achieving truly energy-efficient wireless ECG node requires not only ultra-low-power devices and advanced communication protocols but also proper data compression technologies. Although these existing studies explored power saving methods from different aspects, few of them gave out a whole energy-efficient node scheme.

Motivated by these challenges, a digital CS-based single-spot Bluetooth ECG node was designed and implemented. To achieve long-term wireless ECG monitoring, ultra-low-power hardware, such as Bluetooth Low Energy (BLE) communication protocol module, analog front-end (AFE) chips AD8232 and MSP430F1611, were considered in the node design. Meanwhile, the CS-based compression and the periodic sleep/wake-up scheme, which aims at minimizing energy consumption of data communication, were proposed. Particularly, the tiny node taking advantages of low computation complexity, a sparse binary measurement matrix, was implanted in to realize the CS-based compression. The compression technology and sleep strategy can not only reduce the amount of the transmitted data but also decrease the airtime over energy-hungry wireless links, thus improving the node's energy efficiency. To identify the specifics of the prototype node, the experiments were carried out. Also, the results were compared with three commercial nodes.

The paper is organized as follows. Section 2 elaborated the design of the proposed wireless ECG node. The details

of digital CS-based compression and dual-clock source-based periodic sleep/wake-up scheme are illustrated in this section. In Section 3, experimental setups were introduced, including the experimental data and the evaluation indices. Section 4 demonstrated the experimental results over optimal parameters of CS compression, collected ECG signals under daily activities, energy consumption, and so forth. Section 5 discussed the advantages and the potential limitation of our node. The summarization of this study was presented in Section 6.

2. Designed Wireless ECG Node

In a wireless ECG node, the limited battery power is mainly consumed by three components: sensing, computing, and communication. High-energy consumption hardware, poor power management, and direct transmission of ECG data are energy wasting. To reduce the energy consumption, the proposed node optimized for hardware design, a periodic sleep/wake-up scheme, and CS-based data compression. The objectives of the node are summarized as follows:

- (1) Ultra-low-power hardware: to save energy in circuit
- (2) Periodic sleep/wake-up strategy: to reduce airtime over the power-hungry wireless link
- (3) Compression algorithm with high compression ratio and good recovered quality: to decrease transmission data and guarantee nondistortion diagnosis
- (4) Compact and low complexity: to realize the compression algorithm on resource-constraint sensing nodes
- (5) Real-time: to provide online wireless heart status monitoring

2.1. Hardware Design. The hardware framework of proposed single-spot wireless ECG node is described in Figure 1. The system is powered by one 3 V CR2032 button battery. Through three electrodes, the ECG signal was obtained and transmitted to an AFE for amplifying and filtering. Subsequently, the preprocessed signal is converted into digital signal by the 12-Bit integrated Analog-to-Digital Converter (ADC) module of MSP430 at 200 Hz. After the compression processing, the data is transmitted to a healthcare cloud server-connected gateway (a mobile phone or a base station) through a BLE transceiver. The valuable medical information will be extracted from the reconstructed signals for the authorized doctor, patient, or medical institution, and so forth. Here, AD8232 is chosen as the AFE. AD8232 is a fully integrated single-lead ECG AFE, which has low supply current ($170\ \mu\text{A}$) and high common-mode rejection ratio (80 dB), and also includes multiple amplifiers and filters. The single chip can easily realize traditional complex ECG preprocessing circuit design. The ECG signal is essentially quasi-periodic nonstationary with a small amplitude (0.01~5 mV) and low frequency (0.05~100 Hz) [22]. The gain of AD8232 was fixed as 500, and the frequency band of the filter was set as 0.5~35 Hz. MSP430F1611 was adopted as core processor. The large Flash (48 kB) and RAM (10 kB)

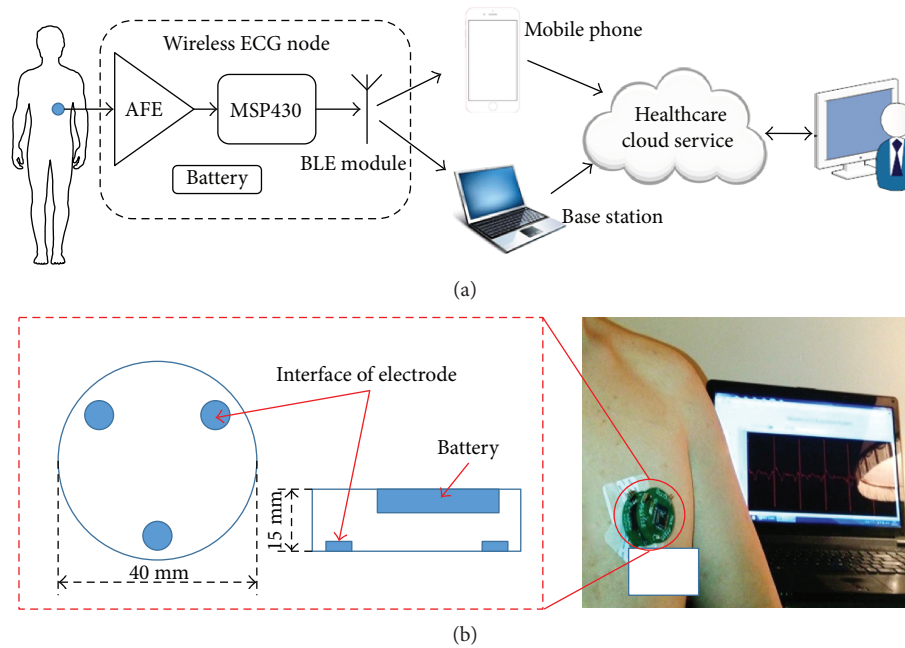


FIGURE 1: Hardware framework of proposed wireless ECG node. (a) System framework (b) structure, and prototype of the proposed node.

ensure that the node has enough resources for algorithm implementation. Also, there two crystal oscillators, 8 MHz and 11.0592 KHz, are set up as master and second clock sources, which provide the conditions for the node to work at high- or low-speed operation modes. Furthermore, as a bridge between the node and gateway, the transceiver HM-11 provides a short-range (10 m), high-throughput (up to 1 Mb/s data rate) BLE wireless data communication.

The final manufactured node can be found in Figure 1(b). It is a circular structure. The diameter and height are 40 mm and 15 mm, respectively. Moreover, the overall weight (including the battery) is 30 g. Three integrated interfaces of electrodes are uniformly distributed on the nodes at 120 degrees, which are used to connect the standard Ag/AgCl electrodes. In practical, the node can firmly stick to the skin.

2.2. Dual-Clock Source-Based Periodic Sleep/Wake-up Scheme. The proposed dual-clock source-based periodic sleep/wake-up scheme is shown in Figure 2. The basic idea of the proposed scheme is that resource allocation is in terms of event slots. Since energy consumption is proportional to clock frequency [9], the node works at high-speed operation mode (HSOM) with the master clock during tasks of data compression and transmission and at low-speed operation mode (LSOM) with the secondary clock in tasks of sampling. Meanwhile, the node periodic sleeps and wakes up in LSOM. The flowchart in Figure 2(a) shows the transformation between the two operation modes. That is, during sampling task, the node is in LSOM, and it keeps sleeping during idle statue and immediately wakes up when periodic sampling event triggered, then followed by filling and data buffer checking. If the data buffer is full, the node moves into HSOM; otherwise, the node keeps in

LSOM and repeat sampling. There is no sleeping in HSOM; the node runs at full speed for CS-based data compression and data transmission. After data transmission, the node moves back to LSOM. The sequence diagram of the operation mode is illustrated in Figure 2(b). The node is working in LSOM with sleep/wake-up at most of the time that guarantees energy saving.

2.3. Implementation of CS-Based ECG Compression. Recently, the compressed sensing theory was proposed [17–19]. It has broken the traditional sampling rule. The basic theory of the CS is that the sparse signals can be reconstructed from incoherent random measurements [23, 24]. The formal definition of CS is $\mathbf{Y} = \Phi\mathbf{X}$, where \mathbf{X} is the N -dimensional input signal, Φ is $M \times N$ measurement matrix ($M < N$), which represents dimensionality reduction, and \mathbf{Y} is the collected M -length compressed vector. Using CS can reduce the wirelessly transmitted data during the signal acquisition.

There are three critical aspects in ECG compression: the sparsity of the ECG signal, the measurement matrix, and the recovery algorithm. ECG is sparse or sparse in some domains has already been proven in previous studies [14, 15, 20, 21].

The essential content of digital CS-based compression can be summarized as using measurement matrix multiplication, which includes the multiplication and accumulation, to shorten the signal length. The scheme of the compression is shown in Figure 3. The ECG signal \mathbf{X} is converted to digital signal following the “Nyquist” sampling rate f_s , and then the measurement matrix Φ multiplies \mathbf{X} to get compressed signal \mathbf{Y} . The digital CS combined the traditional “Nyquist” sampling and the principle of CS signal acquisition; it is suitable for the scenario of sparsity signal compression when ADC can provide enough sampling rate.

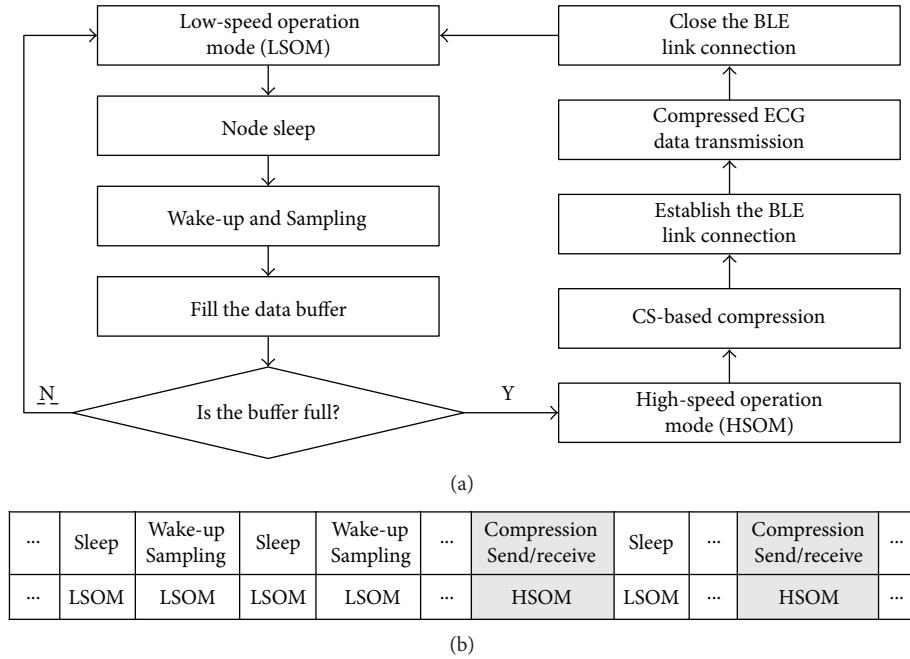


FIGURE 2: Dual-clock source-based periodic sleep/wake-up scheme. (a) Flowchart of the operation modes. (b) Sequence diagram of the operation modes.

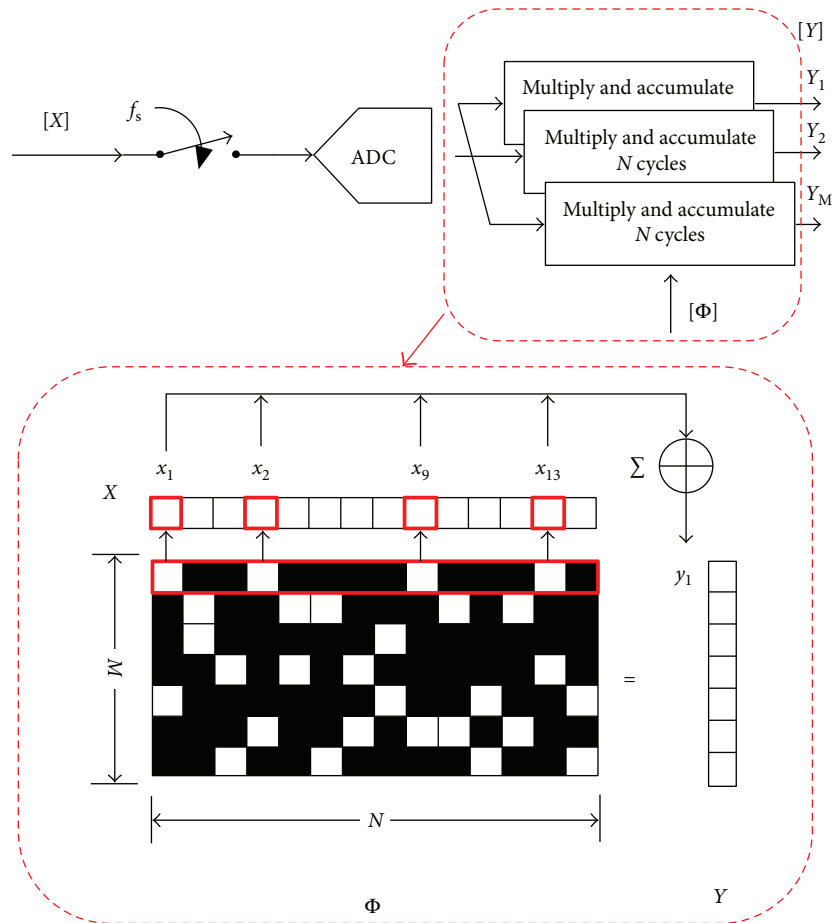


FIGURE 3: Scheme of digital CS compression on node.

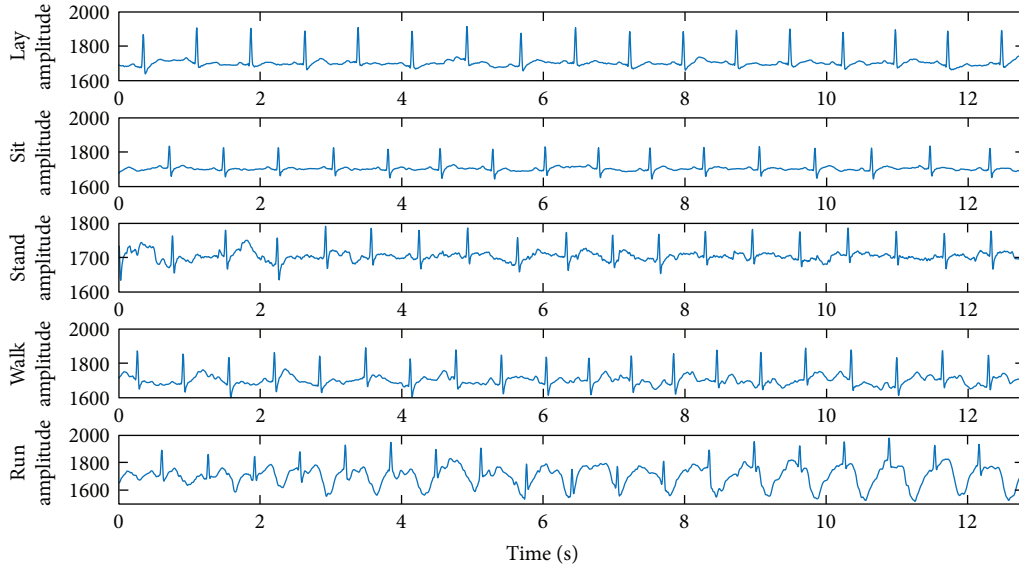


FIGURE 4: The ECG signals for compression tests.

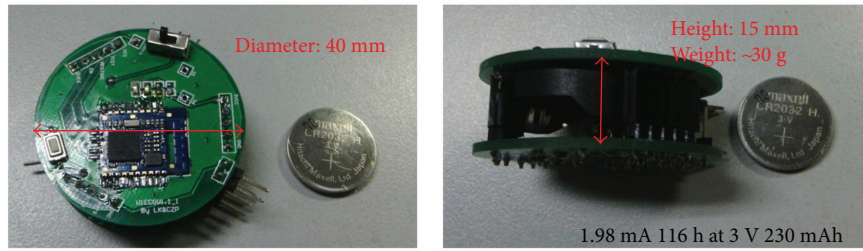


FIGURE 5: The prototype of single-spot Bluetooth ECG node.

The measurement matrix is the key to CS-based compression. The parameters of measurement matrix, which include the bit precision of coefficients, the type of random distribution, and the structure of the matrix, directly affect the compression efficiency and the computation complexity. Commonly used measurement matrices include Gaussian distribution matrix, Bernoulli distribution matrix, and uniform distribution matrix. The bit precision of matrix coefficient ranges from 1 to 64. The Gaussian, Bernoulli, or uniform distribution matrices with high bit coefficient precision are costly because they are difficult to generate and store in a resource constraint nodes; moreover, they bring more computation and higher energy consumption. In comparison, sparse binary matrix (SBM) is more suitably used in a resource-constraint node as measurement matrix [17–19].

SBM has characteristics of sparsity, binary, and incoherent, which is described as $M \times N$ sparse matrix with K as one of the elements in each column ($K < M$). ϕ_{ij} ($\phi_{ij} \in [0,1]$) represents the element of Φ . In each column of Φ , the number of one is far less than the number of zero, and the locations of the one element are random and satisfy the condition of independent identically distributed (i.i.d.).

The implementation of SBM-based compression is marked by the red dashed line in Figure 3. Let $P_i = \{p_i^1, p_i^2, \dots, p_i^j\}$ denote the locations of one entry in the i th row of Φ , and the compressed measurement results $y^{(i)}$ can be updated by (1) without the multiplier.

$$y_i = \sum x_{p_i^j}. \quad (1)$$

Figure 3 shows an example, the length of X is 14, and Φ is a 7×14 SBM with $K = 2$. The locations of one entry in the first row are $\{1, 4, 9, \text{ and } 13\}$, then $y_1 = x_1 + x_4 + x_9 + x_{13}$. Repeating processing of each row of Φ , then the compressed data Y is achieved.

2.4. Implementation of ECG Reconstruction. The high signal quality recovery algorithm is the key to ECG reconstruction implementation. It will run on a powerful computing gateway or cloud healthcare servers. Assume α is a sparse vector and Ψ is a sparse basis, signal X can expand as $X = \Psi\alpha$; then the compressed signal is $Y = \Phi\Psi\alpha$. According to the CS theory, it is highly possible to get exact α when the measurement matrix and the sparsity of the signal satisfy the restricted isometry property [23, 24]. In the proposed framework, lots of excellent algorithms, such as the basis pursuit denoising

TABLE 1: PRD of the recovered signal under different sparsity bases and recovery algorithms, $N = 512$, $M = 256$, $K = 4$.

Experimental conditions	PRD (%)				
	Lay	Sit	Stand	Walk	Run
BSBL + WT [20]	6.35	6.20	9.58	5.66	7.23
BSBL + DCT [20]	3.54	2.28	2.91	1.39	2.52
OMP + WT [14]	7.69	10.35	21.34	12.01	11.85
L1 + WT [15]	10.68	11.67	20.05	16.30	11.80

(BPDN) model, smoothed l0 algorithm, orthogonal matching pursuit, and block sparse Bayesian learning (BSBL), can be used for CS recovery [25–28]. For example, using BSBL and discrete cosine transform (DCT) basis for wireless CS compressed ECG recovery. If the measurement matrix Φ and DCT basis Ψ are known, the solution $\hat{\alpha}$ is output after $\Phi\Psi$, and received Y is fed in the BSBL algorithm; then the recovered ECG is $\hat{X} = \Psi\hat{\alpha}$ when $\hat{\alpha}$ is got. The comparison results of different recovery algorithms are demonstrated in the Results section.

3. Experiment Designs

The proposed node was evaluated in data compression and energy consumption. The experiment setups are similar to our previous work [1]. The testbed consists of the proposed node, a data acquisition (DAQ) card (National Instrument USB6009, 14 bits, maximum 48K sampling rate), and a laptop (Intel i7 4720qm, 8G RAM, Bluetooth 4.0) with Matlab 2016a and LabVIEW 2013. The DAQ card is connected to the laptop by USB cables. The node is wirelessly connected to the base station (the laptop). The measurement matrix is SBM, and the length of ECG signal N is 512 in all experiments.

As shown in Figure 4, the 12.8 s (2560 points) ECG data were used for compression tests, which were sampled by the proposed node in five predefined daily activities, such as lay, sit, stand, walk, and run. The original signal and compressed data were transmitted to the base station, where the ECG signals were reconstructed by the recovery algorithm.

To quantify the compression performance, the percentage root-mean-square difference (PRD) with different normalization [29] is used to quantify the recovered signal quality.

$$\text{PRD} = \frac{\|X - Y\|_2}{\|X - \bar{X}\|_2} \times 100. \quad (2)$$

X is the original signal, Y is the reconstructed signal, and \bar{X} is the mean of X . Meanwhile, the parameters M and K , which closely relate to compression ratio and computational complexity, are adopted to evaluate the compression efficiency.

In the energy consumption tests, the power supply is 3 V, and a 10 Ohm precise resistor is used to transform current to voltage. The DAQ card records the node voltage V_{node} and resistor voltage V_R . The card sampled the analog voltages at 5 KHz and then calculated the node's power and energy

consumptions in the digital domain. The power consumption P is calculated as

$$P = V_{\text{node}} \left(\frac{V_R}{R} \right), \quad (3)$$

where R represents the value of the resistor. The energy consumption E is given by the summation of the power consumption at a time interval T :

$$E = V_{\text{node}} \left(\sum_T \frac{V_R}{R} \right). \quad (4)$$

After all experiments, the proposed node was compared with three commercial ECG nodes, such as Shimmer2, ZMP® ECG2, and Zio Patch monitor concerning size, weight, lifetime, and so forth.

4. Results

The prototype of proposed single-spot Bluetooth ECG node is shown in Figure 5. The size and weight of proposed node are 40 (diameter, D) \times 15 (height, H), and 30g, respectively.

The comparison experiment was carried out to identify proper recovery algorithm and sparse basis. The PRDs of recovered ECG signals were calculated and reported in Table 1. It is observed that the combination of BSBL [20] and DCT basis achieves the highest signal recovery quality, and the PRDs are less than 3.6%. Besides, the BSBL also beats the recovery algorithms of orthogonal matching pursuit (OMP) [14] and L1 convex optimization [15] under wavelet transform (WT) basis. Since ECG signal is block sparse and correlation structure, BSBL algorithm, which considers such characteristics in the solution of CS, obtained good performance in ECG recovery. The results suggest that the combination of BSBL and DCT basis is a good choice for the base station. The rest experiments are based on BSBL and DCT basis.

Parameters of measurement matrix play an important role in the performance of data CS compression. SBM has three parameters, which are N , M , and K . In this study, N is fixed to 512, which means each time the compression algorithm will process segmented 2.56 s ECG signal; due to compression ratio equal to M/N , parameter M takes a significant role in compression efficiency; and it needs $N \times K$ times accumulation to achieve compressed signal. Parameter K is a critical measure for computation of compression.

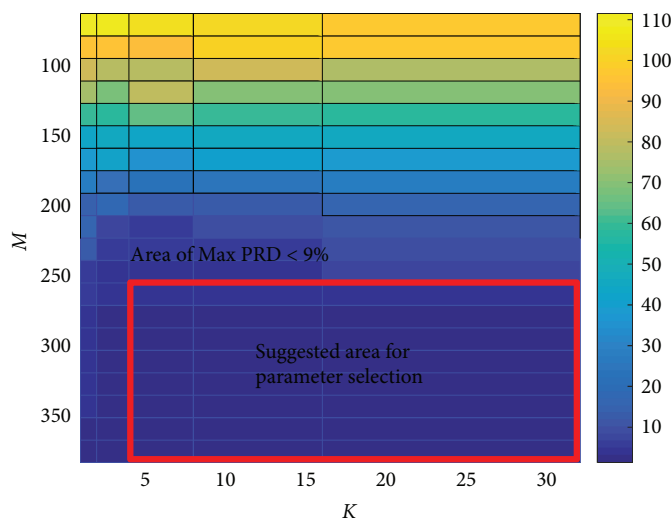


FIGURE 6: The relationships of signal distortion (PRD), compression efficiency (M), and computation complexity (K).

To decrease the risk of signal distortion, the maximum PRDs were preserved under M and K verified from 64 to 384 and 1 to 32, respectively. The relationships of the signal distortion, compression efficiency, and computation complexity are shown in Figure 6. The PRD decreases with the increasing M but is insensitive to the change of K . Considering the cases with $\text{PRD} < 9\%$ will not lead diagnostic distortion [29]; a blue marker of $\text{PRD} = 9\%$ is overlapped in Figure 6 as a benchmark of the accepted recovery area. Meanwhile, considering generalization risk of recovery, the area marked by a solid red rectangle (as shown in Figure 6) is suggested as the parameter selection area, and $M = 256$ and $K = 4$ are the best choice. The computation of the confirmed optimal SBM is 2048 accumulation, which is suitable for the proposed node. It can be concluded that the SBM CS compression is low computation complexity.

The visual inspection of five original and recovered ECG signals is illustrated in Figure 7. It is observed that the PRDs of all records are less than 9%; the proposed system can achieve high-quality ECG signal recovery and guarantee the nondistortion diagnosis. Compared with the length of original signals, half of the data was reduced, which indicates that the proposed method has good potential in energy saving during ECG data wireless transmission. Moreover, the proposed CS compression is nonadaptive. No matter what the original ECG with different rhythms and morphological characteristics was fed in the framework, the same length of compressed data is achieved. Furthermore, all R -peaks of recovered ECG signals were detected in Figure 7. It is believed that the proposed system can achieve the recovered signal without diagnosis distortion; the proposed node is qualified for the ambulatory ECG monitoring.

The power consumptions of the node are demonstrated in Figure 8. It is observed that the power of the normal scheme (Figure 8(a)) holds steady about 70 mW if it ignores the energy consumption of 200 Hz ADC sampling. The node is energy wasting in the normal scheme because the radio is always on; in the S/W scheme, the node periodically sleeps

or wakes up, and it turns off or on the radio according to the requirement of the task. The power trace of S/W scheme is like a periodic pulse curve in Figure 8(b). In the last CS + S/W scheme (Figure 8(c)), the time interval of radio off is two times larger than that of S/W scheme, which proves that the CS compression reduces half of the data. The energy consumption of the proposed node is elaborated in Figure 9. The consumed energy in normal, S/W, and CS + SW schemes is 28.87 mJ, 8.85 mJ, and 6.53 mJ, respectively. Assume the energy consumption of radio is 100% in the normal scheme, and it reduces to 30.61% and 22.63% in S/W and CS + SW schemes, respectively. The energy consumption of CS code execution accounts for only 1.3% of the total energy consumption. The results indicate that the proposed node is energy efficient.

The specifics of the proposed node and the comparison with three commercial nodes are reported in Table 2. The proposed node is a light, low-cost, energy-efficient, single-spot wireless ECG node, it can provide real-time ambulatory ECG monitoring, and the lifetime of the node is 116 hours at 3 V battery.

5. Discussions

The advantages of the proposed ECG node include energy efficient, low computational complexity compression, real-time, and wireless. By using the ultra-low-power chips, periodic sleep/wake-up strategy, and CS compression, the transmission data was nonadaptive reducing 50% and recovered signal without diagnosis distortion. As indicated in Section 4, sleep/wake-up strategy and CS compression reduce 77.37% radio energy consumption. Meanwhile, the compression algorithm is a low computational complexity. The energy consumption of CS code execution is negligible due to the light computation load of accumulation. Furthermore, the ECG signal can be provided real-time to a user through the proposed system framework.

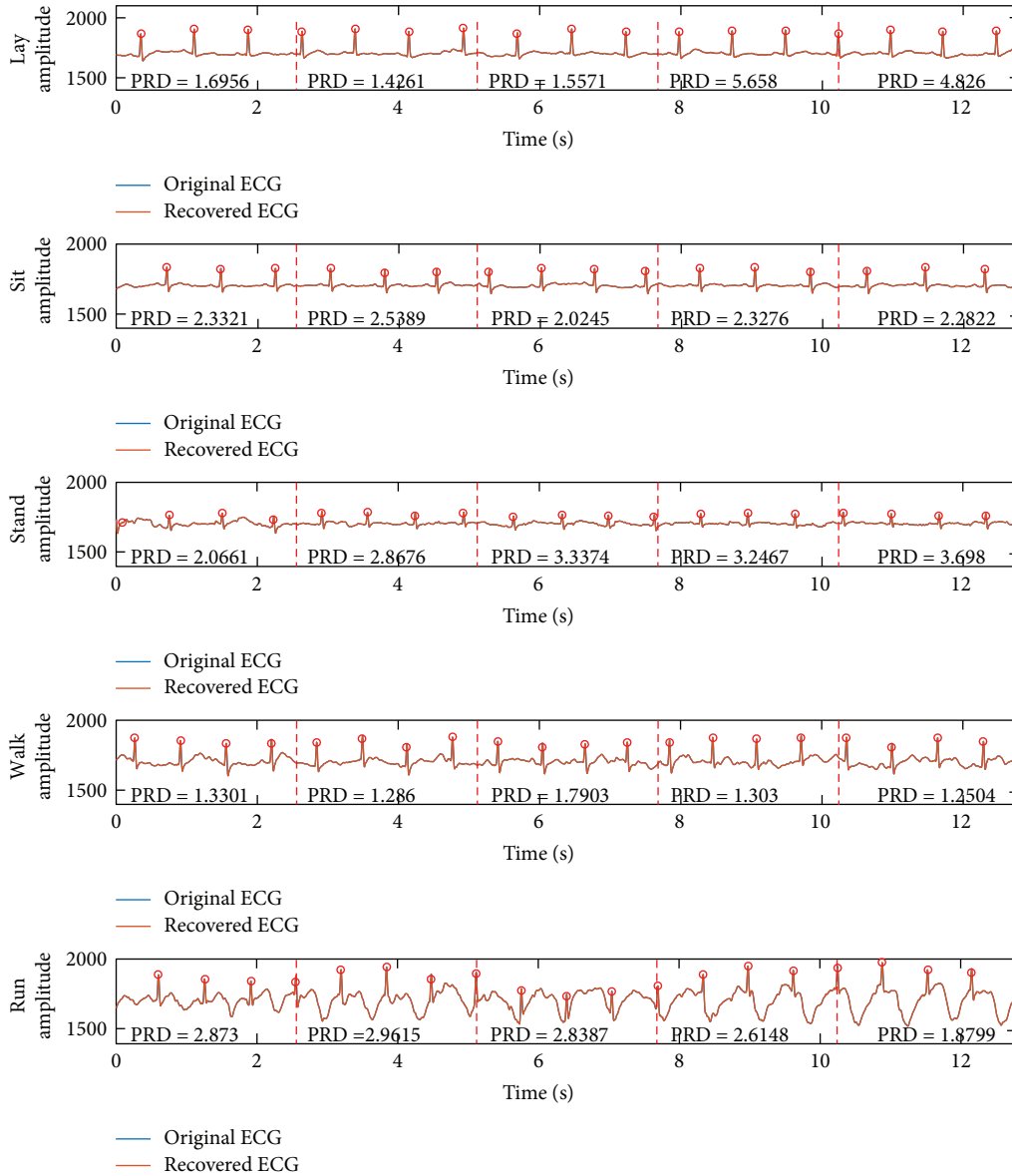


FIGURE 7: The visual inspection results. The recovery algorithm and sparse bases are BSBL and DCT, respectively: $N = 512$, $M = 256$, and $K = 4$; Pan-Tompkins method [30] was used for R-peak detection in the recovery signals. The red dotted lines are the segmented indicators of every frame, and the signal quality of each recovered frame was evaluated by PRD.

In the first subfigure of Figure 7, it can be found that the morphological similarity of ECG signal is high and the noise level of ECG signal is stable, but the PRDs are suddenly increased. ECG signal is typically characterized by localized information where essential and valuable diagnostic information is concentrated at the small interval and high-amplitude QRS complex. CS is a sampling method following the “information rate.” The whole QRS complex is segmented into two parts which leads to information loss that leads to distortion. The 10-point delayed recovered ECG is shown in Figure 10, and it is observed that there is no great variation of PRD.

The distortion caused by QRS complex location is the major shortcoming in our proposed ECG system, which is

expected to be solved by the information-enhanced sparse binary matrix [32].

6. Conclusion

CS is capable of achieving high compression ratios with low computational and memory requirements, making it suitable for being used in wireless ECG nodes. A digital compressed sensing-based single-spot Bluetooth ECG node was proposed in this study. The node was optimized for hardware, sleep/wake-up strategy, and CS compression and achieved good performance in energy saving. The proposed node reduces 77.37% radio energy consumption under compressed half of the data. The SBM-based compression algorithm is a low

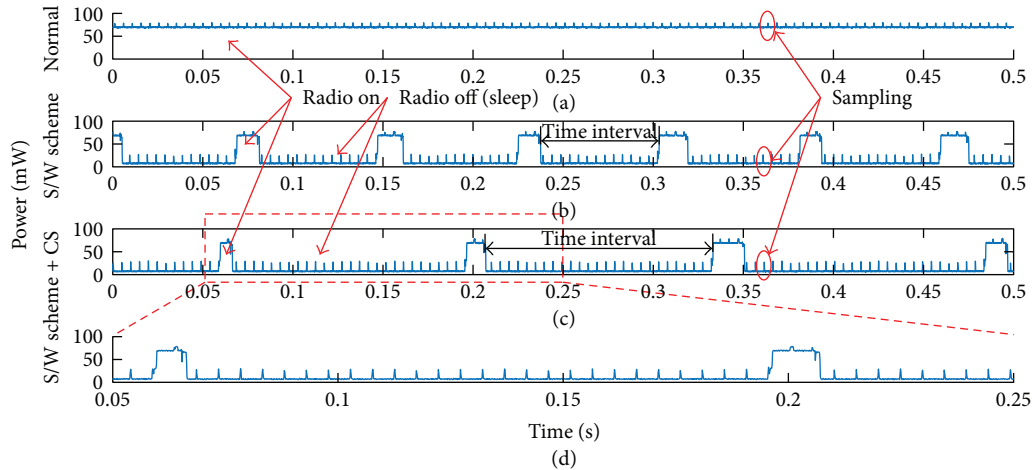


FIGURE 8: Power traces of the proposed node during different schemes. (a) The normal scheme, no energy saving strategy is used. (b) The S/W scheme. (c) The S/W scheme + CS. (d) The detailed figure of (c). The sampling energy consumption is marked by the red ellipses in (a–c).

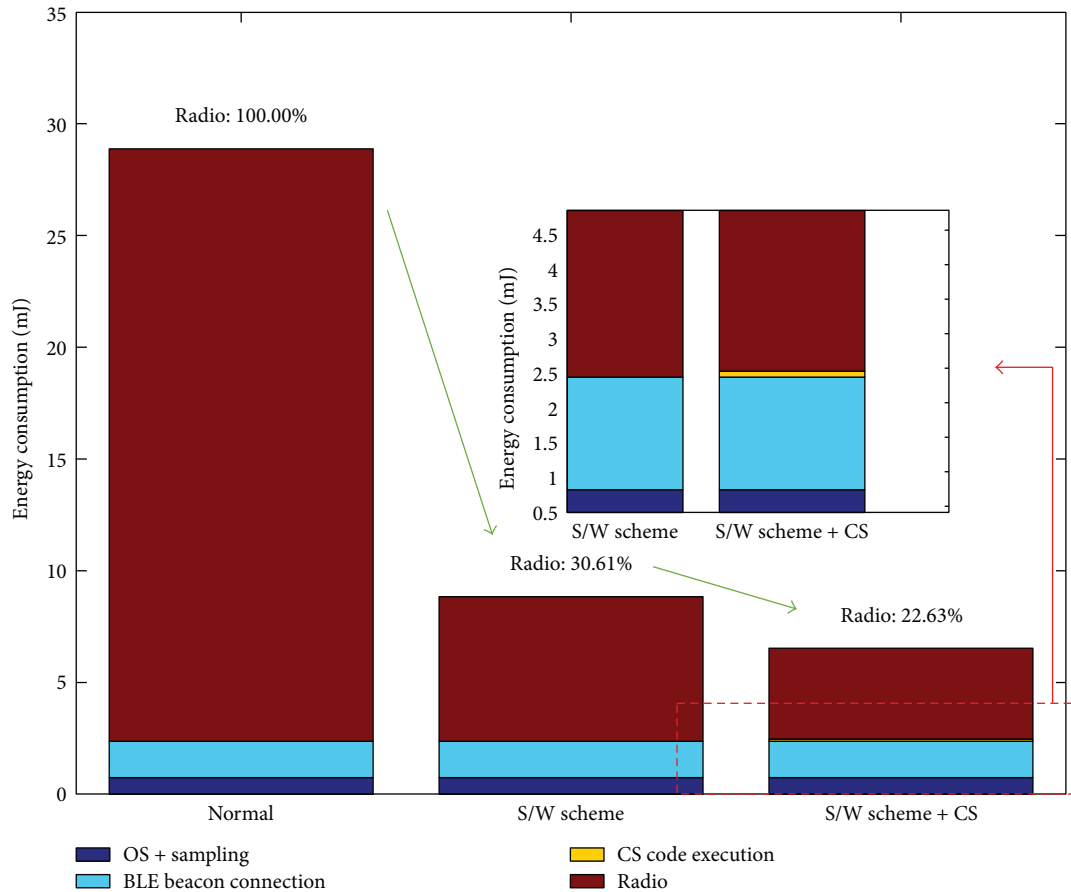


FIGURE 9: Energy consumption of the proposed node during different schemes.

computational complexity and nonadaptive, and the energy consumption of CS code execution is negligible. The recovered signals are essentially undistorted. Thus, it can be concluded that the proposed node can reduce the energy

requirement in transmitting ECG data and retaining the information content for diagnosis. The comparison with other ECG node shows that the advantages of the proposed node include light, low-cost, single-spot, real-time and wireless.

TABLE 2: Comparison of the proposed node with commercial ones.

	Proposed node	Shimmer2	ZMP ECG2	Zio Patch [31]
Size (mm)	40 (D) × 15(H)	53 × 32 × 23	44 × 41 × 9.34	123 × 53 × 10.7
Weight (g)	30	32	15	34
Current				
OS + sampling	0.23 mA	0.1 mA (only OS)	~1.35 mA	—
Wireless	1.98 mA at 200 Hz	~20 mA	~3.00 mA	No radio
Deep sleep	5.2 μ A	0.14 mA	~4 μ A	—
Lifetime	116 h at 3 V 230 mAh	~24 h at 3.7 V 450 mAh	72 h at 3.3 V 230 mAh	<14 day
Location	Single-spot	Traditional three lead	Single-spot	Single-spot
Price (RMB)	<400 (hardware cost)	>2800	>20000	—

Shimmer2: <http://www.shimmersensing.com/>; ZMP ECG2: <https://www.zmp.co.jp>; and Zio Patch monitor: <http://irhythmtech.com/>.

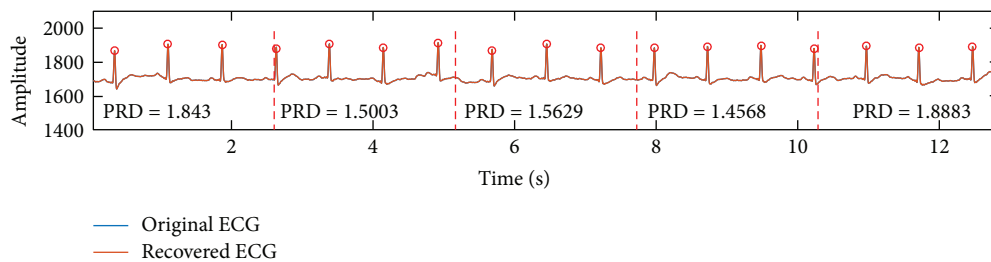


FIGURE 10: The recovered signal with 10 points delay.

Conflicts of Interest

The authors declare that they have no conflicts of interest.

Acknowledgments

This research was supported in part by the National Natural Science Foundation of China (NNSFC) under Grant 61601124 and Grant 61571113, the research project of Fujian University of Technology under Grant GY-Z160058, Fujian Province outstanding youth in university scientific research-supported program, the research project of Fujian Key Laboratory of Automotive Electronics and Electric Drive, and the Program for Postgraduates Research Innovation in the University of Jiangsu Province under Grant KYCX17_0067.

References

- [1] K. Luo, J. Li, and J. Wu, "A dynamic compression scheme for energy-efficient real-time wireless electrocardiogram biosensors," *IEEE Transactions on Instrumentation and Measurement*, vol. 63, no. 9, pp. 2160–2169, 2014.
- [2] D. E. Bloom, D. Chisholm, E. Jan et al., "From burden to "best buys": reducing the economic impact of non-communicable disease in low-and middle-income countries," *Program on the Global Demography of Aging*, 2011.
- [3] D. W. Smith, D. Nowacki, and J. K. Li, "ECG T-wave monitor for potential early detection and diagnosis of cardiac arrhythmias," *Cardiovascular Engineering*, vol. 10, no. 4, pp. 201–206, 2010.
- [4] P. Kulkarni and Y. Ozturk, "mPHASIS: mobile patient health-care and sensor information system," *Journal of Network and Computer Applications*, vol. 34, no. 1, pp. 402–417, 2011.
- [5] Y. Zheng, X. Ding, C. C. Y. Poon et al., "Unobtrusive sensing and wearable devices for health informatics," *IEEE Transactions on Biomedical Engineering*, vol. 61, no. 5, pp. 1538–1554, 2014.
- [6] E. S. Winokur, M. K. Delano, and C. G. Sodini, "A wearable cardiac monitor for long-term data acquisition and analysis," *IEEE Transactions on Biomedical Engineering*, vol. 60, no. 1, pp. 189–192, 2013.
- [7] R. F. Yazicioglu, T. Torfs, J. Penders et al., "Ultra-low-power wearable biopotential sensor nodes," in *2009 Annual International Conference of the IEEE Engineering in Medicine and Biology Society*, pp. 3205–3208, Minneapolis, MN, USA, 2009.
- [8] T. Tsai, J. Hong, L. Wang, and S. Lee, "Low-power analog integrated circuits for wireless ECG acquisition systems," *IEEE Transactions on Information Technology in Biomedicine*, vol. 16, no. 5, pp. 907–917, 2012.
- [9] R. Yan, H. Sun, and Y. Qian, "Energy-aware sensor node design with its application in wireless sensor networks," *IEEE Transactions on Instrumentation and Measurement*, vol. 62, no. 5, pp. 1183–1191, 2013.
- [10] J. Pandey and B. P. Otis, "A sub-100 μ W MICS/ISM band transmitter based on injection-locking and frequency multiplication," *IEEE Journal of Solid-State Circuits*, vol. 46, no. 5, pp. 1049–1058, 2011.
- [11] B. H. Calhoun, J. Lach, J. Stankovic et al., "Body sensor networks: a holistic approach from silicon to users," *Proceedings of the IEEE*, vol. 100, no. 1, pp. 91–106, 2012.

- [12] R. Kannan and C. Eswaran, "Lossless compression schemes for ECG signals using neural network predictors," *EURASIP Journal on Applied Signal Processing*, vol. 2007, no. 1, article 035641, 2007.
- [13] A. Kadrolkar, R. X. Gao, Y. Ruqiang, and G. Weibo, "Variable-word-length coding for energy-aware signal transmission," *IEEE Transactions on Instrumentation and Measurement*, vol. 61, no. 4, pp. 850–864, 2012.
- [14] H. Mamaghalian, N. Khaled, D. Atienza, and P. Vandergheynst, "Compressed sensing for real-time energy-efficient ECG compression on wireless body sensor nodes," *IEEE Transactions on Biomedical Engineering*, vol. 58, no. 9, pp. 2456–2466, 2011.
- [15] A. M. R. Dixon, E. G. Allstot, D. Gangopadhyay, and D. J. Allstot, "Compressed sensing system considerations for ECG and EMG wireless biosensors," *IEEE Transactions on Biomedical Circuits and Systems*, vol. 6, no. 2, pp. 156–166, 2012.
- [16] A. S. Lalos, L. Alonso, and C. Verikoukis, "Model based compressed sensing reconstruction algorithms for ECG telemonitoring in WBANs," *Digital Signal Processing*, vol. 35, pp. 105–116, 2014.
- [17] E. J. Candes and T. Tao, "Near-optimal signal recovery from random projections: universal encoding strategies?," *IEEE Transactions on Information Theory*, vol. 52, no. 12, pp. 5406–5425, 2006.
- [18] J. Jian, G. Yuantao, and M. Shunliang, "A stochastic gradient approach on compressive sensing signal reconstruction based on adaptive filtering framework," *IEEE Signal Processing Society*, vol. 4, no. 2, pp. 409–420, 2010.
- [19] M. Mishali, Y. C. Eldar, O. Dounaevsky, and E. Shoshan, "Xampling: analog to digital at sub-Nyquist rates," *IET Circuits, Devices & Systems*, vol. 5, no. 1, pp. 8–20, 2011.
- [20] Z. Zhang, T. Jung, S. Makeig, and B. D. Rao, "Compressed sensing of EEG for wireless telemonitoring with low energy consumption and inexpensive hardware," *IEEE Transactions on Biomedical Engineering*, vol. 60, no. 1, pp. 221–224, 2013.
- [21] Z. Zhang, T. Jung, S. Makeig, and B. D. Rao, "Compressed sensing for energy-efficient wireless telemonitoring of noninvasive fetal ECG via block sparse Bayesian learning," *IEEE Transactions on Biomedical Engineering*, vol. 60, no. 2, pp. 300–309, 2013.
- [22] N. V. Thakor, J. G. Webster, and W. J. Tompkins, "Estimation of QRS complex power spectra for design of a QRS filter," *IEEE Transactions on Biomedical Engineering*, vol. BME-31, no. 11, pp. 702–706, 1984.
- [23] E. J. Candès, J. K. Romberg, and T. Tao, "Stable signal recovery from incomplete and inaccurate measurements," *Communications on Pure and Applied Mathematics*, vol. 59, no. 8, pp. 1207–1223, 2006.
- [24] E. J. Candès and T. Tao, "Decoding by linear programming," *IEEE Transactions on Information Theory*, vol. 51, no. 12, pp. 4203–4215, 2005.
- [25] L. Wei and N. Vaswani, "Modified basis pursuit denoising(modified-BPDN) for noisy compressive sensing with partially known support," in *2010 IEEE International Conference on Acoustics, Speech and Signal Processing*, pp. 3926–3929, Dallas, TX, USA, 2010.
- [26] J. A. Tropp and A. C. Gilbert, "Signal recovery from random measurements via orthogonal matching pursuit," *IEEE Transactions on Information Theory*, vol. 53, no. 12, pp. 4655–4666, 2007.
- [27] G. Da Poian, R. Bernardini, and R. Rinaldo, "Separation and analysis of fetal-ECG signals from compressed sensed abdominal ECG recordings," *IEEE Transactions on Biomedical Engineering*, vol. 63, no. 6, pp. 1269–1279, 2016.
- [28] Z. Zhang and B. D. Rao, "Sparse signal recovery with temporally correlated source vectors using sparse Bayesian learning," *IEEE Journal of Selected Topics in Signal Processing*, vol. 5, no. 5, pp. 912–926, 2011.
- [29] Y. Zigel, A. Cohen, and A. Katz, "The weighted diagnostic distortion (WDD) measure for ECG signal compression," *IEEE Transactions on Biomedical Engineering*, vol. 47, no. 11, pp. 1422–1430, 2000.
- [30] J. Pan and W. J. Tompkins, "A real-time QRS detection algorithm," *IEEE Transactions on Biomedical Engineering*, vol. BME-32, no. 3, pp. 230–236, 1985.
- [31] M. P. Turakhia, D. D. Hoang, P. Zimetbaum et al., "Diagnostic utility of a novel leadless arrhythmia monitoring device," *The American Journal of Cardiology*, vol. 112, no. 4, pp. 520–524, 2013.
- [32] K. Luo, Z. Wang, J. Li, R. Yanakieva, and A. Cuschieri, "Information-enhanced sparse binary matrix in compressed sensing for ECG," *Electronics Letters*, vol. 50, no. 18, pp. 1271–1273, 2014.

Research Article

A Novel Sleep Respiratory Rate Detection Method for Obstructive Sleep Apnea Based on Characteristic Moment Waveform

Yu Fang ¹, Zhongwei Jiang ¹ and Haibin Wang ²

¹Graduate School of Science and Engineering, Yamaguchi University, Yamaguchi, Japan

²School of Electrical Engineering and Electronic Information, Xihua University, Chengdu, China

Correspondence should be addressed to Haibin Wang; ddwang@mail.xhu.edu.cn

Received 9 June 2017; Revised 24 September 2017; Accepted 9 October 2017; Published 10 January 2018

Academic Editor: Chengyu Liu

Copyright © 2018 Yu Fang et al. This is an open access article distributed under the Creative Commons Attribution License, which permits unrestricted use, distribution, and reproduction in any medium, provided the original work is properly cited.

Obstructive sleep apnea (OSA) affecting human's health is a kind of major breathing-related sleep disorders and sometimes leads to nocturnal death. Respiratory rate (RR) of a sleep breathing sound signal is an important human vital sign for OSA monitoring during whole-night sleeping. A novel sleep respiratory rate detection with high computational speed based on characteristic moment waveform (CMW) method is proposed in this paper. A portable and wearable sound device is used to acquire the breathing sound signal. And the amplitude contrast decreasing has been done first. Then, the CMW is extracted with suitable time scale parameters, and the sleep RR value is calculated by the extreme points of CMW. Experiments of one OSA case and five healthy cases are tested to validate the efficiency of the proposed sleep RR detection method. According to manual counting, sleep RR can be detected accurately by the proposed method. In addition, the apnea sections can be detected by the sleep RR values with a given threshold, and the time duration of the segmentation of the breath can be calculated for detailed evaluation of the state of OSA. The proposed method is meaningful for continued research on the sleep breathing sound signal.

1. Introduction

Humans spend almost 30% of the time in sleeping, and the sleep quality is very important for human's health. Breathing-related sleep disorders are characterized by abnormalities of the respiratory pattern or the quantity of ventilation during sleep [1]. It is considered a chronic illness which needs long-term treatment and management. Obstructive sleep apnea (OSA) is a kind of major breathing-related sleep disorders, and it is described by full or partial occlusion of the upper airway during sleep which can produce repeated oxyhemoglobin desaturations and sleep fragmentation [2]. OSA which is considered a main risk factor for cardiovascular disease affects human's health and sometimes leads to nocturnal death [3, 4].

OSA is commonly defined as a minimum of 10 s interval pause of breath. The Apnea-Hypopnea Index (AHI) is described by the number of apnea and hypopnea events per hour to assess OSA severity. AHI of 5–15 indicates mild OSA; 15–30, moderate; and over 30, severe [5].

Sleep respiratory rate (RR) is an important indicator for serious illness [6], especially for OSA monitoring. RR of healthy adults in a relax state is about 12–20 times per minute. However, the RR will be abnormal for the OSA case while the sleep breathing becomes slowed or stopped by the apnea [7]. Hence, sleep RR is an early and vital indicator for OSA patients.

Polysomnography (PSG) is often used to detect OSA in clinic which acquires a series of monitoring indices including RR. But PSG with many sensors is not only expensive but also complicated for common patients [8]. Moreover, it is uncomfortable for the testers during their sleep, so the results of PSG will be influenced by the low-quantity sleep of the testers. With the development of a smart wearable device, several researchers have interests in RR detection by acoustic signals.

The acoustic signals mainly come from two aspects, breathing sound signals of the nose and the mouth [9] and tracheal signals from the throat [10] and the suprasternal notch [6, 11]. For RR detection via a tracheal signal, Hilbert

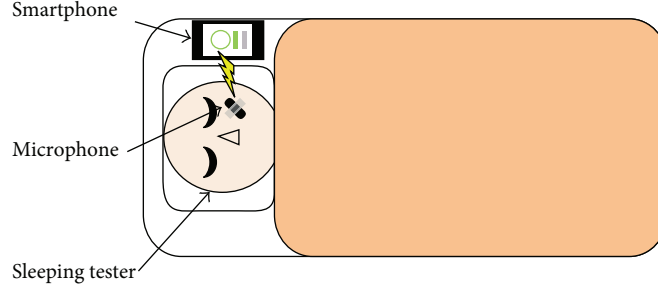


FIGURE 1: Sleep respiratory signal acquisition system.

transform was applied to extract the sound envelope and wavelet was applied for frequency content decomposition with a success rate of 96% for healthy volunteers and 85% for patients suffering from chronic pulmonary diseases [10]. A respiratory phase segmentation method based on a genetic algorithm was applied to monitor the RR which was enhanced by exploiting the signal redundancy [11]. The short-time Fourier transform, Shannon entropy, and autocorrelation were calculated to detect the RR value [6]. It is found that the previous RR detection methods are mainly based on the tracheal signal, and the acquisition of the tracheal signal is not convenient as a sleep breathing sound signal. And the selection of a threshold value which plays an important role in envelope extraction will change accompanied by the speed of breathing for different individuals. So the adaption of the threshold values, that is, the time scale parameters, will affect the accuracy of sleep RR detection and should be solved for further research. The OSA monitoring should be completed all night, and the results of sleep RR detection need to be transferred to an analysis system correctly and timely. In the previous research, the RR estimation via finding the largest spectral peaks of autoregressive power spectral analysis has been proposed [9]. And the successful rates for the patients' RR detection by the breathing sound from the mouth and nose were 85% and 84%, respectively [10]. They are not effective for the OSA case with apnea and not satisfied with the practical demand. In this paper, a RR detection method via a sleep breathing sound signal based on characteristic moment waveform is proposed.

This paper is divided into 6 sections. Section 2 introduces sleep breathing sound signal acquisition. Section 3 describes details of the characteristic moment waveform extraction method. Section 4 gives the introduction of the sleep RR detection method. The results and analysis are disclosed in Section 5, and conclusions will be drawn in Section 6.

2. Sleep Breathing Sound Signal Acquisition and Preprocessing

2.1. Acquisition System of the Sleep Breathing Sound Signal.

The sleep breathing sound signal is collected by a portable and wearable acquisition device for high sleep quality, including a smart phone with an android system and a wireless microphone. The purpose of our research is to develop a cheap and easy-to-use sleeping monitoring system for home use, so that the commercial wireless headset

(such as PTM 165) will be one better choice for our research. Compared with the acquisition positions inferred, the microphone is fixed near the nose by a kind of makeup tape to acquire a stable breath signal during whole-night sleeping. The environment of data acquisition is shown in Figure 1. The original sample frequency is 44.1 kHz.

2.2. *Preprocessing for Amplitude Contrast Diminution.* In fact, the intensity of the sleep breathing sound signal will change greatly and impact the efficiency of the proposed sleep RR detection method. The weak breathing sound will be covered by the heavy breathing and the surrounding noise. Therefore, the amplitude contrast of different breathing cycles should be decreased first. The enhanced preprocessing method is first introduced in detail as follows. The entropy of the original signal $H(t)$ is defined as

$$H(t) = E[y(t)] = -\xi y(t) \cdot \ln(y(t)), \quad \begin{cases} \xi = -1 (y(t) > 0) \\ \xi = 0 (y(t) = 0) \\ \xi = 1 (y(t) < 0). \end{cases} \quad (1)$$

Then, decrease the volume and intensity difference by cutting off the strong intensity part; the output signal is

$$H_{\text{cut}}(t) = a \cdot H(t) \pm b \cdot \text{av}(|H(t)| > \text{av}), \quad (2)$$

$$H_{\text{cut}}(t) = c \cdot H(t) (|H(t)| < \text{av}),$$

where av is the mean value of the $H(t)$, a and b are weakening factors, and c is the enhancement factor.

According to the experimental results by trial and error, a is selected as 0.4, b is 0.6 when $H(t)$ is positive and -0.6 when $H(t)$ is negative, and c is set as 1.5 to enhance the amplitude of a weak breathing cycle.

The final preprocessed signal is given by

$$y_{\text{enhance}}(t) = H_{\text{cut}}(t) \cdot (1 - l) + l \cdot H_{\text{cut}}(t)^N, \quad (3)$$

where l experimentally set as 0.85 is the limiting amplitude factor and N is set as 20 by experience.

A section of the sleeping breathing sound signal with large intensity variation is shown in Figure 2(a). Compared with the cycles in the both ends, the amplitude of three breathing cycles in the middle is too small to be detected. And after a series of processing shown in Figures 2(b) and 2(c), it is clearly found that the amplitude contrast of each

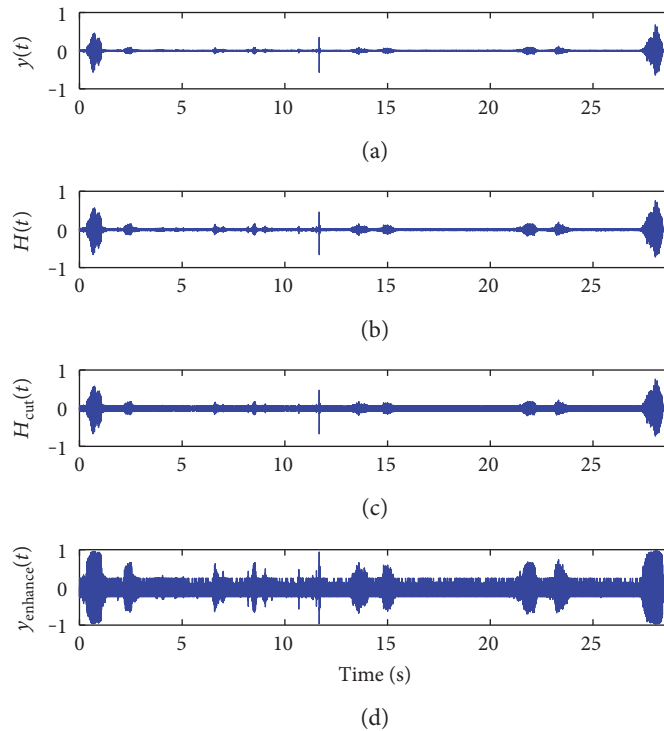


FIGURE 2: Sleep breathing sound signal waveforms, (a) original signal waveform, and (b–d) the procedure of the preprocessing.

breathing cycle has been shrunk shown in Figure 2(d), and it will improve the accuracy of the sleep RR detection.

3. Characteristic Moment Waveform Extraction of the Breathing Sound

A sleep breathing sound signal is generated by the movement of air through the respiratory system, the nose, and the mouth. It is always affected by a tester's healthy condition, mental state, sleeping environment, and so on. It is considered a quasiperiodic signal, and the sleep RR index can be computed by counting the number of the breathing period per minute in clinic.

3.1. Characteristic Moment Waveform (CMW). Waveform extraction is always applied at the beginning of the signal processing in a time domain. The waveform should keep the useful information of the sleep breathing sound signal as much as possible and make the impact of noise as less as possible. Commonly, Hilbert transform and Shannon entropy are used for waveform extraction [10, 12, 13]. According to the features of the biomedical signals, one single freedom model [13], a homomorphic filter [14], and other means are also applied for extracting the waveform. In this paper, the time characteristic waveform (TCW) is extracted first with multiscale adjustment. And then, the characteristic moment waveform (CMW) is proposed for sleep RR detection based on TCW.

The precondition is assuming the noise part of the sleep breathing sound signal as the signal with zero mean and unit variance. Suppose the sleep breathing sound signal is $r(t)$, the random noise signal is $n(t)$, and the real output signal is

$y(t) = r(t) + n(t)$. TCW of the sleep breathing sound signal, marked as $c(t, \delta)$, defined as the variance of the output $y(t)$ can be gotten by

$$\begin{aligned} c(t, \delta) &= \sigma^2(y) = \int_{t-\delta}^{t+\delta} (y(\tau) - \bar{y}(t))^2 d\tau \\ &= \int_{t-\delta}^{t+\delta} y(\tau)^2 d\tau - 2\delta\bar{y}(t)^2, \\ \bar{y}(t) &= \frac{1}{2\delta} \int_{t-\delta}^{t+\delta} y(\tau) d\tau. \end{aligned} \quad (4)$$

Then, the CMW is calculated by the thought of image shape identification in image processing with another time scale l , which is represented by $I(t, \delta, l)$. It is calculated as follows:

$$I(t, \delta, l) = \int_{t-l}^{t+l} (\tau - t)^2 c(\tau, \delta) d\tau. \quad (5)$$

And the normalization presentation is presented as

$$n(t, \delta, l) = \frac{\int_{t-l}^{t+l} (\tau - t)^2 c(\tau, \delta) d\tau}{\int_{t-l}^{t+l} c(\tau, \delta) d\tau}, \quad (6)$$

where δ and l are neighborhood of time t , which is called the width time scale.

It is easy to find that the calculated amount will increase with a larger time scale δ and l . The integral waveforms are applied to compute the TCW and CMW. The calculations of TCW and CMW are independent of the time scale

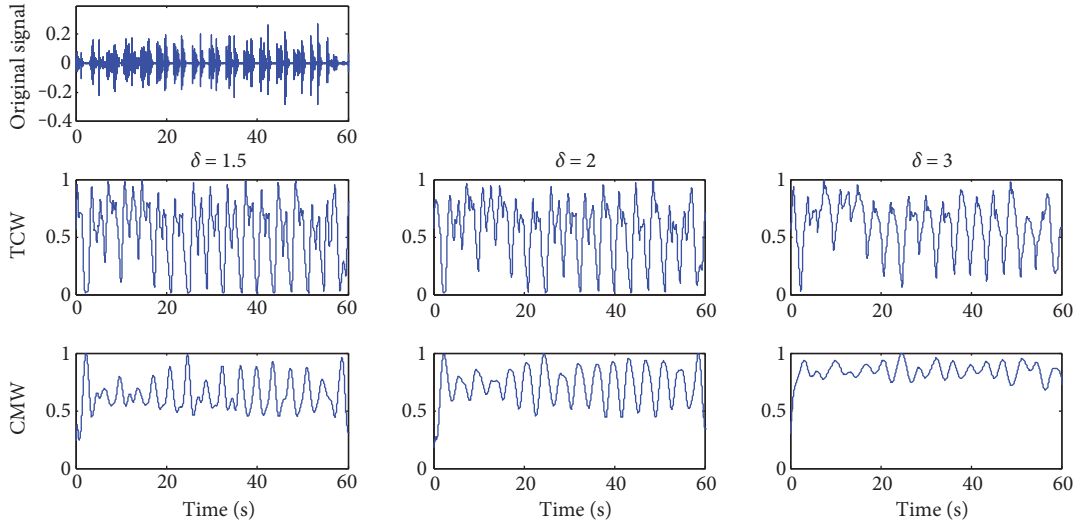


FIGURE 3: Time characteristic waveforms (TCW) and moment waveforms (CMW) of the breathing sound signal in the normal case while $l = 0.1$ and $\delta = 1.5, 2.0,$ and $3.0,$ respectively, from left to right.

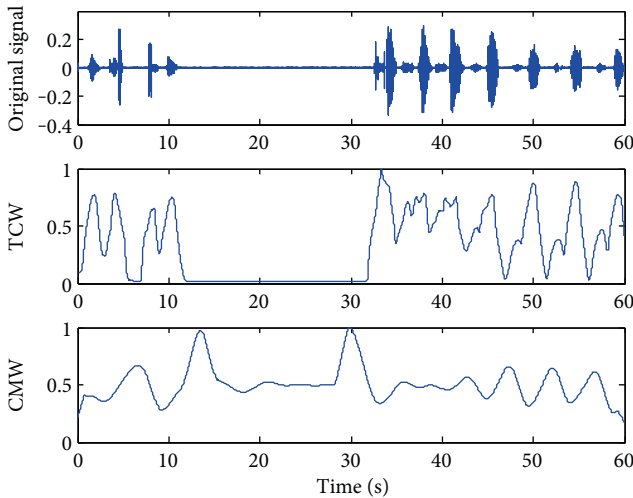


FIGURE 4: TCW and CMW of the breathing sound signal in the apnea case while $\delta = 2.5$ and $l = 0.1$.

parameters and fast with a very simple algorithm, just using additions and multiplications [15].

3.2. Scale Choice for TCW and CMW. A breathing cycle is constructed by four phases: inhalation, inspiratory pause, exhalation, and period of rest; the RR value is defined by the time duration during two consecutive inspirations [16]. According to our experimental statistic, a normal sleep breathing cycle is about 3 to 5 seconds and the time inspiration/expiration phase duration has a range of (0.3, 1) seconds. So the scale δ is usually set to (1.5, 3), about half of the sleep breathing cycle. The accuracy of CMW is not required in high level for sleep RR detection, and the time scale l is set as 0.1, about 1/10 of the phase duration. And the affection of the scale δ is shown directly in Figure 3.

The TCW and CMW of a stable sleep breathing sound signal are shown in Figure 3 while δ is set as 1.5, 2, and 3, respectively. For this case, a sleeping breathing cycle lasts about 4 seconds and δ is set to 2.0 as the most suitable value based on the rules of the scale selection. While $\delta = 1.5$, the waveforms of TCW and CMW are not smooth for the next segmentation. While $\delta = 3$, the necessary details of the waveforms are ignored which weakens the periodicity. For the abnormal breathing case shown in Figure 4, δ is set to 2.5 as the breathing cycle lasting about 5 seconds.

In addition, according to the extracted waveforms, the most useful information of the original sleep breathing sound signal can be kept from the TCW waveform. And CMW with clear periodicity is convenient for finding the sleep RR index.

4. Respiratory Rate Detection Method

After choosing the suitable time scales, TCW and CMW are extracted according to (4), (5), and (6) and the sleep RR index can be detected using the following steps [15].

- Step 1: Calculate the maximum point sequence of CMW.
- Step 2: Find the local maximum point sequence by computing the maximum value of the point sequence gotten from Step 1.
- Step 3: Calculate the local minimum point sequence of TCW shown in the middle plants of Figures 5 and 6.
- Step 4: Adjust the cycle segment points by a computation window with the central point as the local minimum point sequence of TCW and the segment points shown in the bottom of Figures 5 and 6.
- Step 5: Count the number of the cycle segment point per minute as the RR value.

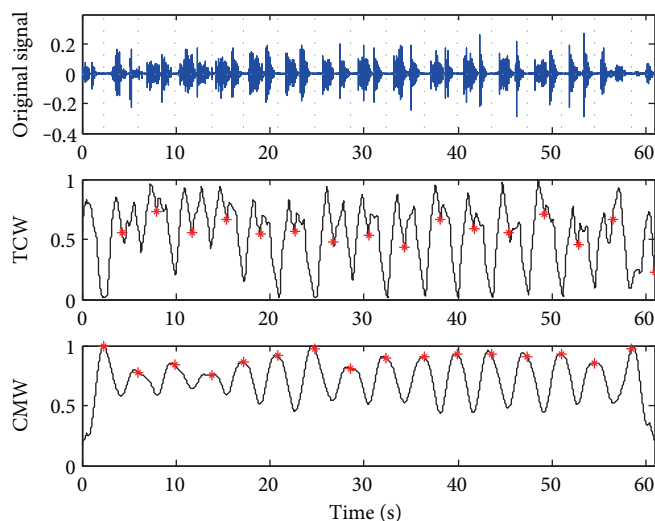


FIGURE 5: Results of the breath cycle segmentation of the case in Figure 3.

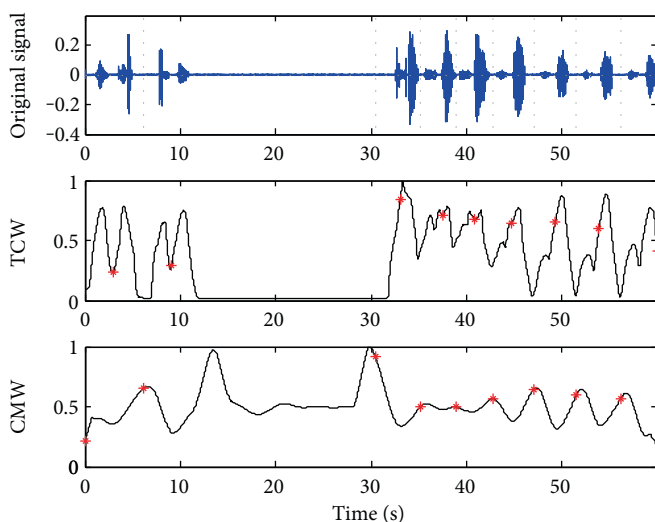


FIGURE 6: Results of the breath cycle segmentation of the case in Figure 4.

Take the cases shown in Figures 3 and 4 for example; the breathing cycles are segmented correctly based on the TCW and CMW displayed by the gray dot line in Figures 5 and 6. Even there is some noise coming from the movements of the mouth, the segment results have not been affected. 16 breathing cycles in Figure 5 and nine breathing cycles in Figure 6 are extracted correctly. The proposed method shows outstanding stability and accuracy in sleep RR value detection.

5. Experiment

5.1. The Information of Experimental Data. Five young students (21 ± 1 years old) and a 59-year-old man who was diagnosed with OSA in the clinical setting are selected as testers.

Utilizing the acquisition system of the sleeping breathing sound signal, we recorded about 374-minute-length data and counted the breathing cycles manually with the

guidance of the prodoctor for the reference. The information of the experimental data is listed in Table 1, and the OSA case is number 6.

5.2. The Efficiency of the Preprocessing. Through a series of processing introduced in Section 2.2, the intensity difference between strong and weak respiratory signals becomes small and its efficiency is validated.

The results of breathing cycle segmentation before and after applying the enhanced preprocessing method are summarized in Table 2. Without preprocessing, the scale parameters (δ , l) are selected as (2, 0.1), (2, 0.1), (2.5, 0.1), (2.5, 0.1), (3, 0.1), and (3, 0.1) for test cases orderly. While applying the enhanced preprocessing method, the scale parameters (δ , l) are set as (2.5, 0.1) for all cases.

From Table 2, it seems that the method without preprocessing can detect the breathing cycle with a success rate of at least 93.06%. And the total successful rate is improved to

TABLE 1: Experimental data.

Case number	1	2	3	4	5	6	Total
Test time (min)	57	62	85	50	60	60	374
Test cycle number (manual counting)	890	891	1177	702	678	663	5001

TABLE 2: Detection results of the respiratory cycle segmentation.

Case number	Without preprocessing		With preprocessing	
	Cycle number	Successful rate (%)	Cycle number	Successful rate (%)
1	849	95.39	872	97.98
2	851	95.51	865	97.08
3	1156	98.22	1172	99.58
4	683	97.29	694	98.86
5	667	98.38	672	99.12
6	617	93.06	646	97.44
Total	4823	96.44	4921	98.40

Successful rate = segmented cycle number/test cycle number by counting manually.

98.40% with the same predicted time scale parameters for different cases when applying the enhanced preprocessing method. Especially, the successful rate of the OSA case that improved to 97.44% can satisfy the experimental requirement of the sleep RR detection. Therefore, the use of the enhanced preprocessing method shows more adaptability and veracity in this experiment.

5.3. The Sleep RR Detection for OSA Analysis. The sleep RR value per minute is computed by counting the number of the segmented breathing cycles. The average values of the sleep RR index of each case are expressed by the bar graph shown in Figure 7. The blue bars in the left show the manual counting results and the red bars in the right show the average sleep RR via the proposed detection method.

It is known that the sleep RR of healthy young men is from 13 to 15 times per minute. And the sleep RR of the OSA case is the slowest among the entire tester which is related to the age and presence of the OSA disease. Specially, the sleep RR of case 5 is closed to that of the OSA case (case 6). Hence, these two cases will be analyzed in detail in the following.

The plot of the sleep RR value of the OSA case (number 6) in one hour is shown in Figure 8. In order to detect the apnea events, a threshold value T_{RR} is set by

$$T_{RR} = RR_{stable} - 10 * \frac{RR_{stable}}{60}, \quad (7)$$

where RR_{stable} is the stable or normal respiratory rate in sleeping. The apnea should last more than 10 seconds according to the clinical definition. In another explanation, 10 seconds can be counted as $10 * RR_{stable}/60$ times/min. Based on the result in Figure 8, the RR_{stable} is 11 times/min; therefore, $10 * RR_{stable}/60$ is calculated as 1.8 times/min and T_{RR} is around 9 times/min. It is found that seven points,

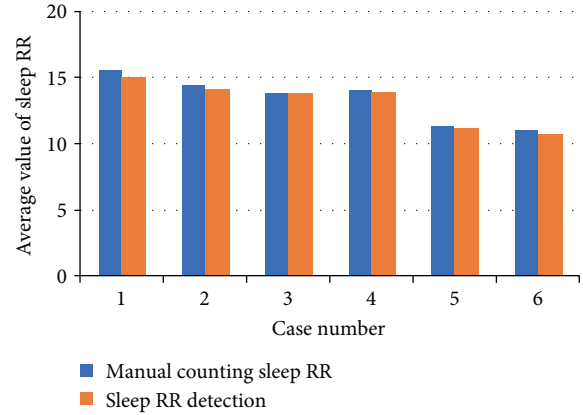


FIGURE 7: Sleep RR statistic average values of the six cases.

denoted by A_i , are the satisfying condition $RR < T_{RR}$ as shown in Figure 8.

In another way to describe the apnea event detection, we can calculate the RR time interval $dd(i)$ of the segmentation directly. As the results shown in Figure 6, since each segmented part contains a breathing signal, the apnea pause time can be calculated as $dd(i) - 60/RR_{stable}$ as shown in Figure 9. Figure 10 shows the time duration values $dd(i)$ of each segmented breathing cycle. It shows that the stable or normal breathing cycle is about 5 seconds and the longest apnea is about 40.

Figure 11 shows the pause time calculation results at apnea event points A1 to A7 of Figure 8. The pause time durations of A1 to A7 are 14.39 s, 13.28 s, 25.31 s, 15.31 s, 31.06 s, 16.97 s, and 13.92 s, respectively. Therefore, there are 7 apnea events lasting more than 10 s; the tester might be identified as having mild OSA because of $AHI = 7$. The sleep RR detection will be acquired for more times of all-night monitoring in order to get more accurate results.

In addition, the signal waveform of the AX section is shown in Figure 12. Since the largest breathing pause is about 7 s, the AX section can be diagnosed as the hypopnea case, a kind of abnormal sleep breath. The abnormal breathing cycles will be meaningful for sleep monitoring.

As mentioned in Figure 7, the data of case number 5 is from a young student and its statistic average value of sleep RR is closed to that of OSA. In the same way, the plot of the time duration values $dd(i)$ of each segmentation is shown in Figure 13. The stable breathing cycle lasts about 5 seconds, and nine breathing cycles with apnea are detected.

The breathing sound signal waveforms with apnea are displayed in Figure 14. Although there are lots of noise chips during the apnea duration and the intensity of the breathing changes greatly, the breathing cycle can be segmented

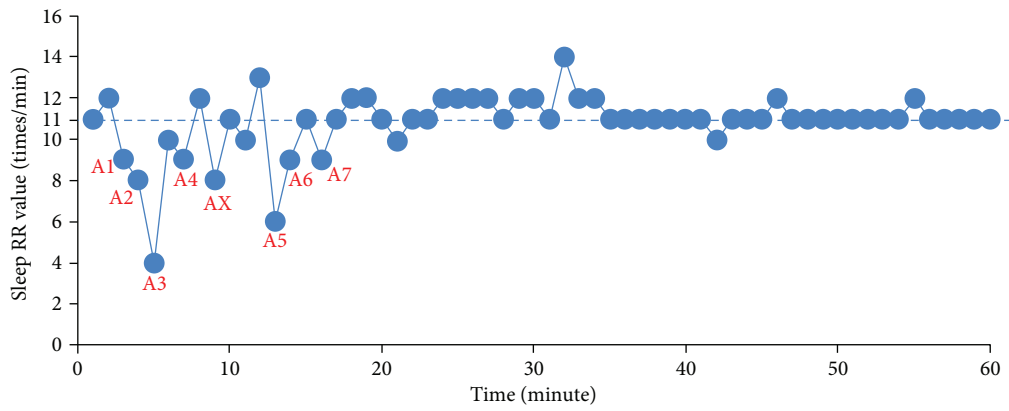


FIGURE 8: Sleep RR values in the OSA case (number 6).

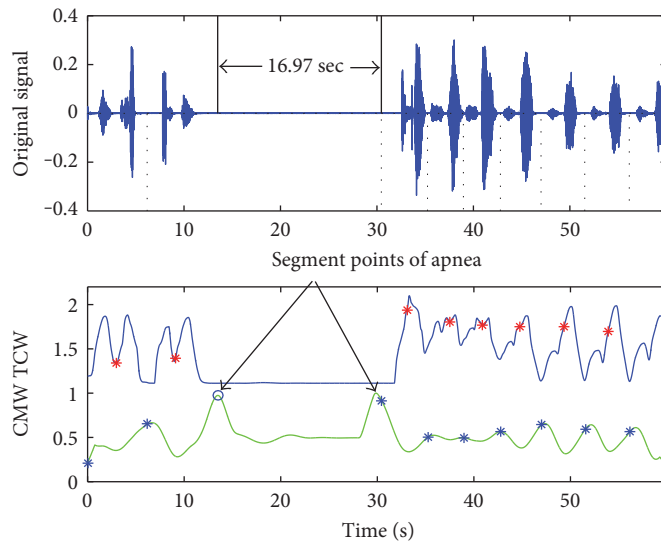


FIGURE 9: Extraction of time duration for apnea.

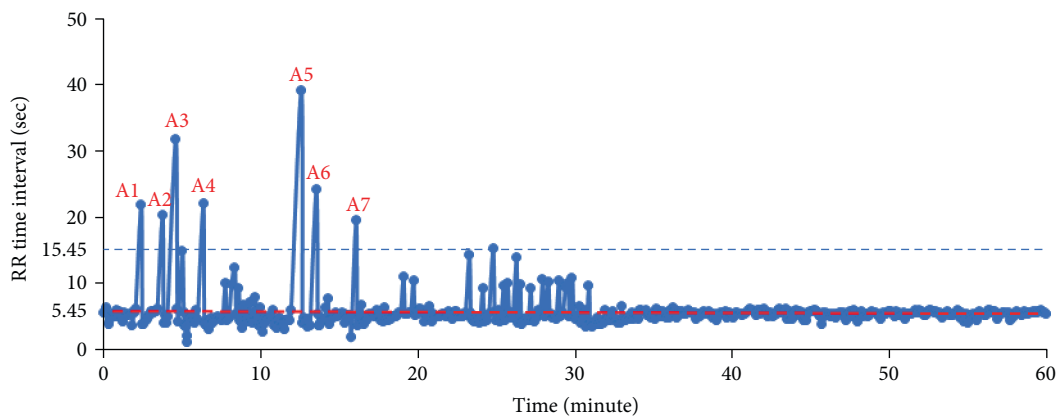


FIGURE 10: Time duration values of each segmented breath cycle for the OSA case.

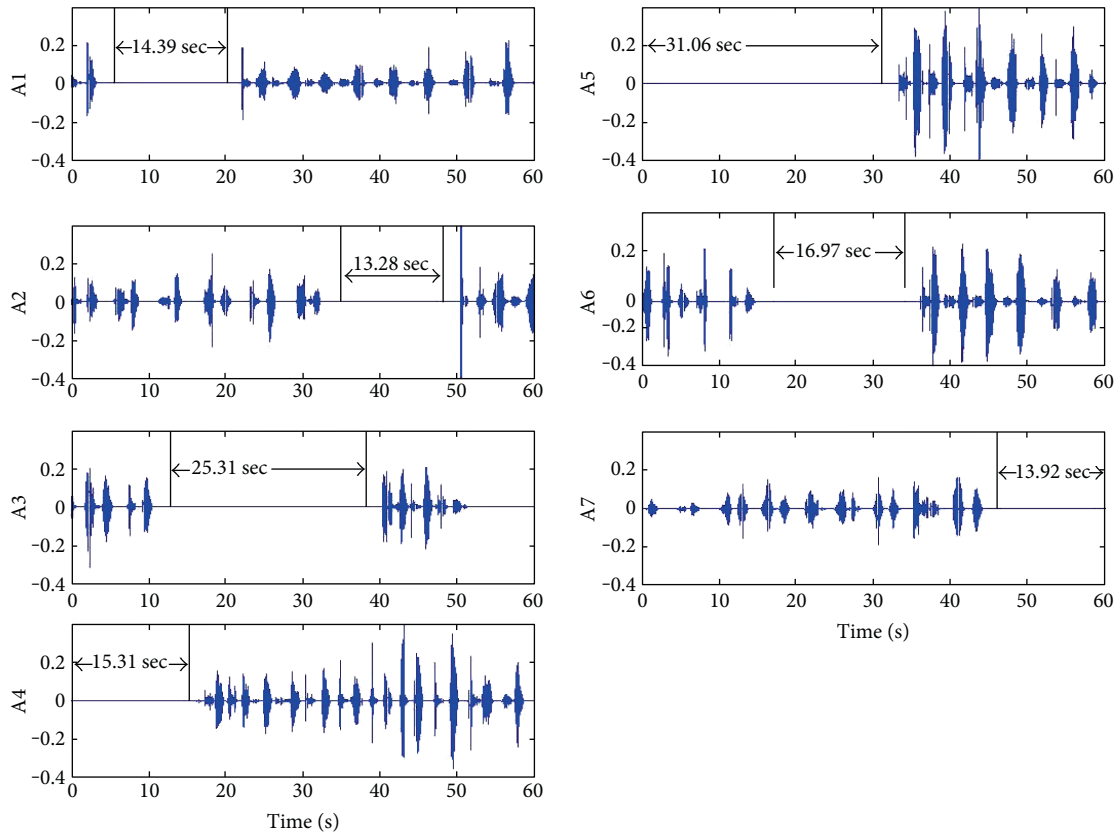


FIGURE 11: Sleep breathing sound signal waveforms with apnea events (number 6).

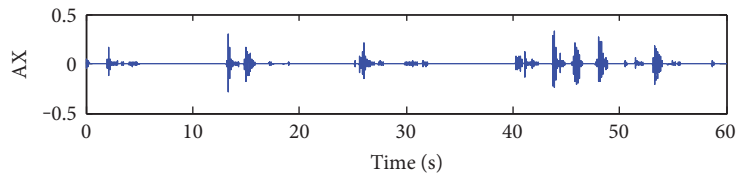


FIGURE 12: A case of abnormal sleep breathing sound signal waveforms (hypopnea case).

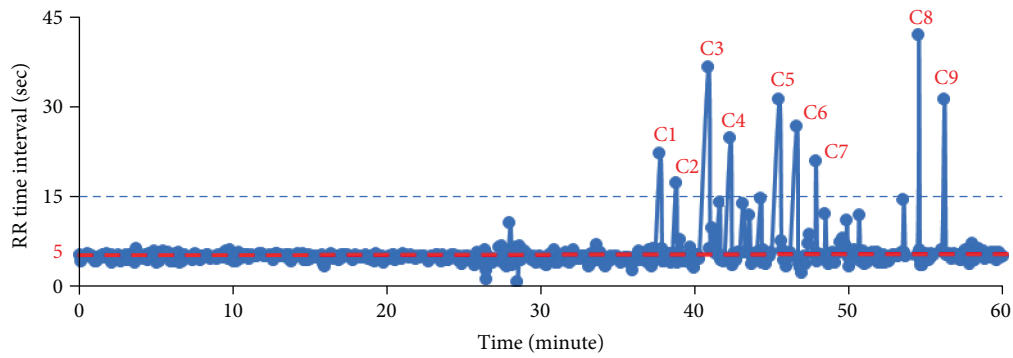


FIGURE 13: Time duration values of each segmented breath cycle for case number 5.

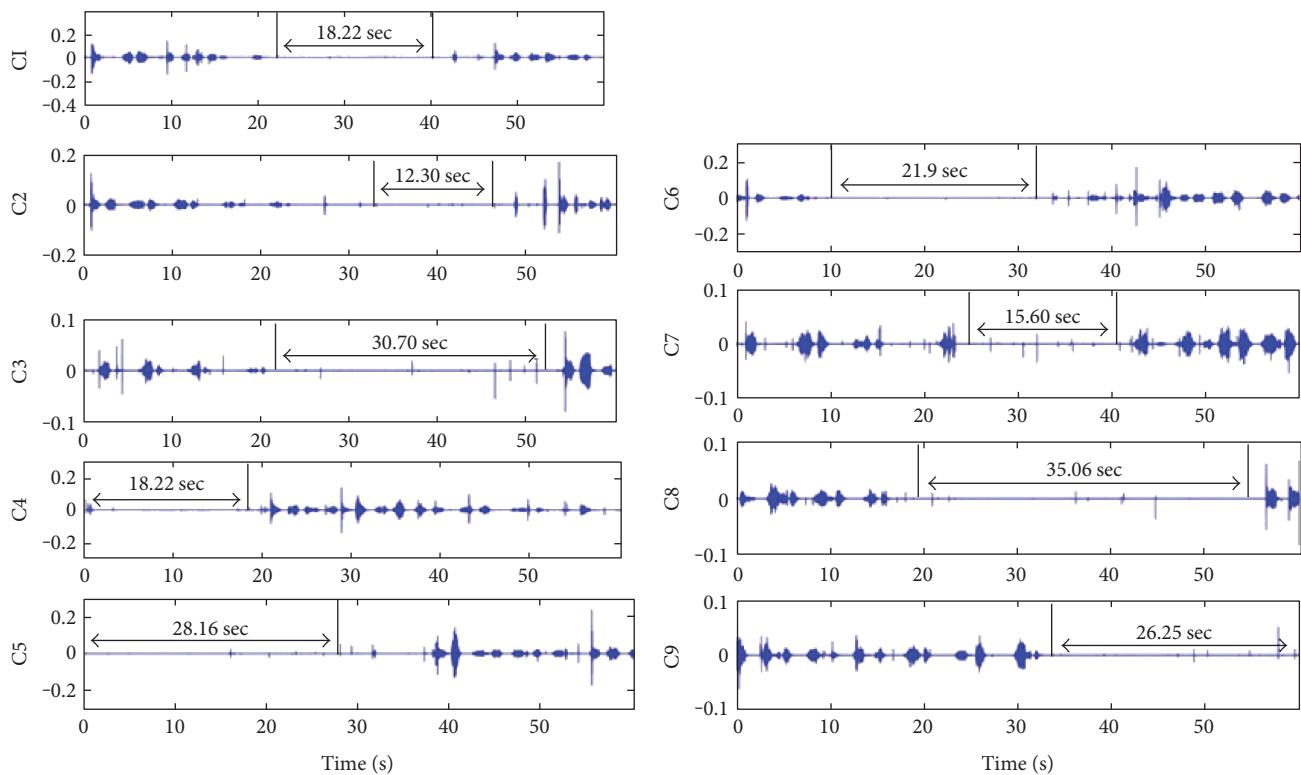


FIGURE 14: Sleep breathing sound signal waveforms with apnea events (number 5).

correctly and the apnea can be extracted successfully. It shows that the proposed method has high anti-interference and accuracy on signal segmentation and apnea event extraction.

6. Conclusion

Sleep RR is one of the significant human vital signs. The sleep RR and intensity are changed a lot during the whole-night monitoring, and the real-time RR detection will be influenced by strong volume noise. This paper utilizes the characteristic moment waveform for sleep RR detection from the sleep breathing sound signal which is acquired by a wearable sound device. At the first part, the enhanced preprocessing method is applied to reduce the amplitude contrast of the original recording signal. The accuracy of the sleep RR detection and the adaptation of the time scale parameters for different individuals have been improved. According to the results of the experiment, the successful rate of the sleep RR detection can reach to 98.40%. And the sleep breathing sound of subjects with OSA disease can be analyzed easily by the sleep RR value. Moreover, the time interval of apnea can be calculated by the breathing cycle segmentation based on the characteristic moment waveform. The proposed sleep RR detection method is effective for the sleep condition monitoring and OSA disease analysis.

Conflicts of Interest

The authors declare that they have no conflicts of interest.

Acknowledgments

This project is supported by the National Natural Science Foundation of China (Grant no. 61571371) and the Ministry of Education, Culture, Sports, Science and Technology of Japan, Grant-in-Aid for Scientific Research (C), 2012–2014, 24560261.

References

- [1] C. Doukas, T. Petsatodis, C. Boukis, and I. Maglogiannis, "Automated sleep breath disorders detection utilizing patient sound analysis," *Biomedical Signal Processing and Control*, vol. 7, pp. 256–264, 2012.
- [2] C. A. Kushida, M. R. Littner, M. Hirshkowitz et al., "Practice parameters for the use of continuous and bilevel positive airway pressure devices to treat adult patients with sleep-related breathing disorders," *Sleep*, vol. 29, no. 3, pp. 375–380, 2006.
- [3] N. Takama and M. Kurabayashi, "Influence of untreated sleep disordered breathing on the long-term prognosis of patients with cardiovascular disease," *The American Journal of Cardiology*, vol. 103, no. 5, pp. 730–734, 2009.
- [4] G. Hamilton, I. Meredith, A. Walker, and P. Solin, "Obstructive sleep apnea leads to transient uncoupling of coronary blood flow and myocardial work in humans," *Sleep*, vol. 32, no. 2, pp. 263–270, 2009.
- [5] L. Almazaydeh, K. Elleithy, M. Faezipour, and A. Abushakra, "Apnea detection based on respiratory signal classification," *Procedia Computer Science*, vol. 21, pp. 310–316, 2013.
- [6] J. Zhang, W. Ser, and D. Y. T. Goh, "A novel respiratory rate estimation method for sound-based wearable monitoring

- systems,” in *2011 Annual International Conference of the IEEE Engineering in Medicine and Biology Society*, pp. 3213–3216, Boston, Massachusetts USA, August–September, 2011.
- [7] M. A. Cretikos, R. Bellomo, K. Hillman, J. Chen, S. Finfer, and A. Flabouris, “Respiratory rate: the neglected vital sign,” *The Medical Journal of Australia*, vol. 188, no. 11, pp. 657–659, 2008.
- [8] Z. Moussavi, A. Elwali, R. Soltanzadeh, C. A. MacGregor, and B. Lithgow, “Breathing sounds characteristics correlate with structural changes of upper airway due to obstructive sleep apnea,” in *2015 37th Annual International Conference of the IEEE Engineering in Medicine and Biology Society (EMBC)*, pp. 5956–5959, Milan, Italy, August 2015.
- [9] Y. Nam, B. A. Reyes, and K. H. Chon, “Estimation of respiratory rates using the built-in microphone of a smartphone or headset,” *IEEE Journal of Biomedical and Health Informatics*, vol. 20, no. 6, pp. 1493–1501, 2016.
- [10] G. Sierra, V. Telfort, B. Popov, L. G. Durand, R. Agarwal, and V. Lanzo, “Monitoring respiratory rate based on tracheal sounds. First experiences,” in *The 26th Annual International Conference of the IEEE Engineering in Medicine and Biology Society*, San Francisco, CA, USA, September 2004.
- [11] F. Jin, F. Sattar, D. Y. T. Goh, and I. M. Louis, “An enhanced respiratory rate monitoring method for real tracheal sound recordings,” in *2009 17th European Signal Processing Conference (EUSIPCO 2009)*, pp. 642–645, Glasgow, UK, August 2009.
- [12] A. Kulkas, E. Huupponen, J. Virkkala et al., “Intelligent methods for identifying respiratory cycle phases from tracheal sound signal during sleep,” *Computers in Biology and Medicine*, vol. 39, no. 11, pp. 1000–1005, 2009.
- [13] S. Choi and Z. Jiang, “Comparison of envelope extraction algorithms for cardiac sound signal segmentation,” *Expert Systems with Applications*, vol. 34, no. 2, pp. 1056–1069, 2008.
- [14] J. Liu, H. Wang, W. Liu, and J. Zhan, “Autonomous detection and classification of congenital heart disease using an auscultation vest,” *Journal of Computational Information Systems*, vol. 8, no. 2, pp. 485–492, 2012.
- [15] Z. Yan, Z. Jiang, A. Miyamoto, and Y. Wei, “The moment segmentation analysis of heart sound pattern,” *Computer Methods and Programs in Biomedicine*, vol. 98, no. 2, pp. 140–150, 2010.
- [16] *Respiratory Cycle: Definition and Explanation*, <http://physician-diary.com/respiratory-cycle-definition-and-explanation/>.

Research Article

A Remote Health Monitoring System for the Elderly Based on Smart Home Gateway

Kai Guan, Minggang Shao, and Shuicai Wu

College of Life Science & Bioengineering, Beijing University of Technology, Beijing, China

Correspondence should be addressed to Shuicai Wu; wushuicai@bjut.edu.cn

Received 8 April 2017; Revised 16 August 2017; Accepted 10 September 2017; Published 24 October 2017

Academic Editor: Chengyu Liu

Copyright © 2017 Kai Guan et al. This is an open access article distributed under the Creative Commons Attribution License, which permits unrestricted use, distribution, and reproduction in any medium, provided the original work is properly cited.

This paper proposed a remote health monitoring system for the elderly based on smart home gateway. The proposed system consists of three parts: the smart clothing, the smart home gateway, and the health care server. The smart clothing collects the elderly's electrocardiogram (ECG) and motion signals. The home gateway is used for data transmission. The health care server provides services of data storage and user information management; it is constructed on the Windows-Apache-MySQL-PHP (WAMP) platform and is tested on the Ali Cloud platform. To resolve the issues of data overload and network congestion of the home gateway, an ECG compression algorithm is applied. System demonstration shows that the ECG signals and motion signals of the elderly can be monitored. Evaluation of the compression algorithm shows that it has a high compression ratio and low distortion and consumes little time, which is suitable for home gateways. The proposed system has good scalability, and it is simple to operate. It has the potential to provide long-term and continuous home health monitoring services for the elderly.

1. Introduction

Recent years have witnessed China entering the aging society. The issue of population aging seems more and more serious. Physical conditions of the elderly, including cardiac function and the ability of maintaining gait balance, are declining. Health care and safety monitoring for the elderly is becoming an urgent issue to be solved.

The healthcare Internet of things (IoT) based on medical digital devices makes the home health monitoring for the elderly possible. By establishing an IoT-based home care monitoring system, the elderly can know about their health condition and get services provided by the health care center without walking out of home. It would also make the government and the society able to cushion the blow of the aging population.

In the home care monitoring system, the smart home gateway collects signals from the body sensor network (BSN) and transmits them to the health care server. The development of home gateway-based homecare monitoring systems has been through three stages. In the first stage, the telephone modem acts as the home gateway, and data was

transmitted through the telephone line. Maiolo et al. [1] and Vitacca et al. [2] proposed monitoring systems by using modems for patients with chronic respiratory failure. This kind of health care systems can transmit a limited amount of data with a limited transmitting speed, which restricts the expansibility of the system. Meanwhile, when the data need to be transmitted, it needs to be manipulated by the patient, which seems not user-friendly. The popularization of the personal computer (PC) drives the health care monitoring system to its second stage. In the second stage, PCs were used as the home gateway, and data was transmitted through broadband. There is no doubt that PCs have enough operation ability to process data, while they consume large electric power. The third stage of health care monitoring system is characterized by embedded devices and smart devices [3–5]. Bansal et al. [6] and Jung et al. [7] proposed health care monitoring systems based on mobile gateways, like smart phones. Lin et al. [8] designed a set-top box-based homecare system. Spinsante and Gambi [9] proposed the TV-based mode of home care. Rahmani et al. [10] developed a smart home gateway and a corresponding monitoring system based on embedded technology; it can monitor multiphysiological

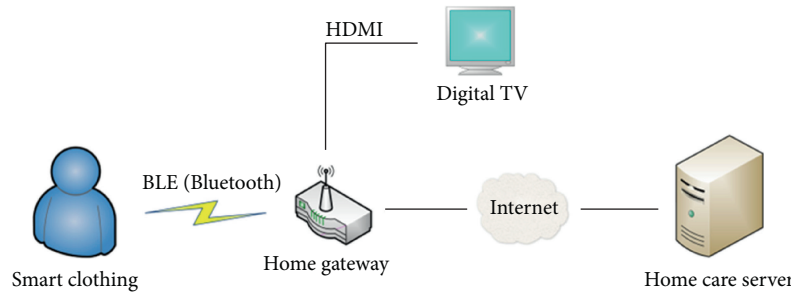


FIGURE 1: Architecture of the health monitoring system.

signals of the elderly. Although each of these methods has their own advantages, there are also some drawbacks. The mobile gateway cannot guarantee long-term and continuous measurement. The set-top box-based system did not provide the measurement of ECG, which is the most important physiological signal for patients with cardiovascular diseases. Meanwhile, these solutions cannot guarantee 24 hours of monitoring for the elderly, and they are too sophisticated for the elderly to use.

Moreover, a huge amount of physiological data would generate during the process of health monitoring. It may cause problems of data overload and network congestion, which is a big burden for home gateway. The storing strategy of combining local storage and cloud storage proposed by Lin et al. [8] can reduce the storage pressure of the home gateway, but it consumes too much system resources when transmitting data. Previous studies [11–16] introduced the concept of data compression, which can reduce the amount of data effectively.

To implement long-term monitoring of the elderly, resolve issues of data overload and network congestion, and make it easy to operate for the elderly, a smart home gateway-based home care monitoring system was proposed in this paper. First, the system design is described. Then the principle and workflow of the ECG compression algorithm are presented. Lastly, the whole system and the compression algorithm are tested and evaluated.

2. Materials and Methods

2.1. System Design. Figure 1 shows the architecture of the proposed system. The system comprises three parts, namely, the smart clothing for ECG and motion signals collection, the home gateway for data transmission, and the health care server for data storage and user information management.

Three-lead ECG signals and three-axis acceleration signals are obtained when the elders are wearing the smart clothing. The ECG signals are used to monitor the heart condition of the elderly, especially those with heart failure; the acceleration signals are used to monitor the body states of the elderly, such as walking and falling down. The smart clothing sends these signals to the home gateway via low-energy Bluetooth (BLE). And the home gateway gets data from the smart clothing through a Bluetooth connection. After local data processing, compression, and storage, the gateway transmits these data to the health care server via

the Internet. The home gateway also provides service of video communication, which makes the connection between the elderly and doctors more convenient. The health care server is designed on the WAMP platform, and it is transplanted to the Ali Cloud® platform. It is used for long-term data storage and user information management.

2.1.1. Wearable Smart Clothing. The ECG cables and the signals acquisition unit of smart clothing are designed separately. A cloth was designed with the ECG cables and the electrodes embedded in it. And the signal acquisition unit can be connected to the cloth through four metal buttons. The signal acquisition unit acquires three-lead ECG signals and three-axis acceleration signals and sends data to the home gateway via BLE. It is easy to operate and has low power consumption.

STM32F401 is used as the microprocessor unit (MPU) of the signal acquisition unit. The ECG data acquisition module, the acceleration signal acquisition module, and the BLE module are designed. Figure 2 shows the hardware design of the smart clothing. The prototype of smart clothing is shown in Figure 3.

The signal acquisition unit is powered by a rechargeable lithium battery, which has an On-The-Go (OTG) port for power charging. When the unit is fully charged, it would wait for connection with a home gateway. Once receiving a connection request, it would respond and connect with the gateway. Then the signal acquisition unit would send data to the gateway continuously. The sampling frequency of ECG signals is 250 Hz, and the sampling frequency of acceleration signals is 100 Hz. The data package sent to the gateway is shown in Table 1. The first two bytes of the package are the header, which is used to recognize each package; the following bytes are the ECG data and the motion data.

2.1.2. Home Gateway

(1) Hardware Design. Exynos 4412 produced by Samsung was used as the MPU of the home gateway. It supports Linux and Android operation systems and is widely used in the consumer electronics field. To shorten the development cycle and ensure the stability of the home gateway, a kernel board is selected as the control module. An Exynos 4412, a power management integrated circuit (PMIC)—S5M8767, 1 GB flash memory, 4 GB embedded MultiMediaCard (EMMC), and an USB3503A hub controller are integrated on it. In order to make a prototype of the home gateway, the network

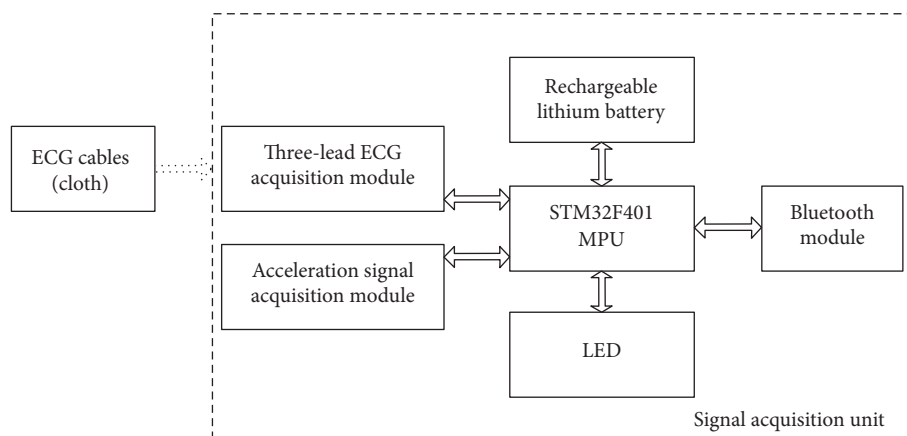


FIGURE 2: Hardware design of smart clothing.



FIGURE 3: Prototype of smart clothing.

TABLE 1: Data packet format of the signal acquisition unit of smart clothing.

Header	Count	ECG lead I	ECG lead II	ECG lead III	X	Y	Z
0xA5 0xA5	Data	Data	Data	Data	Data	Data	Data

communication modules, the power module, and other modules are also designed on the circuit board. The prototype of the home gateway is shown in Figure 4.

A 5 V power adapter is used as the main power supply of the home gateway. The kernel board functions at 4 V, so a level conversion chip is used to convert the 5 V voltage to 4 V. The S5M8767 chip on the kernel board provides different ranges of power for other modules.

The network communication modules of the home gateway include BLE, Wi-Fi for local connection, and Ethernet

for remote connection. A MT6620 combo module (Wi-Fi and BLE) is selected as the local connection module, and a DM9621 module as the remote connection module.

To make it convenient for the elderly, a High-Definition Multimedia Interface (HDMI) port for TV connection and an Infrared Data Association (IrDA) port for an infrared remote control are designed. The audio module is also designed by using a WM8960 chip. It is connected to the kernel board via inter-integrated circuit sound (I2S) and inter-integrated circuit (I2C) ports. To simplify the design of the home gateway, three Universal Serial Bus (USB) ports are developed to connect a camera or other modules.

(2) *Software Design.* Firstly, the Android operating system is transplanted onto the kernel board. Then an application (App) is developed based on the Android platform. The structure of the App is shown in Figure 5.

A key capability of home gateways is the identification of different users. Generally, typing the username and password is used to identify different users, but it is not convenient for the elderly. In the proposed system, the Bluetooth address of the smart clothing is used as the identification code (ID), which is bound to an elder. That means, by identifying different smart clothings (different Bluetooth addresses), the system can recognize different users. In order to make it easy to operate, we allocate a quick response (QR) code to each smart clothing, and the information included in the QR code is the Bluetooth address of the clothing.

The App starts and enters the login page when the gateway is powered on. The elderly can use a camera connected to the home gateway to scan the QR code of his or her smart clothing to log in. Then the login page will jump to the main menu thereupon. In the main menu, there are four modules. These are “Monitoring Center,” “Health Records,” “Connection,” and “System Settings.” The “Monitoring Center” module is used for connecting the smart clothing, adopting data, processing data, and displaying heart rate or other information. The “Health Records” module can provide the user’s ECG records, motion information, and the auto-diagnosis information from the gateway. The “Connection” module is used for establishing the connection between the

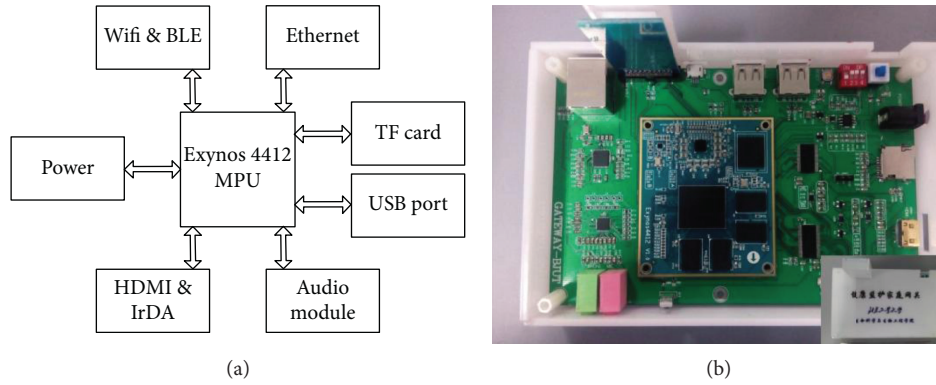


FIGURE 4: Home gateway. (a) Hardware design of home gateway. (b) Prototype of home gateway.

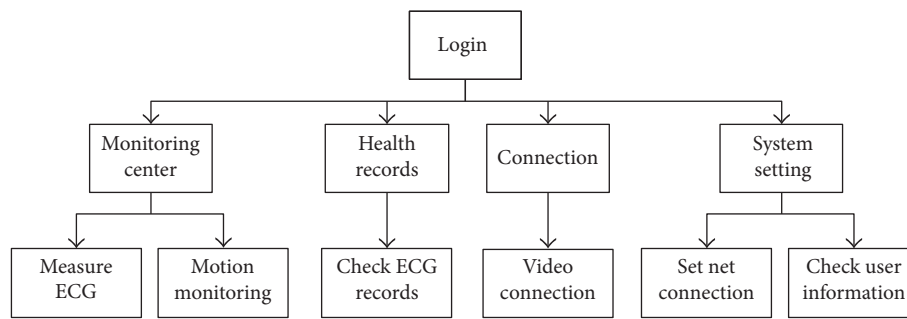


FIGURE 5: Structure of the App of home gateway.

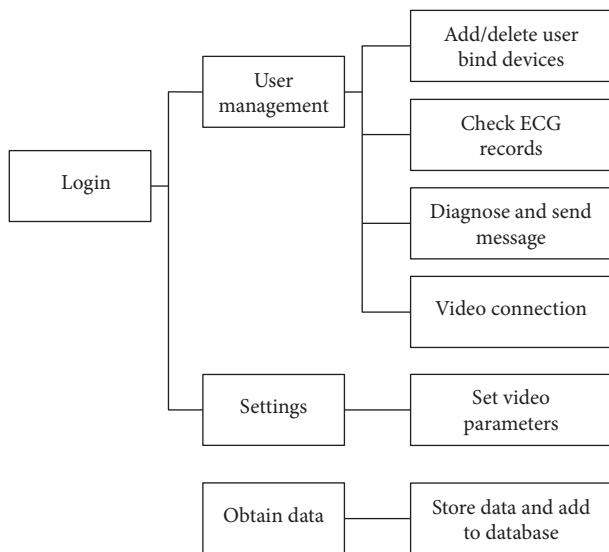


FIGURE 6: Website design.

elderly and doctors through a camera. Doctors would contact the elderly in a regular time to confirm their health condition, and for the urgent situation, both the doctors and elderly can contact each other at any time. In the “System Setting” module, the elderly can set the net connection mode and check his basic information.

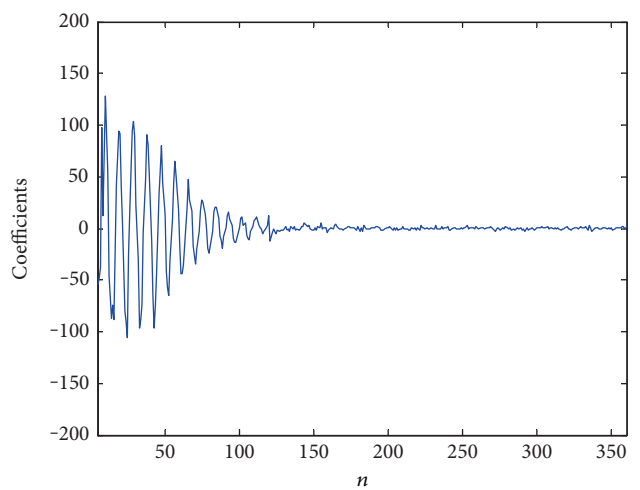


FIGURE 7: DCT of ECG (number 100).

There are two main methods of remote data transmission, that is, transmitting data packets in real time and transmitting data files at regular time intervals. The first method can guarantee the server getting the real-time data, but the data packet loss is severe. The second method can reduce the packet loss rate although it cannot ensure real-time data transmission. The health care system designed in this paper

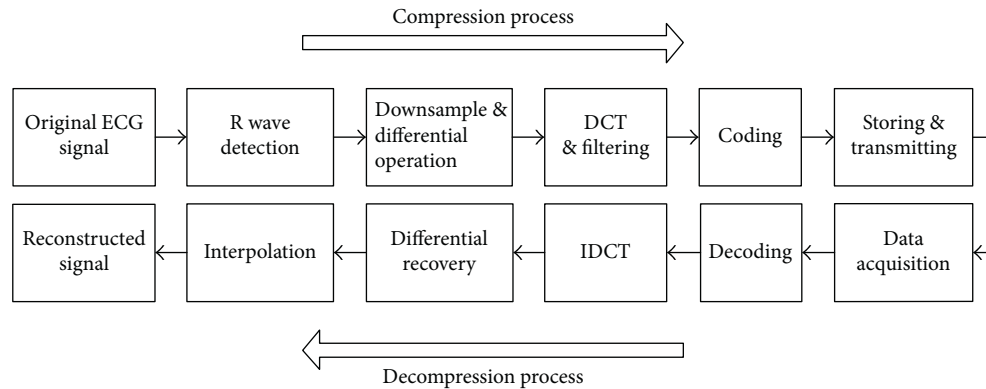


FIGURE 8: Process of data compression and decompression.

adopts the second way, and a local database is constructed by using SQLite to manage the local data.

2.1.3. Health Care Server. The health care server has sufficient operating capability of mining the ECG and motion data. The technologies of distributed system and cloud computing introduced in recent years make the big data processing and information mining possible. In the proposed system, the server is developed on the WAMP platform and is transplanted onto the Ali Cloud platform.

The realization of health care server includes database design and website design. The database is used for information storage, and the website is used to realize the functions of managing user information, reading data files, and so on. PHP language is used to develop the website.

MySQL is chosen to design a database to store the information of the elderly and doctors. Four tables entitled “User,” “Doctor,” “UserData,” and “UserDiag” are built. Table “User” and table “Doctor” are used to store the basic information of the elderly and doctors. Table “UserData” stores the index of ECG files, and table “UserDiag” stores the doctors’ diagnostic information.

Figure 6 shows the functions of the website, including receiving data files from the home gateway, saving data files, and managing the database according to users’ information. When the doctors log in to the website, they can add/delete users or allocate a smart clothing to an elder. They can also read ECG records, make diagnoses based on the ECG records, mark the ECG graph, send diagnostic information or advice to the home gateway, and accept video connection requests from the elderly.

2.2. Data Compression Algorithm. The ECG sampling frequency of the signal acquisition unit in the smart clothing is 250 Hz with 12-bit resolution over a -5.27 mV to 5.27 mV range, so the data quantity of three leads is 4050000 bytes per hour. Thus, it is a high load for the home gateway to store or transmit the data. The most direct and effective way to reduce the resource consumption of the home gateway is to compress the data.

Data redundancy would be caused if the sampling rate is too high when a signal is decimated. Reducing the sampling rate can decrease the data quantity. The main frequency

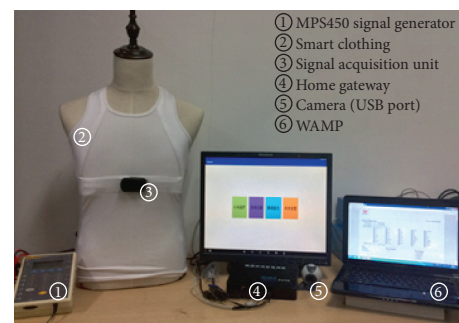


FIGURE 9: Testing environment of the system.

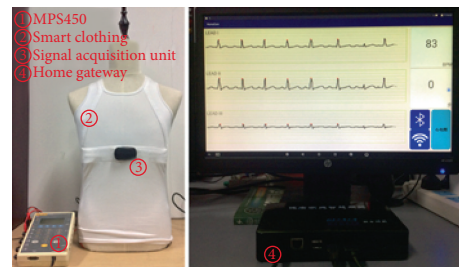


FIGURE 10: Data transmission test of smart clothing and home gateway.

spectrum of the ECG signal ranges from 0.05 Hz to 50 Hz. If the sampling frequency is greater than or equal to 200 Hz, this signal can be downsampled by factor 2, which can decrease the data quantity and keep the frequency range at the same time [12]. The original signal can be reconstructed from the downsampled signal by conducting the interpolation process with acceptable distortion. Discrete cosine transform (DCT) can transform a signal to the frequency domain and preserve the real number only. In addition, the DCT has the property of energy compaction, and the ECG signal information tends to be concentrated in a few low-frequency components of its DCT signal, which can be seen in Figure 7. According to this, the high-frequency part of DCT signal can be abandoned to decrease

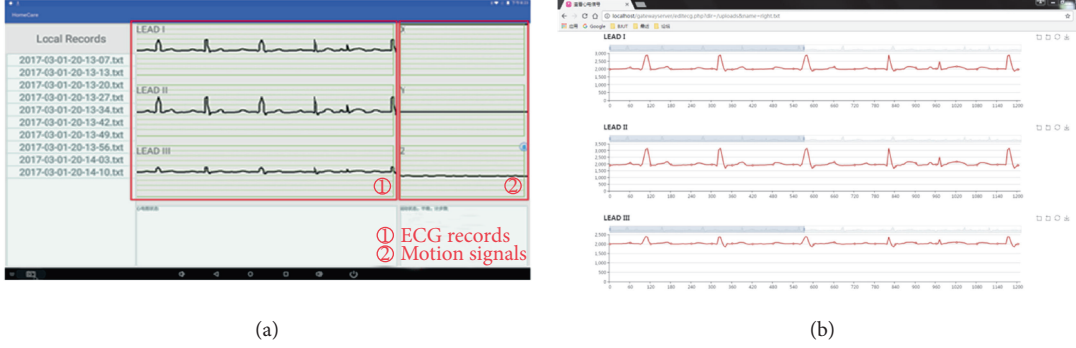


FIGURE 11: Remote data transmission test. (a) ECG and motion signals displayed by gateway. (b) ECG records displayed by a webpage.

the number of ECG data. The method of combining the sampling rate conversion and DCT is used in the design to compress the ECG data.

The process of the data compression is as follows (Figure 8): step 1—detect the R wave locations of ECG signal and choose the data from one R wave location to its next R wave location as the original signal. The R wave locations were detected by using the Pan-Tompkins algorithm [17]. Step 2—decimate the original signal by factor 2 and conduct forward-differential operation. Step 3—get the linear transformation (DCT) of the differential signal. It can be seen that most coefficients are nearly zero from 20% of the signal to the last. So we conserve the first 20% points of the DCT signal (20% filtering window). Step 4—code the filtered DCT signal. The data are encoded by using a fixed encoding table according to the probability of all filtered DCT data, rather than using the Huffman coding method which uses dynamic encoding tables. When decoding, the conserved DCT data are recovered according to the encoding table, and the whole DCT signal was recovered by filling zero at the end of the recovered signal in the previous step. Then the downsampled data are recovered from the reconstructed DCT data, and the original ECG signals are reconstructed by data interpolation.

Data from the MIT-BIH Arrhythmia database (acquired at 360 Hz) and several ECG records collected by using the smart clothing are employed to evaluate the ECG compression algorithm. Compression ratio (CR), distortion rate (DR), and quality score (QS) are used to evaluate the algorithm. CR is the ratio of the data amount before and after compressing, which reflects the decreasing ratio of data after implementing the algorithm. DR refers to the distortion ratio of the reconstructed signal after compression, which is usually measured by percent root-mean-square difference (PRD). QS is the ratio of CR to PRD. The higher the QS is, the higher the CR is and the lower the DR is. The three parameters are computed by

$$CR = \frac{N_{\text{original}}}{N_{\text{reconstructed}}}, \quad (1)$$

$$PRD = \sqrt{\frac{\sum_{i=1}^n (X(i) - \hat{X}(i))^2}{\sum_{i=1}^n (X(i))^2}}, \quad (2)$$



FIGURE 12: Video communication test.

where $X(i)$ denotes the raw data and $\hat{X}(i)$ is the compressed data.

$$QS = \frac{CR}{PRD}. \quad (3)$$

3. Results and Discussion

3.1. System Demonstration. To validate the functionality of the whole system, a test environment is established (shown in Figure 9) and several demonstrations of the proposed system are presented. The MPS450 ECG signals generator is used to generate three-lead ECG signals. The smart clothing is connected to the MPS450 to simulate the process of signal collection. The home gateway is attached to a PC monitor through the HDMI port to simulate the digital TV. It is connected to the Internet via Wi-Fi. A web browser on another PC and a smart phone are used to test the functions of the health care server. The system demonstration includes three main parts, that is, the demonstration of local data transmission, the demonstration of remote data transmission, and the demonstration of video communication function.

Figure 10 shows the validation of local data transmission. On the left side of the figure is the MPS450 ECG signal generator; the smart clothing is connected to it. On the right side are the home gateway and the monitor. The monitor displays the ECG signal collected from the smart clothing in real-time. In the process of long-term ECG data acquisition, the delay of signals is ignorable. We have conducted an experiment of data collecting for 6 hours, and the result shows no data lost during the process. Apart from the ECG graph, the heart rate and the number of steps of the elderly are

TABLE 2: Result of compression algorithm on MIT-BIH database (20% DCT window size).

Number	CR	Evaluation parameters		Time (ms)
		PRD (%)	QS	
100	12.47	1.04	11.99	481
101	12.57	0.99	12.70	300
102	12.48	0.97	12.87	285
103	12.58	1.45	8.68	292
105	12.23	0.67	18.25	294
106	12.62	1.74	7.25	291
107	11.93	1.57	7.60	316
108	12.88	0.60	21.47	241
109	12.14	0.64	18.97	299
111	12.60	0.83	15.18	269
112	12.16	0.77	15.79	275
113	12.91	1.50	8.61	301
114	13.01	0.91	14.30	216
115	12.77	1.97	6.48	288
116	10.42	2.98	3.50	306
117	13.18	0.92	14.33	264
119	12.64	1.70	7.44	315
121	12.79	0.63	20.30	256
122	12.13	1.82	6.66	289
123	13.11	1.52	8.63	298
124	13.21	1.52	8.69	302
200	12.01	1.20	10.01	294
201	11.98	0.61	19.64	272
202	13.10	0.55	23.82	252
203	11.56	1.42	8.14	307
207	12.72	0.62	20.52	267
208	12.08	1.10	10.98	313
209	11.95	1.44	8.30	280
210	12.06	0.70	17.23	271
212	12.02	1.28	9.39	297
214	12.33	1.01	12.21	289
215	11.44	1.28	8.94	302
217	12.47	1.11	11.23	314
219	12.33	1.87	6.59	294
220	12.46	2.25	5.54	290
221	12.34	0.99	12.46	287
222	12.52	0.83	15.08	251
223	12.3	1.26	9.76	292
228	12.38	0.72	17.19	284
230	12.34	1.91	6.46	293
231	12.81	1.37	9.35	307
232	12.64	0.80	15.80	223
233	11.39	1.45	7.86	309
234	12.00	1.00	12.00	282

calculated and shown at the right side of the ECG graph. Figure 11 shows the demonstration of remote data transmission. The home gateway transmits data files to the server by

TABLE 3: Comparison of different compression algorithm (number 100).

Compression algorithm	CR	PRD (%)	QS
EMD [16]	8.86	15.69	0.56
EMD + wavelet [14]	18.16	7.25	2.50
DCT (20% filtering window) [15]	17.21	1.95	8.83
DCT + Huffman [12]	5.14	0.65	7.91
Adaptive run length encoding [11]	5.86	4.08	1.44
Proposed (20% filtering window)	12.47	1.04	11.99

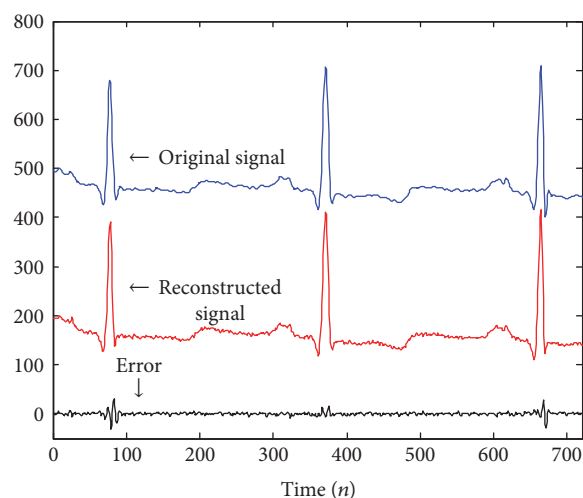


FIGURE 13: Comparison of original and reconstructed signals (number 100).

the Hyper Text Transfer Protocol (HTTP). Figure 11(a) is the ECG graph and the motion signals displayed by home gateway. Figure 11(b) is the ECG signal displayed by a web browser, the data are read from the database of the health care server. It can be found that the ECG graph in Figure 11(a) is the same as the ECG graph in Figure 11(b). The demonstration of video communication is shown in Figure 12. The smart phone on the left side shows the image from the doctors' view; the home gateway displays the corresponding image on the smart phone.

3.2. Data Compression Evaluation. To evaluate the proposed ECG compression algorithm, the first 36000 points (100 s) of each record in MIT-BIH Arrhythmia database are used. The CR, PRD, QS, and the time consumption of each record is shown in Table 2. Compared with the run length encoding method [11], the DCT-based [12, 15] method and the empirical mode decomposition- (EMD-) based method [14, 16] are shown in Table 3. Figure 13 shows the comparison between the original ECG signal and the reconstructed signal of the number 100 record.

It can be seen in Table 3 that the average CR of ECG signals is 12.47 when the first 20% points of DCT signal is conserved (filtered by a 20% window) and the PRD can be

TABLE 4: Result of compression algorithm on data collected by the smart clothing.

Record	Evaluation parameters		
	CR	PRD (%)	QS
001	11.58	1.65	7.03
002	11.19	1.72	6.50
003	10.85	2.19	4.97
004	11.69	1.58	7.39
005	11.72	1.55	7.55
006	11.29	1.65	6.86
007	11.26	2.17	5.20
008	11.59	1.59	7.31
009	11.35	1.76	6.45
Average	11.39	1.76	6.58

controlled around 1.04%. The CR of the proposed method is higher than those of the EMD-based [16] method and the DCT-based [12] method without filtering. The CRs of EMD-wavelet-based [14] method and DCT-based (with 20% filtering window) method [15] are higher than that of the proposed method in this paper, but the PRDs of such two methods are over 2%, which is unsuitable for diagnosing [15]. Also, the run length encoding [11] method has lower CR and higher PRD. In the test, the average processing time is 290 ms, which is suitable for the real-time storage and transmission. The original signal, the reconstructed signal, and the error of reconstruction of the number 100 ECG record are shown in Figure 13. It can be seen that the distortion ratio is low and the error is around zero, demonstrating that the proposed algorithm is effective.

Also, in order to verify the effectiveness of the algorithm in a real scenario, experiments of using data acquired by smart clothing were conducted. Each ECG record was collected by 10 seconds (2500 points), and the test results are listed in Table 4. As shown in Table 4, the average CR is 11.39, and the average PRD is controlled below 2%, which demonstrates that the proposed algorithm is effective.

4. Conclusions

In this paper, a remote health monitoring system for the elderly based on the smart home gateway is proposed. The system has good scalability and operates easily. It can provide long-term and continuous monitoring for the elderly. In consideration of the mass data generated in the monitoring process, an ECG compression algorithm is designed. Demonstrations of the system validate that the whole system is effective and has the potential to be used in a real scenario. The test of the compression algorithm shows the possibility of applying the compression method to the real-time monitoring system.

Conflicts of Interest

The authors declared that they have no competing interest.

Acknowledgments

This work was supported by the National Natural Science Foundation of China (no. 71661167001).

References

- [1] C. Maiolo, E. I. Mohamed, C. M. Fiorani, and A. De Lorenzo, "Home telemonitoring for patients with severe respiratory illness: the Italian experience," *Journal of Telemedicine and Telecare*, vol. 9, no. 2, pp. 67–71, 2003.
- [2] M. Vitacca, G. Assoni, P. Pizzocaro et al., "A pilot study of nurse-led, home monitoring for patients with chronic respiratory failure and with mechanical ventilation assistance," *Journal of Telemedicine and Telecare*, vol. 12, no. 7, pp. 337–342, 2006.
- [3] M. M. Baig, H. Gholamhosseini, and M. J. Connolly, "A comprehensive survey of wearable and wireless ECG monitoring systems for older adults," *Medical & Biological Engineering & Computing*, vol. 51, no. 5, pp. 485–495, 2013.
- [4] M. M. Baig, H. Gholamhosseini, and M. J. Connolly, "Mobile healthcare applications: system design review, critical issues and challenges," *Australasian Physical & Engineering Sciences in Medicine*, vol. 38, no. 1, pp. 23–38, 2015.
- [5] M. Chen, J. Wan, S. González-Valenzuela, X. Liao, and V. C. Leung, "A survey of recent developments in home M2M networks," *IEEE Communications Surveys & Tutorials*, vol. 16, no. 1, pp. 98–114, 2014.
- [6] A. Bansal, S. Kumar, A. Bajpai et al., "Remote health monitoring system for detecting cardiac disorders," *IET Systems Biology*, vol. 9, no. 6, pp. 309–314, 2015.
- [7] S. J. Jung, R. Myllylä, and W. Y. Chung, "Wireless machine-to-machine healthcare solution using android mobile devices in global networks," *IEEE Sensors Journal*, vol. 13, no. 5, pp. 1419–1424, 2013.
- [8] B. S. Lin, P. C. Hsiao, P. H. Cheng, I. J. Lee, and G. E. Jan, "Design and implementation of a set-top box-based homecare system using hybrid cloud," *Telemedicine and e-Health*, vol. 21, no. 11, pp. 916–922, 2015.
- [9] S. Spinsante and E. Gambi, "Remote health monitoring by OSGi technology and digital TV integration," *IEEE Transactions on Consumer Electronics*, vol. 58, no. 4, 2012.
- [10] A. M. Rahmani, N. K. Thanigaivelan, T. N. Gia et al., "Smart e-health gateway: bringing intelligence to internet-of-things based ubiquitous healthcare systems," in *2015 12th Annual IEEE Consumer Communications and Networking Conference (CCNC)*, pp. 826–834, Las Vegas, NV, USA, January 2015, IEEE.
- [11] C. M. Agulhari, I. S. Bonatti, and P. L. D. Peres, "An adaptive run length encoding method for the compression of electrocardiograms," *Medical Engineering & Physics*, vol. 35, no. 2, pp. 145–153, 2013.
- [12] D. C. Pandhe and H. T. Patil, "ECG data compression for a portable ECG recorder and transmitter," in *2014 International Conference on Advances in Communication and Computing Technologies (ICACACT)*, pp. 1–5, Mumbai, India, August 2014, IEEE.
- [13] M. S. Manikandan and S. Dandapat, "Wavelet-based electrocardiogram signal compression methods and their performances: a prospective review," *Biomedical Signal Processing and Control*, vol. 14, pp. 73–107, 2014.

- [14] X. Wang, Z. Chen, J. Luo, J. Meng, and Y. Xu, "ECG compression based on combining of EMD and wavelet transform," *Electronics Letters*, vol. 52, no. 19, pp. 1588–1590, 2016.
- [15] S. J. Lee, J. Kim, and M. Lee, "A real-time ECG data compression and transmission algorithm for an e-health device," *IEEE Transactions on Biomedical Engineering*, vol. 58, no. 9, pp. 2448–2455, 2011.
- [16] K. Khaldi and A. O. Boudraa, "On signals compression by EMD," *Electronics Letters*, vol. 48, no. 21, pp. 1329–1331, 2012.
- [17] J. Pan and W. J. Tompkins, "A real-time QRS detection algorithm," *IEEE Transactions on Biomedical Engineering*, vol. BME-32, no. 3, pp. 230–236, 1985.